学位論文

Formation of supermassive stars and black holes via direct gravitational collapse of primordial gas clouds

(始原ガス雲の重力崩壊による超大質量星形成およびブラックホール形成)

平成29年12月 博士（理学）申請

東京大学大学院理学系研究科
物理学専攻

鄭 昇明

Copyright © 2018, Sunmyon Chon.

Abstract

Recent observations report that SuperMassive Black Holes (SMBHs) reside at the center of local galaxies. They are also common in the early universe, as we have now observed more than one hundred SMBHs at $z > 6$. The fact that they are observed at the cosmic age of $\lesssim 0.8$ Gyr gives a clue to understand the formation history of SMBHs. Historically, Rees (1978) compiles a number of the formation channels of SMBHs known at that time. They are divided largely into two classes: the channels with and without SuperMassive Stars (SMSs) formation.

This thesis studies the formation of SMSs in the early universe as possible seeds for the observed SMBHs. How massive the first generation stars can be, has been intensely studied for the last few decades (e.g. Hirano *et al.*, 2014). The recent discovery of the atomic-cooling path suggests a promising formation channel of SMSs (e.g. Omukai, 2001; Bromm & Loeb, 2003). The cloud collapsing along this evolutionary path radiates away the internal energy by H atomic emission, not by H_2 molecular emission as in the normal primordial star formation. The atomic-cooling clouds can yield the SMSs with 10^5 – 10^6 $M_\odot$ (e.g. Latif *et al.*, 2013). Such massive stars collapse into massive BHs due to the general relativistic instability (Iben, 1963), and then grow into SMBHs with further mass accretion. This SMBH formation channel is often dubbed as “Direct Collapse (DC)” scenario.

Our main goal is to test the DC scenario in the cosmological context. In the last few years, various authors study the SMS formation under the idealized environment (Shang *et al.*, 2010). They focus on arbitrary atomic-cooling halos and artificially turn off molecular cooling. In reality, however, the molecular hydrogen should be destroyed due to i.e. the radiation from a nearby star-forming galaxy. To learn whether an SMS forms in realistic environments set by the cosmological initial conditions, we for the first time demonstrate the SMS formation fully consistent with the formation of galaxies which provide molecular dissociating photons. Specifically, we perform hydrodynamics simulations that start from the cosmological initial conditions, solving the radiation transfer from the star-forming galaxies.

We have found several important effects for the SMS formation that have been overlooked in the previous studies. Tidal force is one of such effects, which counteracts the self-gravity of the collapsing cloud and can prevent the cloud collapse. Since a luminous and massive galaxy is located just close to the collapsing cloud, tidal force significantly affects the cloud evolution in most of the cases. We have performed the simulations for 42 candidate clouds in the simulation box with 20 h^{-1}Mpc on a side and found that only two out of 42 candidates collapse into the protostellar cores. The two “successful” samples experience a major merger just before the onset of the cloud collapse, which transports the gas toward the cloud center where tidal force is weak. Our results indicate that the environmental effects, such as tidal field from the source galaxy, reduce the SMS formation rate by an order of magnitude, compared with the previous studies that do not consider such effects.

We have also examined the effects of the ionizing radiation coming from the source galaxy. What we have found is that the ionizing radiation has large impact on the cloud evolution when the candidate cloud is located inside the void region. Meanwhile in reality, the cloud approaches mainly along the filament that protects the cloud from the ionizing radiation. Therefore, the ionizing radiation can only have small impact on the cloud evolution since these filaments attenuate the ionizing radiation.

We further follow the cloud evolution after the protostellar cores are formed at the cloud centers. Starting from the two “successful” clouds, we perform radiation hydrodynamics simulations that follow the long-term evolution for 0.1 million years. Interestingly, tidal force still has great impacts on the cloud evolution at 10^2 – 10^4 AU scale. One cloud suffers from the strong tidal force from the nearby galaxy, which yields an order of ten SMSs with 10^3–10^4 $M_\odot$ after the stellar lifetime. The other one suffers from relatively weak tidal force, and that a few SMSs with 10^4–10^5 $M_\odot$ will be expected. The reason why the tidal force is important at such small scales is owing to the nature of isothermal collapse, which enhances the bar-mode perturbation during the collapse. In fact, the tidal force itself is not important at 10^2 – 10^4 AU scale. The tidal force only seeds the initial bar-mode perturbation, which grows during the collapse to finally cause the fragmentation of the filamentary cloud. The stellar multiplicity is enhanced by this effect. These SMSs will collapse into BHs, after they exhaust the nuclear hydrogen or during the hydrogen burning stage due to general relativistic instability.

Future gravitational wave (GW) observations can give some implications about the formation process of SMBHs. Our simulations have shown that several BH binaries will appear as a result of the cloud fragmentation. If they merge as interacting with the other gaseous or stellar components, we can observe the GW signals by future space GW observatories, LISA and DECIGO. We expect a number of GW signals by BH binary mergers with 10^4–10^5 $M_\odot$, if the DC scenario provides a dominant fraction of seed BHs.

These are the first examples of the seed BH formation that is predicted by DC scenario. To compare our results with the observed number density of the $z > 6$ QSOs, we should further follow the growth of seed BHs. In fact, the number density of formed SMSs in our simulations ($\sim 10^5$ Gpc^{-3}) is much larger than that of the observed $z > 6$ QSOs (~ 1 Gpc^{-3}), while the number density of SMSs we found is by an order of magnitude smaller than the previous studies. The further mass growth of such seed BHs is expected because the cloud containing the BH will fall into the UV-illuminating galaxy center, which has a plenty of gas to feed the BH. The efficient Eddington accretion allows these BHs to attain the masses of 10^9 $M_\odot$ at $z \gtrsim 6$. We should also uncover whether these

massive SMBHs provide us the observable signals. If the BHs are embedded in the dense surroundings, we may not observe their existence. These two factors – the BH growth and the observability of the SMBHs – can resolve the discrepancy of the number density of SMSs and the observed SMBHs.

Contents

Abstract **i**

Contents viii

List of Figures xix

List of Tables xxi

1 **Introduction** **1**

2 **A Brief Summary of the Massive BH Formation in the Early Universe** **4**
- 2.1 Black Holes in the Universe 4
- 2.2 Eddington Limit of Mass Accretion Rate 5
- 2.3 Chemo-thermal Evolution of Primordial Star-forming Clouds 7
  - 2.3.1 Birth place of primordial stars 8
  - 2.3.2 Structure of H_2 10
  - 2.3.3 H_2 Formation 11
  - 2.3.4 H_2 cooling 12
  - 2.3.5 The impact of the external radiation field 13
- 2.4 Population III Star Formation 14
  - 2.4.1 Collapse phase 14
  - 2.4.2 Accretion phase 16
  - 2.4.3 Protostellar evolution and radiation feedback 16
    - 2.4.3.1 contracted ZAMS phase ($\dot{M}_* < 0.004\ M_\odot\ \mathrm{yr}^{-1}$) 17
    - 2.4.3.2 oscillating protostar phase ($0.004 < \dot{M}_* < 0.04\ M_\odot\ \mathrm{yr}^{-1}$) 17
    - 2.4.3.3 supergiant protostar phase ($\dot{M}_* > 0.04\ M_\odot\ \mathrm{yr}^{-1}$) 17
- 2.5 Supermassive Star Formation by the Direct Collapse Model 18
  - 2.5.1 Star formation after the population III formation 18
  - 2.5.2 Supermassive star formation 19
- 2.6 Fate of the Primordial Stars 20
- 2.7 Mass Evolution of Black Hole Seeds 22
  - 2.7.1 Multi-dimensional simulation of mass growth of population III remnant black holes 22

2.7.2 Multi-dimensional simulation of mass growth of supermassive star remnant black holes . . . 23

3 **Searching Candidate Site for SMS Formation** **25**
3.1 Overview . . . 25
3.2 Methodology . . . 25
3.2.1 Parent N-body simulations . . . 25
3.2.2 Construction of merger tree . . . 26
3.2.3 Semianalytic model for star and galaxy formation . . . 26
3.2.3.1 Population III star formation and metal enrichment 27
3.2.3.2 Population II star formation . . . 27
3.2.4 LW radiation field . . . 28
3.2.4.1 Population III star formation under the LW radiation . . . 29
3.2.5 Selection of DC halos . . . 29
3.3 Results from the N-body Simulation . . . 31
3.3.1 Star formation and the LW radiation . . . 31
3.3.2 DC candidate halos . . . 32
3.3.3 Spins of DC candidate halos . . . 34

4 **Cosmological Hydrodynamics Simulation for SMS Formation** **35**
4.1 Overview . . . 35
4.2 Methodology . . . 36
4.2.1 Hydrodynamical simulation . . . 36
4.3 Cloud Collapse in DC candidate Halos . . . 37
4.3.1 Case F1: collapse prevented by strong tidal force . . . 37
4.3.2 Case F2: collapse prevented by ram pressure stripping . . 40
4.3.3 Cases S1 and S2: DC clouds . . . 44
4.3.3.1 The evolution of S1 . . . 44
4.3.3.2 The evolution of S2 . . . 46
4.3.4 Thermal evolution of DC gas clouds . . . 48
4.4 Formation of a protostar . . . 49
4.5 Cloud Collapse under Strong Tidal Field . . . 51
4.5.1 Evolution of tidal radius . . . 52
4.5.2 Onset of the cloud collapse . . . 55
4.6 Discussion . . . 59
4.6.1 Critical LW intensity for DC . . . 59
4.6.2 Effects of ionization photons and X-Ray . . . 60
4.6.3 Effect of metal enrichment . . . 62
4.7 Chapter Summary . . . 63

5 **The Impact of Ionizing Radiation on the SMS Formation** **65**
5.1 Overview . . . 65

5.2 Methodology 66
5.2.1 Hydrodynamical calculation 66
5.2.2 Radiation transfer 66
5.2.2.1 Low energy radiation($h\nu < 13.6$ eV) 66
5.2.2.2 Ionizing radiation($h\nu > 13.6$ eV) 67
5.3 Result 69
5.3.1 Cloud collapse 69
5.3.2 Visual inspection 72
5.3.3 Temperature profiles around the DC cloud 76
5.4 Discussion 77
5.4.1 Size of HII region 77
5.4.2 Ionization of the DC candidate halos 78
5.4.3 Environment dependence of $R_{\rm st}$ 79
5.4.4 Spectrum of the radiation source 81
5.4.5 Effect of radiation pressure 82
5.4.6 Effect of the dust attenuation 83
5.5 Chapter Summary 85

6 Radiation Hydrodynamics Simulations of the SMS Formation 86
6.1 Overview 86
6.2 Methodology 87
6.2.1 Initial condition 87
6.2.2 Chemistry 89
6.2.3 Particle splitting 89
6.2.4 Sink particle 89
6.2.5 Stellar evolution model 91
6.2.5.1 Supergiant protostar phase 91
6.2.5.2 ZAMS phase 91
6.2.6 Transfer of ionizing radiation 92
6.3 Results 92
6.3.1 Early collapse phase 92
6.3.2 Later accretion phase 96
6.3.2.1 Disk and protostar evolution 97
6.3.2.2 Stellar mass growth histories and disk fragmentation 102
6.3.2.3 Mass distribution of the protostars 103
6.3.2.4 Merger and ejection of protostars 104
6.4 Radiation Feedback 108
6.4.1 Limitation of our radiative transfer model 109
6.4.2 Radiation feedback with higher resolution 109
6.5 Discussion 110
6.5.1 Final mass of the SMS and its fate 110

6.5.2 Evolution of the DCBH binaries 111
6.5.3 The impact of FUV radiation inside the circumstellar disk 114
6.5.4 limitations in numerical method 115
6.6 Chapter Summary 115

7 Conclusion 117
7.1 Summary 117
7.2 Future Prospects 118

A Basics in Star Formation 123
A.1 Collapse Phase 123
A.1.1 Linear analysis 124
A.1.2 Onset of the collapse in the isothermal cloud 125
A.1.3 Runaway collapse 126
A.2 Accretion Phase 128

B Implementation of Radiation Transfer 130

C Particle De-refinement Prescription 132

D The Infalling Velocities of DC Candidate Halos 134
D.1 Linear Over Density within R 134
D.2 Enclosed Mass and Turnaround Radius 135

E Analytic Estimate of the Radiation Feedback Effects 137

Bibliography 140

List of Figures

2.1 Projected DM density distribution at $z \sim 20$. The large-scale structure, such as the cosmic filament and halos are shown. White circles indicate the mini halos, at which the primordial stars are thought to be born. . 9

2.2 Effective potentials energy of H_2 as functions of the separation of two protons. The solid lines show the energy for the different electron states, labeled $\mathrm{X}^1\Sigma_\mathrm{g}$ (ground state), $\mathrm{B}^1\Sigma_\mathrm{u}$, and $\mathrm{C}^1\Pi_\mathrm{u}$ from the bottom to top (Kołos & Wolniewicz, 1965, 1966). The horizontal thin lines show the vibration states ($v = 0, 5, 10,$ and 14) with the electron ground state (Kolos & Wolniewicz, 1968). The upper dotted line represents the Lyman-limit ($h\nu$ = 13.6 eV), above which the radiation will be mainly consumed by the ionization of the hydrogen atoms. 10

2.3 Phase diagram of the temperature and the H_2 fraction f_{H2}. Inside the shaded region, the cloud satisfies $t_{\mathrm{cool}} = t_{\mathrm{Hubble}}$ (eq. 2.18) and the cloud collapse thought to be initiated by H_2 cooling. The dashed line represents the typical abundance of H_2 (eq. 2.14). 12

2.4 The temperature evolutions of the collapsing primordial gas cloud under the different FUV intensity. The calculation is based on so-called “one-zone” model, at which the density increases at a rate of the free-fall time. In the calculation, we solve the non-equilibrium chemistry and the energy equations. From the bottom to top lines, we represent the cloud evolutions under no FUV (blue), FUV intensity with J_{21} = 0.01, 1 (black), and 100 (red). 15

2.5 Schematic picture of the cosmic environment after the light sources appear in the universe. We assume here the light source to be the Pop III stars or the galaxy. Just around the light source, the gas is ionized and no star formation is expected in this region since the gas temperature is too high. The metal enriched region extends a little further, inside which the low mass Pop II stars will form. The primordial and H_2 photo-dissociated region (PDR) extends ∼Mpc. In this region, the cloud evolution differs from those of the isolated Pop III stars. Especially, if H_2 is completely destroyed and the molecular cooling rate becomes negligible, the SMSs can emerge. 18

2.6 The final fate of the primordial stars as a function of the stellar mass at the main-sequence phase. 21

2.7 The mass evolutions of the BHs, starting from (1) the remnant BHs of Pop III stars (blue) and (2) the remnant BHs of SMSs (green). The solid and dashed lines assume the accretion with $f_{\rm Edd} = 1$ and 0.6, respectively. Stellar symbols represent the mass and the redshift of the SMBHs at $z \gtrsim 5.5$. SMBH samples are taken from the results of NIR spectroscopies, listed at Table 2.1. 23

3.1 Distributions of the LW intensities $J_{21}^{\rm III}$ and $J_{21}^{\rm II}$ at the primordial halos center at (a) $z = 23.1$ and (b) $z = 9.3$. The dashed lines show the critical intensities for Pop II (red) and Pop III sources (blue). 31

3.2 (a) Number of DC candidate halos (black) and the Pop III SFRD (red) as functions of the redshifts for all the zoom-in regions. (b) Time evolution of the fraction of metal-enriched halos. Each line indicates the fraction for halos of $T_{\rm vir} = 2000$ (purple), 3000 (green), 4000 (blue), and 6000 K (yellow). 33

3.3 Spin parameter distributions for all the halos (dashed) and DC candidate halos (solid). The vertical axis shows the fraction of halos in each bin (dex^{-1}). Red arrows represent the angular momentum for S1 and S2 halos, which will collapse into the protostellar cores (see Section 4.3). . 33

4.1 (a) Merger tree for case F1 (DC14). The blue, black, and red circles represent halos with $T_{\rm vir} < 2000$ K, $2000 < T_{\rm vir} < 8000$ K, and $T_{\rm vir} > 8000$ K, respectively. (b) Evolution of J_{21} at the halo center. The solid line indicates the evolution of the LW intensity, and the dashed line shows the critical LW intensity required for the DC criteria, $J_{21}^{\rm crit} = 100$. (c) Time evolution of the maximum gas density inside the candidate halos. (d) Tidal radius normalized by $R_{\rm vir}$ of the candidate halo. The dashed line indicates where the tidal radius becomes comparable to the virial radius of the host halo. Inside the shaded region, $T_{\rm vir}$ exceeds 8000 K, at which the atomic H cooling operate. Epochs A, B, C, and D are the reference epochs attached in Figure 4.2. The redshifts are also shown at the top of panel (a). The reference dynamical time at $t = 0$ is 0.04 Gyr, indicated by the black arrow in panle (b). 38

4.2 Time evolution of the F1 halo at four epochs attached in Figure 4.1. Left: temperature-density phase diagram of the halo gas. The color scale represents the cell mass in each bin. Middle: the projected DM density map around the F1 halo. The large clump at the bottom-left corner in each panel corresponds to the source halo. The candidate halo is located inside the white box. The color scale represents the DM density. Right: the projected gas density around the halo. There are two main clumps in each panel, and the clump on the left is the DC candidate halo (contained by the circle). The other clump is a halo in which a Pop III star is already formed. In each panel, the comoving length-scales of 20 h^{-1}kpc and 5 h^{-1}kpc are represented with the arrows. 39

4.3 (a) Evolution of the gas density in the DC cloud for case F2 (DC2). The horizontal axis shows the elapsed time since the host halo satisfies DC criteria and normalized by the dynamical time at $t = 0$. (b) Evolution of the tidal radius divided by the virial radius of the host halo. The dashed line indicates where the tidal radius becomes comparable to the virial radius of the host halo. (c) Ratio of the ram pressure exerted on the cloud (eq. 4.2) and the gravitational force per unit area. The dashed line shows where the magnitudes of ram pressure and the gravitational force becomes comparable. The epochs A, B, C, and D are the reference epochs used in Figure 4.4. The reference dynamical time at $t = 0$ is $t_{\rm dyn} = 27.7$ Myr. . 41

4.4 Time evolution of F2 halo at the four reference epochs attached in Figure 4.3(c). Left: the projected DM density distributions. The large clump at the top-left corner in each panel corresponds to the source halo. The candidate halo is located inside the circle. Right: the projected gas density around the candidate halo, the same region as in the left column. The elapsed time t from epoch A is attached to each panel. 42

4.5 Radial density profiles of the (a) DM and (b) baryons for the F2 halo at the four reference epochs shown in Figure 4.3(c). The horizontal axis represents the distance from the density maxima of the cloud. To compare the DM density with the gas density, we convert the DM density into the corresponding baryon number density by $n_{\rm DM} \equiv f_{\rm b}\rho_{\rm DM}/(1.2m_{\rm p})$, where 1.2 is the mean molecular weight of the neutral gas. 43

4.6 Same as Figure 4.1but for case S1. There are two main branches (A and B), and the DC candidate halo is the product of the major merger of these two branches. The solid blue and green lines in panel (b) represent the evolutiond of the LW intensity at the halo center of branches A and B. The reference dynamical time at $t = 0$ is $t_{\rm dyn} = 26.9$ Myr. 45

4.7 Evolution of gravitational radii (blue; eq. A.17) and the tidal radii (green) for (a) S1 and (b) F1, where each radii are normalized by the virial radii. The time origin $t = 0$ is set to be the moment at which the halo satisfies the DC criteria, and the time is normalized by the halo dynamical time at $t = 0$. 46

4.8 Same as Figure 4.2, but for four reference epochs for case S1 shown in Figure 4.6. We can observe six small clumps in epochs A and B that are merged into the DC candidate halo in epochs C and D. 47

4.9 Radial profiles of the enclosed mass before ($z = 24.1$; black dashed) and after the major merger ($z = 19.5$; black solid) for the S1 halo. The red line shows the profile of the Bonnor–Ebert mass after the merger. . . . 48

4.10 Time evolution of 16 gas clouds hosted by DC candidate halos. (a) Evolution of the central gas density n as functions of time t. We stress the four representative cases with thick lines: F1 (green), F2 (blue), S1 (red solid), and S2 (red dashed). The blue and green lines show the uncollapsed clouds that satisfy the DC criteria before and after $z = 17$, respectively. At the end of each line, the target halo merges with the light source halo, except for the collapsed clouds. (b) Temperature evolution as functions of the density for the 15 representative cases (S2 is not plotted since it follows almost the same path as for S1). The vectors represent the evolution at every $0.25t_{\rm dyn}$ for cases F1, F2, and S1 as in panel (a). For the other 12 DC clouds, we only plot the evolution paths on the plane, and the evolution is averaged for every $t_{\rm dyn}$. The black solid line indicates the adiabat, $T \propto n^{2/3}$. In each panel, the shaded region shows $T_{\rm vir} > 8000$ K, at which atomic hydrogen cooling operate. 49

4.11 Bottom left: the schematic figure of the locus of the S1 halo relative to the radiation source. The red arrow represents the path of the DC halo. Bottom-right, top-right, top-left: The projected gas density distributions around the DC halo at the different epochs of $t = 48.9$, 52.3, and 52.7 Myr counterclockwise. This reference epochs correspond to the positions of 1, 2, and 3 in the bottom-left panel. The time origin is again the moment when the halo satisfies the DC criteria. 50

4.12 Radial gas density profiles in the S1 halo at $t = 48.9$, 52.3, and 52.7 Myr. The dashed line represents the tidal radius at which the tidal force dominates over the self-gravity of the gas cloud at $t = 52.7$ Myr. 51

4.13 Instantaneous mass infall rates $|\dot{M}| = 4\pi r^2 \rho |v|$ as functions of the enclosed mass $|M(< R)|$. The infall rates are estimated from the snapshots, at which the central density reaches 2×10^7 cm^{-3}. We show the profiles for S1 (red) and S2 (blue). The solid lines show the mass infall rates, while the dashed lines show the mass outflow rates. 52

4.14 Time evolution of the source halo mass M_s and the comoving distance between the DC candidate and source halos d_dist for all 68 candidate halos. Panels (a), (b), and (c) represent the snapshots at the different epochs $t = 0$, 0.5, and $1.0 t_\mathrm{dyn}$, respectively. The candidate halos satisfy the DC criteria at $t = 0$. The symbol colors show the virial temperature of the halos, $T_\mathrm{vir} < 8000$ K (red) and > 8000 K (green). The filled and open circles represent whether the hydrodynamical simulations (HS) are performed. The halos that host the collapsed clouds (S1 and S2) are emphasized by the larger circles. In each panel, the shaded area indicates $R_\mathrm{tid} < R_\mathrm{vir}$, at which the tidal force is strong enough to disrupt the halo envelope. The solid line shows the critical points for $R_\mathrm{tid} = R_\mathrm{vir}$. 53

4.15 Infall time of the target halo from d_LW (eq. 4.5) to d_tid (eq. 4.6), normalized by the dynamical time at each epochs. The lines show the evolution for the source halos formed around 3σ (green), 5σ (purple), and 7σ (orange) initial density peaks. The solid and dotted lines are the results for the fiducial and enhanced star formation efficiency, $f_* = 0.005$ and 0.1, respectively. The other two cases with 3σ and 5σ with $f_* = 0.005$ are not presented since d_LW is always smaller than d_tid. The horizontal dashed line denotes $t_\mathrm{inf} = t_\mathrm{dyn}$. 54

4.16 (a) Entropies of the cloud core normalized by K_{200} (eq. 4.8). The colored symbols represent the collapsed halos S1 (red) and S2 (blue), whereas the gray symbols show the uncollapsed clouds. The open and filled symbols show the entropies of collapsed clouds before and after the major merger, respectively. The dashed line shows the averaged value of the entropy estimated from the universal profile. (b) Evolution of the core radius and core density after the host halo satisfies the DC criteria. The start (filled circle) and end points of each arrow indicate the core properties when the halos satisfy the DC criteria and $1 t_\mathrm{dyn}$ after that moment, respectively. The black solid line represents the analytical core radius–density relation estimated by eq. (4.11). The cloud gets gravitationally unstable inside the shaded region, satisfying eq. (4.12). 56

4.17 (a) Thermal evolution of the collapsing cloud S1 with the reduced LW luminosities of the light source halo: 0.5% (green), 0.8% (blue), 1% (red), and 2% (black) of the original luminosities. (b) Time evolution of J_{21} for the same cases. The crosses represent the moments at which the cloud density reaches $n_\mathrm{LTE} = 10^3\ \mathrm{cm}^{-3}$. The dashed line represents the evolution of LW intensity for $n > n_\mathrm{LTE}$. 58

4.18 (a) Evolution of the temperature with the increasing density with and without ionizing radiation. The lines shows the evolution with the black-body radiation with $T_{\rm eff} = 10^4$ K(blue) and without ionizing photons (black). The dashed line corresponds to the result of 3D simulation (S1), while the solid lines are those of the one-zone calculation. In the presented one-zone models, the density evolution is taken from our 3D hydrodynamical simulation (see eq. 4.13). The radiation intensity is the same as the normalization of the intensity at the LW bands, $J_{21,\rm LW}$. (b) Evolution of the temperature with and without X-rays of the QSO-type spectra, $J_{21} = J_{21,\rm X}(\nu/\nu_0)^{-\alpha}$. The black line represents the evolution without the X-rays, while the green, blue, and red lines represent those with $J_{21,\rm X} = 1$, 10^2, and $10^3 \times FJ_{21,\rm LW}$, respectively. 61

5.1 Time evolution of (a) source luminosity and (b) stellar mass for Model 1e41 (magenta), 1e42 (blue), SFE0.1 (red), and SFE0.005 (green). Time origin is set to be the moment when the source galaxy starts to emit ionizing photons. The dashed lines A, B, and C are the reference points used in the later discussion. The stellar masses for SFE0.1 and SFE0.005 are directly obtained from semianalytic calculation, whereas for 1e41 and 1e42, the stellar mass is given by eq. (5.1). The dotted line in panel (a) shows the LW intensity J_{21}, which is assumed to be the same for all models. 67

5.2 Evolutions of (a) density and (b) temperature of the DC clouds for Models 1e41 (magenta), 1e42 (blue), SFE0.1 (red), and SFE0.0005 (green). Time origin is the moment when the galaxy starts to emit ionizing photons. The grey line shows the virial temperature of the host halo in panel (b). The virial temperature turns to decrease at $t \sim 0.07$ Gyr due to the tidal disruption. 68

5.3 We show gas properties for Model SFE0.005, $X_{\rm ion}$, n, and temperature at the left, middle, and, right columns, respectively. Each row A, B, and, C corresponds to the snapshot at the reference epoch marked in Figure 5.1. The Black solid circle and the square box in each panel indicates the ionizing source and the focused DC halo and its progenitors, respectively. In this model, no ionized region expands around the ionizing source. . . 70

5.4 Same as Figure 5.3but for Model SFE0.1. The HII region expands in anisotropic manner reflecting the structures (voids, filaments, etc) in the universe. The DC cloud itself is surrounded by the dense filament so that the cloud remain neutral. At epoch C, the DC cloud collapses into the dense core. 71

5.5 Same as Figure 5.3but for Model 1e41. The overall evolution is similar with the case for SFE01, in a sense that the ionized region expands in anisotropic manners. Since the luminosity is larger at the early epoch than SFE01, a part of the DC cloud gets photo-evaporated around epochs A – B, compared with SFE01. As a result, the DC cloud does not collapse in this model. 72

5.6 Same as Figure 5.3but for Model 1e42. In this model, gas in the DC halo gets photo-evaporated just after the ionizing radiation turns on. 73

5.7 Projected density (top) and $X_{\rm ion}$ (bottom) maps for Model 1e41 at epoch C in Figure 5.1. The circles and boxes represent the positions of the ionizing source and the DC halo, respectively. Thick arrows indicate another collapsing cloud near the DC halo ("2nd DC halo"). 74

5.8 Radial temperature profiles around the DC halo for Models 1e41 (magenta), 1e42 (blue), SFE0.005 (green), and SFE0.1 (red). Each panel corresponds to the profiles at the reference epochs A, B, and C in Figure 5.1. 75

5.9 Radial density profiles around the source halo for Model SFE0.1. The black lines represent the spherical averaged profiles, while the red lines represent the density profiles along the ray which is directed toward the DC cloud. Each row corresponds to the profile at the reference epochs A, B, and C in Figure 5.1. 76

5.10 Mean number density $\bar{n}$ versus distance from the source halo R is plotted for 68 DC halos found in the N-body simulation shown in Chapter 3. Panels (a) and (b) show the snapshots at different epochs, $t = 0$ and $1t_{\rm dyn}$, where the time origin is the moment when the halos satisfy the DC criteria. Filled circles correspond to the DC halos confirmed to collapse by hydrodynamical simulation. The blue filled circle corresponds to the halo whose evolution is calculated by the radiative hydrodynamical simulation in this chapter. The end points of arrows in panel (a) show values at $t = 1t_{\rm dyn}$. The dashed lines represent the cosmic mean density at $z = 15$ and the shaded regions indicate $R < R_{\rm st}$ for $L_{\rm UV} = 10^{41}$ erg s^{-1}. 79

5.11 (a) The radial density structures around the halo, whose mass is $10^7\ M_\odot$ at $z = 27$. The purple lines show the mean density profiles around the halo, while the green and blue lines show the density structures around the halo at the filamentary and void regions, respectively. (b) The radial profiles of the required UV luminosity, $L_{\rm UV}$, to ionize hydrogen under the density profiles given in panel (a). 80

5.12 R_{st} (eq. 5.2) and R_{J21} (eq. 5.4) as a function of the mean number density, $\bar{n}$ under the UV luminosity of (a) 10^{41} erg s^{-1} and (b) 10^{42} erg s^{-1}, respectively. The purple lines show R_{st}, while dotted lines show R_{J21} assuming the black-body spectra with $T_{\mathrm{eff}} = 10^4$ (green), 2×10^4 (blue) , and 10^5 K (yellow). R_{J21} does not depend on $\bar{n}$ since we assume LW radiation is completely optically-thin. 81

6.1 Schematic view showing the locations of the spherical and the filamentary clouds. The clouds are taken from a large-scale cosmological simulation with the box size of 20 h^{-1}Mpc on a side. In Chapter 4, the cloud evolution has been followed until the central density reaches 10^8 cm^{-3} during the early runaway collapse. We further follow the subsequent long-term evolution for ~ 0.1 Myr in this chapter. 88

6.2 Mass distribution on the density-temperature phase diagram for (a) the filamentary and (b) the spherical clouds. The snapshots are taken when the maximum density reaches 10^{12} cm^{-3} in the early runaway stage. We divide the whole domain into 200×200 cells. The color scale shows the gas mass contained within each cell. 93

6.3 (a) Radial density profiles for the filamentary (green) and the spherical (blue) clouds. Three vertical lines A, B, and C indicate the characteristic length-scales, where the filamentary cloud shows the density bumps. The power-law profile with $n \propto R^{-2}$ is also depicted as the black solid line. (b) Radial profiles of the infall mass rate ($\dot{M}_{\mathrm{infall}}$, eq 6.7). 94

6.4 Projected density maps in the filamentary cloud when the maximum density reaches 10^{12} cm^{-3}. The physical scales become smaller from top to bottom. Left and right panels show the density maps projected onto the different planes, which are perpendicular to each other ("xy" and "xz"). Solid circles (A, B, and C) represent the scales shown in Figure 6.3. . . . 95

6.5 Evolution of the axial ratios $\mathcal{Q}$ during the cloud collapse for the filamentary (blue) and the spherical (green) clouds. To derive $\mathcal{Q}$, we first fit the iso-density region by sets of ellipsoids. The ratio, $\mathcal{Q}$ is then defined as the ratio of a_3 to a_1, where a_1 and a_3 are the length of longest and shortest axes of fitted ellipsoids. The upper horizontal axis denotes the Jeans length (eq. 6.8) the fixed temperature at 8000 K. The vertical dashed lines A, B, and C indicate the reference scales shown in Figure 6.3(a). 96

6.6 Distributions of Toomre-Q parameters (eq. 6.9) around the central protostar for the filamentary (top) and the spherical (bottom) clouds. The snapshot is ~ 1500 yr after the central protostar is formed. 97

6.7 Face on view of the disk and stellar system in the filamentary (top) and the spherical (bottom) clouds. White asterisks represent the protostars. and the colors scale represents the column density of gas. Time origin is the moment at which the central protostar is formed. We note that no protostars are ejected outside the shown region. 98
6.8 Filament fragmentation just occuring in the filamentary cloud. Arrows indicate where the new star and disk system forms through such an event. In panel (b), the white circles A and B indicate the reference scales shown in Figure 6.3. 99
6.9 Evolutions of (a) the stellar mass, (b) the mass accretion rate, (c) the disk mass, and (d) the number of the protostars for the filamentary (green) and the spherical (blue) clouds. In panel (a), the solid and dashed lines represent the primary and total protostellar masses, respectively. Here, the primary protostar is the protostar which is first produced in the calculation. In panel (b), the dashed line indicates the critical mass accretion rate, below which the protostars contract into the ZAMS stage (Section 6.2.5). The accretion rate is averaged for every 30 years. 99
6.10 Mass evolution of all the protostars for the filamentary (left) and the spherical (right) clouds. The stellar mergers are marked as the vertical jumps shown in some lines. Note that the end point of each line represents the merger partner. The red lines show mass evolution of the primary protostars. 100
6.11 (a) Stellar mass distribution at $t = 100$ kyr for the filamentary (top) and the spherical (bottom) clouds. Purple histograms show the stellar mass in the simulation, while green histograms show the mass distribution with “Models with merge”. In this model, we first pick up protostar pairs that experienced close encounters with < 200 AU and assume these protostar pair merges into a single protostar. The mass of combined protostar is the total mass of the original protostar pair. (b) Mass accretion rates ($\dot{M}$) versus stellar masses (M_*) at $t = 100$ kyr for the filamentary (green) and the spherical (blue) clouds. The dashed line indicates the critical mass accretion rate, below which the protostar contracts into the ZAMS stage. 101
6.12 Separations and total masses of binaries found in the filamentary (green) and the spherical (blue) clouds. Different symbols represent the different epochs, $t = 43$ (cross) and 100 kyr (circle). The solid and dashed lines show the stellar radii, assuming member stars are in supergiant stage with the mass ration q to be 0.5 and 1, respectively. Once the binary enters the shaded region, it is assumed to coalesce in our simulation. Shaded region represents where the binary separation becomes smaller than the stellar radius. The arrows denote the evolution of the same binaries between two different epochs. 104

6.13 Examples of the time evolution of the binary separations. Shown are the merged binaries typical in the filamentary (green) and the spherical (blue) clouds. The solid and dashed lines show the separation and the radii of the binary stars, respectively. The start and end points of each line represent the epochs of formation and merger of the binary, respectively. 105

6.14 Distributions of (a) Ionization degree, (b) temperature, and (c) density distribution in the filamentary cloud at $t = 38$ kyr. The asterisks stress the position of the protostars. In panel (b), the white arrows indicate three protostars A, B, and C that emitting ionizing photons. 106

6.15 The ratios of the Stromgren radius ($R_{\rm St}$) to the smoothing length ($h_{\rm sml}$) of the SPH particles as functions of a stellar mass. The different lines show the ratio at the different densities with $n = 10^7$ (purple), 10^{10} (green), and 10^{13} cm^{-3} (cyan). The dashed line divides the regions where $R_{\rm St}$ becomes larger / smaller than $h_{\rm sml}$. Inside the shaded region, $R_{\rm St}$ becomes greater than $h_{\rm sml}$. When calculating $h_{\rm sml}$ following eq. (6.15), we use particle mass 1.6 $M_\odot$ ($n = 10^7$ cm^{-3}) and 9.6×10^{-3} $M_\odot$ ($n = 10^{10}$ and 10^{13} cm^{-3}) as in the simulation (Section 6.2.3). 106

6.16 Projected temperature (left) and $X_{\rm ion}$ distribution around the protostar 100 yr after the splitting. The arrows show the velocity field of the infalling gas. 108

6.17 Radial profiles of (a) enclosed mass and (b) gas infall velocity at 0.1 Myr after the primary protostar formation for the filamentary (green) and the spherical (blue) clouds. The horizontal axis shows the distance (R) from the primary protostars In the panel (a), the dashed lines indicate the outer boundaries of the clouds, above which the gas is outflowing. In the panel (b), the dashed line shows the boundary between the inflow and outflow. Note that a positive velocity corresponds to the outflow in this plot. . . 111

6.18 Characteristic strain amplitudes for merging BH binaries and a noise amplitude of the future space GW detectors. We consider equal mass binaries, with member masses of 10^4 (blue) and 10^5 $M_\odot$ (red). The solid and dashed lines show the binaries at $z = 10$ and 30, respectively. The black solid lines indicate the noise amplitudes of LISA (Danzmann et al., 2016 and fitting by Cornish & Robson, 2017) and DECIGO (Kawamura *et al.*, 2011). 113

6.19 Time evolution of the separations between the most massive protostar and the closest protostar with different $n_{\rm adib}$, above which the gas particle evolves adiabatically. The separation and the time is normalized by the Jeans length with the fixed temperature $T_{\rm gas} = 8000$ K and free-fall time at $n_{\rm adib}$. The time origin is set to be the moment at which the first fragment appears in the disk. 114

7.1 DM density distribution around the DC halo (the filamentary cloud in Chapter 6) after the formation of SMSs and the remnant DCBHs. The bottom three panels represent the time evolution of the density structure around the DC halo. The DC halo sinks toward the center of the massive galaxy at $z = 8.9$. 119

7.2 The mass evolutions of the BHs, starting from the remnant DCBHs of SMSs found in our simulations (Chapter 6). The blue and green lines show the mass evolutions for the seed BHs formed in the spherical and the filamentary clouds. The solid and dashed lines assume the accretion with $f_{\rm Edd} = 1$ and 1.2, respectively. Stellar symbols represent the mass and the redshift of the SMBHs at $z \gtrsim 5.5$. SMBH samples are taken from the results of NIR spectroscopies, listed at Table 2.1. 120

A.1 The pressure P versus the cloud size R for the isothermal hydrostatic cloud. 125

A.2 The radial density profiles for the collapsing cloud. At the time t_0, the central density diverges and the protostar is though to be formed there. We set the density ρ_0 arbitrarily and set the corresponding free-fall time and Jeans length as $t_{\rm ff,0}$ and $\lambda_{\rm J,0}$, respectively. (a) the self-similar profiles obtained by Larson (1969) and Penston (1969) at $t < t_0$, just before the protostar formation. (b) the self-similar profiles obtained by Shu (1977) at $t > t_0$, just after the protostar formation. 127

B.1 Schematic picture for estimating the optical depth τ from the ionizing radiation source to the SPH particle i. 130

C.1 Effects of varying the particle de-refinement criteria for the density evolution for the S1 halo. The lines show the evolution without (black) and with de-refinement with (R_1, R_2) = (30 comoving kpc, 50 comoving kpc) (purple), and (R_1, R_2) = (50 comoving kpc, 70 comoving kpc) (green). . 133

E.1 Ratios of the Strömgren radius $R_{\rm St}$ (eq. E.3) to gravitational radius of the ionized gas $R_{\rm B,II}$ as a function of the mass of the central star. The red, green, cyan, and blue lines represent the different density profiles within the gravitational radius (eq. E.1) with α = 1, 1.2, 1.4, and 1.5. The horizontal solid line is a critical line of $R_{\rm st} = R_{\rm B,II}$, above which a photoionized region extends beyond the gravitational radius. The horizontal dotted line is also another critical line for the breakout of the ionized region $R_{\rm st} = 0.1 R_{\rm B,II}$, considering the effect of the radiation pressure against the gravity (see text). 139

List of Tables

2.1 Masses and redshifts of the mass-estimated high-z SMBHs ($z > 5.5$). . . 6
2.2 Cosmological parameters used for a part of cosmological simulations in this thesis (Planck Collaboration *et al.*, 2014). 8
2.3 The summary of works that focus on the later accretion stages of the atomic-cooling cloud. 19

3.1 30

5.1 Summary of $J_{21,\rm crit}$ and β for the three different spectra. 81

6.1 statistical properties of protostars at t = 100 kyr. Each column show the number of protostars in total, the number of survived and ejected protostars, and the number of protostars which belong to any binaries at $t = 100$ kyr from left to right. 105

Chapter 1

Introduction

Recent observations report that SuperMassive Black Holes (SMBHs) reside at the center of matured galaxies. They are the most massive compact objects in the universe and of great interest in the physical and astronomical contexts. Tremendous energy is radiated away when the gas accretes around the Schwarzschild radius of SMBHs, which are observed as “Quasars (QSOs)”. This energetic phenomenon provides us valuable knowledge about the structure formation history in the early universe. We have now observed more than one hundred QSOs at $z > 6$ and the most distant QSO resides at $z = 7.541$ with the estimated mass of $8 \times 10^8\ M_\odot$ (ULAS J1342+0928; Bañados *et al.*, 2017). The fact that they are observed at the cosmic age of $\lesssim 0.7$ Gyr gives a clue to understand the formation history of SMBHs.

Forming SMBHs before the cosmic age of $\lesssim 0.7$ Gyr is so challenging, since the radiation liberated when the matter accretes onto the BHs strongly prevents the further mass accretion. This limits the mass accretion rate at the so-called “Eddington” accretion rate. One naive formation scenario of the observed SMBHs is that they are seeded by the remnant BHs of the massive stars. The seed BHs grow in mass with accreting the surrounding gas at the Eddington accretion rate. This scenario, however, requires massive seed BH with $\gtrsim 10^3\ M_\odot$, which is much larger than those of the ordinary stars observed around our local Universe.

Population III (Pop III) stars, which are the first generation stars in the universe, can offer such massive seed BHs. They are still beyond our observation today and their properties are mainly studied by the numerical simulation. These studies show that Pop III stars typically have the masses of $100 - 1000\ M_\odot$ (e.g. Hirano *et al.*, 2014), which is much greater than those of the normal stars. If the remnant BHs of these stars acquire the mass at the Eddington rate, they can barely attain $10^9\ M_\odot$ at $z \gtrsim 6$. Meanwhile, numerical simulations show that the efficient Eddington accretion can be easily prevented by the various feedback processes such as X-ray radiation from the central BHs (Yoshida, 2006; Park & Ricotti, 2012). Thus, more massive seed is favorable for the high-z SMBH formation.

The recent discovery of the atomic-cooling path provides a possible formation channel of more massive stars (e.g. Omukai, 2001; Bromm & Loeb, 2003). The cloud collapsing along this evolutionary path radiates away the internal energy by H atomic emission, not by H_2 molecular emission as in the normal primordial star formation. The atomic-cooling clouds can yield the stars with 10^5 – 10^6 $M_\odot$ (e.g. Latif *et al.*, 2013), which is referred to as "supermassive stars (SMSs)". Such massive stars collapse into massive BHs due to the general relativistic instability (Iben, 1963), and then grow into SMBHs with further mass accretion. Numerical studies show that these massive seed BHs can safely grow into SMBHs before $z \gtrsim 6$ (e.g. Volonteri, 2010). This SMBH formation channel is often dubbed as "Direct Collapse (DC)" scenario.

There are a few formation pathways to realize SMS formation, among which ultra-violet (UV) radiation driven collapse is one of the most intensely studied scenario (e.g. Regan *et al.*, 2017). The Lyman-Werner (LW; $11.2\ \mathrm{eV} \leq h\nu \leq 13.6\ \ \mathrm{eV}$) radiation emitted by nearby galaxies can photo-dissociates H_2 molecules in the primordial cloud. If such a cloud is hosted by a massive dark halo with $T_{\rm vir} \gtrsim 8000$ K (the so-called atomic-cooling halo), the cloud collapses isothermally with keeping $T \simeq 8000$ K via atomic hydrogen cooling. Such a high temperature gas collapse induces rapid mass accretion onto a protostar with a large rate of $\dot{M} \gtrsim 0.1\ M_\odot\ \mathrm{yr}^{-1}$ (e.g. Latif *et al.*, 2013). If the efficient accretion continues, the stellar mass attains 10^5 $M_\odot$ within the stellar lifetime of about a few million years.

Many authors have calculated the event rate of SMS formation. Studies by Dijkstra *et al.* (2008, 2014) adopt a semi-numerical model to count the number of halos irradiated by sufficiently strong UV radiation. They combine the halo mass function and the correlation function of the halos to assess the number density of the halos appropriate for the SMS formation. Relevant baryonic physics such as the metal enrichments are implemented in a phenomenological fashion. This allows to study the event rate in a large spatial volume ($\sim$ Gpc) considering its parameter dependencies. Agarwal *et al.* (2012) employ a semianalytic galaxy formation model using halo merger trees. Since they construct merger trees based on N-body simulations, they only survey the DC event in the region with $\sim$Mpc scale. Their study finds several candidate halos for SMS formation. Johnson *et al.* (2013) and Habouzit *et al.* (2016) employ the radiation hydrodynamics simulations to find the primordial clouds which are irradiated by the strong UV radiation. Importantly, many of the previous studies only count the number density of the halos, which satisfy a few necessary conditions for DC. They do not directly follow the DC cloud collapse, so that they cannot determine robustly whether SMSs really form in the identified halos or clouds.

These studies justify their number estimation citing works that study the SMS formation inside the arbitrary selected atomic-cooling halos. However, the cosmologically selected atomic-cooling halos, which is consistent with the nearby galaxy formation, can suffer from many environmental effects since there exists a luminous and massive galaxy in the close vicinity. These massive galaxies exert i.e. strong tidal force and ionizing radiation, which can greatly alter the picture of the cloud collapse compared to those at the isolated environment. Under such an extreme environment, whether the SMS can really form is still uncertain.

Given these facts, we directly follow the SMS formation using the radiation hydrodynamics simulations starting from the cosmological initial condition. Following the formation and the evolution of the galaxies, we first pick up the potential sites for the SMS formation as in Agarwal *et al.* (2012) based on the semianalytical galaxy formation model (Chapter 3). Next, we follow the hydrodynamical evolution of the selected candidate clouds. We study a variety of the environmental effects, such as the tidal force from the source galaxy, the ram pressure stripping (Chapter 4), and the ionizing radiation feedback from the source galaxy (Chapter 5). Finally, we further follow the evolution after the protostellar cores are formed inside the candidate clouds (Chapter 6). The set of simulation above allows us to estimate the number density of the SMS formation in a more accurate manner than before. The conclusion is summarized in Chapter 7 and we briefly extrapolate the further mass evolutions of the expected seed BHs.

Chapter 2

A Brief Summary of the Massive BH Formation in the Early Universe

2.1 Black Holes in the Universe

Today, we have known that Black Holes (BHs) widely exist around us. They are literally dim and emit no electro-magnetic signals. Recent detections of gravitational wave (GW) from merging BH binaries establish their existence (e.g. Abbott *et al.*, 2016a). Even prior to their direct detection by GW observations, the electro-magnetic observations strongly suggest that massive and compact objects exist in the universe. The observed BHs are divided into two classes; stellar mass BHs ($\lesssim 100\ M_\odot$) and supermassive BHs (SMBHs; $\gtrsim 10^6\ M_\odot$). Stellar mass BHs are thought to be formed when the massive stars ($\gtrsim 20\ M_\odot$) end their lives. Apart from GW observations, merely $\gtrsim 20$ BHs are observed as a member of X-ray binaries so far. The number of stellar mass BHs in the Milky Way galaxy is estimated to be $\sim 10^5$ from the star formation history, so that most of them remain invisible to us.

SMBHs have masses between 10^6 and $10^{10}\ M_\odot$ and are located at the center of the galaxies. Analyzing stellar dynamics, Tonry (1984) found that the dark massive object with $\sim 10^9\ M_\odot$ exists at the center of M32. The density of the central object is so high that this is thought to be a single BH for now (Maoz, 1998). Subsequent observations reveal that virtually all the massive galaxies host SMBHs at their center (Kormendy & Ho, 2013), while some dwarf galaxies including M33 are reported to lack the central SMBH (Merritt *et al.*, 2001). The BH masses show a tight correlation with the properties of their host galaxies, such as the velocity dispersion of the bulge stars, bulge mass, and bulge luminosity (Magorrian *et al.*, 1998). This fact invokes the picture of “co-evolution”; the evolution of the SMBH and its host galaxy are closely related. In other words, the SMBH should have strong impact on the formation and evolution of the host galaxy.

Strong gravity originating from SMBHs drives various energetic phenomena. Quasars

(QSOs) are one such example and one of the most energetic events in the universe, which are now thought to be powered by mass accretion onto the SMBHs. The gravitational energy of accreting matter is liberated as radiation and makes QSOs as the luminous objects. This tremendous energy allows us to access the universe as early as $z \sim 7$ (e.g. ULAS J1120+0640; Mortlock *et al.*, 2011). Indeed, recent observations have shown that more than one hundred QSOs exist at $z \gtrsim 6$. Table 2.1 shows the mass and redshift of the mass-estimated QSOs. Mass estimation of high-z SMBH requires near infrared spectroscopy. This is so expensive that we only know the BH mass for a fraction of the detected QSOs. These mass-estimated SMBHs give us valuable information about the SMBH formation process.

2.2 Eddington Limit of Mass Accretion Rate

When the matter accretes onto a compact object (i.e. BH), the gravitational energy of the accreting matter is liberated and converted into the radiation energy. This radiation pushes out the accreting matter by radiation pressure. Under the isotropic radiation with the luminosity L, the radiation pressure $P_{\rm rad}$ acting on the matter at the distance R from the radiation source can be written as,

$$P_{\rm rad} = \frac{L}{4\pi R^2 c}, \tag{2.1}$$

where c is the speed of the light. The radiation force acting on the hydrogen atom is $\sigma_{\rm Th} P_{\rm rad}$, where $\sigma_{\rm Th} = 6.65 \times 10^{-25}\ {\rm cm^2}$ is the Thomson scattering cross section. There is a critical mass accretion rate, at which the radiation pressure balances with the gravitational force from the compact object.

$$\sigma_{\rm Th} P_{\rm rad} = \frac{G M_{\rm BH} m_{\rm p}}{R^2}, \tag{2.2}$$

where G is the gravitational constant, $M_{\rm BH}$ is the mass of the central object, and $m_{\rm p}$ is the proton mass. This equation gives the critical luminosity $L_{\rm Edd}$, where

$$L_{\rm Edd} = \frac{4\pi c G M_{\rm BH} m_{\rm p}}{\sigma_{\rm Th}} = 1.26 \times 10^{38}\ {\rm erg\ s^{-1}} \left(\frac{M_{\rm BH}}{M_\odot}\right). \tag{2.3}$$

Assume a fraction ϵ of the accreting mass is converted into radiation energy and remaining mass accretes onto the BH, that is, $L = \epsilon \dot{M} c^2$ and $\dot{M}_{\rm BH} = (1-\epsilon)\dot{M} c^2$, where $\dot{M}$ is the mass accretion rate onto the BH+surrounding system and $\dot{M}_{\rm BH}$ is that onto the central BH itself. This gives the critical mass growth rate of the BH, so-called "Eddington accretion rate" $\dot{M}_{\rm Edd}$, which is

$$\dot{M}_{\rm Edd} = \frac{1-\epsilon}{\epsilon} \frac{4\pi G M_{\rm BH} m_{\rm p}}{\sigma_{\rm Th} c}, \tag{2.4}$$

where $\epsilon = 0.1$ is assumed, which is appropriate for the non-spinning BH. This $\dot{M}_{\rm Edd}$ gives one of the characteristic mass growth rates of the BH, which is regulated by the radiation pressure.

survey		$z_{\rm MgII}$	$M_{\rm BH}[M_\odot]$	...	reference
ULAS	J1342+0928	7.541	7.8×10^8	...	Bañados *et al.* (2017)
ULAS	J1120+0641	7.085	2×10^9	...	Mortlock *et al.* (2011)
ULAS	J2348-3054	6.886	2.1×10^9	...	Venemans *et al.* (2013)
ULAS	J0109-3047	6.745	1.5×10^9	...	Venemans *et al.* (2013)
HSC	J1205-0000	6.73	4.7×10^9	...	Matsuoka *et al.* (2016)
PSO	J338.2298	6.658	3.7×10^9	...	Venemans *et al.* (2015)
ULAS	J0305-3150	6.604	1×10^9	...	Venemans *et al.* (2013)
PSO	J323.1382	6.592	1.4×10^9	...	Mazzucchelli *et al.* (2017)
PSO	J231.6575	6.587	3.1×10^9	...	Mazzucchelli *et al.* (2017)
PSO	J036.5078	6.527	1.9×10^9	...	Venemans *et al.* (2015)
PSO	J167.6415	6.508	4.9×10^8	...	Venemans *et al.* (2015)
PSO	J247.2970	6.476	5.2×10^8	...	Mazzucchelli *et al.* (2017)
CFHQS	J0210-0456	6.438	8×10^7	...	Willott *et al.* (2010)
CFHQS	J2329-0301	6.417	2.5×10^8	...	Willott *et al.* (2010)
SDSS	J1148+5251	6.41	3×10^9	...	Willott *et al.* (2003)
SDSS	J1148+0702	6.339	2×10^9	...	Jiang *et al.* (2016)
SDSS	J1030+0524	6.302	2×10^9	...	De Rosa *et al.* (2011)
SDSS	J0100+2802	6.3	1.2×10^{10}	...	Wu *et al.* (2015)
CFHQS	J0050+3445	6.253	2.6×10^9	...	Willott *et al.* (2010)
SDSS	J1623+3112	6.211	2.2×10^9	...	De Rosa *et al.* (2011)
SDSS	J1048+4637	6.198	6×10^9	...	De Rosa *et al.* (2011)
CFHQS	J0221-0802	6.161	7×10^8	...	Willott *et al.* (2010)
CFHQS	J2229+1457	6.152	1.2×10^8	...	Willott *et al.* (2010)
ULAS	J1319+0950	6.13	2.7×10^9	...	Mortlock *et al.* (2009)
CFHQS	J1509-1749	6.121	3×10^9	...	Willott *et al.* (2010)
CFHQS	J2100-1715	6.087	9.4×10^8	...	Willott *et al.* (2010)
SDSS	J0303-0019	6.079	5×10^8	...	De Rosa *et al.* (2011)
SDSS	J0353+0104	6.072	2.4×10^9	...	De Rosa *et al.* (2011)
SDSS	J0842+1218	6.069	2.9×10^9	...	De Rosa *et al.* (2011)
SDSS	J1630+4012	6.058	1.7×10^9	...	De Rosa *et al.* (2011)
CFHQS	J1641+3755	6.047	2.4×10^8	...	Willott *et al.* (2010)
SDSS	J1306+0356	6.017	1.7×10^9	...	De Rosa *et al.* (2011)
SDSS	J2310+1855	6.002	3.9×10^9	...	Wang *et al.* (2013)
CFHQS	J0055+0146	5.983	2.4×10^8	...	Willott *et al.* (2010)
SDSS	J1411+1217	5.93	1.1×10^9	...	Fan *et al.* (2006)
SDSS	J0005-0006	5.85	3×10^8	...	Jiang *et al.* (2008)
SDSS	J0836+0054	5.82	2.7×10^9	...	Fan *et al.* (2006)
SDSS	J1044-0125	5.784	1.1×10^{10}	...	Jiang *et al.* (2007)

Table 2.1. Masses and redshifts of the mass-estimated high-z SMBHs ($z > 5.5$).

Consider the BH gains mass at a rate of the Eddington accretion rate $\dot{M}_{\rm Edd}$. Since $\dot{M}_{\rm Edd}$ is proportional to the BH mass, we can immediately obtain the growth history of the BH mass as follows,

$$\frac{\mathrm{d}M_{\rm BH}}{\mathrm{d}t} = \dot{M}_{\rm Edd} \equiv \frac{M_{\rm BH}}{t_{\rm Sal}} \qquad \therefore M_{\rm BH} = M_{\rm ini}\exp(t/t_{\rm Sal}), \tag{2.5}$$

where $M_{\rm ini}$ is the initial BH mass and $t_{\rm Sal} \equiv \sigma_{\rm Th} c\epsilon/4\pi G m_{\rm p}(1-\epsilon) = 5.25\times10^{7}$ yr and gives the typical growth time-scale of the BH mass. The parameter $M_{\rm ini}$ reflects the formation process of the seed BH.

We know the massive stars leave the remnant BH after they exhaust nuclear hydrogen and end their lives. The mass of the remnant BH depends on the metallicity and is usually much smaller than that of the progenitor star due to the stellar mass loss (e.g. Belczynski *et al.*, 2010). Stars with the solar metallicity $Z \sim Z_\odot = 0.02$ (Population I star, Pop I star) leave BHs with $\lesssim 10\ M_\odot$. Stars with lower metallicity ~ 0.01–$0.1\ Z_\odot$ (Population II star, Pop II star) can leave more massive remnant BH than Pop I remnant BH, $\lesssim 80\ M_\odot$. Still, the exact mass of the remnant BHs is theoretically uncertain due to the mass loss model. The observations of X-ray binaries reveal the stellar mass BHs with $\lesssim 20\ M_\odot$ (e.g. Casares & Jonker, 2014). Recent GW observation of BH mergers finds the stellar mass BHs with $\sim 30\ M_\odot$ (Abbott *et al.*, 2016b). Assuming that the typical mass of remnant BHs is $\sim 30\ M_\odot$, we can calculate the mass evolution under the Eddington accretion based on eq. (2.5). The BH only reaches $\sim 10^{8}\ M_\odot$ at $z = 7$. This mass-scale is an order of magnitude smaller than the observed SMBH mass at $z \sim 7$ (e.g. ULAS J1120+0640; Mortlock *et al.*, 2011).

In the above discussion, the mass accretion is limited to the Eddington rate. Thus the fact that there is not enough time for BHs to evolve into the observed SMBH mass directs us to two possible formation scenarios of SMBHs at high-z universe.

1. The seed BH mass is much larger than that of the stellar mass BHs, which we observe today.
2. The mass accretion rate exceeds the Eddington value during some epochs of evolution history of BHs.

Above two scenarios are intensely studied so far. In this paper, we mainly focus on the former scenario. This scenario is closely related to the star formation in the early universe since massive star formation is just followed by the massive BH formation (Section 2.6). To know how massive stellar mass we can attain in the early universe is the important key in the former scenario, in which we start from the massive seed BHs.

2.3 Chemo-thermal Evolution of Primordial Star-forming Clouds

In the very early universe, just after the Big-bang, the inter-galactic gas is mainly composed of hydrogen (H) and helium (He). The heavier elements such as carbon (C) are produced by nucleosynthesis inside stars and dispersed only after the first generation stars end their lives as a Super Novae (SNe) explosion. Consequently, the first generation of

Parameter	Value	
H_0	67.77	... Current expansion rate in km s^{-1} Mpc^{-1}
Ω_Λ	0.6914	... Dark energy density today divided by the critical density
Ω_m	0.3086	... Matter density today divided by the critical density
Ω_baryon	0.04825	... Baryon density today divided by the critical density
σ_8	0.8288	... RMS matter fluctuations today in linear theory
n_s	0.9611	... Scalar spectrum power-law index

Table 2.2. Cosmological parameters used for a part of cosmological simulations in this thesis (Planck Collaboration *et al.*, 2014).

stars should be born out of the gas cloud which is composed only by H and He. These first generation stars are referred to as primordial stars and the gas which is not polluted by the elements heavier than C is referred to as primordial or pristine gas. In this section, we first overview the birth place of the primordial stars. Then, we review the energy structure and formation process of the hydrogen molecule (H_2), which is the most important coolant in the early universe. Next, we see the cooling process of the collapsing primordial clouds, in which H_2 plays important roles. Finally, we discuss how the external radiation field alters the chemo-thermal evolution of the collapsing primordial clouds.

2.3.1 Birth place of primordial stars

The recent observations of Cosmic Microwave Background (CMB) gives us valuable information about the history of the structure formation in the universe. Observations show that a small density fluctuation is already seeded at $z \gtrsim 1000$. The cosmological parameters used in this thesis is tabulated in Table 2.2. According to the linear perturbation theory, different Fourier modes of the density fluctuation grow independently via gravitational instability. When the fluctuation over the comoving scale R grows and enters a non-linear regime, the Lagrangian region containing the mass $M \propto R^3$ decouples from the background expansion ("Hubble flow") and collapses. The collapse continues until the velocity dispersion seeded from the initial condition is balanced by the gravitational acceleration ("virialization"). This kind of the virialized object is called a "halo".

The halo is characterized by several parameters. The spherical collapse model gives the typical density inside the halo, which is $18\pi^2$ times the cosmic background density. Virial theorem relates the kinetic energy K and the potential energy U as follows,

$$\langle K \rangle = -\frac{1}{2}\langle U \rangle, \tag{2.6}$$

where the bracket defines the long-term average, i.e. $\langle f \rangle \equiv \lim_{T\to\infty} T^{-1} \int_0^T \mathrm{d}t f(t)$. We can estimate the characteristic size, temperature, velocity of the halo based on the virial theorem above. These quantities are referred to as virial radius R_vir, virial temperature T_vir, and the circular velocity V_c and expressed in terms of the halo mass M_h and the

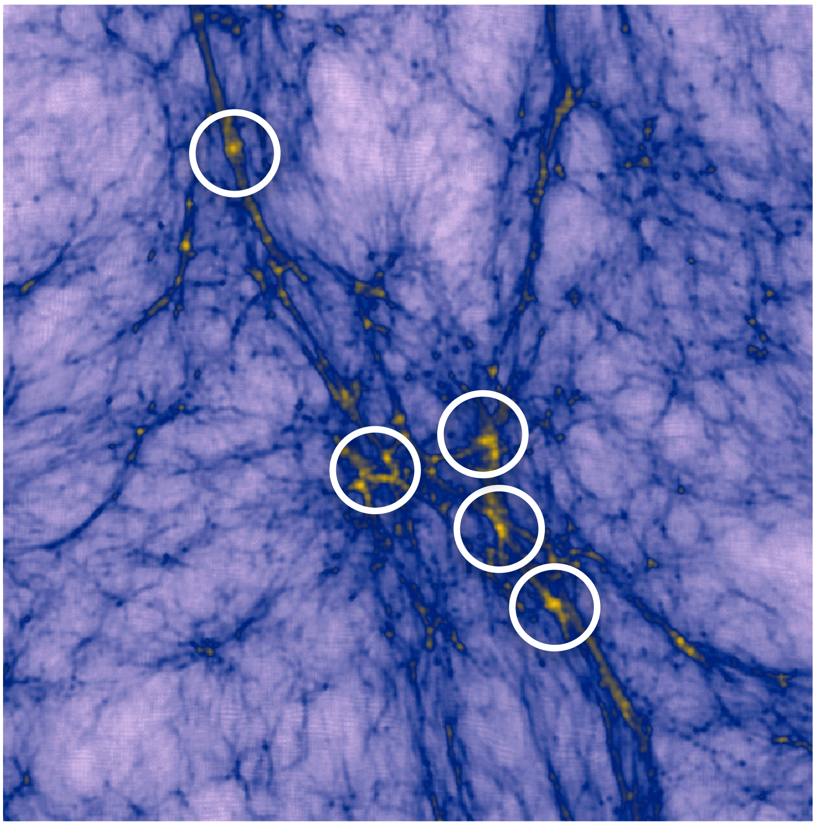

Figure 2.1. Projected DM density distribution at $z \sim 20$. The large-scale structure, such as the cosmic filament and halos are shown. White circles indicate the mini halos, at which the primordial stars are thought to be born.

redshift z as,

$$R_{\rm vir} = 39\ h^{-1}\ {\rm pc} \quad \left(\frac{M_{\rm h}}{10^5\ h^{-1}M_\odot}\right)^{1/3} \left(\frac{1+z}{20}\right)^{-1}, \tag{2.7}$$

$$T_{\rm vir} = 800 \quad {\rm K} \left(\frac{\mu}{1.2}\right) \left(\frac{M_{\rm h}}{10^5\ h^{-1}M_\odot}\right)^{2/3} \left(\frac{1+z}{20}\right), \tag{2.8}$$

$$V_{\rm c} = 3.3 \quad {\rm km\ s^{-1}} \left(\frac{M_{\rm h}}{10^5\ h^{-1}M_\odot}\right)^{1/3} \left(\frac{1+z}{20}\right)^{1/2}, \tag{2.9}$$

where μ is the mean molecular weight of the primordial gas. To derive $T_{\rm vir}$, we assume the specific kinetic energy inside the halo is equal to the internal energy of the gas. Numerical simulations show that the temperature of the adiabatically collapsing gas cloud roughly follows the virial temperature of the host halo (Yoshida *et al.*, 2003).

As the halo mass grows, the gas temperature inside the halo increases due to the adiabatic compression. Once $T_{\rm vir}$ exceeds a critical temperature for the cooling $T_{\rm cool}$, then the cloud begins to lose internal energy and collapse. In the remaining of this section, we will evaluate the value of $T_{\rm cool}$ for the primordial cloud, considering the radiation process.

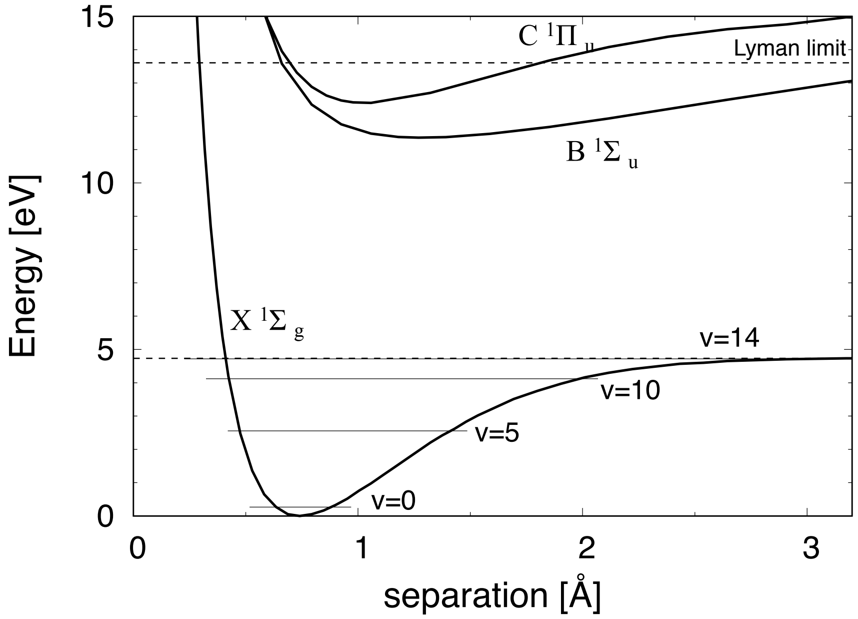

Figure 2.2. Effective potentials energy of H_2 as functions of the separation of two protons. The solid lines show the energy for the different electron states, labeled $X^1\Sigma_g$ (ground state), $B^1\Sigma_u$, and $C^1\Pi_u$ from the bottom to top (Kołos & Wolniewicz, 1965, 1966). The horizontal thin lines show the vibration states ($v = 0, 5, 10,$ and 14) with the electron ground state (Kolos & Wolniewicz, 1968). The upper dotted line represents the Lyman-limit ($h\nu$ = 13.6 eV), above which the radiation will be mainly consumed by the ionization of the hydrogen atoms.

2.3.2 Structure of H_2

The energy levels of H_2 is characterized by three quantized parameters, the electron state, the vibration state v, and the rotational state J. According to their electron states, they are labeled X, B, C, ... from the lowest to higher energy. Figure 2.2 shows the potential energy curves as functions of the separation of hydrogen atoms. The solid lines correspond to the energies for the electron state in the bonding orbit of the three lowest energy, labeled $X^1\Sigma_g$ (ground state), $B^1\Sigma_u$, and $C^1\Pi_u$. The electron ground state $X^1\Sigma_g$ is composed of quantized vibrational states with $v = 0 - 14$ and the continuum states with $v > 14$. Once the vibrational state transits to $v > 14$, two hydrogen atoms becomes no more bound each other. Hydrogen molecules in the intergalactic medium (IGM) stays in the ground state $X^1\Sigma_g$ with $v = J = 0$.

2.3.3 H_2 Formation

Since there is no dust nor metal in the early universe, the primordial cloud loses the internal energy via H_2 cooling. The H_2 formation in the primordial clouds proceeds in a two-step manner, in which the intermediate products (H^- and H_2^+) are first formed and processed into H_2. Here, we list the two main channels of the H_2 formation:

1. H^- channel;

$$\mathrm{H} + \mathrm{e}^- \longrightarrow \mathrm{H}^-, \tag{2.10}$$

$$\mathrm{H}^- + \mathrm{H} \longrightarrow \mathrm{H}_2 + \mathrm{e}^-. \tag{2.11}$$

2. H_2^+ channel;

$$\mathrm{H} + \mathrm{H}^+ \longrightarrow \mathrm{H}_2^+, \tag{2.12}$$

$$\mathrm{H}_2^+ + \mathrm{H} \longrightarrow \mathrm{H}_2 + \mathrm{H}^+. \tag{2.13}$$

In channels 1 and 2, H^- and H_2^+ act as the catalyzers for the final product H_2, respectively. Note that H_2 is mainly formed through H^- channel at $z \lesssim 100$. The reason why we consider the two-step formation process is as follows. Since H_2 has no electric dipole moment, the transition rate from two unbound hydrogens to the bound pair of hydrogens is negligibly small. Quadrupole transition allows the direct formation of H_2, while the formation rate appears to be much smaller than those by the two step processes (Forrey, 2016).

The formation rate of H_2 is mainly determined by the rate of reaction (2.10), since reaction (2.11) proceeds at a much faster rate than reaction (2.10). The rate of reaction (2.10) is proportional to the electron density, which decreases with increasing cosmic age due to the recombination. The recombination time-scale t_{rec} is $(\alpha n x_{\mathrm{i}})^{-1}$, where α is the recombination coefficient, n is the number density of the proton, and x_{i} is the primordial abundance of the electron set by the Big-bang nucleosynthesis. We can estimate the H_2 abundance f_{H2} by integrating the formation rate as following manner (Tegmark *et al.*, 1997):

$$\begin{aligned} f_{\mathrm{H2}} = \int^{t} \mathrm{d}t k_{\mathrm{form}} n x(t) \sim k_{\mathrm{form}} n x_{\mathrm{i}} t_{\mathrm{rec}} = \frac{k_{\mathrm{form}}}{\alpha} \\ \sim 3.5 \times 10^{-4} \left(\frac{T}{1000\ \mathrm{K}}\right)^{1.52} \equiv f_{\mathrm{H2,s}}, \end{aligned} \tag{2.14}$$

where k_{form} is the reaction rate of (2.10) and T is the cloud temperature. We assume the initial H_2 abundance is negligibly small and $t > t_{\mathrm{rec}}$, at which the electron density becomes negligible and further H_2 formation is no more expected. The above estimation indicates that the H_2 abundance is at most $\sim 10^{-4}$ in the primordial environment. The

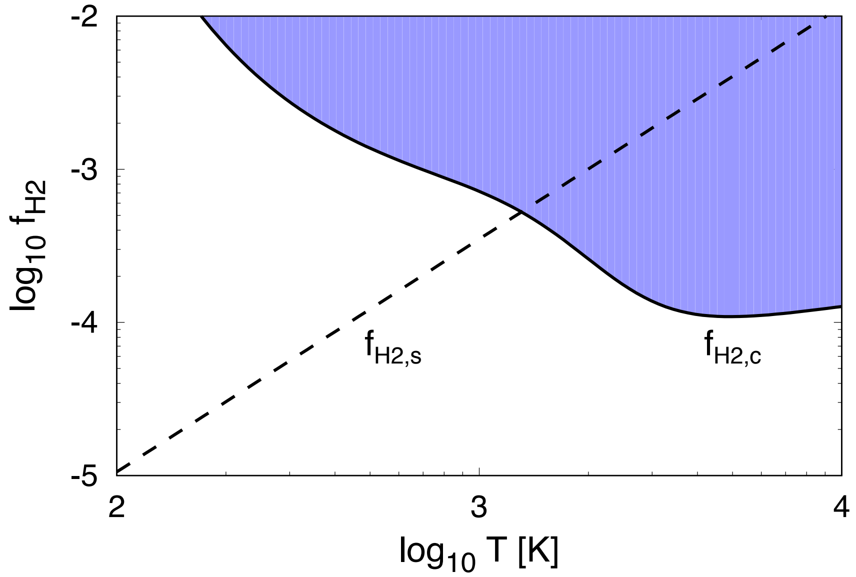

Figure 2.3. Phase diagram of the temperature and the H_2 fraction $f_{\rm H2}$. Inside the shaded region, the cloud satisfies $t_{\rm cool} = t_{\rm Hubble}$ (eq. 2.18) and the cloud collapse thought to be initiated by H_2 cooling. The dashed line represents the typical abundance of H_2 (eq. 2.14).

numerical calculations which solves non-equilibrium chemistries in the collapsing cloud also support the above estimation (Tegmark *et al.*, 1997; Machacek *et al.*, 2001; Yoshida *et al.*, 2003)

2.3.4 H_2 cooling

The cloud collapses, as it loses the internal energy by radiation. One criterion for the collapse is $t_{\rm cool} < t_{\rm Hubble} = H^{-1}$. Here, $t_{\rm cool}$ is a time-scale for the cooling and defined as,

$$t_{\rm cool} = \frac{E}{|\dot{E}|} = \frac{3k_{\rm B}T}{2n\Lambda(T)}, \tag{2.15}$$

where E is the specific heat energy of the gas and $\Lambda(T)$ is called the cooling function. Since the optically-thin limit, the collision rate and thus the rate of energy loss is proportional to n^2 and then $\Lambda(T)$ is independent of the density.

The cooling rate by H_2 is studied by many authors based on quantum mechanics. The most efficient cooling process at $T < 1000$ K is the cooling due to the transition between the rotational state $J = 0$ and 2 by the collisional (de-)excitation. The cooling rate is then described as follows (Hollenbach & McKee, 1979),

$$\Lambda(T) = 5 f_{\rm H2} \gamma_2^{\rm H,H_2} \exp\left[-\left(\frac{E_2 - E_0}{k_{\rm B}T}\right)\right](E_2 - E_0), \tag{2.16}$$

$$\gamma_J^{\rm H,H_2} = \left[\frac{10^{-11}T_3^{-1/2}}{1+60T_3^{-4}} + 10^{-12}\right]\left\{0.33 + 0.9\exp\left[-\left(\frac{J-3.5}{0.9}\right)^2\right]\right\}{\rm cm^3 s^{-1}}, \tag{2.17}$$

where $T_3 = T/10^3$ K, E_0 and E_2 are the energy of the rotational state $J = 0$ and 2, respectively. The energy difference between these states $(E_2 - E_0)/k_{\rm B}$ is about 512 K, so that H_2 cooling becomes efficient only when $T \gtrsim 512$ K. The critical condition at which $t_{\rm cool} < t_{\rm Hubble}$ can be written as,

$$f_{\rm H2} > f_{\rm H2,c} \equiv 5 \times 10^{-4} \exp\left(\frac{512\ {\rm K}}{T}\right)\left(\frac{21}{1+z}\right)^{-3/2}\left(\frac{n}{1\ {\rm cm^{-3}}}\right). \tag{2.18}$$

The discussion in the previous section (eq. 2.14) shows the H_2 abundance is at most $f_{\rm H2,s}$.

Figure 2.3 shows the phase-diagram of temperature and H_2 abundance. The solid and dashed lines show $f_{\rm H2,c}$ and $f_{\rm H2,s}$, respectively. Here, we assume $z = 20$ and $n = 1\ {\rm cm^{-3}}$. Inside the shaded region, H_2 cooling operates and the primordial cloud begins to collapse. The critical temperature and H_2 fraction at which $t_{\rm cool} = t_{\rm Hubble}$ and the cloud can collapse is $T \sim 1000$ K and $f_{\rm H2} \gtrsim 10^{-4}$.

Since the gas temperature approximately follows the virial temperature of the host halo, the cloud collapse is initiated when $T_{\rm vir} > T_{\rm cool} \sim 1000$ K is satisfied. The corresponding mass of the host halo is $M_{\rm h} \sim 10^5 - 10^6\ M_\odot$. The halos with this mass-scale are called “minihalos”.

2.3.5 The impact of the external radiation field

In this section, we discuss how the external radiation alters the qualitative picture of primordial star formation. If the cloud is irradiated by ionizing radiation with $h\nu > 13.6$ eV, the cloud temperature rises up to several 10^4 K. In such cases, the cloud will evaporate and escape from the halo potential. Then, we here limit our consideration to the impact of the radiation with $h\nu < 13.6$ eV (Far-UltraVioret radiation, FUV).

FUV radiation dissociates H_2 within the primordial cloud and makes the cloud temperature high. The binding energy of H_2 is 4.48 eV, while the direct transition from the ground state $v = 0$ to the unbound state $v > 14$ is strongly prohibited by the selection rule. Instead, there are two main processes to destroy H_2 by some indirect processes.

1. Solomon process;
   Two-step H_2 dissociation process (Stecher & Williams, 1967). Firstly, the radiation excites the electron state to $B^1\Sigma_{\rm u}$ or $C^1\Pi_{\rm u}$. The electron in the excited state spontaneously decays into the ground state. Some of them decay into the vibration states with $v > 14$ and are finally dissociated into two distinct hydrogen atoms. The required energy to excite the electron from the ground state to $B^1\Sigma_{\rm u}$ or $C^1\Pi_{\rm u}$ is 11.2 eV. Thus, the radiation with $11.2 < h\nu < 13.6$ eV can dissociate H_2 and is called “Lyman-Werner (LW) radiation”.

2. Photo-attachment of H^-;
   Removal of the catalyzer of the H^- channel, which reduces the formation rate of H_2 and then effectively destroys H_2. The radiation with $h\nu > 0.76$ eV can dissociate H^- since the binding energy of H^- is 0.76 eV. Note that the estimation of H_2 abundance in eq. (2.14) assumes no removal of H^-.

The strength of the FUV intensity is often represented by J_{21}, which is the mean intensity at $11.2 < h\nu < 13.6$ eV and normalized by 10^{-21} erg $\mathrm{s^{-1}cm^{-2}Hz^{-1}str^{-1}}$.

As the FUV intensity increases, the H_2 abundance decreases and the cloud temperature increases. The increased internal energy delays the cloud collapse due to the strong pressure support (Machacek *et al.*, 2001; O'Shea & Norman, 2008a). Under the extremely strong FUV radiation, the cloud cannot cool by H_2 any more. In such cases, hydrogen atoms become the dominant coolant instead of H_2 (Omukai, 2001). When the cloud density is small ($n < 10^4$ $\mathrm{cm^{-3}}$), the bound-bound transition between 1s and 2p (Lyman-α) radiates the internal energy. Since the cooling rate strongly depends on the cloud temperature, the temperature is strongly regulated to 8000 K and the cloud collapse proceeds almost isothermally. This dramatically changes the mass infall profile of the primordial cloud and thus the final mass of the primordial stars. In such an environment, the cloud collapses only when the host halo mass M_h becomes larger than 10^7–10^8 $M_\odot$, at which $T_\mathrm{vir} \gtrsim T_\mathrm{cool} \sim 8000$ K (called an "atomic-cooling halo").

2.4 Population III Star Formation

Primordial stars are almost unobservable today since they are located too far from us ($z \gtrsim 10$). Their properties (mass, luminosity, etc) are studied mainly by the numerical simulations. Primordial stars are classified into several types, depending on their surrounding environments. One is so-called normal "Population III (Pop III) stars", which are the first stars formed in the pure primordial environment. That is, star formation in this class is not affected by the surrounding stars already formed before. We also consider "direct collapse (DC) mode", which yields stars with much larger mass than Pop III stars. This mode is realized in the cloud, where the radiation from the surrounding stars or galaxies completely destroys the molecular hydrogen and dramatically increases the cloud temperature. In this section, we first focus on Pop III star formation process.

2.4.1 Collapse phase

The primordial cloud under no FUV radiation collapses owing to H_2 cooling. The blue line in Figure 2.4 shows the temperature evolution of the collapsing primordial cloud. Once H_2 cooling sets in, the cloud temperature decreases down to ~ 200 K. Around $n \sim 10^4$ $\mathrm{cm^{-3}}$, the energy level population of H_2 approaches LTE. This results in the decrease of the cooling rate, and that the cloud temperature starts to increase with the adiabatic index $\gamma = 1.1$ (Omukai & Nishi, 1998). Around $n \gtrsim 10^8$ $\mathrm{cm^{-3}}$, the following

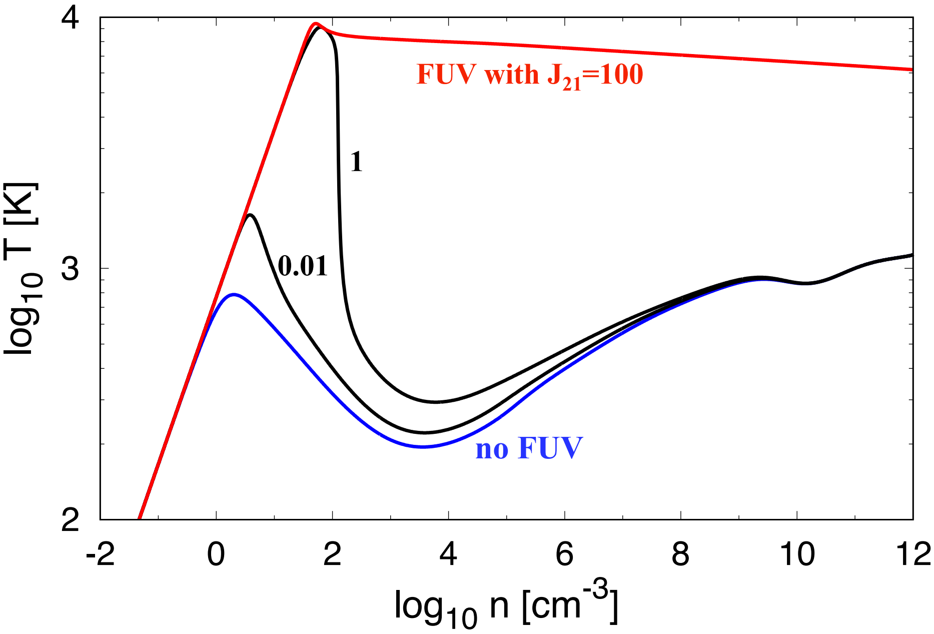

Figure 2.4. The temperature evolutions of the collapsing primordial gas cloud under the different FUV intensity. The calculation is based on so-called "one-zone" model, at which the density increases at a rate of the free-fall time. In the calculation, we solve the non-equilibrium chemistry and the energy equations. From the bottom to top lines, we represent the cloud evolutions under no FUV (blue), FUV intensity with $J_{21} = 0.01$, 1 (black), and 100 (red).

three-body reactions operate and the cloud approaches fully molecular,

$$\mathrm{H} + \mathrm{H} + \mathrm{H} \longrightarrow \mathrm{H}_2 + \mathrm{H}, \tag{2.19}$$

$$\mathrm{H} + \mathrm{H} + \mathrm{H}_2 \longrightarrow \mathrm{H}_2 + \mathrm{H}_2. \tag{2.20}$$

During this phase, the cloud collapses almost isothermally because the formation of H_2 releases the energy of 4.48 eV per a molecular hydrogen, but this released energy is consumed by H_2 cooling. At $n \gtrsim 10^{14}\ \mathrm{cm}^{-3}$, all the H_2 line emission becomes optically-thick and cooling by collision induced emission (CIE) becomes efficient. At $n \gtrsim 10^{16}\ \mathrm{cm}^{-3}$, CIE also becomes optically-thick. The cloud then evolves adiabatically and the optically-thick protostar forms, whose mass is $\sim 0.01\ M_{\odot}$.

Recent hydrodynamical simulations follow the formation of primordial stars starting from the cosmological initial condition. Yoshida *et al.* (2006, 2008) perform the three dimensional hydrodynamical simulations and follow the collapse of the primordial cloud until the central protostar is formed.

2.4.2 Accretion phase

The evolution at the later accretion phase is also followed by various authors. The analytical work by McKee & Tan (2008a) indicates that the UV radiation feedback plays a key role to determine the final stellar mass, which shut off the further mass accretion. Hosokawa *et al.* (2011) find the UV radiation from the accreting protostar really quenches the mass accretion and the final mass of the primordial star becomes 40 $M_\odot$, which is much smaller than the cloud mass $\sim$ 1000 $M_\odot$. Hirano *et al.* (2014, 2015) extend their studies and investigate the final stellar mass distribution for the primordial clouds. They find that the typical mass is $\sim$ 100 $M_\odot$ and some stars attain the masses with 10^3 $M_\odot$.

The multiplicity of the formed stars is another important factor to determine the final stellar mass, since the cloud mass is distributed among multiple stars and each stellar mass decreases. Disk fragmentation is one such mechanism to increase the multiplicity. A number of studies indicate that the rapid mass accretion triggers the disk fragmentation due to the gravitational instability (Clark *et al.*, 2011; Greif *et al.*, 2012; Machida & Doi, 2013a; Stacy *et al.*, 2016; Hosokawa *et al.*, 2016). Susa *et al.* (2014) study the multiplicity of the primordial cloud using the three dimensional radiation hydrodynamical simulation, starting from the cosmological initial condition. They find more than two thirds of the primordial clouds yield the multiple stellar systems.

2.4.3 Protostellar evolution and radiation feedback

The radiation feedback is a key to understand the final mass of the Pop III stars. To assess whether the UV radiation halts the accreting flow, we here review the evolution and the UV emissivity of the accreting primordial stars. Since the accreting matter injects a copious amount of entropy into the stellar envelope, the stellar structure of rapidly accreting stars can differ from those of non-accreting stars (Omukai & Palla, 2003; Hosokawa *et al.*, 2012, 2013). Specifically, the injected entropy inflates the stellar envelope and cools the surface temperature of stars. Depending on the mass accretion rate, the stellar structures are roughly divided into three stages: (1) contracted zero-age main sequence (ZAMS) phase, (2) oscillating protostar phase, and (3) supergiant protostar phase.

Important quantities which dictate whether the stellar envelope remains inflated and the Kelvin-Helmholz (KH) time $t_{\rm KH}$ and the accretion time $t_{\rm acc}$, defined as

$$t_{\rm KH} = \frac{GM_*^2}{R_* L_*}, \qquad t_{\rm acc} = \frac{M_*}{\dot{M}_*}, \tag{2.21}$$

where M_* is the stellar mass, R_* is the stellar radius, L_* is the stellar luminosity, and $\dot{M}_*$ is the mass accretion rate. Since the star loses the gravitational energy from the stellar surface and contract in a quasi-static manner, $t_{\rm KH}$ represents the time-scale of the energy loss and the contraction of the stellar surface (e.g. Stahler *et al.*, 1986). Meanwhile, $t_{\rm acc}$ represents the time-scale of the entropy injection and the inflation of the stellar surface.

The stellar radius at the early evolution phase ($M_* \sim 1\ M_\odot$) is about 10–100 $R_\odot$. The mass accretion rate determines the evolution of the stellar radius afterwards.

2.4.3.1 contracted ZAMS phase ($\dot{M}_* < 0.004\ M_\odot\ \mathrm{yr}^{-1}$)

Once the KH time becomes smaller than the accretion time ($t_{\mathrm{KH}} < t_{\mathrm{acc}}$), the stellar envelope begins to contract as the gravitational energy is radiated away at the time-scale of t_{KH}. The stellar radius follows the mass radius relation of ZAMSs after the contraction (Bromm *et al.*, 2001),

$$M_* = 370\ M_\odot \left(\frac{R_*}{10\ R_\odot}\right)^{2.2}, \qquad T_{\mathrm{eff}} = 1.1 \times 10^5\ \mathrm{K} \left(\frac{M_*}{100\ M_\odot}\right)^{0.025}, \tag{2.22}$$

where T_{eff} is the effective temperature of the star. As a result, the effective temperature increases up to 10^5 K, and that a large number of ionizing photons are emitted during this phase.

2.4.3.2 oscillating protostar phase ($0.004 < \dot{M}_* < 0.04\ M_\odot\ \mathrm{yr}^{-1}$)

Since the luminosity cannot exceed the Eddington luminosity, the stellar radius expands as the mass accretion rate increases and the accretion luminosity increases. The critical accretion rate, at which the stellar radius cannot follow eq. (2.22) and starts to expand is $\sim 0.004\ M_\odot\ \mathrm{yr}^{-1}$ (Omukai & Palla, 2003). After the stellar envelope expands, the Eddington ratio decreases and the protostar contracts and the stellar radius approaches ZAMS radius again.

2.4.3.3 supergiant protostar phase ($\dot{M}_* > 0.04\ M_\odot\ \mathrm{yr}^{-1}$)

When the mass accretion rate exceeds $0.04\ M_\odot\ \mathrm{yr}^{-1}$, the stellar envelope is kept bloated (Hosokawa *et al.*, 2012, 2013). During this phase, the effective temperature is severely regulated to $\sim$ 5000 K due to the strong temperature dependence of the H^- opacity (Hayashi, 1961). Since the stellar luminosity is close to the Eddington luminosity, the mass-radius relation follows

$$R_* = 38\ \mathrm{AU} \left(\frac{M_*}{1000\ M_\odot}\right). \tag{2.23}$$

In this phase, $t_{\mathrm{KH}} < t_{\mathrm{acc}}$ is satisfied as the stellar mass increases, while the stellar envelope continues to be expanded. Indeed, the star in this phase has inhomogeneous structure, that is, the contracted core with cool bloating envelope. Most of the mass is condensed at the core and the envelope has only a fraction of the total stellar mass ($\sim 5\%$; Hosokawa *et al.*, 2013).

Once the accretion rate becomes smaller than $0.04\ M_\odot\ \mathrm{yr}^{-1}$, the stellar envelope starts to cool and contract. The time-scale of cooling is the KH time of the stellar envelope $t_{\mathrm{KH,\ surf}}$, which is about ten times larger than t_{KH} (Sakurai *et al.*, 2015),

$$t_{\mathrm{KH,\ surf}} = 1000\ \mathrm{yr} \left(\frac{M_*}{500\ M_\odot}\right)^{1/2}. \tag{2.24}$$

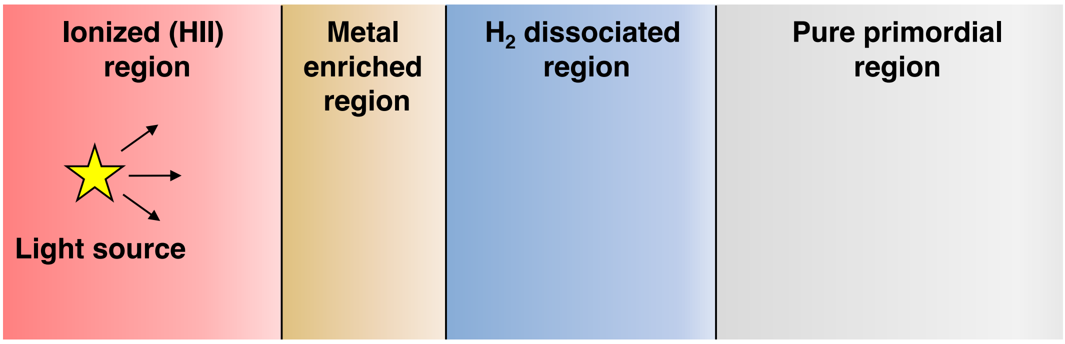

Figure 2.5. Schematic picture of the cosmic environment after the light sources appear in the universe. We assume here the light source to be the Pop III stars or the galaxy. Just around the light source, the gas is ionized and no star formation is expected in this region since the gas temperature is too high. The metal enriched region extends a little further, inside which the low mass Pop II stars will form. The primordial and H_2 photo-dissociated region (PDR) extends ∼Mpc. In this region, the cloud evolution differs from those of the isolated Pop III stars. Especially, if H_2 is completely destroyed and the molecular cooling rate becomes negligible, the SMSs can emerge.

After the epoch $\dot{M}_* < 0.04\ M_\odot\ \mathrm{yr}^{-1}$ continues for $t_{\mathrm{KH,\ surf}}$, the stellar envelope starts to contract and the stellar structure approaches that in the ZAMS phase.

Since the effective temperature is small ~ 5000 K, the UV emissivity of the stars in this phase is very small. Actually, the UV photon emissivity is by ten orders of magnitudes smaller than that in ZAMS phase (Hosokawa *et al.*, 2013). The number of hydrogen atoms accreting per unit time ($\dot{M}_*/m_\mathrm{p}$) is larger than the UV photon emissivity, and that all the ionizing photons are consumed by ionization of the infalling atomic hydrogen. Therefore, UV radiation does not evacuate the surrounding material and the star can grow efficiently during this phase (Hosokawa *et al.*, 2016).

2.5 Supermassive Star Formation by the Direct Collapse Model

2.5.1 Star formation after the population III formation

After the first generation stars are formed, they dramatically alter the surrounding environment (i.e. UV radiation feedback and SNe explosion). Figure 2.5 shows the schematic picture of the environment around the first stars or the evolved galaxies. Just around the light source, the gas is ionized by the UV radiation or enriched by the metals and dusts due to the SNe winds. Inside the ionized region, the star formation is no more expected since the gas temperature is too high for the cloud collapse. Inside the metal enriched region, the gas cools by the metals and dusts, and the expected stellar mass becomes smaller than the primordial stars (Chiaki *et al.*, 2016). The stars formed in the metal enriched region is called Population II (Pop II) or low-metal stars.

reference	resolution [AU]	duration [year]	multiplicity	
Latif *et al.* (2013)	5×10^3	2×10^4	1	3D
Becerra *et al.* (2015)	6×10^{-4}	17	several	3D
Sakurai *et al.* (2016)	110	10^5	1	2D
Shlosman *et al.* (2016)	2×10^3	2×10^6	1	3D

Table 2.3. The summary of works that focus on the later accretion stages of the atomic-cooling cloud.

Another important region is called H_2 photo-dissociated region (PDR). Since the mean free path of the FUV photons are much larger than that of ionizing photons, PDR extends to about ~ 20 comoving Mpc, whose size is much larger than those of the ionized region or the metal enriched region. If the primordial clouds inside PDR collapse, their temperature evolutional path in the density-temperature diagram becomes much different than that of the cloud outside the PDR. The black and red lines in Figure 2.4 show the evolutional paths under the FUV radiation with the intensities of $J_{21} = 0.01, 1, 100$.

There is a critical FUV intensity ($J_{21,\ \mathrm{crit}}$) which apparently divides the evolutionary tracks into two classes. When the FUV intensity is moderate ($J_{21} < J_{21,\ \mathrm{crit}}$), the temperature evolution converges to that under no FUV radiation at $n \gtrsim 10^5\ \mathrm{cm}^{-3}$. In such cases, H_2 cooling operates at some point and the temperature decreases down to several hundreds K. When the FUV intensity is strong enough ($J_{21} > J_{21,\ \mathrm{crit}}$), the cloud cannot cool by the molecular hydrogen. Instead of H_2 cooling, atomic hydrogen cooling regulates the cloud temperature with 8000 K. This evolutional path is called "atomic-cooling path". The mass accretion rate is much higher than the cloud with molecular cooling and thus the supermassive stars (SMSs) with $\sim 10^5\ M_\odot$ will be born in such environments. The exact value of $J_{21,\ \mathrm{crit}}$ is intensely studied by various authors (Omukai, 2001; Shang *et al.*, 2010; Latif *et al.*, 2014; Sugimura *et al.*, 2014). Since the low energy photons ($h\nu > 0.76$ eV) destruct H^- and reduce the abundance of H_2, the radiation spectra becomes important under the fixed FUV intensity. Specifically, softer radiation spectra with fixed FUV intensity destroy more H_2 and then yield smaller H_2 abundance. For example, detailed 3D simulations by Shang *et al.* (2010) show that

$$J_{21,\ \mathrm{crit}} = \begin{cases} 10^4 & (\text{for Pop III sources}) , \\ 100 & (\text{for Pop II sources}) , \end{cases} \tag{2.25}$$

where the black-body spectra of $T_{\mathrm{eff}} = 10^5$ and 10^4 K are assumed for the Pop III and II sources, respectively.

2.5.2 Supermassive star formation

Various authors numerically follow the collapse of the atomic cooling clouds. Bromm & Loeb (2003) first show the possibility of the SMS formation. They perform the three dimensional hydrodynamical simulation starting from the cosmological initial condition, where they artificially switch off H_2 cooling to realize the atomic cooling path. What they find is that the gas of 10^5 – 10^6 $M_\odot$ condenses inside the region with ∼pc without any fragmentation. Since they adopt the optically-thin Lyman-α cooling even at the region where the Lyman-α photons becomes optically-thick ($n \gtrsim 10^4$ cm^{-3}), their calculation underestimates the cooling rate (Omukai, 2001). Inayoshi *et al.* (2014) follow the collapse of the atomic-cooling cloud solving the full energy transfer of hydrogen atoms. Their calculation shows a single protostar is formed at the cloud center. Still, these studies only follows the early collapse phase of the atomic cooling clouds, until when the protostellar core just appears.

After the protostar formation, the protostar grows in mass as the surrounding gas accretes. Since the typical mass accretion rate is as high as 0.1–1 $M_\odot$ yr^{-1}, the stellar envelope expands and the UV emissivity dramatically reduces (see Section 2.4.3.3). As a result, the surrounding gas avoids the photo-evaporation and most of the infalling gas is likely to accrete onto the protostar.

Some studies follow the later accretion phase of the atomic-cooling cloud by the hydrodynamical simulations. Becerra *et al.* (2015) perform the hydrodynamical simulation resolving the protostellar core. After the first protostar formation, they further follow the cloud evolution for $\lesssim$ 20 yr. They find the multiple protostellar cores appear due to the disk fragmentation at the accretion phase. Still, their calculation is too short to discuss the final mass and multiplicity of final stellar system. Three studies follow the long-term evolution of the later accretion phase of the atomic-cooling cloud (Latif *et al.*, 2013; Sakurai *et al.*, 2016; Shlosman *et al.*, 2016). These three calculations report that a single SMS with the mass of 10^4–10^6 $M_\odot$ forms at the cloud center. Table 2.3 summarizes the properties and some results of their simulations.

2.6 Fate of the Primordial Stars

Here, we overview the final fate of the primordial stars. We focus on the stars with > 10 $M_\odot$, since the primordial stars are typically massive (Hirano *et al.*, 2015). After all the hydrogen is consumed, heavier elements (He, C, etc) are synthesized. Since the primordial stars are massive and experience almost no mass loss, they leave massive He core. Nuclear fusion continues until the formation of nickel (Ni), which finally decays into iron (Fe). The iron core loses the internal energy via neutrino emission and collapses in a quasi-static manner. Once the core temperature increases high enough, the core starts to be photo-disintegrated into He and finally into protons and neutrons. According to the core mass, the fate of the core is divided into the following five classes depending on the stellar mass M_* (Figure 2.6).

I. Formation of neutron stars ($M_* \lesssim 30$ $M_\odot$)
Once the core density reaches the atomic nuclei ($\rho \sim 10^{14}$ g cm^{-3}), the collapse is halted and the strong shock is formed between the infalling envelope and the core. The recent numerical simulations show that the neutrino strengthen this shock and the shock finally evacuates the infalling envelope, while leaving the neutron star at

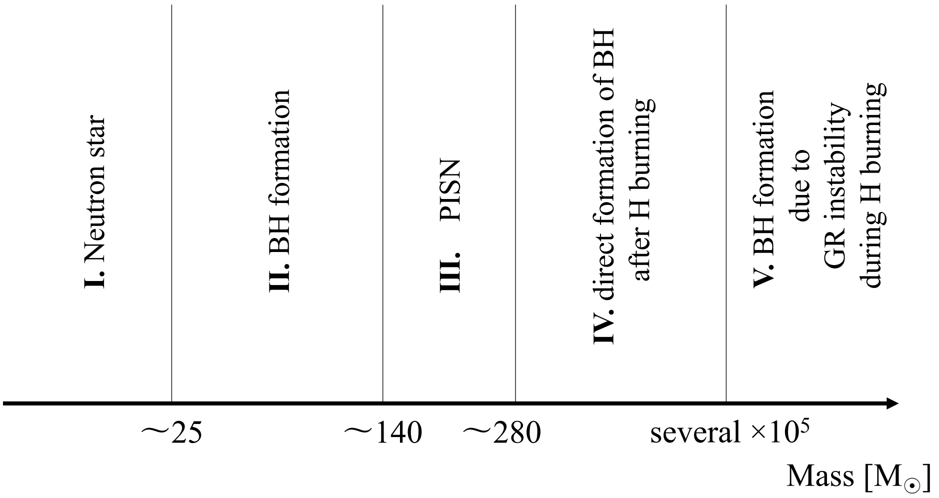
I. Neutron star
II. BH formation
III. PISN
IV. direct formation of BH after H burning
V. BH formation due to GR instability during H burning
~25
~140
~280
several ×10^5
Mass [M⊙]

Figure 2.6. The final fate of the primordial stars as a function of the stellar mass at the main-sequence phase.

the center (Woosley & Weaver, 1995).

II. Formation of BHs ($30 \lesssim M_* \lesssim 140\ M_\odot$)
When the mass of primordial star is $30 \lesssim M_* \lesssim 40\ M_\odot$, the evacuated gas falls back onto the neutron star. This makes the neutron star massive enough to collapse into the BH. When the mass of primordial star is $40 \lesssim M_* \lesssim 140\ M_\odot$, the shock cannot evacuate the envelope gas and the iron core directly collapses into the BH (Fryer *et al.*, 2001; Heger & Woosley, 2002; Heger *et al.*, 2003).

III. Pair Instability Super Novae (PISNe; $140 \lesssim M_* \lesssim 260\ M_\odot$)
The core temperature becomes high enough and e^+e^- pair production sets in. This reduces the internal energy of the collapsing core and the core starts to dynamically collapse. As a result, the violent oxygen (O) burning operates and it produces a copious amount of the energy. This finally disrupts all the star and no compact objects are left after the explosion.

IV. direct BH formation after H burning ($260 \lesssim M_* \lesssim 10^5\ M_\odot$)
When the stellar mass exceeds 260 $M_\odot$, the energy produced during the violent O burning are completely consumed by the photo-disintegration of Ni and He (Bond *et al.*, 1984). Thus the core finally collapses directly into the BH in the same manner as stars with $40 \lesssim M_* \lesssim 140\ M_\odot$.

V. direct BH formation due to general relativistic (GR) instability during H burning phase ($10^5\ M_\odot \lesssim M$)

When the stars are too massive, the GR instability sets in during the H burning stage (Fuller *et al.*, 1986; Umeda *et al.*, 2016; Woods *et al.*, 2017). The threshold mass for the GR instability depends on the mass accretion history, since the rapid mass accretion alters the stellar structure (see Section 2.4.3).

So far, we have neglected the stellar rotation. The rotation does not qualitatively alter the above picture, that is, massive primordial stars collapse into BHs. When the rotating stars collapse, the disks are formed around the collapsed BHs. The numerical simulations of primordial stars with $10^5\ M_\odot$ show that the resultant BH mass is 90% of that of the progenitor star (Shibata *et al.*, 2016; Uchida *et al.*, 2017).

2.7 Mass Evolution of Black Hole Seeds

After the BHs are formed, they accrete the surrounding gas and grow in mass. Based on the discussion in the previous section, we here assume following two models for seed BH formation as, (1) remnant BHs of Pop III stars ($M_{\rm init} = 10^2\ M_\odot$ at $z \sim 30$) and (2) remnant BHs of SMSs ($M_{\rm init} = 10^5\ M_\odot$ at $z \sim 20$). Figure 2.7 shows the mass evolution starting from the above two seed models under the accretion with $f_{\rm Edd} \equiv \dot{M}/\dot{M}_{\rm Edd} = 1.0$ (solid) and 0.6 (dashed). Stellar symbols represent the observed mass and redshift of high-z SMBHs ($z \gtrsim 5.5$), for which the mass is observationally estimated by the NIR spectroscopy (see Table 2.1). As seen from the figure, we cannot explain the observed SMBH mass starting from the Pop III remnant BHs even if the efficient Eddington accretion continues for the whole cosmic time. In contrast, starting from the remnant BHs of SMSs, the BHs attain $10^9\ M_\odot$ until $z \lesssim 7$ with the Eddington accretion.

2.7.1 Multi-dimensional simulation of mass growth of population III remnant black holes

Starting from the Pop III remnant BHs, growing BHs seems to be able to attain a part of the observed mass at $z \sim 6$ (Li *et al.*, 2007). However, since the Pop III stars are formed inside the minihalo, the halo gas is easily evacuated. For example, the UV radiation can heat the halo gas up to 10^4–10^5 K, while the virial temperature of the halo is several×1000 K. This means the halo gas becomes unbound from the halo potential due to the UV heating. One such a UV radiation source is the evolving Pop III stars (Yoshida, 2006; Yoshida *et al.*, 2007; Johnson & Bromm, 2007; Abel *et al.*, 2007; Alvarez *et al.*, 2009). Pop III stars emit a large number of UV photons and evacuate the surrounding gas from the minihalos. As the halo mass grows, the evacuated gas falls back and accumulates at the halo center again. This fall-back takes about a few×100 Myr, so that the efficient mass growth of Pop III remnant BH is impeded for a few×100 Myr just after its appearance.

The X-ray radiation from the circum-BH disk also prevents the further mass accretion at the minihalo scale (Pelupessy *et al.*, 2007; Alvarez *et al.*, 2009). The idealized simulations resolving the Bondi radius of the Pop III remnant BH show that once the gas around the

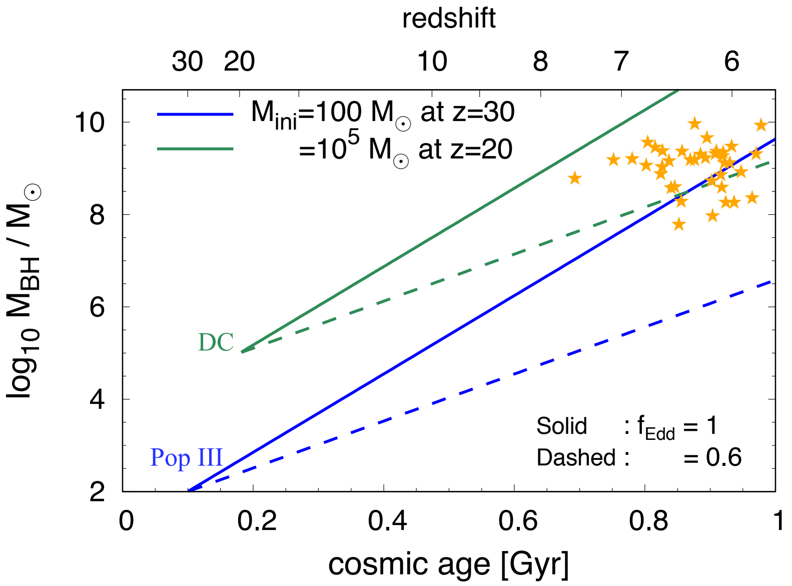

Figure 2.7. The mass evolutions of the BHs, starting from (1) the remnant BHs of Pop III stars (blue) and (2) the remnant BHs of SMSs (green). The solid and dashed lines assume the accretion with $f_{\rm Edd} = 1$ and 0.6, respectively. Stellar symbols represent the mass and the redshift of the SMBHs at $z \gtrsim 5.5$. SMBH samples are taken from the results of NIR spectroscopies, listed at Table 2.1.

BH is photo-ionized and heated, the gas is pushed outward by the thermal pressure and no more bound by the central BH (Milosavljević *et al.*, 2009; Park & Ricotti, 2012). The realized accretion rate onto BH in average is much smaller than the Eddington accretion rate ($f_{\rm Edd} = 0.1$–0.3). Therefore, it is hard for the Pop III remnant BHs to attain the mass of 10^7–$10^{10}\ M_\odot$ before $z \sim 6$.

2.7.2 Multi-dimensional simulation of mass growth of supermassive star remnant black holes

If we start from massive BH seeds $\sim 10^5\ M_\odot$, the remnant BHs of SMS, a large amount of the gas can easily accretes around the BHs since the massive BHs strongly attracts the surrounding gas. In other words, the typical mass accretion rate determined by the gravity of the BH is larger for the massive seed BH. The accretion rate is characterized by the Bondi accretion rate,

$$\dot{M}_{\rm B} = \frac{\pi \rho G^2 M_{\rm BH}^2}{c_{\rm s}^3}, \tag{2.26}$$

where ρ is the gas density around the BH. There is another advantage of starting from the remnant BHs of SMSs. As discussed in Section 2.5.2, the surrounding gas avoids the photo-evaporation owing to the cool atmosphere of the supergiant stars. As a result, a large amount of the gas is available and the BH can efficiently grow in mass just after its appearance.

The X-ray feedback from the BH accretion disk can shut off the further mass accretion (Johnson *et al.*, 2011; Aykutalp *et al.*, 2014). To resolve this problem, various authors indicate that the large-scale accretion flow helps the BH growth. For example, Dekel *et al.* (2009) propose the cold accretion flow along the cosmic filament efficiently fuels a large amount of gas around the BHs. Actually, numerical simulations show that the seed BHs with $10^5\ M_\odot$ can efficiently grow with the aid of the cold accretion flow and attain the mass of $10^9\ M_\odot$ before $z = 7$ (Di Matteo *et al.*, 2012; Feng *et al.*, 2014). Galaxy mergers also provide the sufficient gas to the growing BHs (Kauffmann & Haehnelt, 2000; Hopkins *et al.*, 2006; Li *et al.*, 2007; Sijacki *et al.*, 2009; Bellovary *et al.*, 2013). The merger wakes strong non-axissymetric perturbation and removes the angular momentum of the gas, which fuels the gas onto BHs at the rate of $\sim 10^4\ M_\odot\ \mathrm{yr}^{-1}$ (Mayer *et al.*, 2010). The statistical studies of the BH growth employing a large cosmological simulation box reveal that the seed BHs with $10^5\ M_\odot$ can explain the population of the SMBHs at $z \sim 6$ (e.g. Dubois *et al.*, 2014).

Chapter 3

Searching Candidate Site for Supermassive Star Formation

3.1 Overview

SMS formation is one promising pathway to form the observed high-z SMBHs. To investigate whether such massive stars actually form in our universe, we perform a suite of numerical simulations, whose scale ranges from the cosmological (∼Mpc) to the cloud scales (∼AU). In this chapter, we describe the results of cosmological scale simulations, which offer the potential sites for the SMS formation. We perform a set of multi-scale numerical simulations to study the DC model in a realistic cosmological context. We carry out cosmological N-body simulations to construct halo merger trees, for which we develop a semianalytic model of star and galaxy formation. In our model, metal enrichment and buildup of LW radiation field are followed in order to locate potential sites for DC. We adopt the conditions for DC that are widely used in the literature (see Section 3.2.5 below). We identify 68 DC sites selected in this manner inside the simulation box of 20 h^{-1} Mpc on a side. Note that it is still uncertain whether the SMS formation surely occurs in these identified sites. Later in Chapter 4, we further investigate this by following the evolution of the gas clouds with zoom-in N-body/SPH simulations.

The content in this and the next Chapter has been already published in The Astrophysical Journal, Volume 832, Issue 2, article id. 134, 22 pp (Chon *et al.*, 2016).

3.2 Methodology

3.2.1 Parent N-body simulations

We use the parallel Tree-PM code `Gadget-2` (Springel, 2005) to perform our parent cosmological simulation. We generate the initial condition at $z_{\rm ini} = 99$ by `MUSIC` (Hahn & Abel, 2013), which is based on second-order Lagrangian perturbation theory. The box size is set to be 20 h^{-1} Mpc on a side. We employ 256^3 DM particles with the mass of 4.08×10^7 h^{-1} $M_\odot$. The simulation is carried on until $z = 9$. We identify DM halos by the friend-of-friend (FOF) algorithm with a linking parameter $b = 0.2$.

We perform zoom-in simulations to study the detailed evolution of the structure inside the regions that contain potential DC sites. To this goal, we first target 10 most massive halos in our parent simulation, which are located roughly around 3–4σ density peaks. Then, we regenerate the initial conditions for the zoom-in regions with increasing mass resolution and run N-body simulations again. The volume of each zoom-in region is 2.0 $(h^{-1}\ \mathrm{Mpc})^3$, and the refined particle mass is $1.18 \times 10^3\ h^{-1}\ M_\odot$.

Inside the zoom-in region, halos with $M_{\rm halo} \sim 10^5\ M_\odot$ (so-called "minihalos"), possible Pop III star hosts, are resolved by more than one hundred DM particles. Thus we have enough resolution to follow Pop III star formation and the subsequent metal enrichment of the surrounding gas due to the associated SNe.

3.2.2 Construction of merger tree

We utilize the snapshots of the zoom-in simulations to build halo merger trees. In order to resolve the Pop III star formation, the time interval of the two adjacent outputs should be comparable to the lifetime of Pop III stars, ~Myr. However, if the time interval becomes much shorter than the time-scale of the halo mergers, the oscillation of the merging halo appears in the tree. This introduces technical difficulties to the tree construction. Since the merging time-scale is about the dynamical time of the halos, a few ×10 Myr at $10 \lesssim z \lesssim 40$, we set the time interval to be 10 Myr in tree construction. With the frequently dumped snapshots, we can trace the history of Pop III star formation.

Merger trees are constructed mainly by tracing the halo member particles. Progenitor and descendant halos are determined for each halo. A simple particle tracking method sometimes fails since a halo can split into multiple descendants. The halo splitting appears because our time interval of the snapshots are shorter than the time-scale of the halo merger. Therefore, we here employ the subhalo-based merger tree algorithm (Springel *et al.*, 2005). Hereafter, the term "halo" also represents a subhalo.

Subhalos in each FOF halo are identified by `SUBFIND` (Springel *et al.*, 2005). In order to find a descendent halo(s), we trace the subhalo member particles. This method assigns one unique descendant halo for 99% halos, while the remaining 1% suffers still multiple descendants. We simply treat the multiple descendants found in the exceptional cases as a single halo.

We give halo properties as functions of the halo mass M, formation redshift z; the virial radius $R_{\rm vir}$, viral temperature $T_{\rm vir}$, and circular velocity $V_{\rm c}$ following eqs. 2.7, 2.8, and 2.9. These properties are used as the recipe in the semianalytic star and galaxy formation models described in the next section.

3.2.3 Semianalytic model for star and galaxy formation

Here we describe a semianalytic model of star formation and galaxy formation, employed in this study. The method is largely based on the study by Agarwal *et al.* (2012), We briefly describe the implemented physics in the following subsections.

3.2.3.1 Population III star formation and metal enrichment

Once H_2 cooling sets in, the pristine cloud begins to collapse and pop III star formation is initiated. Numerical studies show that cooling becomes efficient in halos with $T_{\rm vir} \gtrsim 2000$ K (e.g., Tegmark *et al.*, 1997; Yoshida *et al.*, 2003). We assume that a Pop III star forms in a halo once the virial temperature becomes larger than 2000 K. We adopt a fixed stellar mass of 100 $M_\odot$ for the Pop III stars, according to the results by e.g. Hirano *et al.* (2015). Our results are not significantly affected by the choice of the Pop III stellar mass above (see Section 3.3.1). The stellar lifetime of a Pop III star is set to be 2 Myr (Schaerer, 2002). We assume that all the gas in the host halo is instantaneously contaminated by heavy elements dispersed due to a supernova (SN) explosion. Hereafter we label halos before and after the Pop III star formation as “pristine” and “metal-enriched”, respectively.

3.2.3.2 Population II star formation

After a massive Pop III star end its life as an SN, further star formation will be suppressed in the same halo for a moment because the gas is evacuated due to the energetic SN. When the halo grows and attains a sufficient mass, continuous Pop II star formation begins. The threshold mass $M_{\rm crit}$ is determined essentially by the condition for efficient gas cooling. We adopt $M_{\rm crit}$ to be $10^7\ h^{-1}\ M_\odot$ (Loeb & Furlanetto, 2013). We refer to the halos with continuous Pop II star formation as “star-forming”.

We divide the baryons inside a halo into three components; “hot gas”, “cold gas”, and “stars”. Then, we model the evolution of the baryonic components as following manner,

1. Halo growth: When a halo mass increases by ΔM, an associated gas of $\Delta M_{\rm gas} = f_{\rm b}\Delta M$ is added to the “hot gas”, as it is shock-heated to the halo virial temperature. Here, $f_{\rm b} \equiv \Omega_{\rm b}/\Omega_{\rm m}$.
2. Gas cooling: The “hot gas” then cools radiatively and turns into “cold gas”. We assume that the cooling time-scale is roughly given by the local dynamical time $t_{\rm dyn} \equiv R_{\rm vir}/V_{\rm c}$.
3. Star formation: The “cold gas” is finally transformed into stars over the time-scale of $t_{\rm SF} \equiv 0.1 t_{\rm dyn}/\alpha$ (e.g., Kauffmann *et al.*, 1993). The parameter α is the star formation efficiency, which is the ratio of the star formation to the cooling time-scale. We set $\alpha = 0.005$, which can compatible with the luminosity function at $z = 6$–7 (Agarwal *et al.*, 2012).
4. Feedback: An SN explosion heats a part of the cold gas component into the hot gas by energy injection. We assume that the mass-converting rate $\dot{m}_{\rm reheat}$ is proportional to the star formation rate (SFR) $\dot{m}_{\rm star}$,

$$\dot{m}_{\rm reheat} = \gamma \dot{m}_{\rm star} = \gamma \frac{m_{\rm cold}}{t_{\rm SF}}, \tag{3.1}$$

$$\gamma = \left(\frac{V_{\rm c}}{V_{\rm out}}\right)^{-\beta} \tag{3.2}$$

(Cole *et al.*, 1994). We use $\beta = 2.0$ and $V_{\rm out} = 110$ km s^{-1} in our calculations

(Dekel & Silk, 1986).

In summary, the four processes presented above can be described by the following differential equations:

$$\begin{aligned}
\frac{\mathrm{d}m_{\mathrm{star}}}{\mathrm{d}t} &= \frac{m_{\mathrm{cold}}}{t_{\mathrm{SF}}}. \\
\frac{\mathrm{d}m_{\mathrm{cold}}}{\mathrm{d}t} &= \frac{m_{\mathrm{hot}}}{t_{\mathrm{dyn}}} - (1+\gamma)\frac{m_{\mathrm{cold}}}{t_{\mathrm{SF}}}, \\
\frac{\mathrm{d}m_{\mathrm{hot}}}{\mathrm{d}t} &= -\frac{m_{\mathrm{hot}}}{t_{\mathrm{dyn}}} + \gamma\frac{m_{\mathrm{cold}}}{t_{\mathrm{SF}}} + f_{\mathrm{b}}\frac{\mathrm{d}m_{\mathrm{halo}}}{\mathrm{d}t},
\end{aligned} \tag{3.3}$$

We solve the above set of equations explicitly for each time step. The time step for the integration is set to be 0.01 Myr.

3.2.4 LW radiation field

The formed stellar components build up background UV radiation, which causes significant impact on structure formation in the early universe through H ionization and H_2 dissociation. The intergalactic medium (IGM) is optically-thick to ionizing photons before the cosmic reionization, and that the ionizing photons have relatively limited impact on the surrounding environment. We do not consider ionizing photons in our semianalytic calculations, but we will later estimate the effect by the hydrodynamics simulations with the ray-tracing scheme in Chapter 5.

H_2 dissociating photons can easily propagate throughout the IGM and affect star formation activity in other (distant) halos. Photons in the LW bands are emitted from both Pop III and II stars. We calculate the LW luminosities originating from them as following manners:

1. Pop III radiation: We adopt the model spectrum of the 100 $M_\odot$ star provided by Schaerer (2002).
2. Pop II radiation: We calculate a spectrum of the galaxy by the population synthesis model `STARBURST99` (Leitherer *et al.*, 1999). We use the Kroupa stellar initial mass function (IMF) and assume the metallicity to be 0.001 $Z_\odot$. The total luminosity at the LW bands at the given time can be obtained by time-integrating the stellar luminosities over the star formation history,

$$L_{\mathrm{LW},0}(t) = \int_{\nu_1}^{\nu_2} L_{\nu,0}(t)\mathrm{d}\nu, \tag{3.4}$$

$$L_{\mathrm{LW,tot}}(t) = \int_{0}^{t_0} \mathrm{d}t'\ \dot{m}_{\mathrm{star}}(t-t')L_{\mathrm{LW},0}(t'). \tag{3.5}$$

Here, $L_{\mathrm{LW},0}(t)$ is the LW luminosity radiated by the stars formed at time t under the unit stellar mass, $L_{\nu,0}(t)$ is the luminosity differentiated per unit wavelength, $L_{\mathrm{LW,tot}}(t)$ is the total luminosity considering the contribution of all the stars formed in the past. The wavelength ν_1 and ν_2 correspond to wavelengths at the both edges of the LW band, which satisfy $h\nu_1 = 11.2$ eV and $h\nu_2 = 13.6$ eV.

The reference time t_0 is the time at which the continuous Pop II star formation sets in.

3.2.4.1 Population III star formation under the LW radiation

The impact of LW radiation on the Pop III star formation is studied in detail by Machacek *et al.* (2001), who give the criterion for Pop III star formation under the LW background radiation as

$$M_{\rm th} = \psi \left(1.25 \times 10^5 + 2.8 \times 10^6 \; J_{21}^{0.47}\right) M_\odot, \tag{3.6}$$

where $M_{\rm th}$ is the critical halo mass above which the primordial gas cloud can cool by H_2 and pop III stars start to form. The non-dimensional parameter $\psi \simeq 4$ is a correction factor introduced by O'Shea & Norman (2008b). When the primordial halo is irradiated by nearby star-forming galaxy or pop III stars, we use the criterion of the Pop III star formation $M_{\rm halo} > M_{\rm th}$, instead of $T_{\rm vir} > 2000$ K.

3.2.5 Selection of DC halos

We pick up DC candidate halos if a halo satisfies the following three criteria:

1. the halo is chemically pristine;
2. the halo is irradiated by LW radiation whose intensity exceeds the critical value $J_{21} > J_{21}^{\rm crit}$; and
3. the halo is massive enough for atomic H cooling to operate, i.e., $T_{\rm vir} > 8000$ K.

The first criterion is required to avoid efficient cooling by metal lines and dust thermal emission. The second condition assures that any normal Pop III stars do not form inside the primordial halo by suppressing H_2 cooling. The last criterion allows rapid atomic H cooling of a massive gas cloud. Here, we set $J_{\rm crit}$ to be 10^4 and 100 for Pop III and Pop II light sources, respectively, as in eq. (2.25). Note that the assumed spectrum here is different from the spectrum directly calculated by the population synthesis method (Section 3.2.4). We give further discussion on $J_{\rm crit}$ in Section 4.2.1.

Above criteria are only the required condition for SMS formation. Other conditions are also conceivable for DC. For example, the angular momentum of a collapsing gas cloud should not be too large because the rotational support significantly reduce the mass accretion rate. Further direct hydrodynamical simulations that follow the cloud collapse are necessary to assess additional, if any, conditions. Indeed, this is the main reason why we conduct costly hydrodynamics simulations. We will show the results of the hydrodynamics simulations in the next chapter.

Table 3.1. properties of DC candidate halos

ID	$M_{\rm halo}$ [$10^6 h^{-1}\ M_\odot$]	z	$R_{\rm vir}$ [h^{-1} kpc]	$R_{\rm dist}$ [h^{-1} kpc]	$t_{\rm ff}$ [Myr]
DC0 (S1)	8.37	21.1	0.23	1.27	80
DC1	6.36	19.8	0.22	0.81	28
DC2 (F2)	5.91	19.1	0.22	1.79	50
DC3	6.45	19.1	0.23	1.99	60
DC4	6.47	19.1	0.23	0.99	37
DC5	6.00	18.7	0.23	1.11	50
DC6	7.32	18.4	0.25	2.57	50
DC7	8.05	17.5	0.27	3.93	60
DC8	6.31	17.5	0.25	3.02	35
DC9	6.21	17.3	0.25	4.48	60
DC10	6.88	17.2	0.26	5.24	65
DC11	7.21	17.2	0.27	4.78	120
DC12	7.78	16.9	0.28	2.79	240
DC13	8.12	16.4	0.29	0.39	35
DC14 (F1)	5.71	16.4	0.26	3.10	70
DC15	6.64	16.4	0.27	2.29	85
DC16	18.3	16.4	0.38	0.17	65
DC17	8.69	16.4	0.30	3.45	100
DC18	9.45	16.2	0.31	5.85	70
DC19	7.16	16.0	0.28	4.96	75
DC20	12.3	15.9	0.34	2.42	25
DC21	8.07	15.7	0.30	5.39	70
DC22	7.81	15.7	0.30	6.88	85
DC23	7.53	15.5	0.30	1.94	50
DC24	7.92	15.5	0.30	1.64	40
DC25	7.96	15.5	0.30	4.06	140
DC26	8.46	15.3	0.31	7.36	120
DC27	10.0	15.1	0.34	3.10	65
DC28 (S2)	7.27	14.9	0.31	6.29	105
DC29	7.04	14.7	0.31	4.45	70
DC30	7.31	14.7	0.31	4.26	65
DC31	4.51	14.2	0.27	1.31	110
DC32	7.61	14.2	0.32	5.92	70
DC33	8.78	14.0	0.34	4.00	65
DC34	10.9	14.0	0.37	4.26	100
DC35	8.98	14.0	0.35	4.07	65
DC36	9.63	13.8	0.36	6.08	80
DC37	9.53	13.5	0.37	8.62	100
DC38	9.50	13.0	0.38	5.71	130
DC39	10.1	12.6	0.40	6.17	70
DC40	11.7	11.8	0.44	3.51	65
DC41	11.4	11.1	0.47	6.19	65

Note. Column 1: ID of the DC halo. Column 2: mass of the DC candidate halo. Column 3: the redshift. Column 4: the virial radius. Column 5: the distance from the source halo. Column 6: the time of the infall to the center of the source halo. Column 2-6 are the value when halos meet the DC criteria.

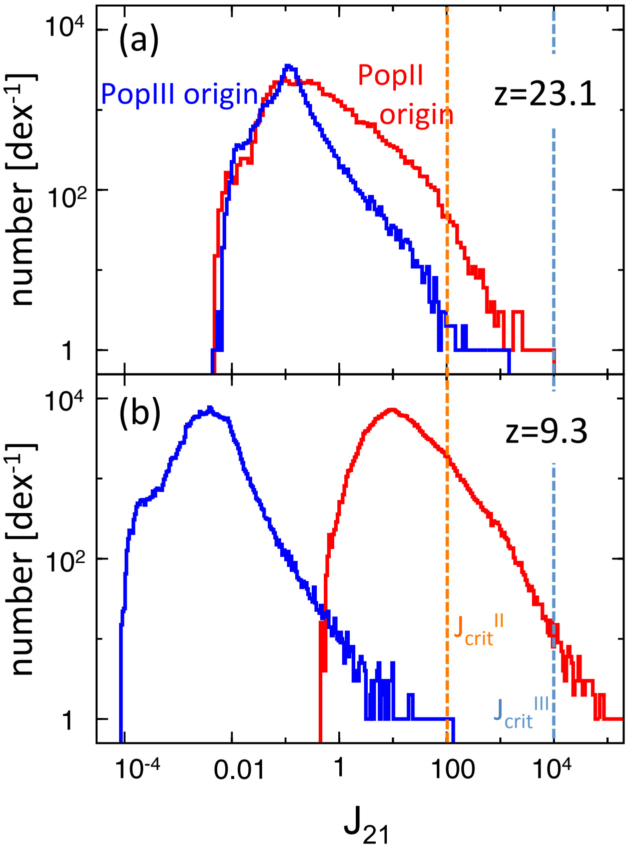

Figure 3.1. Distributions of the LW intensities $J_{21}^{\rm III}$ and $J_{21}^{\rm II}$ at the primordial halos center at (a) $z = 23.1$ and (b) $z = 9.3$. The dashed lines show the critical intensities for Pop II (red) and Pop III sources (blue).

3.3 Results from the N-body Simulation

3.3.1 Star formation and the LW radiation

The Pop III star starts to form after $z \simeq 35$ in the zoom-in region. The background LW radiation builds up and the LW intensity originating from Pop III stars ($J_{21}^{\rm III}$) peaks around $z \simeq 30$, and then gradually decreases. Meanwhile, star formation galaxies first appear at $z \simeq 28$ and J_{21} originating from Pop II sources ($J_{21}^{\rm II}$) increases rapidly to ~ 10 at $z \simeq 10$.

Figure 3.1 represents the J_{21} distribution which is evaluated at all the pristine halos at (a) $z = 23.1$ and (b) 9.3. Except for the shift of the the peak intensity, the overall shape of the distributions appears similar between the two epochs. The distribution scales as $\propto J_{21}^{-1.6}$ for the higher end, and decreases exponentially toward the lower end . Our result is widely consistent with those found in Agarwal *et al.* (2012). Interestingly, the slope at the higher end in our study is much smaller than those obtained by analytical works

(Dijkstra *et al.*, 2008, 2014; Inayoshi *et al.*, 2015; Habouzit *et al.*, 2016), who employ a two-point correlation function to populate galaxies. The difference is likely caused by the galaxy population at the small scale, $r \lesssim 1$ kpc. In their calculation, they placed the luminous galaxies only outside the virial radius of the atomic-cooling halos ∼kpc. Since our semianalytic calculation focuses on the subhalos, the typical separation between the light source halo and the DC halo is much smaller than the virial radius. This increases the number of pristine halos at the high J_{21} end and thus the slope of the distribution function becomes shallower at the high J_{21} end than the analytical studies.

We find that only the LW radiation originating from Pop II galaxies exceeds the critical values for DC. Although the LW luminosity of a single Pop III star is much larger than that of a single Pop II star, the global formation rate density (SFRD) of Pop III stars is smaller than that of Pop II stars. The other reason is that the critical LW radiation intensity for Pop III sources is much larger than that for Pop II sources (vertical dashed lines in Figure 1) due to their higher effective temperatures (eq. 2.25). For these two reasons, Pop II sources is necessary to cause the DC events (Agarwal *et al.*, 2012). Hereafter, we consider mainly the LW radiation coming from Pop II galaxies. We also note here that J_{21} varies in time. As we will see in Section 4.3.3, J_{21} at the collapsing cloud core is larger by an order of magnitude than $J_{21}^{\rm II}$ at the onset of a DC cloud collapses, since the luminous and massive source (galaxy) attracts the DC cloud gravitationally.

3.3.2 DC candidate halos

In the ten zoom-in regions, we find 68 DC candidate halos that satisfy all the three conditions for DC given in Section 3.2.5. Table 3.1 shows the properties of the 42 halos at the moment when each halo satisfies the DC criteria, whose hydrodynamical evolutions are further followed (Chapter 4). Evolutions of the halos labeled by F1, F2, S1, and S2 are presented in Sections 4.3.1, 4.3.2, 4.3.3, and 4.3.3.2, respectively. Our hydrodynamics simulations have revealed that only two cases successfully collapse to trigger DC out of the 42 samples. These two cases are referred as S1 and S2.

Figure 3.2(a) represents the redshift distribution of the DC candidate halos and the Pop III SFRD. The number of candidate halos peaks at $z \simeq 15$ and spread over $\Delta z \sim 10$, while the Pop III SFRD is almost constant from $z = 30$ to 15. The DC candidate halos is likely to appear at lower redshifts than Pop III stars since strong LW radiation sources are necessary for DC. After $z = 15$, the formation rate of DC candidates and the Pop III SFRD decrease simultaneously because the number of newly formed minihalos decreases after $z = 20$.

We can also see a similar trend in Figure 3.2(b), which represents the fraction of metal-enriched halos with $T_{\rm vir} = 2000$, 3000, 4000, and 8000 K (purple, green, blue, and yellow lines, respectively). Around $z = 15$, the metal-enriched fraction starts to increase for all the mass ranges and even for the halos with the smallest mass ($T_{\rm vir} = 2000$ K). After $z = 15$, halos have fewer chances to grow up to $T_{\rm vir} = 8000$ K without being metal-enriched. Metal enrichment reduces the numbers of the DC candidate halos and Pop III stars at $z < 15$.

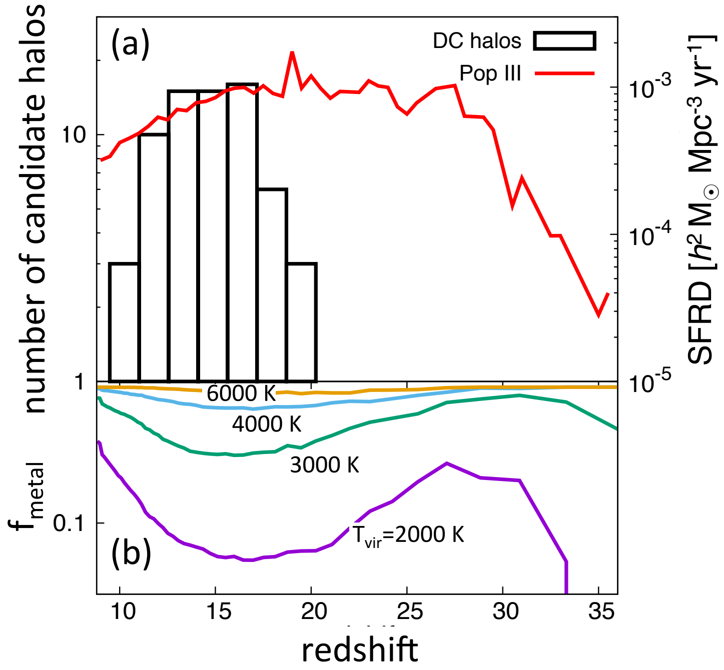

Figure 3.2. (a) Number of DC candidate halos (black) and the Pop III SFRD (red) as functions of the redshifts for all the zoom-in regions. (b) Time evolution of the fraction of metal-enriched halos. Each line indicates the fraction for halos of $T_{\rm vir} = 2000$ (purple), 3000 (green), 4000 (blue), and 6000 K (yellow).

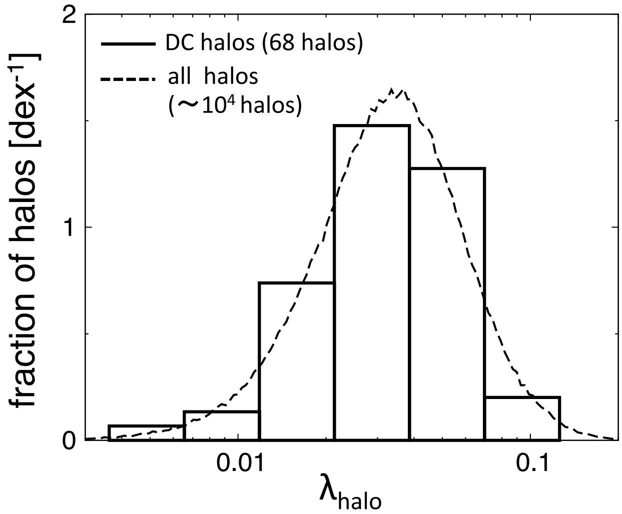

Figure 3.3. Spin parameter distributions for all the halos (dashed) and DC candidate halos (solid). The vertical axis shows the fraction of halos in each bin (dex^{-1}). Red arrows represent the angular momentum for S1 and S2 halos, which will collapse into the protostellar cores (see Section 4.3).

3.3.3 Spins of DC candidate halos

We investigate whether the cloud collapse can be affected by the spin of its host halo. The degree of halo spin is often characterized by the non-dimensional spin parameter defined by Bullock *et al.* (2001):

$$\lambda = \frac{J}{\sqrt{2}\, M V_{\rm c} R_{\rm vir}}, \tag{3.7}$$

where J is the total angular momentum of the halo. The distributions of the spin parameter for DC candidate halos and all the halos are presented in Figure 3.3. The spin distribution can be well fitted by a lognormal distribution as:

$$p(\lambda) = \frac{1}{\sqrt{2\pi}\sigma_\lambda} \exp\left[-\frac{\log^2(\lambda/\bar{\lambda})}{2\sigma_\lambda^2}\right] \frac{{\rm d}\lambda}{\lambda}. \tag{3.8}$$

The best-fit parameters for all halos are $(\bar{\lambda}, \sigma_\lambda) = (0.034, 0.56)$, which is consistent with the result by Bullock *et al.* (2001) though the considered halo mass and redshift ranges here are very different from their sample halos.

The spin parameter distribution for DC candidate halos also follows the lognormal distribution with $(\bar{\lambda}, \sigma_\lambda) = (0.043, 0.78)$. The mean value and the variance of the spin are almost consistent with those of all the halos.

The red arrows in Figure 3.3 indicate the spin parameters of the collapsed DC halos, which host clouds collapsing into the protostellar cores (see Section 4.3). The shown values are comparable to the mean value of our detected DC candidate halo sample and also that of the all the halos appeared in the simulation. This shows that angular momentum cannot be a critical factor in the collapse of DC halos.

The absolute value of the Pop III SFRD in our simulation is higher than those found in the previous studies (Agarwal *et al.*, 2012). This is likely due to the fact that we mainly focus on the zoom-in regions, where the number density of the minihalos is large and the star formation rate is also high.

Chapter 4

Cosmological Hydrodynamics Simulation for Supermassive Star Formation : Halo Mergers, Tidal Disruption, and the Conditions for Direct Collapse

4.1 Overview

The previous chapter has shown that there really exist a number of DC halos, potential sites for the SMS formation. Their number density is several ten halos per our cosmological simulation box, which has 20 h^{-1}Mpc on a side. Still, we do not know whether or not SMSs will form actually in these halos.

In this Chapter, we show the results of hydrodynamics simulations that follow the cloud collapse inside the DC halos identified in the previous Chapter. What we have found is that only two clouds collapse into the protostellar cores. The remaining 40 clouds do not collapse into the SMSs, because environmental effects such as the tidal interaction with the light source galaxy and the ram pressure stripping prevent the collapse. The density within the cloud rather turns to decrease at some point. We further discuss the required condition for the SMS formation: what is the key physics that divides two "successful" cases and other "failed" cases.

4.2 Methodology

4.2.1 Hydrodynamical simulation

The hydrodynamical evolution of the gas inside the DC candidate halos is followed using SPH+Tree code `Gadget-2` (Springel, 2005). We include 14 primordial species, such as e^-, H, H^+, He, He^+, He^{2+}, H_2, H_2^+, H^-, D, D^+, HD, HD^+, and D^-. We solve the non-equilibrium chemistry and follow the chemical and cooling processes. We also include H_2 photo-dissociation by external LW radiation from nearby light source galaxies. The time evolution of the LW intensity are given by the semianalytic calculations described in Section 3.2.4. We also consider attenuation of the LW intensity by the self-shielding using the six-ray evaluation scheme (Yoshida *et al.*, 2003) for H_2 and HD molecules (Wolcott-Green *et al.*, 2011; Wolcott-Green & Haiman, 2011).

The initial DM particle distribution is the same as that in the parent N-body simulation (Section 3.2.1). The gas particles are placed with a separation of a half mesh apart from the DM particle, where the length of one mesh corresponds to the mean separation of the DM particles at the initial condition. The masses of the gas and DM particles are 1.78×10^2 and 1.02×10^3 $h^{-1}M_\odot$, respectively.

We follow the cloud collapse in the DC candidate halos until the central gas density reaches 10^8 cm^{-3} or until the cloud merges with a nearby metal-enriched halo. During the cloud collapse, we split particles so that the local Jeans length is always resolved by 10 times the smoothing length of the gas particle (Truelove *et al.*, 1997). Our particle splitting method is based on Kitsionas & Whitworth (2002). We have confirmed our results converge when using a more strict criterion for the particle splitting, where the local Jeans length is always resolved by more than 20 times the smoothing length of the gas particle.

Occasionally, high-density gas clumps in regions far from candidate halos make the simulation time step to be extremely short. To avoid this difficulty, we use a hard equation of state with $\gamma = 5/3$ once the gas density exceeds $n_{\rm adib} = 100 - 10^4$ cm^{-3} for non-target halos. We further reduce the computational time by employing a “de-refinement” method outside the target DC halos, by which the particles are combined to yield low-resolution particles. Again, this procedure dramatically reduces the computational cost and allows us to follow a long-term evolution of the candidate halos. We present further details in Appendix C.

Here, we use a black-body spectrum with $T_{\rm eff} = 10^4$ K for the external LW radiation. Our main purpose is to study the collapse of the DC halo starting from the cosmological initial condition and to investigate the properties of the cosmologically selected DC halos. To see the effects of the DC halo selection, we have to compare our results with the previous studies on the same conditions except for the proper cosmological settings. Because most of the previous studies use the $T_{\rm eff} = 10^4$ K black-body spectra (Shang *et al.*, 2010; Latif *et al.*, 2014, 2015), we also employ the same spectrum here, and that we adopt $J_{\rm crit} = 100$

for the Pop II galaxies as in Section 3.2.5. Note that more realistic spectra of metal-poor galaxies actually provide radiation with a higher value of $J_{\rm crit} \sim 1000$ (Sugimura *et al.*, 2014).

4.3 Cloud Collapse in DC candidate Halos

We perform hydrodynamic simulations to follow the evolution of the gas clouds hosted by selected DC candidate halos. The calculations are carried out for 42 halos out of the 68 candidates extracted from our parent N-body simulation. We find two "successful" samples, where the gas density at the cloud center reaches 10^8 cm^{-3} after evolving on an isothermal atomic-cooling path with $T \simeq 8000$ K. We expect that an SMS is formed in such a gas cloud. However for other cases, the clouds do not collapse, mostly because the host halo merges with a nearby FUV source halo before the cloud collapses (see Sections 4.3.1 and 4.3.2). In this section, we first present the hydrodynamical evolution of 4 DC candidate halos, labeled as F1, F2, S1, and S2 (DC14, DC2, DC0, and DC28 in Table 3.1, respectively). F1 and F2 are the failed cases, whereas S1 and S2 are successful cases. The overall features of the evolution are shown in Section 4.3.4.

4.3.1 Case F1: collapse prevented by strong tidal force

We first study the evolution of a DC candidate halo in which DC does not occur (F1 in Table 3.1). The merging history and the time evolution of the LW intensity of the F1 halo is presented in Figures 4.1(a) and (b), respectively. Around $z \simeq 24$ at which the halo virial temperature has reached 2000 K, LW radiation turns on. At $z \simeq 16.5$, the LW intensity increases with time and reaches the critical value $J_{21}^{\rm crit} = 100$. Pop III star formation in the halo is suppressed by the strong LW radiation at $16.5 < z < 24$, when the halo virial temperature is in the range $2000 < T_{\rm vir} < 8000$ K. Note that H$_2$ cooling would operate if there is no LW radiation. The halo acquires its mass through smooth accretion and minor mergers, but we observe no major mergers. [*1]

The gas density reaches 5 cm^{-3} when the halo meets the DC criteria (Figure 4.1c). However, the gas collapse does not continue, and the density starts to decrease afterward. Finally, the halo merges with its nearby light source halo at $t \sim 1.3 t_{\rm dyn}$, before the gas cloud gravitationally collapses.

The nearby light source halo affects not only the H$_2$ abundance in the DC halo by photo-dissociation, but also the dynamical evolution by tidal forces. The tidal radius of a halo, $R_{\rm tid}$, outside which the matter will be tidally disrupted, is defined by

$$R_{\rm tid} = \left(\frac{M_{\rm halo}}{3 M_{\rm source}} \right)^{1/3} d_{\rm dist}, \tag{4.1}$$

where $M_{\rm halo}$ is the candidate halo mass, $M_{\rm source}$ is the source halo mass that exerts the tidal force, and $d_{\rm dist}$ is the separation between these two halos (Binney & Tremaine, 1987).

[*1] We here define a major merger as one with a mass ratio $m_1/m_2 < 3$, where m_1 is the mass of the larger halo. Otherwise, we define the merger as a minor merger.

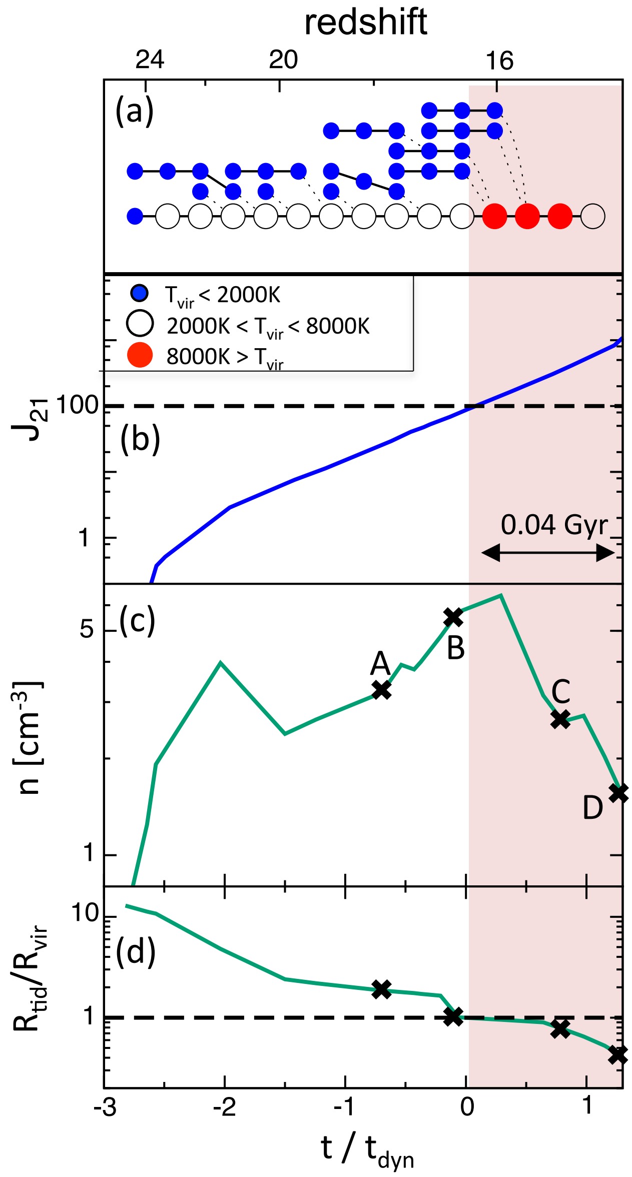

Figure 4.1. (a) Merger tree for case F1 (DC14). The blue, black, and red circles represent halos with $T_{\rm vir} < 2000$ K, $2000 < T_{\rm vir} < 8000$ K, and $T_{\rm vir} > 8000$ K, respectively. (b) Evolution of J_{21} at the halo center. The solid line indicates the evolution of the LW intensity, and the dashed line shows the critical LW intensity required for the DC criteria, $J_{21}^{\rm crit} = 100$. (c) Time evolution of the maximum gas density inside the candidate halos. (d) Tidal radius normalized by $R_{\rm vir}$ of the candidate halo. The dashed line indicates where the tidal radius becomes comparable to the virial radius of the host halo. Inside the shaded region, $T_{\rm vir}$ exceeds 8000 K, at which the atomic H cooling operate. Epochs A, B, C, and D are the reference epochs attached in Figure 4.2. The redshifts are also shown at the top of panel (a). The reference dynamical time at $t = 0$ is 0.04 Gyr, indicated by the black arrow in panle (b).

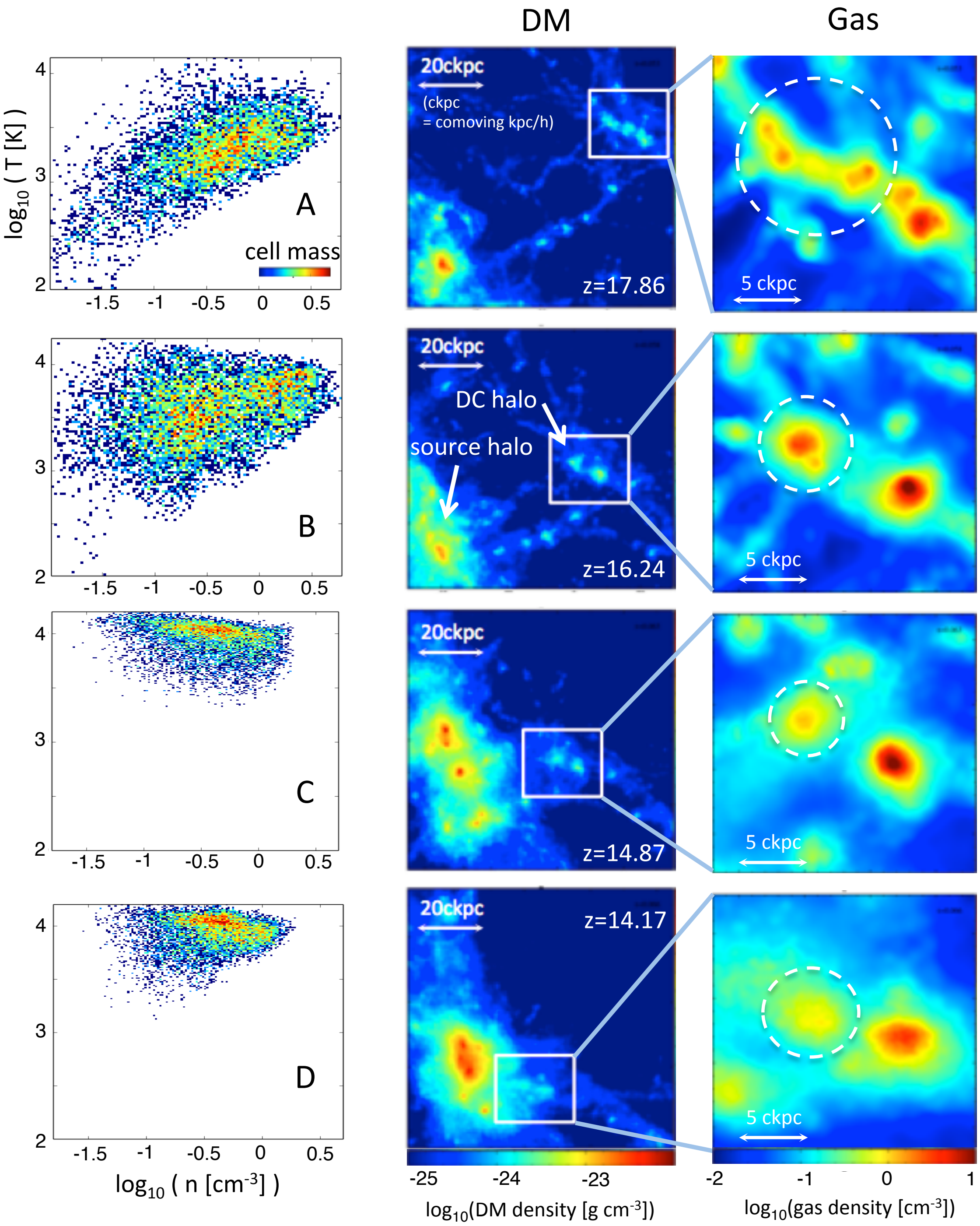

Figure 4.2. Time evolution of the F1 halo at four epochs attached in Figure 4.1. Left: temperature-density phase diagram of the halo gas. The color scale represents the cell mass in each bin. Middle: the projected DM density map around the F1 halo. The large clump at the bottom-left corner in each panel corresponds to the source halo. The candidate halo is located inside the white box. The color scale represents the DM density. Right: the projected gas density around the halo. There are two main clumps in each panel, and the clump on the left is the DC candidate halo (contained by the circle). The other clump is a halo in which a Pop III star is already formed. In each panel, the comoving length-scales of 20 h^{-1}kpc and 5 h^{-1}kpc are represented with the arrows.

In reality, the above expression is modified by a minor factor once we consider the rotation of the candidate halo around the source halo and the density profile of the source halo. These effects, however, introduce only a small change less than a factor of 2 for $R_{\rm tid}$ (Binney & Tremaine, 1987). We thus use eq. (4.1) in the following sections.

Figure 4.1(d) shows the time evolution of $R_{\rm tid}$ divided by the virial radius of the candidate halo, $R_{\rm vir}$. The dashed horizontal line shows where $R_{\rm tid}$ is comparable to $R_{\rm vir}$, that is, the matter at $R_{\rm vir}$ in the DC halo can be disrupted by the tidal field from the source halo. After epoch B, at which $R_{\rm tid} \sim R_{\rm vir}$, the density starts to decrease since the gas cloud is disrupted rather than collapses.

In Figure 4.2, the panels in each row represent the snapshots at the epochs A–D denoted in Figure 4.1(a). The panels in the left column reveal that the temperature of the central part of the cloud reaches 10^4 K at epoch B. The snapshots C and D show that most of the gas particles have temperature around 10^4 K. The panel sequence represents that the candidate halo bounded by the square is attracted by the light source halo through epochs A–D. At D, the candidate halo is completely swallowed by the source halo, together with its surrounding matter. The right panel (D) also shows that the cloud in the candidate halo is stretched toward the source halo and becomes elliptical in shape. This is a characteristic feature of tidal disruption, stretching an object toward the external gravitational source.

Figure 4.1a also shows that the candidate halo experiences multiple minor mergers with less massive halos after the virial temperature reaches 8000 K. The infalling halos inject the kinetic energy into the center of the candidate halo if they survive to reach the center, in a similar fashion to the dynamical disk heating (Toth & Ostriker, 1992). Once energy is deposited in the gas at the candidate halo center, the cloud center starts to expand and the density decreases. Then the cloud gets more susceptible to tidal disruption, since the expanded core is only loosely bound gravitationally, and easily disrupted by tidal force. (Figure 4.2 B). Interestingly, this is a two-step process; minor mergers under the strong tidal force initiate the destruction of the cloud. The density decrease around $z \simeq 22$ ($t \sim -2t_{\rm dyn}$) is caused by a minor merger.

As the discussion in Sections 4.3.3 and 4.5.2, major mergers can induce gravitational instability at the cloud center. The difference from the above discussion is simply whether or not a merger concentrates and brings enough mass toward the cloud center.

4.3.2 Case F2: collapse prevented by ram pressure stripping

Ram pressure often prevents the cloud collapse. Figures 4.3(a) and (b) represent the evolution of the density and the tidal radius. Even after the halo virial temperature exceeds 8000 K at $t = 0$, the density continue to decrease. The tidal force from the light source halo becomes comparable to the gravitational force at $t \sim t_{\rm dyn}$, while the halo experiences neither minor nor major mergers for $\simeq 50$ Myr after the halo satisfies the DC criteria.

We suspect that hydrodynamic effects make the gas cloud to disperse. Ram pressure

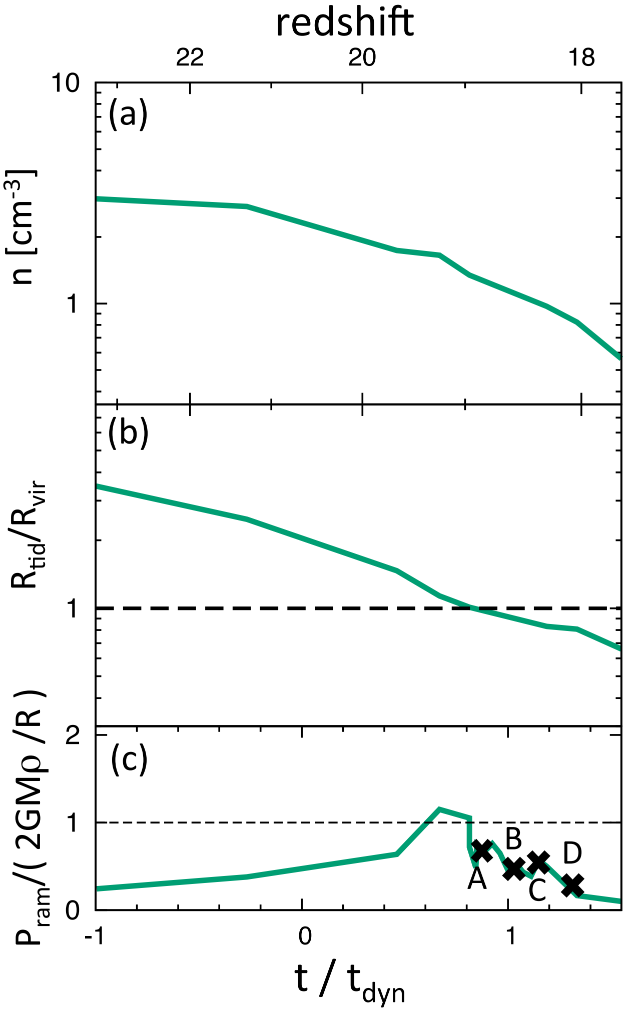

Figure 4.3. (a) Evolution of the gas density in the DC cloud for case F2 (DC2). The horizontal axis shows the elapsed time since the host halo satisfies DC criteria and normalized by the dynamical time at $t = 0$. (b) Evolution of the tidal radius divided by the virial radius of the host halo. The dashed line indicates where the tidal radius becomes comparable to the virial radius of the host halo. (c) Ratio of the ram pressure exerted on the cloud (eq. 4.2) and the gravitational force per unit area. The dashed line shows where the magnitudes of ram pressure and the gravitational force becomes comparable. The epochs A, B, C, and D are the reference epochs used in Figure 4.4. The reference dynamical time at $t = 0$ is $t_{\rm dyn} = 27.7$ Myr.

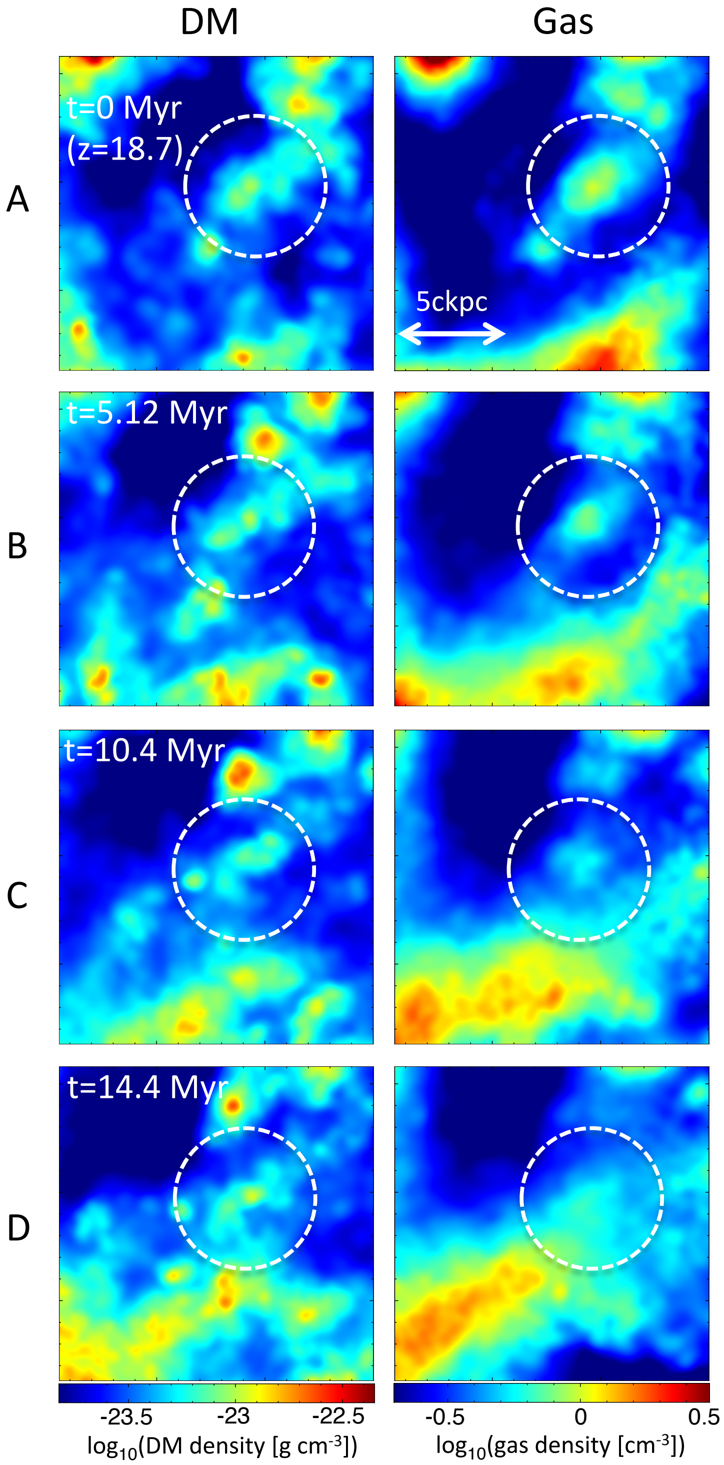

Figure 4.4. Time evolution of F2 halo at the four reference epochs attached in Figure 4.3(c). Left: the projected DM density distributions. The large clump at the top-left corner in each panel corresponds to the source halo. The candidate halo is located inside the circle. Right: the projected gas density around the candidate halo, the same region as in the left column. The elapsed time t from epoch A is attached to each panel.

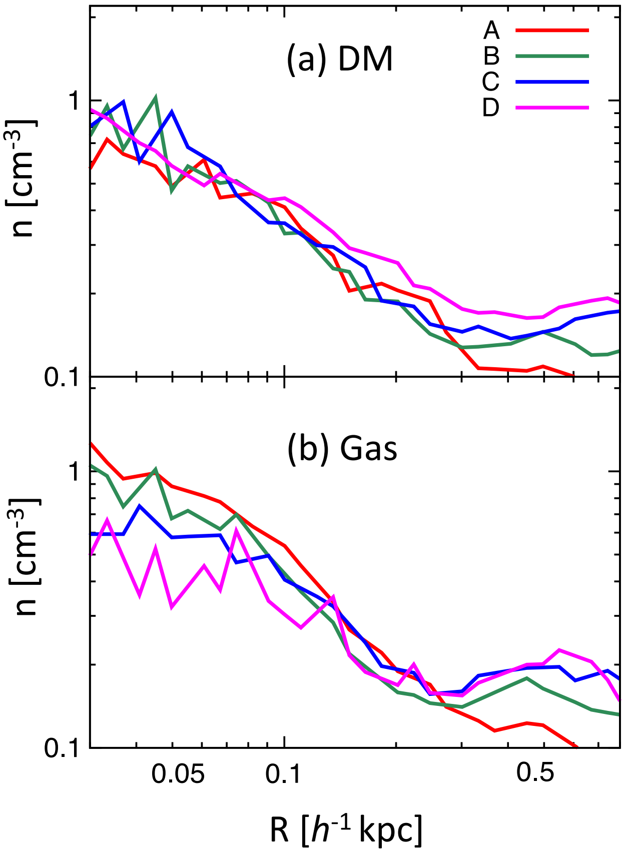

Figure 4.5. Radial density profiles of the (a) DM and (b) baryons for the F2 halo at the four reference epochs shown in Figure 4.3(c). The horizontal axis represents the distance from the density maxima of the cloud. To compare the DM density with the gas density, we convert the DM density into the corresponding baryon number density by $n_{\rm DM} \equiv f_{\rm b}\rho_{\rm DM}/(1.2m_{\rm p})$, where 1.2 is the mean molecular weight of the neutral gas.

can be evalutated by the product of density $\rho_{\rm gas}$ and velocity v as

$$P_{\rm ram} \equiv \rho_{\rm gas} v^2. \tag{4.2}$$

If a cloud is moving in a dense background matter, ram pressure can act on the cloud to strip the outer gas. The condition for the ram pressure stripping is given by

$$P_{\rm ram} > \alpha \frac{GM(<R)\rho_{\rm gas}}{R} \tag{4.3}$$

(Gunn & Gott, 1972; Gisler, 1976), where R is the size of the cloud, $M(<R)$ is the gravitating mass within R including DM, and α is an order of unity non-dimensional parameter characterized by the cloud morphology. The detailed numerical simulations by McCarthy *et al.* (2008) reveal that $\alpha = 2$ is appropriate for a spherical cloud. We find that the ram pressure acting on the cloud is the same order with the gravitational force at $t \sim 0.6t_{\rm dyn}$ (Figure 4.3c).

The discrepancy between the DM and gas density profiles exhibits another evidence for the ram pressure stripping acting on the cloud. Figure 4.4 shows the projected density distributions for DM and baryons at the reference epochs A, B, C, and D in Figure 4.3(c). Figure 4.5 shows the density profiles of the (a) DM and (b) gas at epochs A – D. The gas density decreases with time, while the DM profile remains almost unaffected. This fact implies that as the cloud moves toward the dense filament at the bottom, only the gaseous component suffers from a ram pressure and is dissolved into the surroundings, while the DM structure remains intact.

4.3.3 Cases S1 and S2: DC clouds

In cases S1 and S2, the gas clouds collapse and the central density reach 10^8 cm^{-3}. We mainly discuss the evolution for case S1 below, while the S2 case is briefly described in Section 4.3.3.2 since its overall evolution is so similar compared to that of S1.

4.3.3.1 The evolution of S1

Figures 4.6(a) and (b) show the merging history of halo S1 and the time evolution of the LW intensity at its progenitor center. There are two main tree branches (A and B), which are finally assembled into one candidate halo. Progenitors in both branches are exposed to strong radiation with nearly the same LW intensity, which suppresses Pop III star formation when $T_{\rm vir} > 2000$ K. The halo temperature grows rapidly from $T_{\rm vir} = 2000$ to 8000 K for a time-scale of $\simeq$ 50 Myr, which is shorter by a factor of two than that of halo F1 (Section 4.3.1). The rapid growth of S1 is the result of the major merger of two main branches A and B, at $t \sim 0$. Figure 4.6(c) and (d) represent that the density increases monotonically and that the tidal radius becomes comparable to the virial radius of the halo just after the major merger. The cloud can collapse even under the strong tidal field.

Gravitational collapse can be initiated not only by the self-gravity of the gas cloud but also by the gravity of the DM halo. The DM density profile of the candidate halo, $\rho_{\rm DM}(r)$, just follows a relation with the gas density $\rho(r)$ as $\rho_{\rm DM}(r) = \Omega_{\rm m}/\Omega_{\rm b}\rho(r)$ when the density is smaller than 100 cm^{-3} (Choi *et al.*, 2015). The radius $R_{\rm grav}$ of an isothermal cloud that experiences gravitational collapse is estimated by the ratio of the enclosed mass to the local Bonnor–Ebert mass, defined in Appendix A.17, including the contribution of the DM components. In the expression of eq. (A.17), we neglected the gravitational force originating from the matter outside the virial radius of the halo.

Figure 4.7(a) shows the ratio of two important spatial-scales: gravitational radius $R_{\rm grav}$ and tidal radius $R_{\rm tid}$. Just before $t \sim 0$, $R_{\rm grav}/R_{\rm vir}$ decreases almost by an order of magnitude. The situation where $R_{\rm grav}$ is much smaller than $R_{\rm tid}$ means that the cloud can collapse without being disrupted by the light source halo. In the case of F1, $R_{\rm grav}$ becomes larger than $R_{\rm tid}$ at $t \sim 0$, and that the cloud cannot collapse due to the strong tidal force (Figure 4.7b).

The right panels of Figure 4.8 show how successive mergers take place and lead to DC. Six gaseous clumps are finally merged into a clump at C. The mean temperature of the

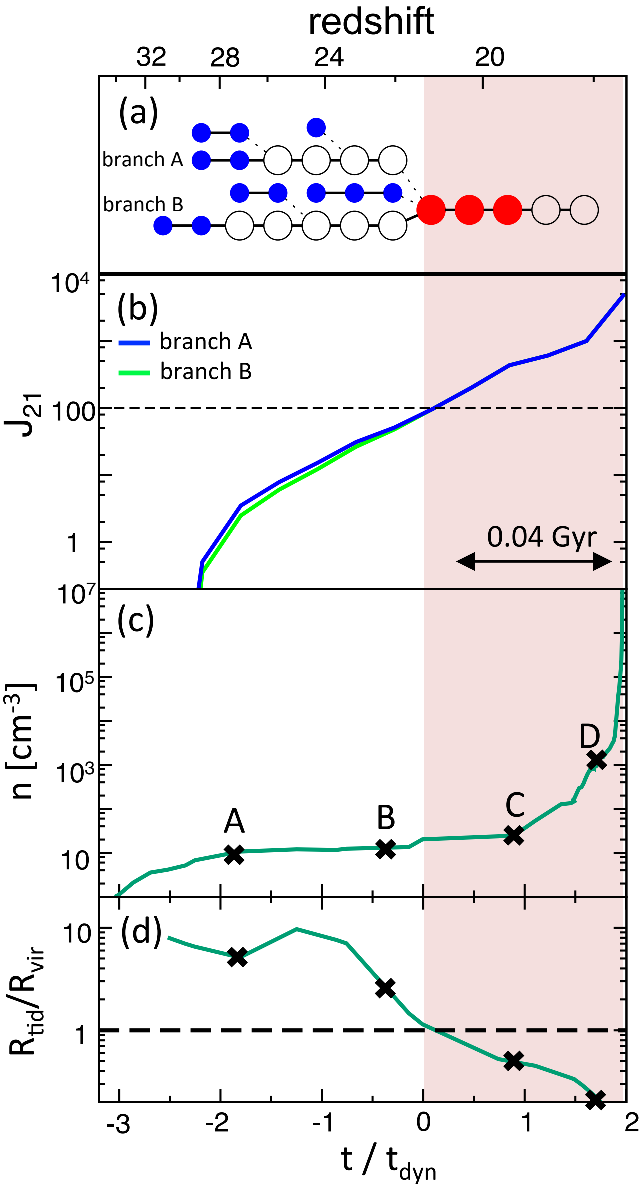

Figure 4.6. Same as Figure 4.1 but for case S1. There are two main branches (A and B), and the DC candidate halo is the product of the major merger of these two branches. The solid blue and green lines in panel (b) represent the evolutiond of the LW intensity at the halo center of branches A and B. The reference dynamical time at $t = 0$ is $t_{\rm dyn} = 26.9$ Myr.

clouds before the merger is $\simeq 4000$ K (left column of Figure 4.8B), which increases up to 8000 K after the merger (left column of Figure 4.8C). The rapid temperature increase is the result of the strong shocks generated by the mergers and enables efficient atomic hydrogen cooling. Radiative cooling reduces the pressure support, promoting the further collapse of the cloud. Interestingly, the two clumps merge at a relative velocity of 23.0 km s^{-1}, which is about twice the sound speed of the cloud.

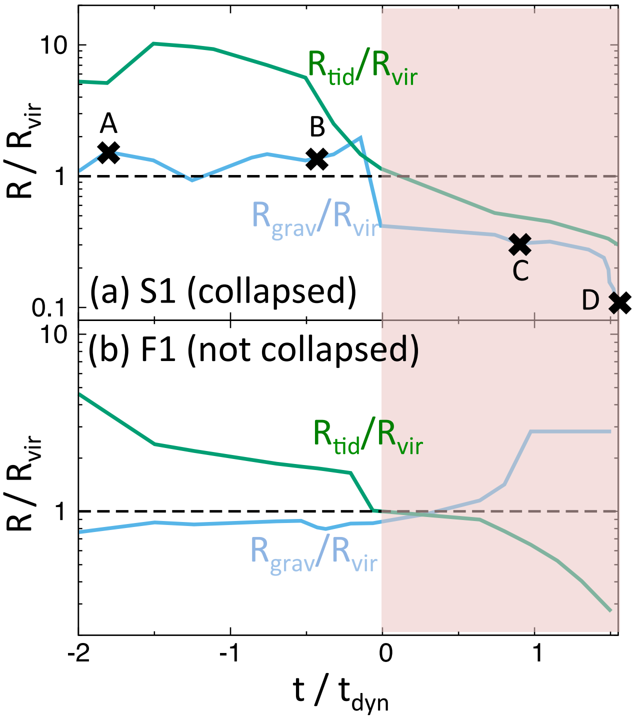

Figure 4.7. Evolution of gravitational radii (blue; eq. A.17) and the tidal radii (green) for (a) S1 and (b) F1, where each radii are normalized by the virial radii. The time origin $t = 0$ is set to be the moment at which the halo satisfies the DC criteria, and the time is normalized by the halo dynamical time at $t = 0$.

The major merger also assembles matters around the halo center. Figure 4.9 represents the enclosed mass within the distance R from the halo center before (dashed) and after the merger (black solid). The mass increases by an order of magnitude at $R \sim 0.1$ kpc. After the merger, the enclosed mass exceeds $M_{\rm BE}$ (red curve in Figure 4.9) at this scale, which leads to the gravitational collapse. Thus, it is the major merger which causes a sudden decrease of $R_{\rm grav}$ by an order of magnitude (Figure 4.7).

Major mergers increase the central density of the cloud, while the minor mergers act in the opposite way as in Section 4.3.1. Around the cloud core, the gravitational force dominates over the pressure force and over the tidal forces exerted by neighboring source halos. Clearly, the final core mass determines whether the cloud expands or contracts. We will discuss this issue more in detail in Section 4.5.2, in which we quantify the core entropy as a proxy to the collapse criteria.

4.3.3.2 The evolution of S2

The cloud in S2 also collapses in almost the same manner as in S1. There are two notable differences. One is that the major merger occurs about one dynamical time after when the halo meets the DC criteria. Here, the merger acts as promoting the collapse as in S1. The other is that the closest light source halo has a similar mass to that of S2. It exceeds the atomic-cooling mass at $20 - 30$ Myr earlier than S2 itself. Clearly, our S2 is a similar

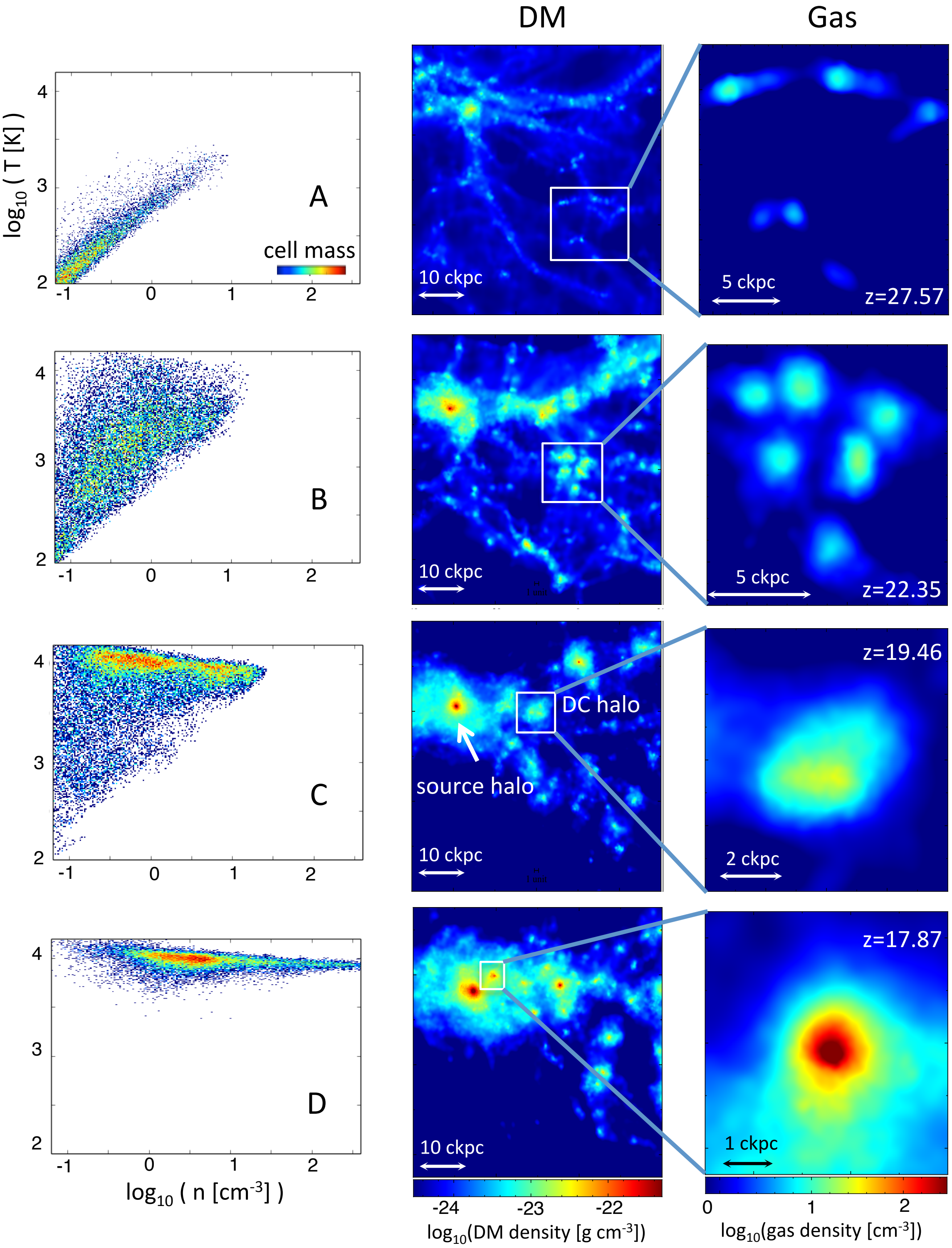

Figure 4.8. Same as Figure 4.2, but for four reference epochs for case S1 shown in Figure 4.6. We can observe six small clumps in epochs A and B that are merged into the DC candidate halo in epochs C and D.

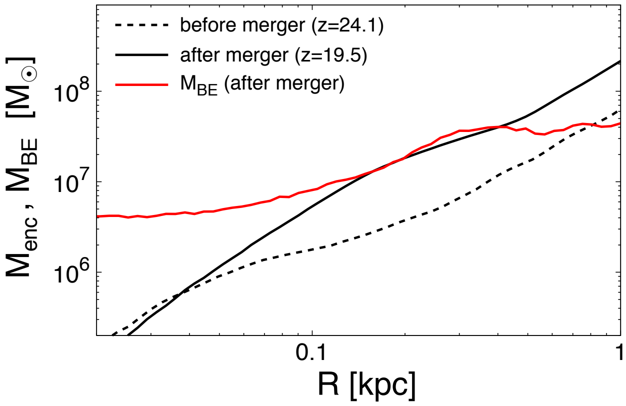

Figure 4.9. Radial profiles of the enclosed mass before ($z = 24.1$; black dashed) and after the major merger ($z = 19.5$; black solid) for the S1 halo. The red line shows the profile of the Bonnor–Ebert mass after the merger.

system to the "synchronized pair" studied in Visbal *et al.* (2014b), where the source and the main DC halo satisfy the atomic-cooling criterion simultaneously. In the case of S2, there is another luminous halo, which contributes about half the total J_{21} at S2.

The mass of the closest light source halo is not massive enough to have significant tidal effects on the main DC halo. We find that $R_{\rm vir}$ is smaller than $R_{\rm tid}$ over about one dynamical time after the halo satisfies the DC criteria. The central density remains high and the cloud 'survives' against tidal disruption until the final major merger triggers DC.

4.3.4 Thermal evolution of DC gas clouds

We here discuss the general features in the evolution of DC clouds. Figure 4.10(a) summarizes the density evolution of the DC candidate halos. We plot the evolution until the host halo completely merges with its nearby light source halo. For the low-z candidates (green lines) that meet the DC criteria at $z < 17$, the density peaks at $n = 1 - 3\ {\rm cm}^{-3}$ at $t \sim 0$, and then gradually decreases afterward. The high-z candidates (blue lines) at $z > 17$ have relatively higher densities than the low-z samples due to the cosmic expansion. Our high-resolution hydrodynamic simulations allow us to robustly determine whether or not DC is triggered in the candidate halos.

Figure 4.10(b) represents the temperature evolution as a function of density. At the early stage of the cloud collapse, the density and temperature follow the adiabatic EOS $T \propto n^{2/3}$. The temperature rises monotonically to $T \simeq 8000$ K, roughly tracing the halo virial temperature (Yoshida *et al.*, 2003). At $T > 1000$ K, the evolution sometimes deviates upward from the adiabatic track because of dynamical heating or shocks associated with mergers. The entropy monotonically increases since radiative cooling is inefficient until the temperature reaches 8000 K.

The density of the uncollapsed cloud reaches at most $\sim 10\ {\rm cm}^{-3}$. The Jeans length at the maximum density under $T = 8000$ K is $10^2 - 10^3$ pc , which is comparable to the

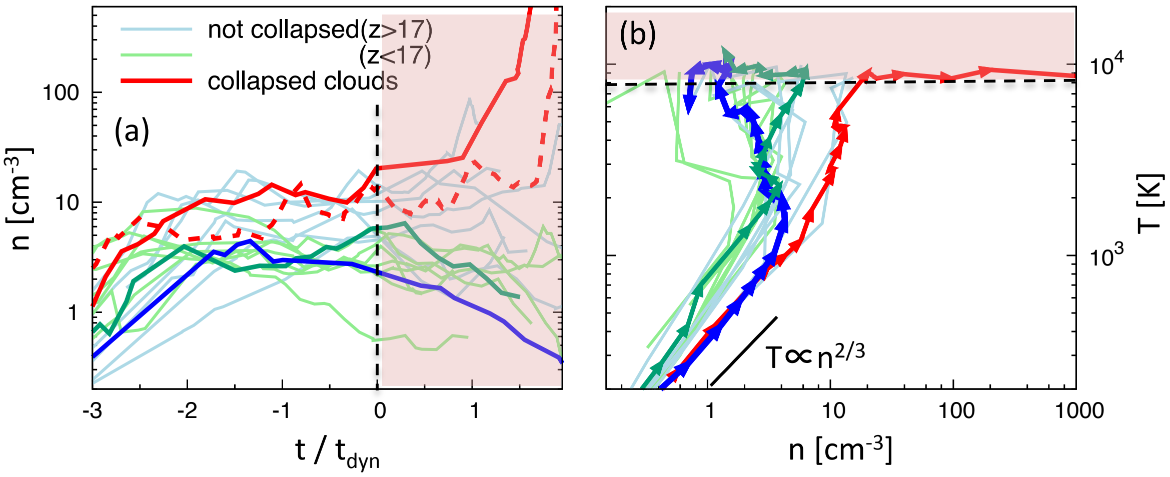

Figure 4.10. Time evolution of 16 gas clouds hosted by DC candidate halos. (a) Evolution of the central gas density n as functions of time t. We stress the four representative cases with thick lines: F1 (green), F2 (blue), S1 (red solid), and S2 (red dashed). The blue and green lines show the uncollapsed clouds that satisfy the DC criteria before and after $z = 17$, respectively. At the end of each line, the target halo merges with the light source halo, except for the collapsed clouds. (b) Temperature evolution as functions of the density for the 15 representative cases (S2 is not plotted since it follows almost the same path as for S1). The vectors represent the evolution at every $0.25t_{\rm dyn}$ for cases F1, F2, and S1 as in panel (a). For the other 12 DC clouds, we only plot the evolution paths on the plane, and the evolution is averaged for every $t_{\rm dyn}$. The black solid line indicates the adiabat, $T \propto n^{2/3}$. In each panel, the shaded region shows $T_{\rm vir} > 8000$ K, at which atomic hydrogen cooling operate.

virial radius of the host halo. In the case of F1, the tidal force at the virial radius is very strong since the DC halo approaches the light source halo rapidly before the host halo satisfies the DC criteria. We will show that similar evolution is observed in many of the other uncollapsed candidates in Section 4.5.1 later.

4.4 Formation of a protostar

We extend the calculations until the central density reaches 10^8 cm^{-3} for the collapsed candidates, S1 and S2. In both the clouds, the target clouds approach quickly the light source halo, while contracting. The bottom-left panel of Figure 4.11 shows a schematic picture of a relative locus of the S1 halo and the light source halo. The cloud is attracted gravitationally and passes by the light source. Figure 4.11 also represents the projected gas density around the DC halo at $t = 48.9$, 52.3, and 52.7 Myr, Again, the time origin is when the halo satisfies the DC criteria. The bottom-right panel ($t = 48.9$ Myr) corresponds to the reference epoch D in Figure 4.6.

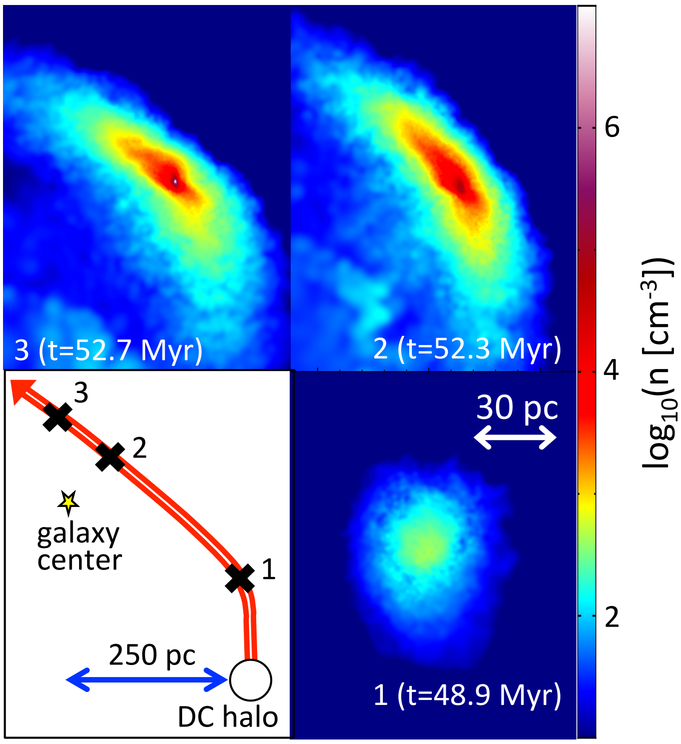

Figure 4.11. Bottom left: the schematic figure of the locus of the S1 halo relative to the radiation source. The red arrow represents the path of the DC halo. Bottom-right, top-right, top-left: The projected gas density distributions around the DC halo at the different epochs of $t = 48.9$, 52.3, and 52.7 Myr counterclockwise. This reference epochs correspond to the positions of 1, 2, and 3 in the bottom-left panel. The time origin is again the moment when the halo satisfies the DC criteria.

At $t = 48.9$ Myr, the cloud has an almost spherical shape while it is tidally elongated at $t = 52.3$ Myr. At $t = 52.3$ Myr, the cloud approaches 100 pc from the light source halo. During the pericenter passage, the cloud density increases and finally reaches 10^8 cm^{-3} quickly. Figure 4.12 represents gas density profiles at the three output epochs. The density evolves self-similarly (Larson, 1969; Penston, 1969), but is perturbed tidally at $R \simeq 4$ pc, deviating from the self-similar profile.

Note that, once the density exceeds $\simeq 3 \times 10^3$ cm^{-3} with $T = 8000$ K, H_2 cooling never becomes efficient (Inayoshi & Omukai, 2012). This region is called "zone of no return", where collisional dissociation efficiently destroys H_2 molecules than the external dissociating field. In our calculation, the cloud enters the regime at $t \simeq 48.9$ Myr, after which H_2 cooling never operate in a contracting gas.

We here estimate the final mass of an SMS to be formed in the gas cloud S1 and S2, from the velocity infall profile at our final snapshots. Figure 4.13 represents the radial distribution of the mass infall rate $\dot{M} \equiv 4\pi R^2 \rho(R) v_{\rm in}(R)$ for S1 (red) and S2 (blue) when the central density reaches 2×10^7 cm^{-3}. Here, $v_{\rm in}(R)$ is the infall velocity. We assume

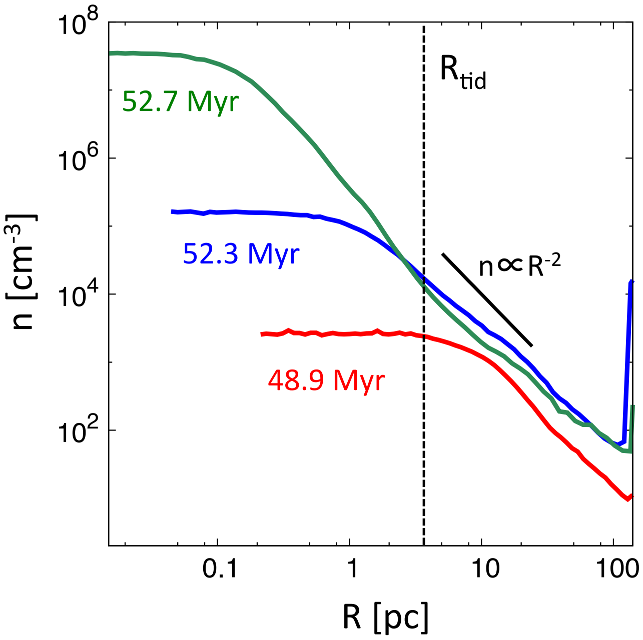

Figure 4.12. Radial gas density profiles in the S1 halo at $t = 48.9$, 52.3, and 52.7 Myr. The dashed line represents the tidal radius at which the tidal force dominates over the self-gravity of the gas cloud at $t = 52.7$ Myr.

that a protostar will accrete the surrounding gas roughly at the instantaneous mass infall rate. The expected mass infall rates are 0.1–1 $M_{\odot}$ yr^{-1} at $10^3\ M_{\odot} \lesssim M \lesssim 10^5\ M_{\odot}$ for S1 and S2 clouds. Interestingly, the mass is outflowing from the cloud at $M \gtrsim 10^5\ M_{\odot}$, which is caused by the tidal force from the source halo.

The obtained $\dot{M}$ is so large, as expected in the DC model. We can estimate the final stellar mass of the SMS without following the evolution in the accretion stage. The stellar evolution calculations represent that the stellar envelope inflates with such rapid mass accretion (e.g., Omukai & Palla, 2003; Hosokawa *et al.*, 2012). The stellar effective temperature is regulated nearly at $\simeq 5000$ K in a so-called supergiant stage. Consequently, the emissivity of ionizing photons is dramatically reduced (e.g., Hosokawa *et al.*, 2013; Schleicher *et al.*, 2013; Sakurai *et al.*, 2015), and that the radiative feedback will be too weak to halt the accretion flow. Thus, the star can finally accrete almost all the infalling gas. The estimated mass from the infalling rate is $2 \times 10^5\ M_{\odot}$ (S1) and $3 \times 10^5\ M_{\odot}$ (S2).

4.5 Cloud Collapse under Strong Tidal Field

In this section, we quantitatively evaluate the tidal effect on the evolution of DC candidate halos. Throughout this section, we refer to a candidate halo as the "target" halo, while a halo that is emitting H_2 dissociation photons is referred to as the "source" halo.

We first consider the magnitude of the tidal force at the virial radius $R_{\rm vir}$ of the target halo, which we compare with the tidal radius given in eq. (4.1). The tidal force by the

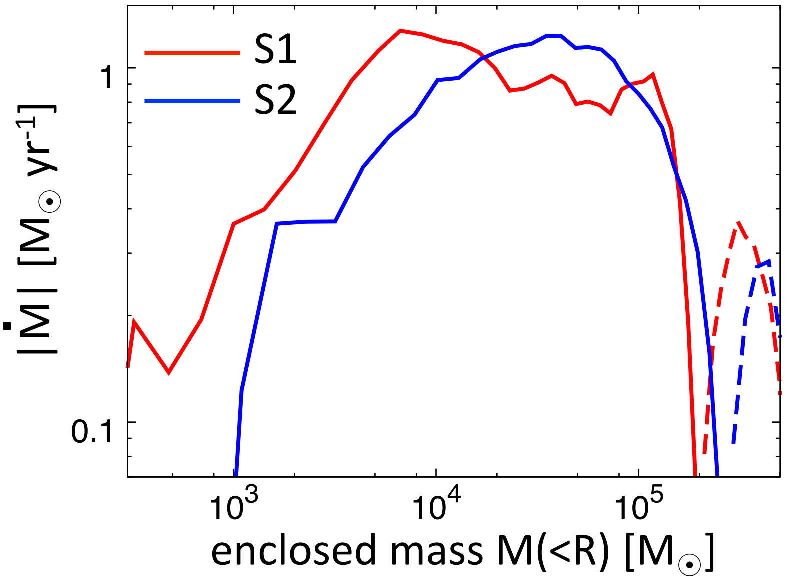

Figure 4.13. Instantaneous mass infall rates $|\dot{M}| = 4\pi r^2 \rho |v|$ as functions of the enclosed mass $|M(< R)|$. The infall rates are estimated from the snapshots, at which the central density reaches $2 \times 10^7\ \mathrm{cm}^{-3}$. We show the profiles for S1 (red) and S2 (blue). The solid lines show the mass infall rates, while the dashed lines show the mass outflow rates.

source halo becomes stronger as the target approaches the source. Thus, the cloud (in the target halo) should collapse within an infalling time-scale after the target halo satisfies DC criteria.

4.5.1 Evolution of tidal radius

We show the time evolution of the source halo mass and separation between the source and target halos in Figure 4.14. Each panel represents the snapshot at (a) $t = 0$, (b) 0.5, and (c) 1.0 $t_{\rm dyn}$ after the target halo satisfies the DC criteria. The shaded region shows $R_{\rm tid} < R_{\rm vir}$, where the outer envelope of the candidate halos is subject to the tidal force from the source.

In most cases, the halo virial temperature becomes smaller than 8000 K as they approach the source halo. The target halo loses its mass by tidal disruption and the tidal disruption prevents the clouds from collapsing. The target halo falls in faster than collapsing. With our model of a UV-emitting galaxy, the LW intensity at the center of the target halo with a separation $d_{\rm dist}$ from the source galaxy is evaluated by Iliev *et al.* (2005);

$$J_{21} = 63 \left(\frac{M_{\rm source}}{10^9\ M_\odot}\right)\left(\frac{f_\gamma}{2.0}\right) \left(\frac{f_{\rm J21}}{0.4}\right)^{-1}\left(\frac{20\ {\rm Myr}}{t_{\rm s}}\right)\left(\frac{1\ {\rm kpc}}{d_{\rm dist}}\right)^2, \tag{4.4}$$

where $t_{\rm s}$ is the mean stellar lifetime of UV-emitting stars in the source halo, $f_{\rm J21}$ is the

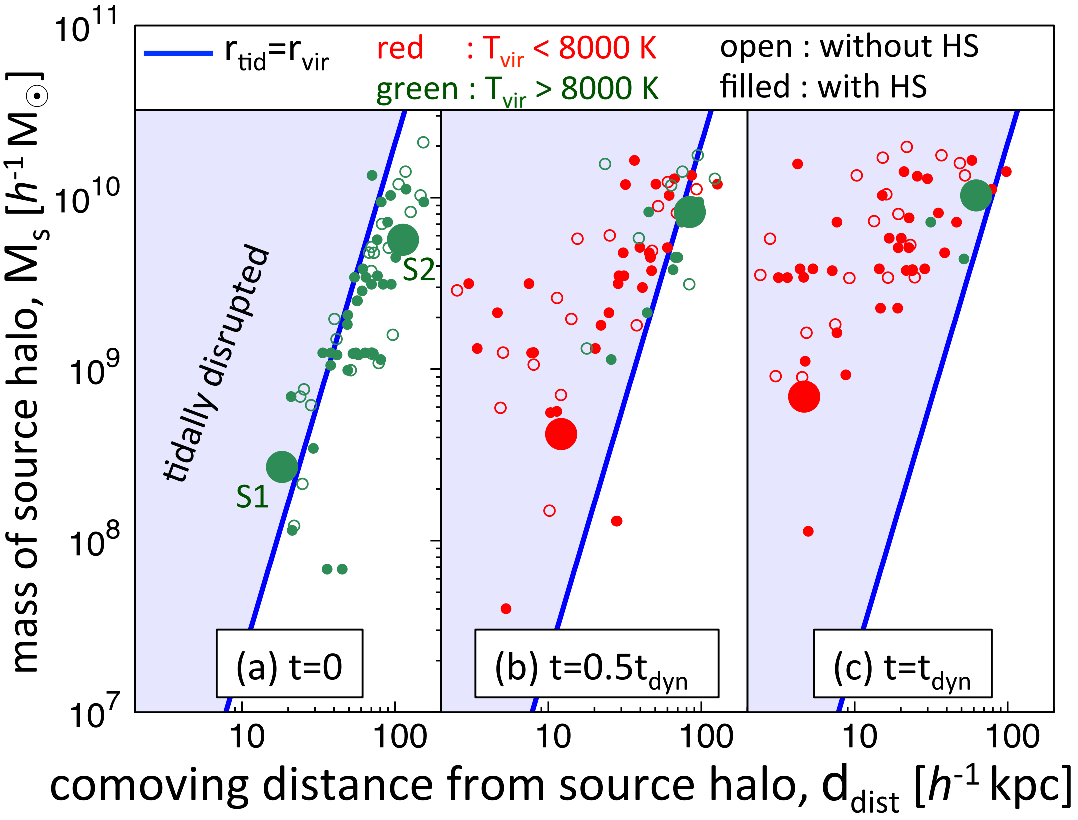

Figure 4.14. Time evolution of the source halo mass M_s and the comoving distance between the DC candidate and source halos d_dist for all 68 candidate halos. Panels (a), (b), and (c) represent the snapshots at the different epochs $t = 0$, 0.5, and $1.0t_\mathrm{dyn}$, respectively. The candidate halos satisfy the DC criteria at $t = 0$. The symbol colors show the virial temperature of the halos, $T_\mathrm{vir} < 8000$ K (red) and > 8000 K (green). The filled and open circles represent whether the hydrodynamical simulations (HS) are performed. The halos that host the collapsed clouds (S1 and S2) are emphasized by the larger circles. In each panel, the shaded area indicates $R_\mathrm{tid} < R_\mathrm{vir}$, at which the tidal force is strong enough to disrupt the halo envelope. The solid line shows the critical points for $R_\mathrm{tid} = R_\mathrm{vir}$.

fraction of the LW intensity originating from the closest luminous galaxy to the total LW intensity, f_γ is defined as $f_\gamma \equiv f_* f_\mathrm{esc} N_\mathrm{i}$, where f_* is the star formation efficiency, which is the fraction of baryons converted to stars, f_esc is the escape fraction of the UV photons, and N_i is the number of the emitted photons per unit stellar mass throughout the mean stellar lifetime t_s. We use the fiducial value of $f_\gamma = 2$ (Iliev *et al.*, 2007) and $f_\mathrm{J21} = 0.4$. The latter choice is motivated by the result of our semianalytic calculation (Section 3.2.3).

Equation (4.4) gives the critical distance d_LW, within which the target halo is irradiated by sufficient LW intensity for DC. With our standard normalizations, the critical distance

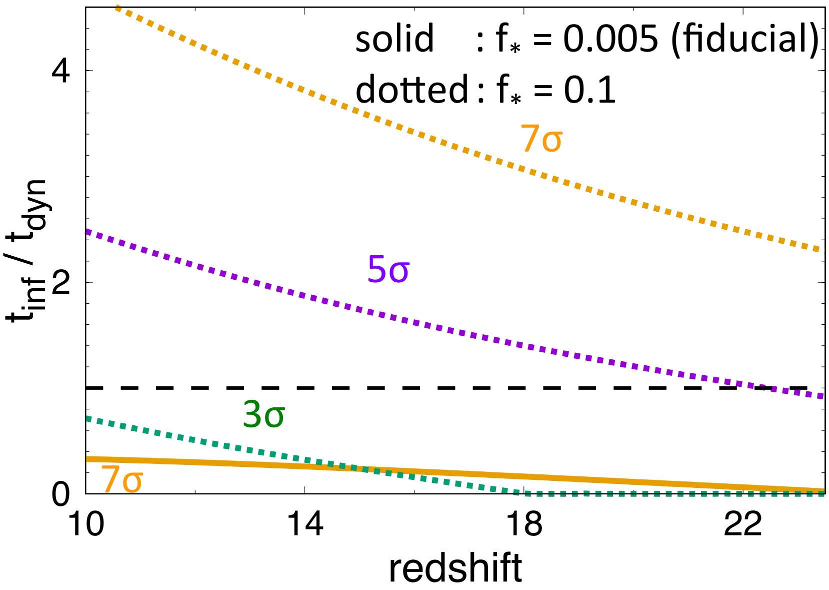

Figure 4.15. Infall time of the target halo from $d_{\rm LW}$ (eq. 4.5) to $d_{\rm tid}$ (eq. 4.6), normalized by the dynamical time at each epochs. The lines show the evolution for the source halos formed around 3σ (green), 5σ (purple), and 7σ (orange) initial density peaks. The solid and dotted lines are the results for the fiducial and enhanced star formation efficiency, $f_* = 0.005$ and 0.1, respectively. The other two cases with 3σ and 5σ with $f_* = 0.005$ are not presented since $d_{\rm LW}$ is always smaller than $d_{\rm tid}$. The horizontal dashed line denotes $t_{\rm inf} = t_{\rm dyn}$.

is written by

$$d_{\rm LW} = 0.2\ {\rm kpc} \left(\frac{M_{\rm source}}{10^8\ M_\odot}\right)^{1/2} \left(\frac{f_\gamma}{2}\right)^{1/2} \left(\frac{f_{\rm J21}}{0.4}\right)^{-1/2} \left(\frac{20\ {\rm Myr}}{t_{\rm s}}\right)^{1/2} \left(\frac{100}{J_{21}^{\rm crit}}\right)^{1/2}. \tag{4.5}$$

The distance at which the tidal radius is equal to the virial radius, $d_{\rm tid}$, is given by eq. (4.1) as

$$d_{\rm tid} = 0.524\ h^{-1}\ {\rm kpc} \left(\frac{M_{\rm source}}{10^8\ h^{-1}\ M_\odot}\right)^{1/3} \left(\frac{10}{1+z}\right), \tag{4.6}$$

where z is the redshift under consideration.

A cloud can collapse when it lies in $d_{\rm tid} < d_{\rm dist} < d_{\rm LW}$, if the collapse is initiated at the scale of the virial radius. Since the source halo also grows in mass, the ratio of $d_{\rm LW}$ to $d_{\rm tid}$ gets larger and the target halo might spend for a longer time in $d_{\rm tid} < d_{\rm dist} < d_{\rm LW}$, because $d_{\rm LW} \propto M_{\rm source}^{1/2}$ while $d_{\rm tid} \propto M_{\rm source}^{1/3}$.

We estimate the infalling time for the target halo moving from the distance $d_{\rm LW}$ to $d_{\rm tid}$, considering the initial infalling velocity at $d_{\rm LW}$. Detailed derivation based on a spherical collapse model is presented in Appendix D. We find that the derived infall time $t_{\rm inf}$ is determined by the source halo mass but independent of the target halo mass.

Figure 4.15 represents the infalling time $t_{\rm inf}$ for the source halo formed at 3σ (green), 5σ (purple), and 7σ (yellow) peaks of the initial density field. The solid line indicates the case with the fiducial values in our semianalytic model. We select 3σ–4σ regions in our hydrodynamical simulation, so the candidate halos should be disrupted by the tidal force from the source halo before the collapse, apart from a few exceptions for which the major merger accelerates the cloud collapse. Even for a 7σ halo, as rare as the observed high-z QSOs ($\sim$ Gpc^{-3}), $t_{\rm inf}$ is much smaller than $t_{\rm dyn}$. The dashed lines indicate the infalling time of the target halo with the enhanced star formation efficiency $f_* = 0.1$, much larger than the typical value $f_* = 0.005$. This is the largest value of f_* compatible with the observed galaxy luminosity functions at $z \sim 6$–7 (Agarwal *et al.*, 2012). The infalling time $t_{\rm inf}$ can exceed $t_{\rm dyn}$ in higher-density peaks, while they are of an order unity even for 7σ peaks in the shown redshift range. This fact suggests that the tidal force still has some impact on the collapse of the target halo since $t_{\rm inf}$ remains comparable to $t_{\rm dyn}$.

The above discussions focus only on the tidal force at the virial radius. We have shown that when an infalling cloud begins collapsing near the virial radius of the target halo, it approaches the source halo so fast that the tidal force becomes strong and prevents the collapse. Therefore, for a cloud to experience DC, gravitational instability should take place well within the inner part of the target halo, where the tidal effect from the source halo is not important.

4.5.2 Onset of the cloud collapse

The DC (candidate) clouds evolve adiabatically, without significant radiative cooling, until the gas temperature reaches 8000 K since H_2 cooling is inefficient. It is known that a gas cloud contracting adiabatically follows a universal entropy profile, as studied in the context of the formation of galaxy clusters (e.g., Voit *et al.*, 2003, 2005). In spite of the enormously different mass-scale, our simulated gas clouds hosted by the candidate halos also reveal such universal features (see also Visbal *et al.*, 2014a).

The "entropy" of an ideal gas is defined by the thermodynamical variables as

$$K = k_{\rm B} T n_{\rm b}^{-2/3}, \tag{4.7}$$

where $k_{\rm B}$ is the Boltzmann constant, T is the temperature, and $n_{\rm b}$ is the baryon number density. We also define a "halo entropy" as

$$K_{200} = k_{\rm B} T_{\rm vir} (200 \bar{n}_{\rm b})^{-2/3}, \tag{4.8}$$

where $\bar{n}_{\rm b}$ is $\Omega_{\rm b}/\Omega_{\rm m}$ times the mean matter density of the universe. The entropy profile of the cloud is composed of two parts, a constant entropy core and an outer envelope with $K \propto (r/r_0)^{1.1}$. During the adiabatic collapse, the core radius and entropy are approximately given by $R_{\rm core} \sim 0.1 R_{\rm vir}$ and $K_{\rm core} \sim 0.1 K_{200}$, respectively (Visbal *et al.*, 2014a). Our simulated DC clouds roughly follow this universal profile. Figure 4.16(a) represents $K_{\rm core}$ of the candidate halos just after they satisfy the DC criteria. The halos have slightly larger entropies than $0.1 K_{200}$ but show little redshift dependence. Interestingly, the two successful cases, S1 (red) and S2 (blue), have the smallest entropies after the

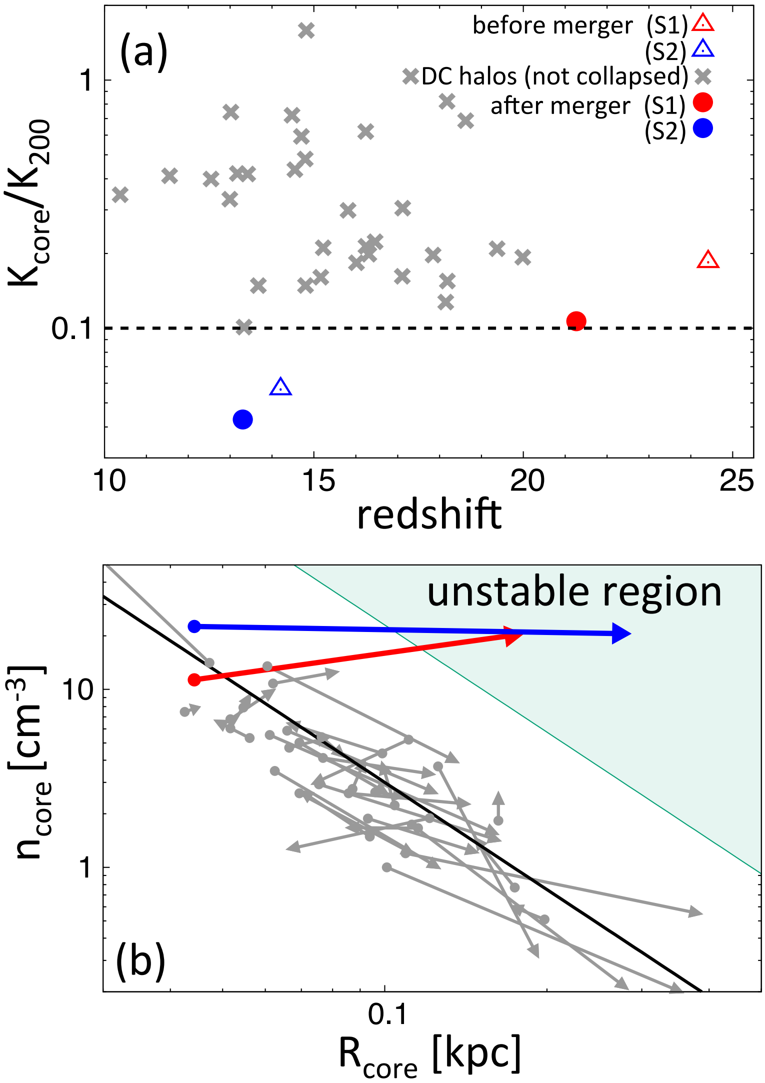

Figure 4.16. (a) Entropies of the cloud core normalized by K_{200} (eq. 4.8). The colored symbols represent the collapsed halos S1 (red) and S2 (blue), whereas the gray symbols show the uncollapsed clouds. The open and filled symbols show the entropies of collapsed clouds before and after the major merger, respectively. The dashed line shows the averaged value of the entropy estimated from the universal profile. (b) Evolution of the core radius and core density after the host halo satisfies the DC criteria. The start (filled circle) and end points of each arrow indicate the core properties when the halos satisfy the DC criteria and $1t_{\rm dyn}$ after that moment, respectively. The black solid line represents the analytical core radius–density relation estimated by eq. (4.11). The cloud gets gravitationally unstable inside the shaded region, satisfying eq. (4.12).

major merger. Figure 4.16(b) shows the evolution of all the DC clouds in the $n_{\rm core}$ - $R_{\rm core}$ from the time when the halo satisfies the DC criteria (initial point) in one dynamical time ($t_{\rm dyn}$) after that moment. The arrows indicate the evolution of these values in the figure. We define $R_{\rm core}$ as the radius at which the density becomes half the maximum density of the cloud. If we assume $K_{\rm core} = 0.1K_{200}$ and $R_{\rm core} = 0.1R_{\rm vir}$, the core properties follow the relations as (Inayoshi *et al.*, 2015):

$$\begin{aligned} R_{\rm core} &= 0.1R_{\rm vir}, \\ &= 35\ h^{-1}\ {\rm pc} \left(\frac{T_{\rm vir}}{10^4\ {\rm K}}\right)^{3/2} \left(\frac{1+z}{16}\right)^{-3/2}, \end{aligned} \tag{4.9}$$

$$n_{\rm core} = \left(\frac{K_{\rm core}}{K_{200}}\right)^{-3/2} \bar{n}_{\rm b} = 22\ {\rm cm}^{-3} \left(\frac{1+z}{16}\right)^{3}. \tag{4.10}$$

By assuming $T_{\rm vir} = 8000$ K, we can obtain an analytical estimate

$$n_{\rm core} = 0.03\ {\rm cm}^{-3} \left(\frac{R_{\rm core}}{1\ {\rm kpc}}\right)^{-2}. \tag{4.11}$$

The estimates are in good agreement with the core properties of our simulated samples (Figure 4.16b).

For a gas cloud to collapse, the core mass should be larger than the Bonnor–Ebert mass (Appendix A.1.2). The core mass can be given by $\sim R_{\rm core}^3\rho_{\rm core}$, and that the condition for the gravitational instability to set in can be written as

$$n_{\rm core} > 0.23\ {\rm cm}^{-3} \left(\frac{R_{\rm core}}{1\ {\rm kpc}}\right)^{-2}, \tag{4.12}$$

which is indicated by the shaded region in Figure 4.16 (b). Note that the critical density is an order of magnitude higher than the actual core densities. Figure 4.16(b) represents that most of the candidate halos, aside from the two successful clouds, lie in the stable region, even one dynamical time after the gas begins cooling. Clearly, the core density needs to grow higher to trigger DC.

We have seen that, in the cases of S1 and S2, major mergers drive the gas cloud collapse. The high-speed mergers with relative velocity of $v_{\rm rel} \sim 2c_{\rm s}$ generate shocks and increase the gas entropy around the cloud center. As can be seen in Figure 4.16(b), the mergers increase not only the core density but also the core size by an order of magnitude. The S1 and S2 clouds jump into the gravitationally unstable region shown in the figure.

We here summarize the discussion in this section. An adiabatically contracting gas cloud follows a universal entropy profile composed of a core and an envelope. For the DC gas clouds in our simulation, the cloud core does not contain large enough mass to gravitationally collapse. The core would grow further in mass through accreting the surrounding gas, but the host halo itself is tidally disrupted rapidly within one dynamical time. Thus, gravitational collapse is often completely halted. The only "successful" way found in this

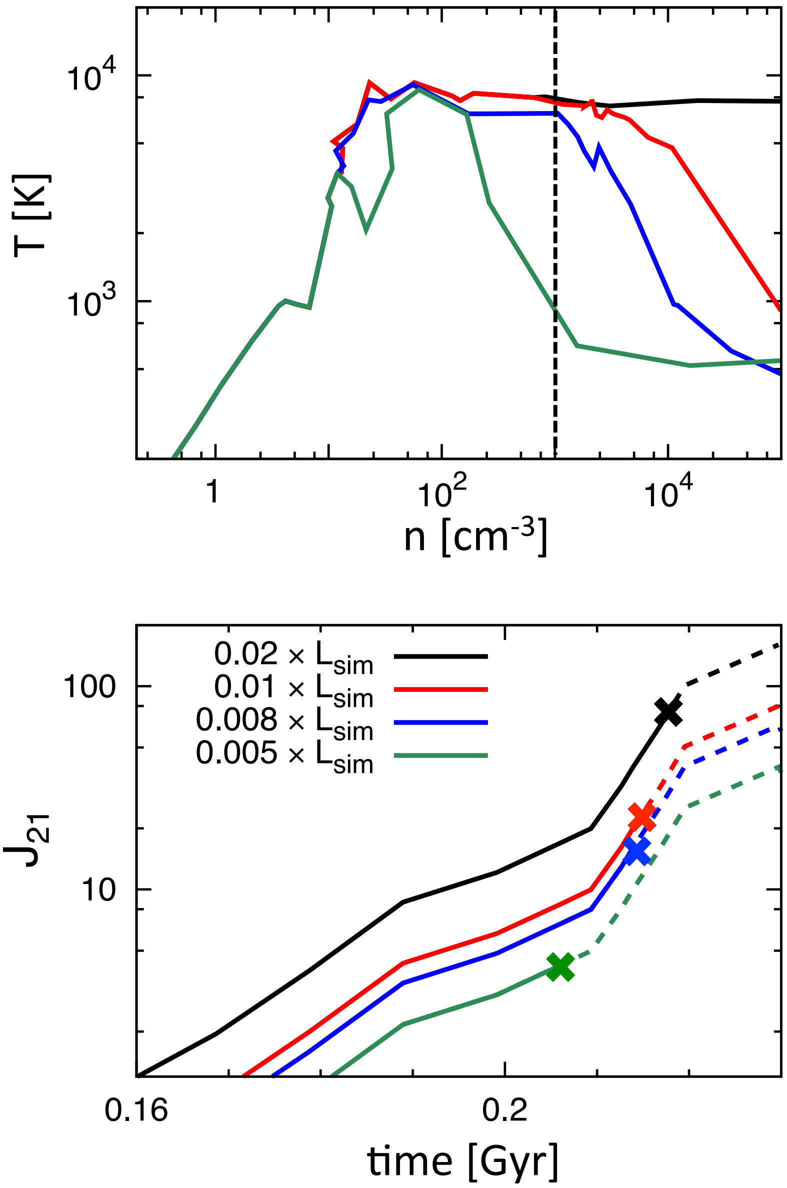

Figure 4.17. (a) Thermal evolution of the collapsing cloud S1 with the reduced LW luminosities of the light source halo: 0.5% (green), 0.8% (blue), 1% (red), and 2% (black) of the original luminosities. (b) Time evolution of J_{21} for the same cases. The crosses represent the moments at which the cloud density reaches $n_{\rm LTE} = 10^3\ {\rm cm}^{-3}$. The dashed line represents the evolution of LW intensity for $n > n_{\rm LTE}$.

chapter is the sudden increase of the core mass by major mergers. We have found that the successful DC systems in our samples actually experience major mergers.

4.6 Discussion

4.6.1 Critical LW intensity for DC

We adopt $J_{21}^{\rm crit} = 100$ as our fiducial critical value for Pop II sources (Shang *et al.*, 2010). We have also found that the LW intensity at a cloud center varies with time as it approaches the light source galaxy. It is important to revisit in detail the critical intensity $J_{21}^{\rm crit}$ for DC.

Whether a gas cloud evolves along the atomic-cooling track is determined by the LW intensity at which the gas density reaches $n_{\rm LTE} \sim 10^3 \ {\rm cm}^{-3}$, the critical density for the H_2 ro-vibrational transitions (e.g., Omukai, 2001; Shang *et al.*, 2010). To study the effect of a time-dependent LW radiation, we carry out several test simulations based on our sample S1 halo.

We first record the time evolution of the LW luminosity of the light source halo $L_{\rm sim}(t)$ in the original case S1. We then follow the collapse of the same gas cloud, with smaller source LW luminosity of 0.5%, 0.8%, 1%, and 2% of the original $L_{\rm sim}(t)$. Note that, for all these models, the LW intensities at the virialization are much smaller than the adopted critical value $J_{21}^{\rm crit} \sim 100$. Figure 4.17(a) represents the evolution of LW intensities for the test cases. We see that even 2% of the original $L_{\rm sim}(t)$ can cause DC, whereas H_2 formation and cooling operate with 1% of $L_{\rm sim}(t)$.

Figure 4.17(b) plots the time evolution of the LW intensity. The crosses represent the epoch when the core density reaches $n_{\rm LTE} = 10^3 \ {\rm cm}^{-3}$. The critical LW intensity at $n \sim n_{\rm LTE}$ is between 20 – 80, and comparable to $J_{21}^{\rm crit}$ obtained by Shang *et al.* (2010). Thus, we suggest that the critical LW intensity for DC should be evaluated at $n \sim n_{\rm LTE}$, not at the time of virialization. The figure also indicates that a slight reduction of the source luminosity results in a dramatically lower value of $J_{21,n_{\rm LTE}}$. With 0.5% of $L_{\rm sim}(t)$, for example, $J_{21,n_{\rm LTE}}$ is lower by an order of magnitude than that with 2% of $L_{\rm sim}(t)$, although the luminosity differs only by a factor of four. This is because, with 0.5% of $L_{\rm sim}(t)$, the collapse advances much earlier owing to efficient H_2 cooling when the cloud is located at a distant place from the source galaxy. Clearly, we should follow both the cloud collapse as well as the halo assembly to derive the LW intensity at the critical density $n_{\rm LTE}$.

The above results suggest that setting $J_{21}^{\rm crit} \sim 100$ at the virialization is too strict for DC. Generally speaking, it takes a few dynamical times from the virialization until the density reaches $n \sim n_{\rm LTE}$. During the collapse, J_{21} increases by an order of magnitude as the cloud approaches the source halo. Therefore, moderate LW intensity at the epoch of the virialization, which is much lower than previously thought, is enough to induce DC.

This opens up a possibility that a larger number of DC halos may exist in the universe since the required LW intensity at the virialization is so small (Dijkstra *et al.*, 2008). For the DC halos in a realistic cosmological context, however, the exact value of $J_{21}^{\rm crit}$ at virialization depends on the subsequent evolution, which can be followed only by hydrodynamical simulations. Ultimately, we need a number of hydrodynamics simulations with a large volume, with which we can find possibly more halos under the moderate LW fields $J_{21} \sim 10$. In such simulations, we should follow the cloud collapse until the central density reaches $n \sim 10^3\ \mathrm{cm}^{-3}$ for each case.

4.6.2 Effects of ionization photons and X-Ray

We only consider UV photons with energies below 13.6 eV since the mean free path of ionizing photons is much smaller than that of the LW photons. If a collapsed cloud approaches the close vicinity of the source galaxy, the cloud might be affected directly by ionizing photons.

The ionizing radiation enhances H_2 cooling, since the electrons catalyze the formation of H_2 via the H^- reaction channel. The increased ionization degree accelerates the formation of H_2, and that may prevent DC. In addition, X-ray photons generated by the light source have large mean free paths, which can have an impact on the evolution of the cloud (Inayoshi & Omukai, 2011; Inayoshi & Tanaka, 2015). In this section, we examine the effect of ionizing photons and X-ray photons by the one-zone model.

It is important to address the impact of the X-rays on the thermal evolution of DC clouds. To this goal, we employ one-zone calculations and follow the evolution of the S1 cloud by including the additional radiation. We directly use the density evolution found in our simulation because the cloud actually collapses over a much longer time-scale than t_{ff}, while we assume that the collapse proceeds at a rate of t_{ff} once H_2 cooling operate. That is, the density evolution can be described as

$$\frac{\mathrm{d}\rho}{\mathrm{d}t} = \begin{cases} \rho/t_{\mathrm{ff}} & \text{(when H}_2\text{ cooling is efficient)}, \\ \dot{\rho}_{\mathrm{sim}}(t) & \text{(otherwise)}, \end{cases} \tag{4.13}$$

where $\dot{\rho}_{\mathrm{sim}}(t)$ is the time derivative of the density of the cloud core found in our simulation. Non-equilibrium chemistry and the energy equation are solved in the same fashion as in our three-dimensional simulations described in Section 4.2.1. The column density N_i of the species i is given by

$$N_i = 0.5\ \lambda_{\mathrm{J}} n y_i, \tag{4.14}$$

where λ_{J}, n, and y_i are the Jeans length, the gas density, and the number fraction of the species i of the cloud core, respectively. The self-shielding against the ionizing and X-ray photons and the secondary ionization are also considered, following Wolfire *et al.* (1995). The LW intensity is assumed to be the same as the intensity in the 3D simulation (S1).

We carry out one-zone calculations for two different types of spectra: a black-body spectrum with $T_{\mathrm{eff}} = 10^4$ K, and soft X-ray radiation with a power-law $J_{21} \propto J_{21,\mathrm{X}} \left(\nu/\nu_0\right)^{-\alpha}$, with $h\nu_0 = 1$ keV and $\alpha = 1.8$. These conditions are, respectively, that the DC cloud is located within the Strömgren radius around its light source halo and that the cloud is irradiated by X-ray radiation from the source. The spectra resemble those of stars and QSOs, respectively. As for the QSO-type spectrum, we give the minimum and the maximum energy as $h\nu_{\mathrm{min}} = 1$ keV and $h\nu_{\mathrm{max}} = 10$ keV.

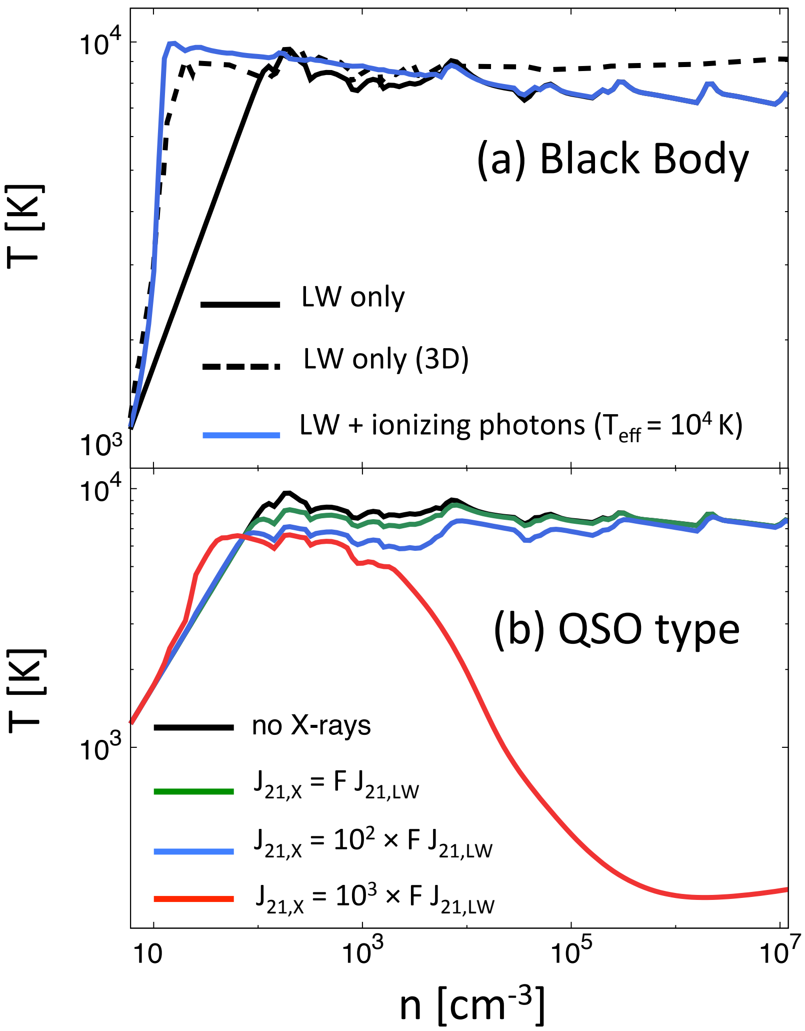

Figure 4.18. (a) Evolution of the temperature with the increasing density with and without ionizing radiation. The lines shows the evolution with the black-body radiation with $T_{\rm eff} = 10^4$ K(blue) and without ionizing photons (black). The dashed line corresponds to the result of 3D simulation (S1), while the solid lines are those of the one-zone calculation. In the presented one-zone models, the density evolution is taken from our 3D hydrodynamical simulation (see eq. 4.13). The radiation intensity is the same as the normalization of the intensity at the LW bands, $J_{21,\rm LW}$. (b) Evolution of the temperature with and without X-rays of the QSO-type spectra, $J_{21} = J_{21,\rm X}(\nu/\nu_0)^{-\alpha}$. The black line represents the evolution without the X-rays, while the green, blue, and red lines represent those with $J_{21,\rm X} = 1$, 10^2, and $10^3 \times FJ_{21,\rm LW}$, respectively.

The X-ray observations of local starburst galaxies suggest a correlation between the X-ray luminosities and SFR as (Glover & Brand, 2003; Grimm *et al.*, 2003):

$$L_{\mathrm{X}} = 6.7 \times 10^{39} \left(\frac{\mathrm{SFR}}{M_{\odot}\ \mathrm{yr}^{-1}} \right) \mathrm{erg\ s}^{-1}. \tag{4.15}$$

Another correlation is known between the LW luminosities and SFR (Inoue, 2011):

$$L_{\mathrm{LW}} = 1.14 \times 10^{43} \left(\frac{\mathrm{SFR}}{M_{\odot}\ \mathrm{yr}^{-1}} \right) \mathrm{erg\ s}^{-1}. \tag{4.16}$$

By eliminating SFR in the above two equations, we get the relation between the intensities $J_{21,\mathrm{LW}}$ and $J_{21,\mathrm{X}}$ as follows (Inayoshi & Tanaka, 2015):

$$J_{21,\mathrm{X}} = 5.7 \times 10^{-6}\ J_{21,\mathrm{LW}} \equiv F J_{21,\mathrm{LW}}. \tag{4.17}$$

Figure 4.18(a) plots the evolution with the stellar radiation case. We divide the ionization radiation intensity at the Lyman-limit, J_{UV}, to be J_{21}. Owing to ionization heating, the temperature rises rapidly to $T \sim 10^4$ K. The subsequent collapse proceeds almost isothermally by efficient atomic hydrogen cooling. The cloud gets optically-thick to the ionization radiation when the density reaches $\sim 10^3\ \mathrm{cm}^{-3}$, and the thermal evolution converges to that of the case without ionizing radiation. This is consistent with the 1D radiation hydrodynamics calculation of Kitayama *et al.* (2001).

Figure 4.18(b) plots the evolution with the QSO-type radiation. For comparison, the evolution under 10^2 and 10^3 times stronger X-ray intensities is also calculated. In the case with 10^3 times stronger X-ray intensity, molecular cooling operates and DC does not occur. This case is an extreme example, and we do not expect that such a strong X-ray spectrum are realized in the early universe. Overall, neither ionizing nor X-ray radiation have a significant impact on the thermal evolution of the DC cloud of S1 (note a similar conclusion by Inayoshi & Tanaka, 2015, for the former case). [*2]

4.6.3 Effect of metal enrichment

Our model includes metal enrichment within progenitor halos (so-called “inherent” metal enrichment), but we do not consider “external” metal enrichment by nearby halos. We have shown that the DC halos approach very close ($\sim$ 100 pc) to the light source halos, in which a huge amount of metal is produced. The separation is well inside the virial radius of the source halo $\simeq$ 700 pc, and that the DC halos could be polluted by metals scattered from the star-forming (light source) halo by, e.g., galactic winds.

We here discuss how far the metals can be dispersed around the star-forming halo as follows. The dynamics of an SN-driven bubble in the expanding universe is described by the Sedov–Taylor-type self-similar solution (Voit, 1996). The evolution of the position R

[*2] The temperature fluctuations appear in the one-zone calculation (Figure 4.18) since we use the density evolution from the hydrodynamical simulation. The fluctuation amplitudes are so small that they do not affect the overall thermal evolution.

of a shell around the bubble can be written by

$$R = 23.6\ \mathrm{ckpc}\left[\left(\frac{f_*}{0.005}\right)\left(\frac{f_\mathrm{b}}{0.16}\right)\left(\frac{f_\mathrm{esc}}{0.1}\right)\left(\frac{M_\mathrm{halo}}{10^8\ M_\odot}\right)\right]^{1/5} \left(\frac{21}{1+z}\frac{\hat{t}}{10^{10}\ \mathrm{yr}}\right)^{2/5}\left(\frac{\alpha}{0.5}\right), \tag{4.18}$$

where $\mathrm{d}\hat{t} = (1+z)^2\mathrm{d}t$, t is the time after the SN explosion, and f_esc is the fraction of the energy injected into the wind to the total SN explosion energy. We here use the conversion efficiency between the SN explosion energy and stellar mass, assuming the Salpeter IMF. The factor α denotes uncertainty due to effects such as the gravitational force from the host halo, external pressure, etc. More detailed numerical calculations show that this factor is around 0.5 (Barkana & Loeb, 2001; Kitayama & Yoshida, 2005), which is adopted for the fiducial value in eq. (4.18). Because the above size is smaller than or comparable to the virial radius of the light source halo, we only consider metal enrichment after the DC cloud plunges into the light source halo.

In our two clouds S1 and S2, the density of the DC cloud reaches $\sim 100\ \mathrm{cm}^{-3}$ when it crosses through the virial radius of the light source halo. Cen & Riquelme (2008) point out that, once such dense cores are formed, metal mixing into the core takes a much longer time than the local dynamical time. Smith *et al.* (2015) also show that the densest part of a cloud collapses before it is significantly enriched by metals transported by mixing. Thus, we expect that the core is not enriched by the metals due to the relatively long mixing time-scale.

4.7 Chapter Summary

We have performed N-body/SPH simulations to follow the evolution of gas clouds in early DM halos. We find two "successful" cases out of 42 candidate samples, where the cloud collapses gravitationally and the gas densities reach $\sim 10^8\ \mathrm{cm}^{-3}$. These two cases are the first examples of DC realized in the cosmological setup, in which the evolution of galaxies is simultaneously followed. The other 40 cases (halos) are identified as potential DC systems, but the clouds do not collapse mainly due to the dynamical interaction with the light source halo. In most of the cases, this is inevitable since strong LW radiation from a nearby massive halo is a necessary condition for the DC. In addition, ram pressure stripping prevents the cloud collapse moving in a dense environment. We will further follow the cloud evolution after the protostar formation in Chapter 6. Here, we briefly summarize the results obtained in this Chapter.

In the two successful cases (S1, S2), the gas cloud is likely to yield a very massive star by the rapid mass accretion. The accretion rates estimated from the radial infall rates at the protostar formation are $\dot{M} \sim 0.1 - 1\ M_\odot\ \mathrm{yr}^{-1}$ for $M(<R) \lesssim 10^5\ M_\odot$. It is interesting that the total mass of the infalling gas is limited by an environmental effect. In particular, the outer envelope of the cloud core is subject to tidal disruption and outflows from the cloud center. Clearly, the tidal force exerted by nearby halos plays a significant role, by

disrupting the gas cloud itself in the failed cases, and by limiting the available gas mass for star formation in the successful cases.

We have also revisited the critical LW intensity required for the DC, considering the environmental effects included in our simulations. DC actually occurs even with 2% of the original LW intensity found in our cosmological simulation. The critical intensity for DC should be estimated at the density of $n_{\rm LTE} \sim 10^3$ cm^{-3}, not at the virialization of atomic-cooling halos as has been often assumed in previous studies. The LW intensity is highly variable in both time and space, and thus we should follow the evolution of a DC system using three-dimensional simulations to determine robustly whether or not DC actually occurs.

Finally, we suggest that the number density of the DC events is significantly smaller than the estimates in the previous studies. The expected number density of DC gas clouds, two in a cube of 20 h^{-1} Mpc on a side, if we naively take our simulation result, is still much larger than that of the observed high-z quasars. In Chapter 6, we will further follow the long-term evolution of the S1 and S2 clouds, and directly derive the protostar masses in these system.

Chapter 5

The Impact of Ionizing Radiation on the Formation of a Supermassive Star in the Early Universe

5.1 Overview

We have found two collapsing clouds, in which the protostellar cores appear, as in the previous chapter. These clouds are special in a sense that a massive source galaxy, which provides copious amount of FUV photons, exists in the close vicinity. We have seen that such an environment specific to DC clouds prevents the cloud collapse in various manners. For example, the tidal field originating from the massive nearby galaxy elongates and disrupts the DC cloud. In the simulation presented in the previous chapter, we have neglected one important physics – ionizing radiation from the source galaxy. Since the final separation of the source galaxy and the collapsing cloud becomes as small as ~ 100 pc, the ionizing radiation can have large impacts on the cloud evolution. If the DC clouds are heated intensely by the ionizing radiation, the cloud gas can escape from the host DC halos and the SMS formation is no more expected in such clouds.

In order to evaluate the effect of the ionizing photons, we have performed hydrodynamic simulations coupled with the transfer of ionizing radiation from the source galaxy. We run the simulation for one of the cloud sample (S1 cloud in Chapter 4) that appears to collapse into the protostellar core if there is no ionizing radiation. To follow the transfer of radiation from the source galaxy, we implement a ray-tracing scheme into our hydrodynamical simulation.

We have found that the radiation does not prevent the cloud collapse under the realistic ionizing luminosity compatible with the star formation in the galaxy. Instead, it sometimes accelerates the cloud collapse because the radiation photo-heats the cloud envelope, which compresses and helps the cloud collapse.

The content in this and the next chapter has been already published in Monthly Notices of the Royal Astronomical Society, Volume 467, Issue 4, p.4293-4303 (Chon & Latif, 2017).

5.2 Methodology

Here, we briefly overview calculation setups and newly added physics.

5.2.1 Hydrodynamical calculation

We perform the hydrodynamical calculation by SPH/N-body code, Gadget-2 (Springel, 2005). We solve non-equilibrium chemical network for 14 species (e^-, H, H^+, He, He^+, He^{2+}, H_2, ${H_2}^+$, H^-, D, D^+, HD, HD^+, and D^-) with an implicit scheme (Yoshida *et al.*, 2003, 2006). We also implement the chemical reaction induced by the stellar radiation. The radiation is divided into two components, low energy ($h\nu < 13.6$ eV) and ionizing radiation ($h\nu > 13.6$ eV). The former photo-dissociates H_2 and HD and photo-detaches H^-, while the latter photo-ionizes atomic hydrogen.

We create a sink particle once the gas particle satisfies the following conditions (Hubber *et al.*, 2013): 1) the gas density reaches 10^3 cm^{-3} and 2) the gas particle is located at the local minimum of the gravitational potential. Each sink particle has a mass and sink radius. The sink particle accretes the gas particle and acquires mass when gas particles enter the region inside the sink radius. The sink radius is set to be 1 comoving kpc, which is comparable to the size of the star cluster in the galaxy center (Wise *et al.*, 2012). We allow the merger of sink particles, when the separation of sink particles becomes smaller than the sum of the sink particles.

We stop the simulation when the central gas density reaches $n = 10^8$ cm^{-3} or the cloud is swallowed by the sink particle, which is located at the center of the source galaxy.

5.2.2 Radiation transfer

In our simulation, we divide the stellar radiation into two components: low energy ($h\nu <$ 13.6 eV) and ionizing ($h\nu > 13.6$ eV) radiations. The luminosity of each component is assigned when a sink particle is created at the galaxy center. In this section, we describe how we give the luminosity and solve the radiation transfer.

5.2.2.1 Low energy radiation($h\nu < 13.6$ eV)

We assume a 10^4 K black-body spectrum for the radiation with $h\nu < 13.6$ eV. We give the time dependent LW luminosity ($L_{\rm LW}$) which is calculated from the semianalytic model (Section 3.2.4). We then compute the intensity at the DC halo center, assuming the radiation is optically-thin ($\propto L_{\rm LW}/r^2$, where r is the separation between the source galaxy and the DC halo). We also assume that the intensity is spatially uniform inside the DC halo.

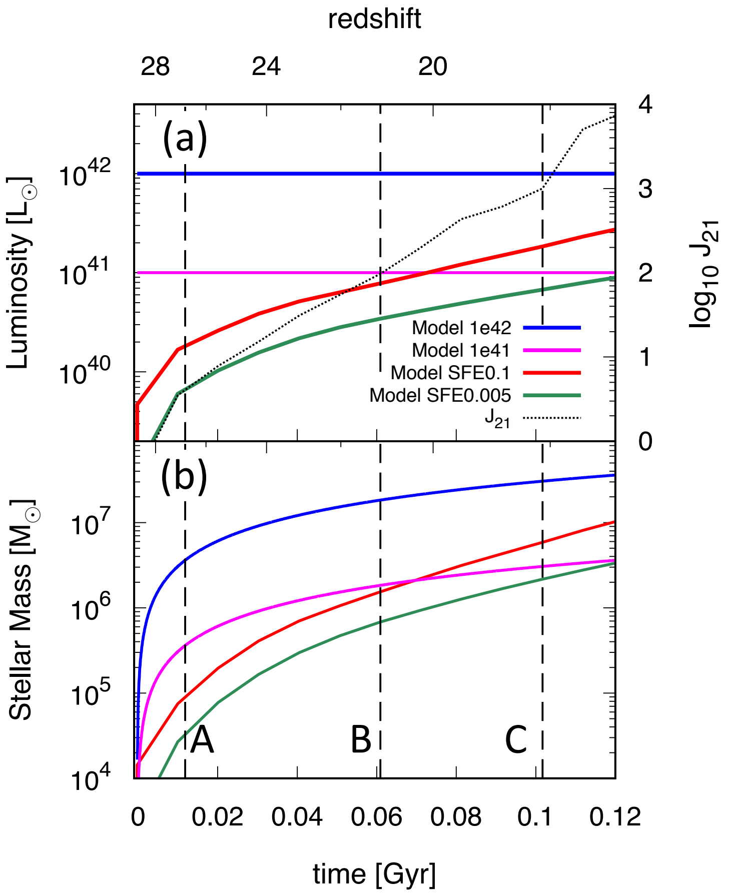

Figure 5.1. Time evolution of (a) source luminosity and (b) stellar mass for Model 1e41 (magenta), 1e42 (blue), SFE0.1 (red), and SFE0.005 (green). Time origin is set to be the moment when the source galaxy starts to emit ionizing photons. The dashed lines A, B, and C are the reference points used in the later discussion. The stellar masses for SFE0.1 and SFE0.005 are directly obtained from semianalytic calculation, whereas for 1e41 and 1e42, the stellar mass is given by eq. (5.1). The dotted line in panel (a) shows the LW intensity J_{21}, which is assumed to be the same for all models.

5.2.2.2 Ionizing radiation($h\nu > 13.6$ eV)

We consider the photo-ionization of the atomic hydrogen and the photo-heating of the gas due to the ionizing radiation. We give luminosity to a sink particle, as the star formation begins in that halo. The spectrum of the ionizing radiation is assumed to be a black-body with 10^5 K. The ionizing luminosity ($L_{\rm UV}$) is calculated for four different models, labeled by Models 1e41, 1e42, SFE0.005, and SFE0.1. In Models 1e41 and 1e42, the luminosity is assumed to be constant in time with 10^{41} and 10^{42} erg s^{-1}, respectively. In Models SFE0.005 and SFE0.1, the luminosity is given by the star formation rate, $\dot{M}_*$, as the stars

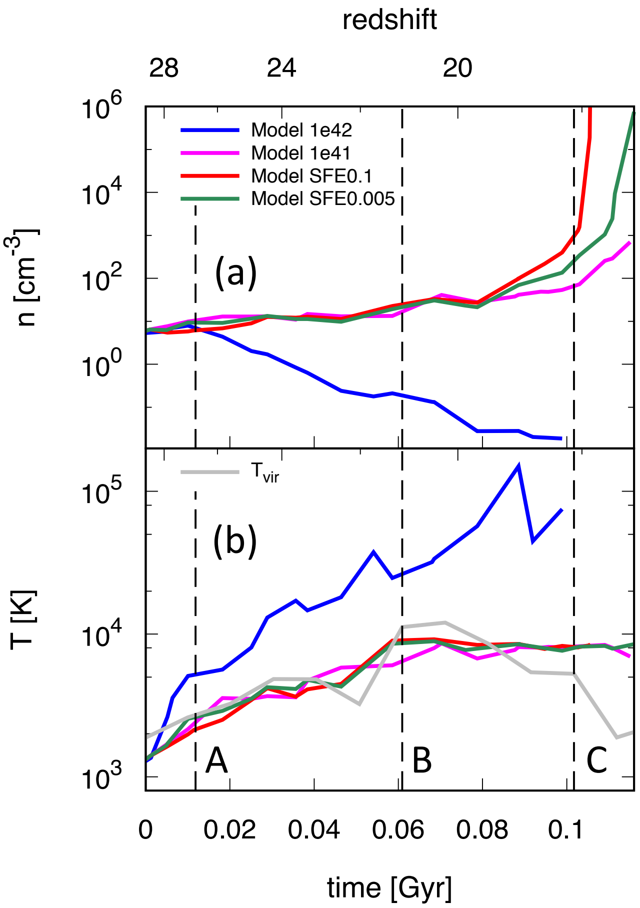

Figure 5.2. Evolutions of (a) density and (b) temperature of the DC clouds for Models 1e41 (magenta), 1e42 (blue), SFE0.1 (red), and SFE0.0005 (green). Time origin is the moment when the galaxy starts to emit ionizing photons. The grey line shows the virial temperature of the host halo in panel (b). The virial temperature turns to decrease at $t \sim 0.07$ Gyr due to the tidal disruption.

formed in the source halo emits ionizing radiation:

$$L_{\rm UV} = 3.3 \times 10^{41} \left(\frac{\dot{M}_*}{1\ M_\odot\ {\rm yr}^{-1}} \right) {\rm erg\ s}^{-1}. \tag{5.1}$$

Here, $\dot{M}_*$ is given by the semianalytic model described in Section 3.2.3. We calculate for the different star formation efficiencies, $\alpha = 0.1$ and 0.005 in the Models SFE0.1 and SFE0.005, respectively. To follow the radiation transfer, we implement the Ray tracing scheme proposed by Susa (2006). The details of this scheme is described in Appendix B.

Note that the ionizing radiation spectrum is inconsistent with the spectrum of low energy radiation. That is, the spectrum is assumed to be $T_{\rm eff} = 10^4$ K black-body spectrum for $h\nu < 13.6$ eV and $T_{\rm eff} = 10^5$ K for $h\nu > 13.6$ eV. We made this choice because our main purpose is to investigate the impact of the ionizing radiation on the cloud collapse. For the comparison with the results by no ionizing radiation, we adopt the 10^4 K black-body spectrum for low energy radiation. If we assume this spectrum for the entire energy range, the number of ionizing photons becomes much lower than that shown in eq. (5.1). Thus we adopt the $T_{\rm eff} = 10^5$ K black-body spectrum for ionizing radiation ($h\nu > 13.6$ eV) to reproduce the ionizing luminosity of the radiation source. This choice allows us to purely extract the effects of ionizing photons on the cloud collapse. We discuss how the different radiation spectra affects our conclusion (see Section 5.4.4).

5.3 Result

We perform hydrodynamical simulation coupled with radiative transfer to investigate whether ionizing photons have impacts on collapse of the DC cloud for Models SFE0.005, SFE0.1, 1e41, and 1e42.

Figure 5.1 shows the evolution of (a) the ionizing luminosity ($L_{\rm UV}$) and the LW intensity at the DC halo (J_{21}) and (b) the stellar mass in the source galaxy. Time origin is set to be the moment at which the star formation begins inside the source halo. In Models 1e41 and 1e42, we integrate eq. (5.1) to yield the stellar masses. Comparing Models SFE0.1 and SFE0.005, the SFR is higher by 20 times, while the stellar mass is only higher by 2–5 times. This comes from the fact that the star formation is mainly regulated by gas cooling in both models, thus the SFR saturates at some point in model SFE0.1.

We stress here that Model 1e42 assumes the extremely strong ionizing luminosity and it is unlikely to occur. For example at $z \sim 25$, the stellar mass reaches $10^7\ M_\odot$, which is comparable to the halo mass. This model just demonstrates that the strong ionizing radiation at the early stage of the structure formation can photo-evaporate the DC cloud. We study the model 1e41 just to compare our results with the previous study by Regan *et al.* (2016). Model SFE0.1 assumes the strongest UV luminosity compatible with the observation.

5.3.1 Cloud collapse

Figure 5.2 shows the time evolution of (a) the cloud density and (b) temperature for Models 1e41 (magenta), 1e42 (blue), SFE0.1 (red), and SFE0.005 (green). In Models SFE0.1 and SFE0.005, the density monotonically increases with time and reaches 10^8 cm^{-3} at $t \sim 0.1$ Gyr . In Model 1e41, the density and temperature evolution is similar to those in Models SFE0.005 and SFE0.1. As we will see later, a part of the gas inside the DC halo is photo-evaporated in the early evolutionary phase, which prevents the cloud collapse. In Model 1e42, the density starts to decrease just after $t = 0$ and completely disappear due to the photo-evaporation.

Panel (b) shows the temperature evolution in the DC halo in all four models. The grey line shows the time evolution of the virial temperature of the DC halo. In Models 1e41, SFE0.005, and SFE0.1, the gas temperatures almost follow the virial temperature until $t < 0.08$ Gyr, which indicates that the gas at the cloud center does not suffer from UV heating. In Model 1e42, however, the gas within the DC cloud is strongly heated by ionizing radiation, and that the temperature exceeds the virial temperature just after

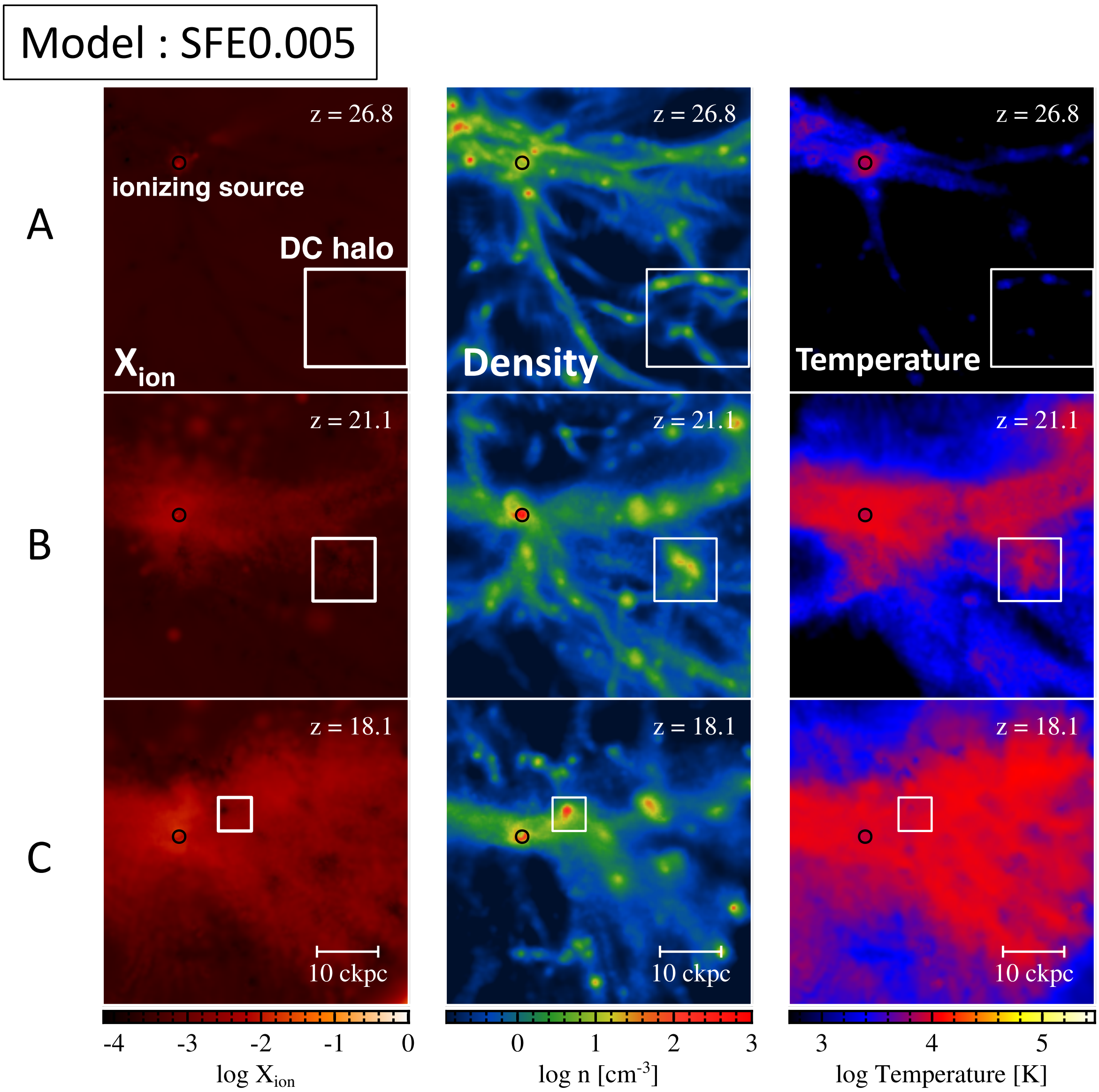

Figure 5.3. We show gas properties for Model SFE0.005, $X_{\rm ion}$, n, and temperature at the left, middle, and, right columns, respectively. Each row A, B, and, C corresponds to the snapshot at the reference epoch marked in Figure 5.1. The Black solid circle and the square box in each panel indicates the ionizing source and the focused DC halo and its progenitors, respectively. In this model, no ionized region expands around the ionizing source.

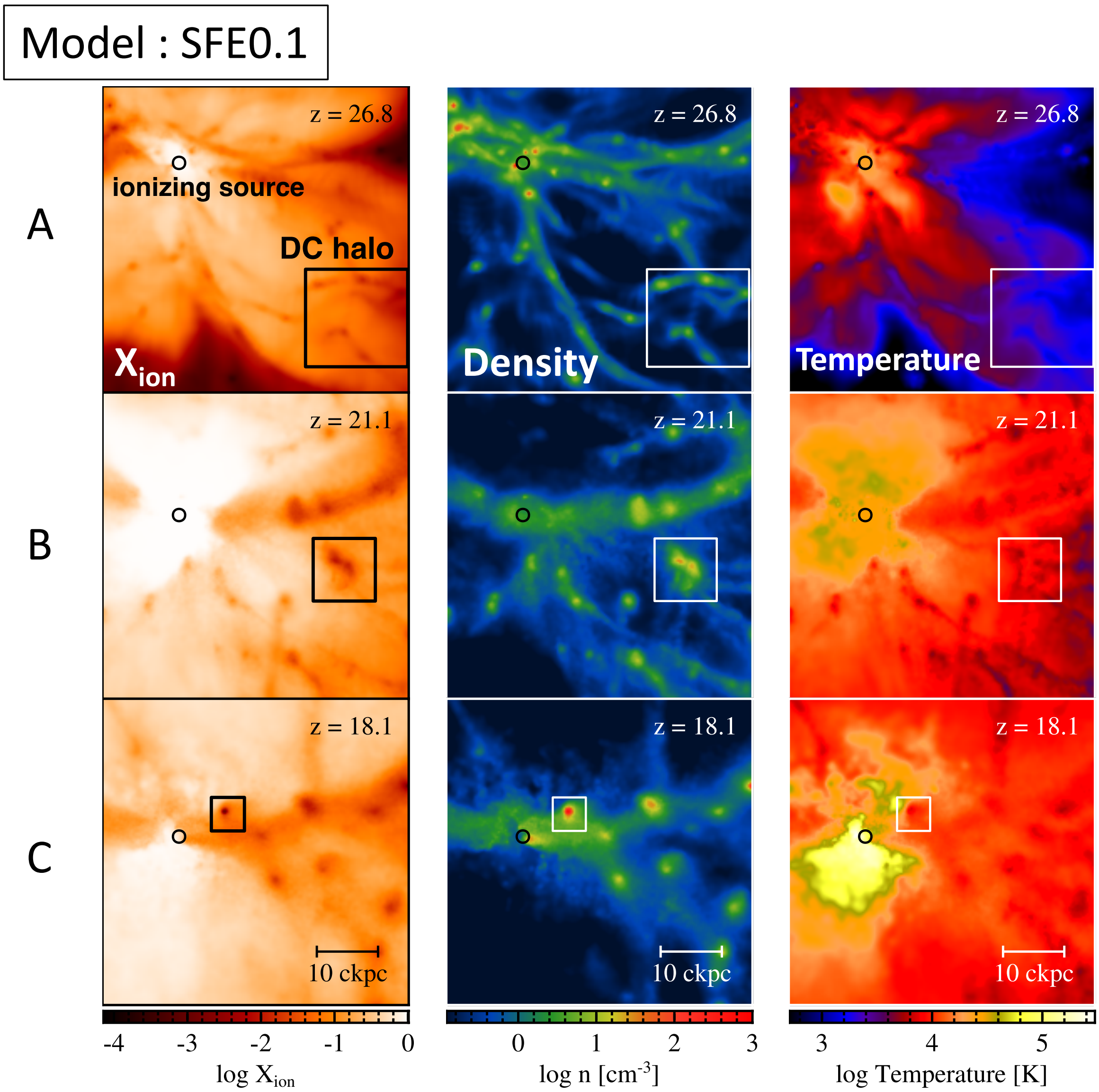

Figure 5.4. Same as Figure 5.3 but for Model SFE0.1. The HII region expands in anisotropic manner reflecting the structures (voids, filaments, etc) in the universe. The DC cloud itself is surrounded by the dense filament so that the cloud remain neutral. At epoch C, the DC cloud collapses into the dense core.

$t = 0$. Thus the gas is no longer bound by the host halo potential and the density decreases with increasing time.

In Models SFE0.1 and SFE0.005, the cloud collapses to reach $n = 10^8$ cm^{-3}. Interestingly, the density grows faster in model SFE0.1 than in SFE0.005. This fact implies that the heated ambient gas accelerates the collapse of the DC cloud. Actually in model SFE0.1, the cloud ambient is heated to 10^5 K, which can compress the DC cloud owing to its high pressure.

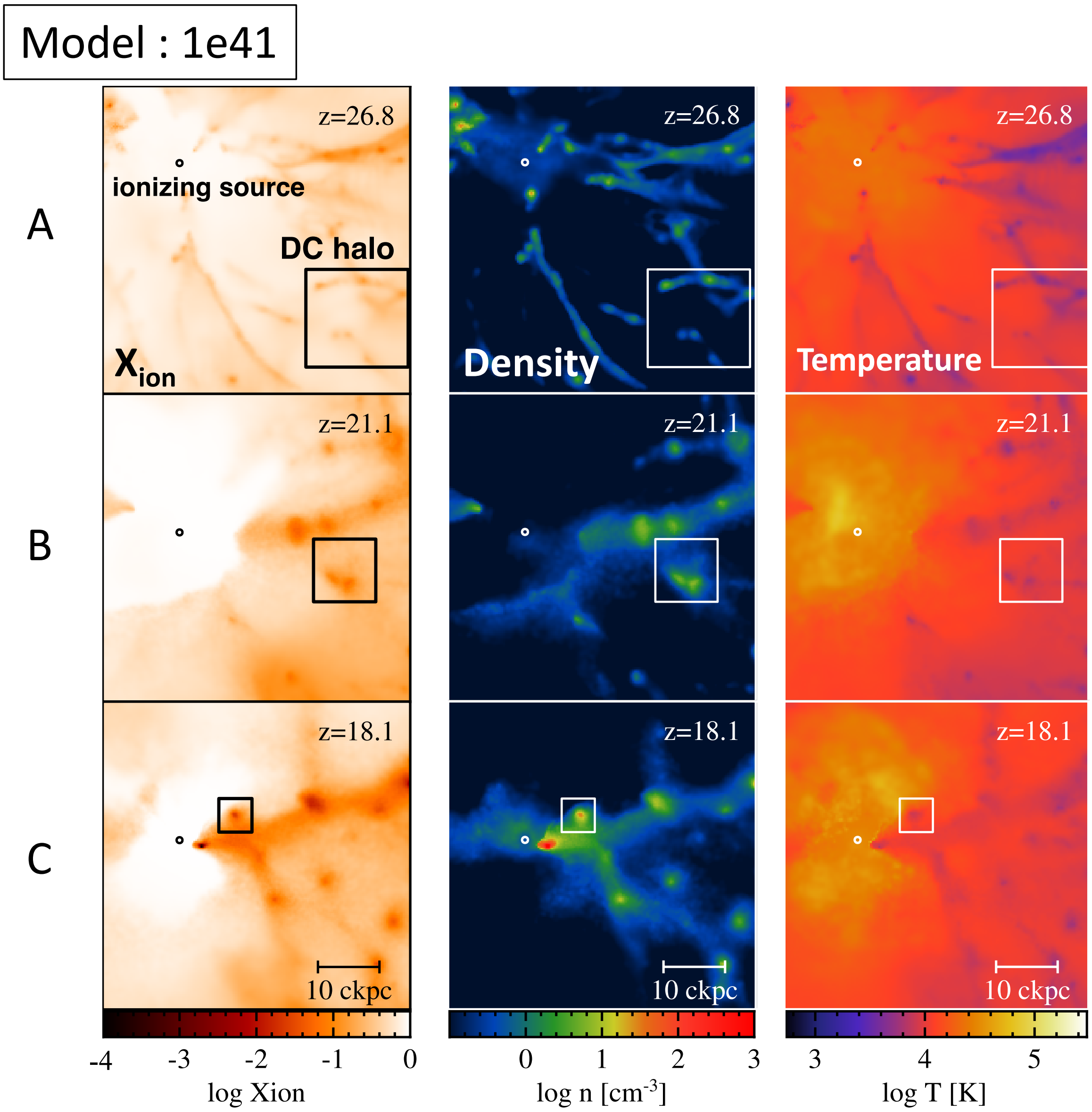

Figure 5.5. Same as Figure 5.3 but for Model 1e41. The overall evolution is similar with the case for SFE01, in a sense that the ionized region expands in anisotropic manners. Since the luminosity is larger at the early epoch than SFE01, a part of the DC cloud gets photo-evaporated around epochs A – B, compared with SFE01. As a result, the DC cloud does not collapse in this model.

5.3.2 Visual inspection

Figures 5.3, 5.4, 5.5, and 5.6 show the projected distributions of ionization degree ($X_{\rm ion}$), number density (n), and the temperature around the source galaxy and DC cloud. Here, $X_{\rm ion}$ is defined as $f_{\rm HII}/(f_{\rm HI}+f_{\rm HII})$, where f_i represents the abundance of the species i. In Model SFE0.005 almost no HII region develops around the source galaxy, so that the cloud

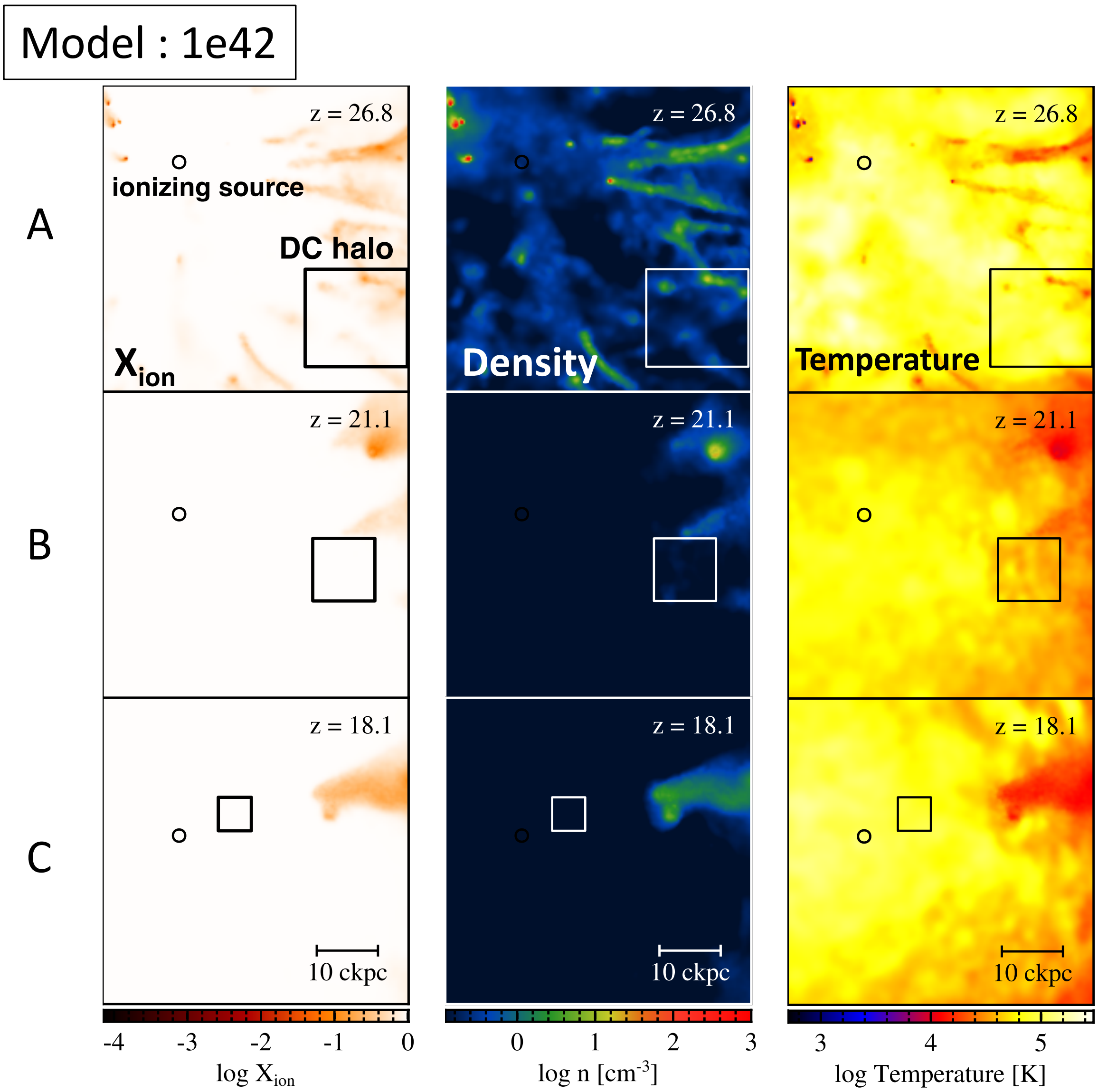

Figure 5.6. Same as Figure 5.3 but for Model 1e42. In this model, gas in the DC halo gets photo-evaporated just after the ionizing radiation turns on.

collapses into a dense core without any effects of ionizing photons. In other three models, the HII region expands around the source halo. Specifically in models SFE0.1 and 1e41, we can observe the ionized region expands in an anisotropic fashion. This anisotropic expansion reflects the large-scale structure around the source halo; halos, filaments and voids. Since the source halo is embedded in the growing dense filament, the expansion of the ionization front is stalled at some pints in the filament. The ionization front continues to expand toward the void region, where the matter density is small. Consequently, $X_{\rm ion}$ remains lower by an order of magnitude in the dense filament.

As the DC cloud approaches the source galaxy, the DC cloud enters the dense filament. The surrounding filament shields the ionizing photons, and that the gas temperature

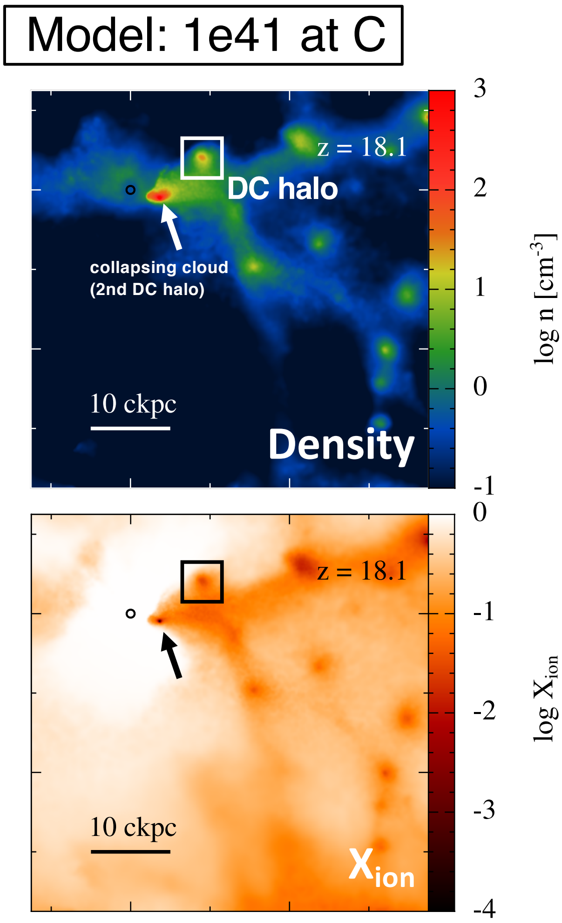

Figure 5.7. Projected density (top) and $X_{\rm ion}$ (bottom) maps for Model 1e41 at epoch C in Figure 5.1. The circles and boxes represent the positions of the ionizing source and the DC halo, respectively. Thick arrows indicate another collapsing cloud near the DC halo ("2nd DC halo").

within the DC cloud remains around $\sim 10^4$ K. This temperature is much smaller than that of surrounding gas, several $\times\, 10^4$ K. This high temperature ambient around the DC cloud is likely to accelerate the cloud collapse (see also Sections 5.3.1 and 5.3.3). In Model SFE0.1, the DC cloud finally collapses into the dense core (Figure 5.4C).

In Model 1e41, the density structure evolves similarly with the case in Model SFE0.1. However, the DC cloud does not collapse into the protostellar core. The central density increases only up to 10^3 cm^{-3} and the cloud finally merged with the source galaxy. The difference of the cloud evolution indicates the importance of the luminosity evolution. In Model 1e41, the strong ionizing radiation in the early evolutionary phase gradually photo-evaporates the DC cloud, and that the cloud loses mass with time. The cloud does not possess enough mass to collapse at last.

Interestingly, another DC halo (hereafter we call it as 2nd DC halo and the collapsed cloud in model SFE0.1 as 1st DC halo) forming in the vicinity of source galaxy collapse into the densities of 10^8 cm^{-3} for model 1e41 (stressed by the arrow in Figure 5.5). The

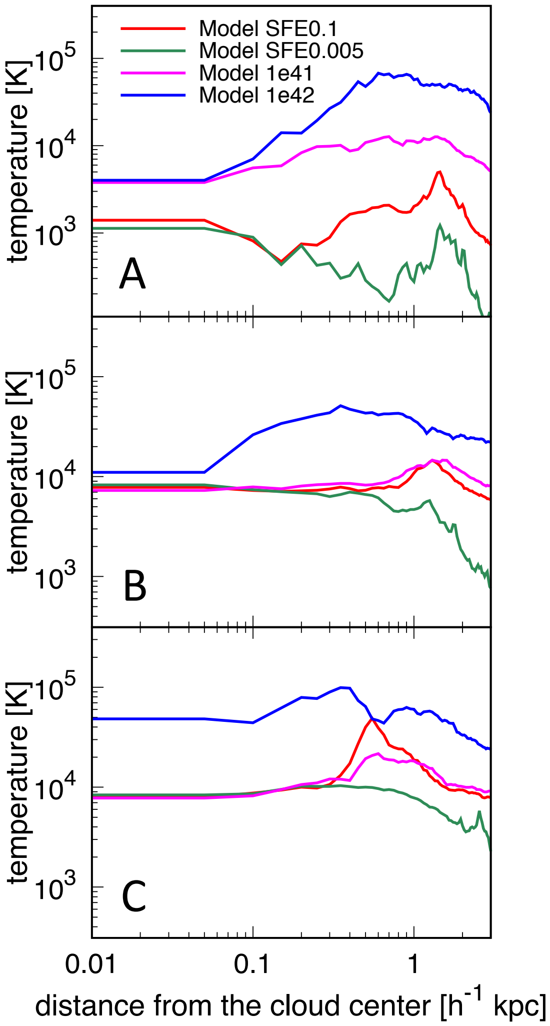

Figure 5.8. Radial temperature profiles around the DC halo for Models 1e41 (magenta), 1e42 (blue), SFE0.005 (green), and SFE0.1 (red). Each panel corresponds to the profiles at the reference epochs A, B, and C in Figure 5.1.

2nd DC halo has different formation history and its progenitors are formed inside the dense filament which kept them shielded from ionizing radiation. The 2nd DC halo collapses at the edge of HII region and its collapse is likely accelerated by the thermal compression as the collapse of the 2nd DC halo is not observed in other models. This suggests that some halos forming in the vicinity of a strong radiation source may survive from ionizing radiation and lead to the formation of an SMS in this model.

To further clarify the difference between two halos for model 1e41, we compute the evolution of the ionizing flux and find that it is very similar for both halos. We find that the 1st DC halo could not collapse because four out of its six progenitors are completely photo-evaporated just after epoch A. Meanwhile, progenitors of the 2nd DC halo are formed in the dense filament and remain shielded from the ionizing radiation. Our results suggest that the formation history of the halo plays an important role in their collapse.

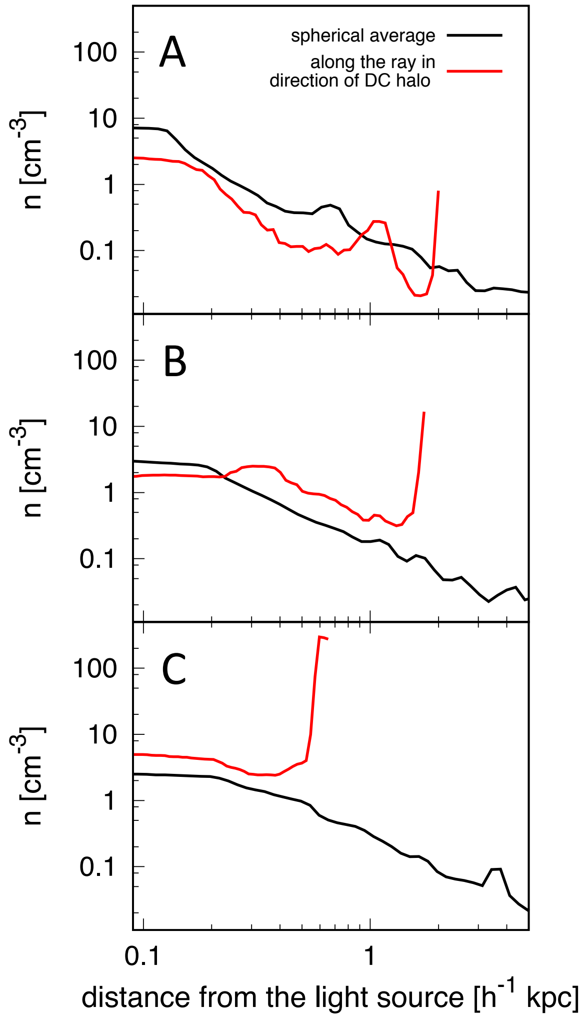

Figure 5.9. Radial density profiles around the source halo for Model SFE0.1. The black lines represent the spherical averaged profiles, while the red lines represent the density profiles along the ray which is directed toward the DC cloud. Each row corresponds to the profile at the reference epochs A, B, and C in Figure 5.1.

5.3.3 Temperature profiles around the DC cloud

Figure 5.8 shows the radial temperature profiles around the DC cloud center at the epochs of A, B, and C. In Model SFE0.005 (green), the cloud temperature never exceeds 10^4 K, which indicates that ionizing photons have almost no impact on the cloud evolution. In Model SFE0.1 (red), the inner part ($R < 0.1$ kpc) of the cloud has the similar profile with in Model SFE0.005. While in the outer part ($R \sim 1$ kpc), the gas is heated up to 10^4 K, which compress the DC cloud by the pressure gradient and accelerates the cloud collapse (Figure 5.2a).

In Model 1e42 (blue line), gas is heated to about 6000 K just after the galaxy starts to emit ionizing photons. Since it is higher than the halo virial temperature, the gas is photo-evaporated from the halo. The cloud temperature continues to increase and all the gas is heated to the temperature higher than 10^4 K at the point C. Consequently, the gas gets completely evaporated and does not collapse any more.

Figure 5.9 shows the spherically averaged density profile and the density along the ray directed towards the DC halo from the source galaxy (we define this as the "ray density") for Model SFE0.1. At point A, the ray density between two halos becomes smaller than the averaged density around the source. However, the ray density increases with time and reaches ~ 2–$3\ \mathrm{cm^{-3}}$ at point C while the averaged density decreases with time. This explains the decrease in ionization fraction (recombination rate is proportional to the square of the cloud density) as the DC halo approaches the source galaxy. The HII region only expands in the void region and filaments remain neutral because of the higher gas density. Thus once the DC halo has been surrounded by the dense filament, it can avoid the effect of ionizing radiation and collapse into a protostellar core.

5.4 Discussion

5.4.1 Size of HII region

We estimate the size of HII region around the light source. The balance between ionization and recombination of atomic hydrogen gives the size of the HII region, $R_{\rm st}$:

$$\begin{aligned} R_{\rm st} &= \left(\frac{3L_{\rm UV}}{4\pi\bar{n}^2\alpha_{\rm B}E_{\rm UV}}\right)^{1/3} \\ &= 1.14\ \mathrm{kpc}\left(\frac{L_{\rm UV}}{10^{42}\ \mathrm{erg\ s^{-1}}}\right)^{1/3}\left(\frac{\bar{n}}{1\ \mathrm{cm^{-3}}}\right)^{-2/3}, \end{aligned} \tag{5.2}$$

where $L_{\rm UV}$ is the UV luminosity of the source, $E_{\rm UV}$ is the mean energy of ionizing photons, and $\bar{n}$ is the mean number density within the HII region, and $\alpha_{\rm B}$ is the case-B recombination coefficient of atomic hydrogen. We assume here $E_{\rm UV} = 13.6$ eV. J_{21} can be written as a function of $L_{\rm UV}$ as follows:

$$J_{21} = \frac{L_{\rm LW}}{4\pi^2 r^2 \Delta\nu} = \frac{\beta L_{\rm UV}}{4\pi^2 r^2 \Delta\nu}, \tag{5.3}$$

where $L_{\rm LW}$ is the luminosity in the LW band, $\Delta\nu$ is the frequency width of the LW band, β is the ratio of LW to UV luminosity, and r is the distance from the source. We neglect the shielding effect of LW radiation, which is revisited at the end of this section. We can define the distance at which the halo receives the critical LW intensity $J_{21,\rm crit}$ as;

$$\begin{aligned} R_{\rm J21} &= \left(\frac{\beta L_{\rm UV}}{4\pi^2\Delta\nu J_{21,\rm crit}}\right)^{1/2} \\ &= 6.77\ \mathrm{kpc}\ \beta^{1/2}\left(\frac{L_{\rm UV}}{10^{42}\ \mathrm{erg\ s^{-1}}}\right)^{1/2}\left(\frac{100}{J_{21,\rm crit}}\right)^{1/2}. \end{aligned} \tag{5.4}$$

Equations (5.2) and (5.4) show that $R_{\rm st}$ scales as $\propto L^{1/3}$ while $R_{\rm J21}$ scales as $\propto L^{1/2}$ under the fixed spectrum. Comparing these two scales, we obtain the critical luminosity $L_{\rm c}$, above (below) which $R_{\rm J21}$ becomes larger (smaller) than $R_{\rm st}$,

$$L_{\rm c} = 2.3 \times 10^{37}\ {\rm erg\ s^{-1}} \beta^{-3} \left(\frac{J_{21,{\rm crit}}}{100} \right)^{3} \left(\frac{\bar{n}}{1\ {\rm cm^{-3}}} \right)^{-4}. \tag{5.5}$$

This equation shows that critical luminosity strongly depends on $\bar{n}$ and the spectrum of radiation. Our parameter choice in the simulation gives $\beta \sim 1 - 10$ and $J_{21,{\rm crit}} = 100$. Thus $L_{\rm c}$ becomes much smaller than the luminosity of the central galaxy, $\sim 10^{41}$ erg s^{-1}. This is one of the reasons why the DC halo can collapse without evaporated by ionizing radiation.

Next, we evaluate the shielding effects of LW radiation. Draine & Bertoldi (1996) evalutae the shielding factor $f_{\rm sh}$ as;

$$f_{\rm sh} = {\rm Min} \left[1, \left(\frac{N_{\rm H_2}}{10^{14}\ {\rm cm^{-2}}} \right)^{-3/4} \right], \tag{5.6}$$

where $N_{\rm H_2}$ is the column density of $\rm H_2$. The column density at $R_{\rm J21}$ can be written as;

$$N_{\rm H_2} = 2.1 \times 10^{13}\ {\rm cm^{-2}}\ \beta^{1/2} \left(\frac{L_{\rm UV}}{10^{42}\ {\rm erg\ s^{-1}}} \right)^{1/2} \left(\frac{100}{J_{21,{\rm crit}}} \right)^{1/2} \left(\frac{f_{\rm H_2}}{10^{-9}} \right) \left(\frac{\bar{n}}{1\ {\rm cm^{-3}}} \right), \tag{5.7}$$

where $f_{\rm H_2}$ is the $\rm H_2$ fraction within HII region. The fiducial value, 10^{-9}, is taken from Omukai (2001) and consistent with our simulation results. Equation (5.7) shows that the shielding can be neglected unless the spectrum is extremely soft ($\beta \gg 1$). The above evaluation is only true for the static medium. The Doppler shift of the radiation reduces the effect of shielding, if the cloud envelope fall with a significant velocity gradient, larger than the sound speed of the source galaxy (Wolcott-Green *et al.*, 2011). In our case the width of the LW line ($\Delta\nu$) is equivalent to the sound speed ($c_{\rm s}$), $\Delta\nu = (c_{\rm s}/c)\nu$, the shielding effect can be almost neglected.

5.4.2 Ionization of the DC candidate halos

We focus on the DC halos selected from the semianalytic simulation and discuss the impact of the ionizing photons on their evolution. The analysis here is based on the discussion in Section 5.4.1. We analyze 68 DC halos found in Chapter 3. Note that not all the DC halos collapse into high density. We have followed the hydrodynamical evolution of 42 halos and find that only 2 halos collapse into protostellar cores. We emphasize that these halos share the similar environments as the two collapsed DC halos.

Figure 5.10 represents the mean density and the separation between the DC halo and the source galaxy for 68 samples. The mean density, n, is calculated from the outputs of the N-body calculation as;

$$n = \left(\frac{\Omega_{\rm b}}{\Omega_{\rm m}} \right) \left(\frac{\rho_{\rm DM}}{\mu m_{\rm p}} \right), \tag{5.8}$$

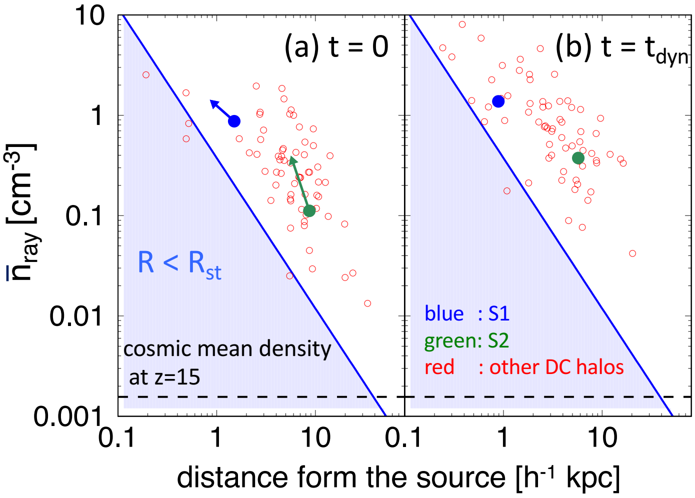

Figure 5.10. Mean number density $\bar{n}$ versus distance from the source halo R is plotted for 68 DC halos found in the N-body simulation shown in Chapter 3. Panels (a) and (b) show the snapshots at different epochs, $t = 0$ and $1t_{\rm dyn}$, where the time origin is the moment when the halos satisfy the DC criteria. Filled circles correspond to the DC halos confirmed to collapse by hydrodynamical simulation. The blue filled circle corresponds to the halo whose evolution is calculated by the radiative hydrodynamical simulation in this chapter. The end points of arrows in panel (a) show values at $t = 1t_{\rm dyn}$. The dashed lines represent the cosmic mean density at $z = 15$ and the shaded regions indicate $R < R_{\rm st}$ for $L_{\rm UV} = 10^{41}$ erg s^{-1}.

where $\rho_{\rm DM}$ is the mean dark matter density, $\mu = 1.2$ is the mean molecular weight of the neutral gas, and $m_{\rm p}$ is the proton mass. The source luminosity $L_{\rm UV}$ is assumed to be 10^{41} erg s^{-1}, which is the mean luminosity of the galaxy in the simulation. We can see that the halos are located outside the HII region ($R > R_{\rm st}$). This suggests that while DC halos approaches the source halo, the mean density increases accordingly and the halo is shielded from the ionizing photons. Thus we expect that ionizing photons do not play a major role for the cloud collapse as we have found by the radiation hydrodynamics simulations.

5.4.3 Environment dependence of $R_{\rm st}$

The size of the ionized region, $R_{\rm st}$, depends on the mean density around the source, $\bar{n}$ (eq. 5.2), while the density structure around the source halo is highly anisotropic (Figure 5.4). Here, we discuss how the different environment affects the expansion of the ionized region.

Figure 5.11 (a) shows the mean density profile and profiles toward the void and filament regions. We assume that the density within the virial radius is constant and equal to $\delta_{\rm c} \equiv 168$ times the cosmic mean density for all three profiles. The averaged density profile outside the virial radius is calculated in two ways: The profile obtained by the

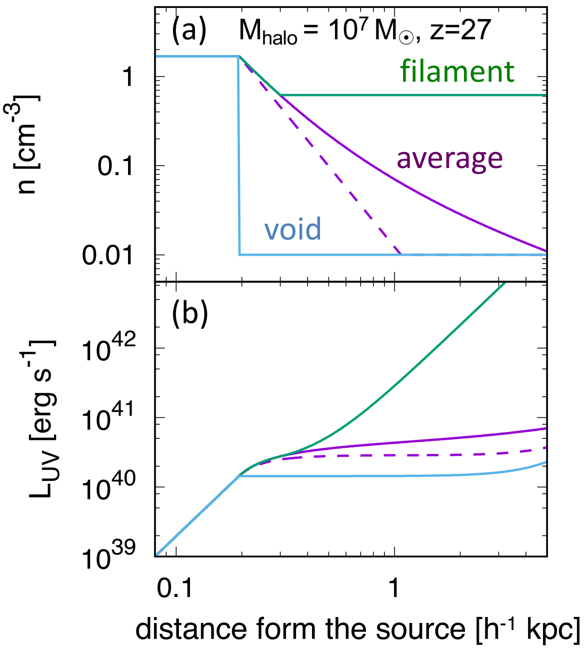

Figure 5.11. (a) The radial density structures around the halo, whose mass is 10^7 $M_\odot$ at $z = 27$. The purple lines show the mean density profiles around the halo, while the green and blue lines show the density structures around the halo at the filamentary and void regions, respectively. (b) The radial profiles of the required UV luminosity, $L_{\rm UV}$, to ionize hydrogen under the density profiles given in panel (a).

first method is presented by the purple solid line, where we combine the extended Press-Schechter model and the spherical collapse model (Barkana, 2004). In the other method, we assume the NFW profile outside the virial radius (dashed line Navarro *et al.*, 1997). In filaments, the density is assumed to be the same as the spherically averaged profile inside the radius of about 200 pc while the density is the fixed at $(1 + \delta_{\rm fil})\bar{\rho}$ outside this radius. Here, we adopt $\delta_{\rm fil} \equiv 100$ as found in our simulations. In the void region, the density is set to be the cosmic mean density. The comparison of density profiles indicates that the density is larger in filaments compared to the mean density of the halo.

We estimate the ionizing luminosity required to ionize the atomic hydrogen within R from the source, where

$$L_{\rm UV} = \int_0^R 4\pi R^2 E_{\rm UV} \alpha_{\rm B} n^2 {\rm d}R. \tag{5.9}$$

Figure 5.11 (b) shows $L_{\rm UV}$ for different environments. The critical UV luminosity, $L_{\rm UV,\,crit}$, above which the region within the virial radius is completely ionized is $L_{\rm UV,\,crit} \sim 1 \times 10^{40}$erg s^{-1}. This suggests that $L_{\rm UV,\,crit}$ in filaments is about two orders of magnitude larger compared to the voids.

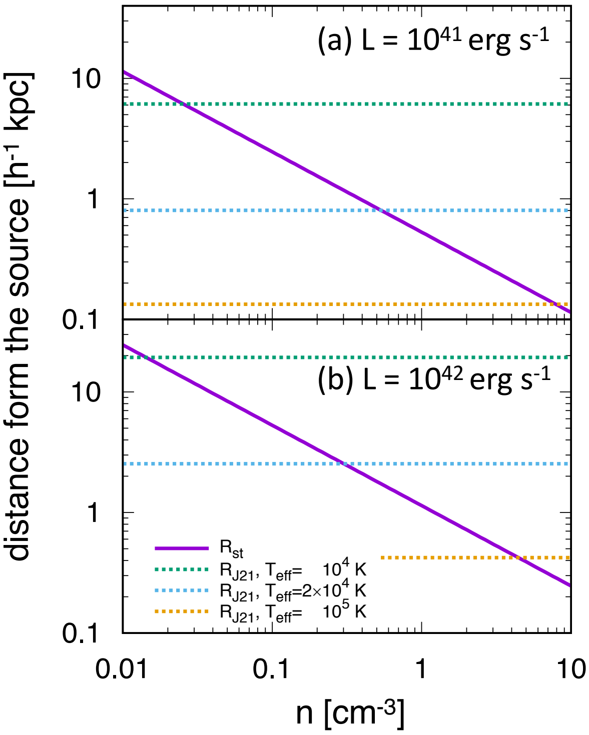

Figure 5.12. $R_{\rm st}$ (eq. 5.2) and $R_{\rm J21}$ (eq. 5.4) as a function of the mean number density, $\bar{n}$ under the UV luminosity of (a) 10^{41} erg s^{-1} and (b) 10^{42} erg s^{-1}, respectively. The purple lines show $R_{\rm st}$, while dotted lines show $R_{\rm J21}$ assuming the black-body spectra with $T_{\rm eff} = 10^4$ (green), 2×10^4 (blue) , and 10^5 K (yellow). $R_{\rm J21}$ does not depend on $\bar{n}$ since we assume LW radiation is completely optically-thin.

	T1e4	T2e4	T1e5
$J_{21,\rm crit}$	100	1000	1000
β	8.43	1.45	0.04

Table 5.1. Summary of $J_{21,\rm crit}$ and β for the three different spectra.

5.4.4 Spectrum of the radiation source

Recent studies discuss the required LW intensity for DC under the realistic radiation spectra, i.e. black-body spectra with $10^4 < T_{\rm eff} < 10^5$ K (Sugimura *et al.*, 2014; Agarwal *et al.*, 2014; Latif *et al.*, 2015). Here, we discuss how different radiation spectra affects the size of HII region. Our discussion is based on eqs. (5.2) and (5.4) in Section 5.4.1.

We consider 3 types of the black-body spectra with $T_{\rm eff} = 10^4$ (T1e4), 2×10^4 (T2e4), and 10^5 K (T1e5). These spectra represent the old galaxy, the starburst galaxy, and the Pop III cluster, respectively. We here list the critical LW intensities and β (the ratio between LW and ionizing luminosities) in Table 5.1.

Figure 5.12 shows $R_{\rm st}$ (solid) and $R_{\rm J21}$ (dotted) for (a) $L_{\rm UV} = 10^{41}$ and (b) $L_{\rm UV} = 10^{42}$ erg s^{-1} as a function of the mean number density, $\bar{n}$. The green, blue, and yellow lines correspond to the spectra of T1e4, T2e4, and T1e5, respectively. $R_{\rm J21}$ does not depend on $\bar{n}$ because we assume LW radiation is optically-thin (see Section 5.4.1). The critical density $\bar{n}_{\rm c}$, at which $R_{\rm st} = R_{\rm J21}$, gets large for the hard spectrum. For the spectrum T2e4, $\bar{n}_{\rm c} \sim 0.3 - 0.5$ cm^{-3}, which corresponds to the filament density found in our simulation (Figure 5.4). For the spectrum T1e5, $\bar{n}_{\rm c} \sim 10$ cm^{-3}, which corresponds to the halo density. This implies that for the spectrum T2e4, DC halos located in the void region are likely captured by the HII region while the halos in a clustered environment (surrounded by a dense filament) may avoid the impact of ionizing radiation in which $\bar{n}_{\rm c}$ is closed to the filament density. For the spectrum T1e5, the DC halos are captured by the HII region even they approach through the filament with ~ 1 cm^{-3}. Hence, the SMS formation in the close vicinity of Pop III might be difficult compared to the Pop II stars.

We assumed a 10^4 K black-body spectrum for LW and 10^5 K for ionizing radiation. The adopted spectrum for LW is softer than the expected spectra of Pop II galaxies and the required stellar mass would be about an order of magnitude larger (Sugimura *et al.*, 2014). The strength of the critical LW flux necessary to enable isothermal DC collapse is 1000 for a realistic spectrum of Pop II galaxies, about an order of magnitude larger than the value adopted in our semianalytic model. This can significantly reduce the number of candidate DC halos. However, the radiation spectrum used in our simulation has $\beta \sim 1$ and the LW intensity reaches $J_{21} \sim 10^3$ during the collapse of DC halo. Therefore, we stress that our results are similar to that for a 2×10^4 K black-body spectrum.

5.4.5 Effect of radiation pressure

Here, we evaluate the contribution of radiation pressure to expansion of the HII region with 1D model, which is not included in our hydrodynamical calculation. We follow the discussion by Krumholz & Matzner (2009). Once the central source starts to emit ionizing photons, ambient gas is heated up to $T_{\rm ion}$. This temperature is usually much higher than surrounding neutral gas. Thus ionized gas sweeps up gas outward and the shell is formed around the HII region.

Expansion of the shell radius r can be described as follows:

$$\frac{\mathrm{d}}{\mathrm{d}t}(M_{\rm sh}\dot{r}) = A_{\rm sh}\left\{\rho_{\rm i}[c_{\rm i}^2 + u_{\rm i}(u_{\rm i} - \dot{r})] + \frac{f_{\rm trap}L}{4\pi r^2 c}\right\}, \tag{5.10}$$

where $M_{\rm sh}$ is the shell mass, $A_{\rm sh}$ is the shell area, $\rho_{\rm i}$ is the density within ionized region, $c_{\rm i}$ is the sound speed of ionized gas, $u_{\rm i}$ is the gas velocity behind the shell, $f_{\rm trap}$ is the factor of the trapping effect which enhances radiation pressure, L is the source luminosity, and c is the speed of light. The term in the left hand side represents the time derivative of the shell momentum. The first term of the right hand represents thermal pressure, the second term represents the momentum flux injected from inner ionized gas, and the third term represents radiation pressure. Following discussion by Matzner (2002) and assuming $c_{\mathrm{i}} \gg u_{\mathrm{i}}$, we neglect the second term of the right hand side.

The balance between ionization and recombination gives c_{i} at the radius r as;

$$\rho_{\mathrm{i}} c_{\mathrm{i}}^2 = \sqrt{\frac{3L_{\mathrm{UV}}}{4\pi\alpha_{\mathrm{B}} E_{\mathrm{UV}}}} \frac{k_{\mathrm{B}} T_{\mathrm{i}}}{r^{3/2}}. \tag{5.11}$$

We can get the characteristic radius, r_{ch}, at which the thermal pressure term is comparable to the radiation pressure term;

$$\begin{aligned} r_{\mathrm{ch}} &= \frac{\alpha_{\mathrm{B}}}{12\pi} \left(\frac{E_{\mathrm{UV}}}{k_{\mathrm{B}} T_{\mathrm{i}}}\right)^2 f_{\mathrm{trap}}^2 \frac{L_{\mathrm{UV}}}{c^2 E_{\mathrm{UV}}} \\ &= 28.4\ \mathrm{pc}\ f_{\mathrm{trap}}^2 \left(\frac{T_{\mathrm{i}}}{10^4\ \mathrm{K}}\right)^{-2} \left(\frac{L_{\mathrm{UV}}}{10^{42}\ \mathrm{erg\ s^{-1}}}\right). \end{aligned} \tag{5.12}$$

The ratio between the Stromgren radius (eq. 5.2) and r_{ch} roughly gives the contribution of radiation pressure to expansion of the ionized region,

$$\begin{aligned} \zeta &\equiv \frac{r_{\mathrm{ch}}}{R_{\mathrm{st}}} \\ &= 2.46 \times 10^{-2}\ f_{\mathrm{trap}}^2 \\ &\left(\frac{T_{\mathrm{i}}}{10^4\ \mathrm{K}}\right)^{-2} \left(\frac{L_{\mathrm{UV}}}{10^{42}\ \mathrm{erg\ s^{-1}}}\right)^{2/3} \left(\frac{\bar{n}}{\mathrm{cm^{-3}}}\right)^{2/3}. \end{aligned} \tag{5.13}$$

Krumholz & Matzner (2009) estimate and find f_{trap} is an order of unity. Thus ζ is much smaller than unity where $\bar{n} < 10^3\ \mathrm{cm^{-3}}$. This shows that radiation pressure is less important than thermal pressure, once the ionized region expands and the mean density around the source decreases. This result is also confirmed by the recent 3D simulation, which shows that photo-ionization is dominant effect and radiation pressure acts as the secondary effect (Sales *et al.*, 2014).

5.4.6 Effect of the dust attenuation

Although the dust is thought to be formed in the UV emitting galaxy, we do not include dusts in the ray-tracing calculation. The dust in the ionized region converts ionizing radiation into longer wavelength and reduces the size of the ionized region. Here, we estimate the impact of dust attenuation on the size of the ionized region. We follow the discussion by Raga & Lora (2015), who apply the Stromgren analysis to estimate the effect of the dust.

The balance between ionization by ionizing photons and recombination and dust attenuation give following equation;

$$S_* = \int_0^{R_0} \left[\int_{\nu_0}^{\infty} \frac{4\pi J_\nu}{h\nu} (n_{\mathrm{HI}}\sigma_{\mathrm{H}} + n_{\mathrm{H}}\sigma_{\mathrm{d}}) \mathrm{d}\nu\right] 4\pi R^2 \mathrm{d}R, \tag{5.14}$$

where S_* is the number of emitted ionizing photons per unit time, R_0 is the size of the ionized region, ν_0 is the frequency of the Lyman-limit ($h\nu = 13.6$ eV), J_ν is intensity of ionizing radiation, n_{HI} is the number density of neutral hydrogen, n_{H} is the total hydrogen number density, σ_{H} is the cross-section of hydrogen with ionizing photons, and σ_{d} is the cross-section of dusts with ionizing photons. Here, we assume the cross-section does not depend on ν. Then we obtain

$$\int_{\nu_0}^{\infty} \frac{4\pi J_\nu}{h\nu} \mathrm{d}\nu = \frac{S_* \mathrm{e}^{-\tau}}{4\pi R^2}, \tag{5.15}$$

where $\tau = \tau_{\mathrm{H}} + \tau_{\mathrm{d}} = \int_0^R n_{\mathrm{HI}} \sigma_{\mathrm{H}} \mathrm{d}R + \int_0^R n_{\mathrm{H}} \sigma_{\mathrm{d}} \mathrm{d}R$.

Inserting eq. (5.15) into eq. (5.14) and use the balance between ionization and recombination of atomic hydrogen, we obtain

$$S_* = \frac{4\pi R_0^3}{3} n_{\mathrm{H}}^2 \alpha_{\mathrm{B}} + n_{\mathrm{H}} \sigma_{\mathrm{d}} S_* \int_0^{R_0} \mathrm{e}^{-\tau} \mathrm{d}\tau. \tag{5.16}$$

If we insert the usual stromgren radius without the dust, R_{st}, into the left hand side of the above equation, we find

$$1 = \left(\frac{R_0}{R_{\mathrm{st}}}\right)^3 + \frac{\lambda_{\mathrm{d}}}{R_{\mathrm{st}}} \int_0^{R_0} \mathrm{e}^{-\tau} \mathrm{d}R, \tag{5.17}$$

where $\lambda_{\mathrm{d}} \equiv n_{\mathrm{H}} \sigma_{\mathrm{d}} R_{\mathrm{st}}$. Finally, assuming that the hydrogen is completely ionized in the ionized region, we can see $\tau_{\mathrm{H}} \ll \tau_{\mathrm{d}}$. Then we obtain the following equation,

$$\left(\frac{R_0}{R_{\mathrm{st}}}\right)^3 = \mathrm{e}^{-\lambda_{\mathrm{d}}(R_0/R_{\mathrm{st}})}. \tag{5.18}$$

This equation shows that λ_{d} is the key parameter for the effect of the dust. When $\lambda_{\mathrm{d}} \ll 1$, the left hand side converges to unity and $R_0 \sim R_{\mathrm{st}}$. Meanwhile, when λ_{d} is comparable to or larger than unity, the left hand side becomes less than unity and R_0 becomes smaller than R_{st}.

The cross-section of the dust with ionizing radiation can be calculated once dust properties, such as the dust mass, size distribution, and density are given. Following the dust model by Yajima *et al.* (2011), σ_{d} can be written as;

$$\sigma_{\mathrm{d}} = 1.3 \times 10^{-21}\ \mathrm{cm}^2 \left(\frac{Z}{Z_\odot}\right), \tag{5.19}$$

where Z is the metallicity within the ionized region. Then we obtain

$$\begin{aligned}
\lambda_{\mathrm{d}} &= n_{\mathrm{H}} \sigma_{\mathrm{d}} R_{\mathrm{st}} \\
&= 3.15 \times 10^{-2} \\
&\left(\frac{\sigma_{\mathrm{d}}}{10^{-23}\ \mathrm{cm}^2}\right) \left(\frac{L_{\mathrm{UV}}}{10^{42}\ \mathrm{erg\ s^{-1}}}\right)^{1/3} \left(\frac{\bar{n}}{\mathrm{cm}^{-3}}\right)^{1/3} \\
&= 4.13 \times 10^{-2} \\
&\left(\frac{Z}{0.01\ Z_\odot}\right) \left(\frac{L_{\mathrm{UV}}}{10^{42}\ \mathrm{erg\ s^{-1}}}\right)^{1/3} \left(\frac{\bar{n}}{\mathrm{cm}^{-3}}\right)^{1/3}.
\end{aligned} \tag{5.20}$$

In the second equation, we use eq. (5.2). Here we assume $Z = 0.01\ Z_\odot$ for the fiducial value, because in our simulation the galaxy is in the evolving stage and the dust mass of the galaxy should be smaller than that of the present day galaxy.

Equation (5.20) shows the dust attenuation effect is small within the ionized region and the size of the ionized region is not affected by the dust in such a low metal galaxy.

5.5 Chapter Summary

We have performed SPH simulation coupled with radiative transfer to investigate the effect of ionizing radiation on the collapse of DC halos, which is not considered in the calculation presented in the previous Chapter. We use a cloud sample taken from one of the collapsed DC halo found in Chapter 3. The UV luminosity is given by the star formation rate in semianalytic model with $f_* = 0.005$ and 0.1, where the latter is the maximum value compatible with the observation of the luminosity function at $z = 6$–7. In both cases, the cloud within DC halo remains neutral and collapses into the density with $\sim 10^8\ \mathrm{cm}^{-3}$. We find that the dense filaments around the galaxy protect the DC halo from ionizing radiation. It is interesting that, for the case of $f_* = 0.1$, the cloud collapses more rapidly than for $f_* = 0.005$ case. This suggests that the photo-heating of surrounding gas accelerates the collapse of the gas cloud.

To compare our results with previous studies, we calculate cloud evolution under the constant luminosity with $L_{\mathrm{UV}} = 10^{41}\ \mathrm{erg\ s}^{-1}$, the same with the work by Regan *et al.* (2016), and $L_{\mathrm{UV}} = 10^{42}\ \mathrm{erg\ s}^{-1}$. We find that the SMS forming cloud is completely photo-evaporated for the model with $L_{\mathrm{UV}} = 10^{42}\ \mathrm{erg\ s}^{-1}$. For the case of $L_{\mathrm{UV}} = 10^{41}\ \mathrm{erg\ s}^{-1}$, the DC cloud is irradiated by the ionizing radiation, and the cloud continues to lose its mass due to photo-evaporation. As a result, the cloud does not collapse since the cloud has not enough mass for the gravitational instability to operate. This fact indicates strong ionizing radiation at the early stage of structure formation can prevent the cloud collapse.

We also estimate the effect of ionizing radiation on the other 68 DC halos, found in Chapter 3, using the the outputs of N-body calculation. The estimated size of the HII region is smaller than the separation for at least one dynamical time for most of the cases. This is because the DC halo approaches the radiation source with time and the mean density increases accordingly. This picture is consistent with our specific sample, where we follow the evolution by the radiation hydrodynamics simulations in Section 5.3. We conclude that in most cases ionizing radiation is shielded by filamentary structure around the source galaxy and does not prevent the formation of SMSs.

Chapter 6

Radiation Hydrodynamics Simulations of the Formation of Direct-Collapse Supermassive Stellar Systems

6.1 Overview

We have seen so far that there are at least two collapsing gas clouds in our simulation box with 20 h^{-1}Mpc on a side. We have followed the cloud collapse until the protostellar cores appear around the cloud centers. The mass infall profiles just at the formation of protostars imply that the mass accretion rates reach ~ 0.1–$1\ M_{\odot}\ \mathrm{yr}^{-1}$. Still, we do not know the final mass of stars which will appear in this system. Indeed, the final mass of an SMS is determined through dynamical interplay between the central protostar(s), the circumstellar disk, and the infalling gas, where gravitational fragmentation may occur. Recent high-resolution simulations show no significant fragmentation during the early collapse phase of a DC cloud (Bromm & Loeb, 2003; Regan & Haehnelt, 2009; Latif *et al.*, 2013; Inayoshi *et al.*, 2014; Choi *et al.*, 2015). In the later accretion phase after the birth of a protostar, however, the circumstellar disk grows in mass and becomes gravitationally unstable to trigger disk fragmentation (e.g., Becerra *et al.*, 2015; Sakurai *et al.*, 2016; Regan & Downes, 2017), possibly leading to formation of a star cluster, rather than the formation of a single SMS. We need further simulations which follow the long-term evolution of the protostars.

Radiative feedback from an accreting protostar is another key process, which can limit the stellar mass growth by halting the accretion (e.g. McKee & Tan, 2008b; Hosokawa *et al.*, 2011). Since the structure of an accreting protostar under the rapid accretion of $\gtrsim 0.1\ M_{\odot}\ \mathrm{yr}^{-1}$ is very different from that of a main-sequence star, with a very bloated envelope, the UV feedback is thought to be weak for the DC case (Hosokawa *et al.*, 2012, 2013; Schleicher *et al.*, 2013). Its effective temperature is only $T_{\mathrm{eff}} \simeq 5000$ K, with which the stellar UV emissivity remains small even when the stellar mass reaches $\sim 10^4$–$10^5\ M_\odot$. The UV feedback strength is intrinsically coupled to the fragmentation described above because individual protostars begin to contract if the accretion rate falls below $\sim 10^{-2}\ M_\odot\ \mathrm{yr}^{-1}$. We need further simulations which follow the long-term evolution of the protostars.

In this chapter, we study the protostellar evolution in the later accretion phase in the DC model. We start our radiation hydrodynamic simulations from the final snapshots of the two collapsing clouds found in Chapter 4, and follow the subsequent evolution for ~ 0.1 Myr. We show that the tidal force exerted on the clouds critically affects the stellar mass growth. In one case, strong tidal field distorts the cloud and induces large-scale filament fragmentation. The mean stellar mass at the end of our simulation is found to be as small as a few $\times\ 10^3\ M_\odot$. The other cloud experiences relatively weak tidal force, and stars with mass greater than $10^4\ M_\odot$ are actually formed within 0.1 Myr. The latter case is a promising SMS formation process, whereas an interesting end-product of the former case is massive star binaries. Both have important implications for direct and indirect observations.

The content in this chapter has been submitted to Monthly Notices of the Royal Astronomical Society (Chon *et al.*, 2017).

6.2 Methodology

We select two clouds as the initial condition from the collapsed cloud in Chapter 4 and follow the long-term evolution of these cloud. To this end, we use the N-body / SPH code, `Gadget2` (Springel, 2005) with following extensions. We implement the sink particle to follow the protostar evolution. Then, we use a stellar evolution model to obtain the stellar luminosity. Finally, we implement the ray tracing scheme to follow the radiation feedback from accreting protostars, which is developed in Chapter 5. In this section, we briefly describe the setup of the numerical calculation.

6.2.1 Initial condition

In Chapter 4, we follow the collapse of clouds in 42 DC halos. Since the massive galaxy which provides a large amount of LW radiation is located in the vicinity of DC halos, the cloud inside the DC halo suffers from the strong tidal field. A large part of the clouds do not collapse because of this disrupting tidal force. These clouds finally merge with the nearby massive galaxy. Only two clouds collapse and the density reaches $10^8\ \mathrm{cm}^{-3}$.

Figure 6.1 summarizes the characteristics of the two clouds, labeled as “filamentary” and “spherical” clouds. The filamentary cloud is located close to a massive galaxy with the separation of ~ 100 pc. This nearby galaxy has a mass of $10^{10}\ M_\odot$, which tidally distorts and elongates the collapsing gas cloud with a filamentary structure (left top panel in Figure 6.1). The spherical cloud is located relatively far away from a massive galaxy with the separation of ~ 5 kpc (right bottom panel in Figure 6.1). The LW radiation is mainly provided by a less massive galaxy with a mass of $\sim 10^7\ M_\odot$ at ~ 400 pc from the

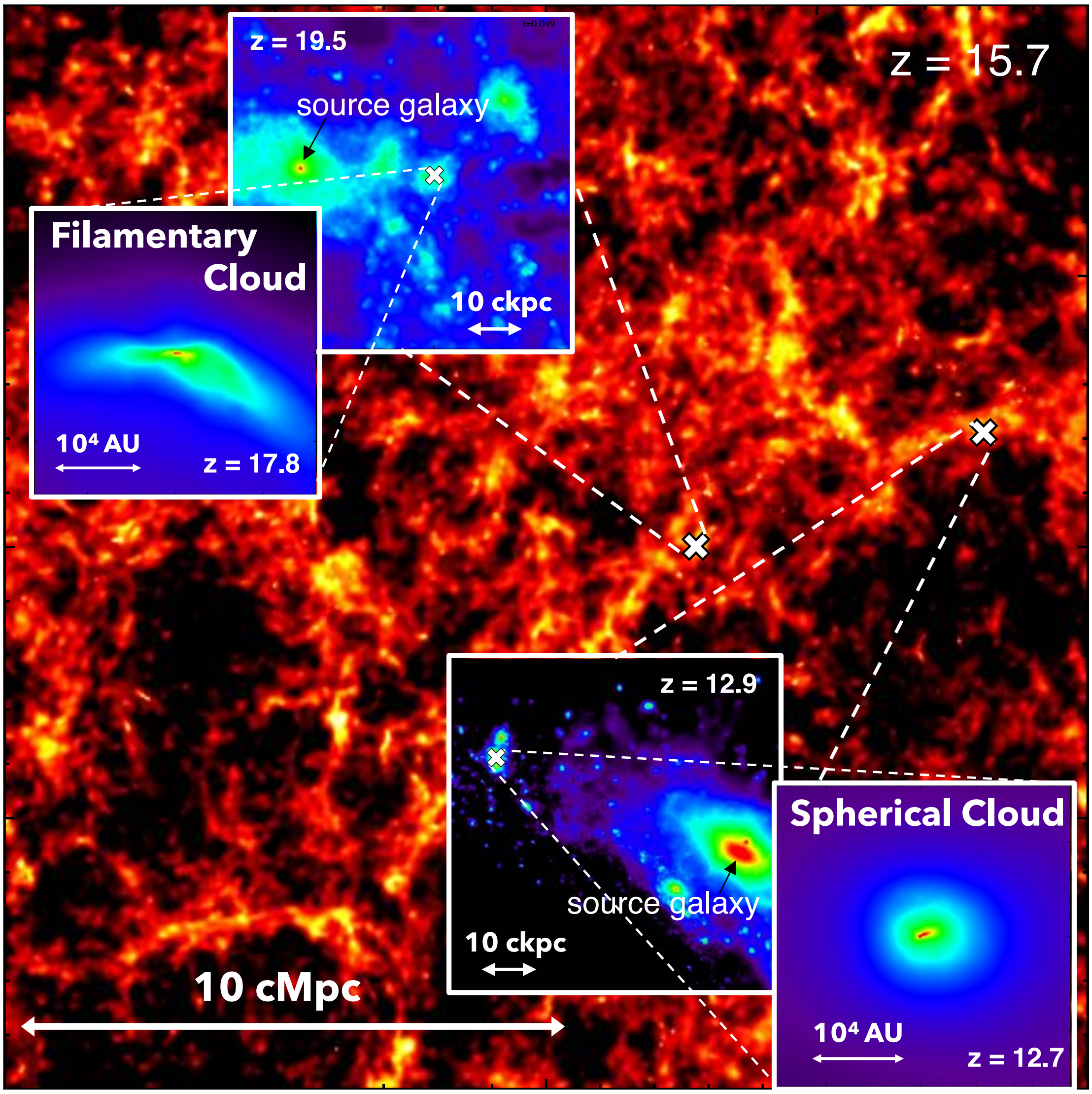
z = 19.5
source galaxy
10 ckpc
z = 15.7
Filamentary Cloud
10^4 AU
z = 17.8
z = 12.9
source galaxy
10 ckpc
Spherical Cloud
10^4 AU
z = 12.7
10 cMpc

Figure 6.1. Schematic view showing the locations of the spherical and the filamentary clouds. The clouds are taken from a large-scale cosmological simulation with the box size of 20 h^{-1}Mpc on a side. In Chapter 4, the cloud evolution has been followed until the central density reaches 10^8 cm^{-3} during the early runaway collapse. We further follow the subsequent long-term evolution for ~ 0.1 Myr in this chapter.

spherical cloud. Thus the cloud can avoid the tidal force from the galaxy and collapses almost keeping a spherical shape (Visbal *et al.*, 2014a).

To reduce the computational cost, we extract the region around the collapsing cloud center when the central density reaches 10^8 cm^{-3}. We extract the region with the radial extension of $\sim$ 10 and 100 pc from the cloud center for gas and dark matter particles, respectively. We include the DM particle in a larger region than the gas particles, since the tidal field from the nearby massive galaxy can be important at the later accretion phase of the collapsing clouds.

6.2.2 Chemistry

We include 9 primordial species (e^-, H, H^+, He, He^+, He^{2+}, H_2, H_2^+, and H^-) and solve the non-equilibrium chemical reaction network and the energy equation considering cooling process. We omit the cooling by species containing deuterium (i.e. HD) because HD cooling is negligible at the typical cloud temperature in the atomic-cooling cloud.

We include external radiation field which dissociates H_2 and H^- as a background. The intensity is taken from the semianalytic calculation as in Chapter 3. The intensity lies $1000 - 3000$ in units of J_{21} and almost constant throughout the calculation. We assume a black-body spectrum with the effective temperature with 10^4 K. To save computational cost, we do not consider the self-shielding of LW radiation. We further discuss the implication of this simple treatment in Section 6.5.3.

We also consider the local ionizing radiation originating from the protostars. In this calculation, we only consider the local ionizing radiation which ionizes atomic hydrogen ($h\nu > 13.6$ eV), and do not consider local radiation with $h\nu < 13.6$ eV. This is because the H_2 dissociation rate by LW radiation is negligible compared to the dissociation rate by the collision with atomic hydrogen.

We assume the optically-thin Lyman-α cooling rate throughout the calculation, even above the density $\sim 10^4$ cm^{-3} where the cloud becomes optically-thick to the Lyman-α radiation. This simplification regulates the cloud temperature with 8000 K, which reproduces the realistic temperature evolution considering other full energy transfer of atomic hydrogen (e.g. 3p-2s transition, H^- continuum, see Becerra *et al.*, 2015).

Since we are interested in the stellar evolution for the time-scale of $\sim$ 0.1–1 Myr, we use the adiabatic equation of state with $\gamma = 5/3$ once the gas density exceeds 10^{13} cm^{-3}. Otherwise, the increased gas density makes the time step too short and the long-term evolution cannot be followed. We discuss how this adiabatic prescription affects the final result in Section 6.5.4.

6.2.3 Particle splitting

In the calculation, we should resolve the local Jeans scale by more than ten times the smoothing length of the gas particles (e.g. Truelove *et al.*, 1997; Nelson, 2006). To keep the enough resolution, we split a gas particle into 13 daughter particles following Kitsionas & Whitworth (2002), when its density reaches $n = 10^8$ and 10^{10} cm^{-3}. The initial mass of the gas particle is 1.6 $M_\odot$ and the gas particle mass with $n > 10^{10}$ cm^{-3} is 9.4×10^{-3} $M_\odot$. This prescription allows us to resolve the Jeans length by more than ten times the smoothing length (e.g. Stacy *et al.*, 2016).

6.2.4 Sink particle

We introduce the sink particle which emulates an accreting protostar, once the gas density exceeds $n_{\rm sink} = 5 \times 10^{13}$ cm^{-3}. A sink particle has two important parameters, a mass and a sink radius (R). The region within R around the sink particle is called the "interaction region" between gas particles and the sink particle. Inside the interaction zone, gas particles accrete onto the sink particle. Gas particles with the density larger than $n_{\rm sink}$ are chosen as the candidates which will be substituted by sink particles. To determine which gas particle should be replaced by the sink particle, we impose the following additional criteria for sink creation (Hubber *et al.*, 2013).

1. Overlap criterion:
   The interaction region of a newly formed sink particle should not overlap with that of a preexisting sink particle j,
   $$r_{ij} > X_{\rm sink} h_i + R_j, \tag{6.1}$$
   where h_i is the smoothing length of the candidate gas particle i, $X_{\rm sink}$ is an order of unity parameter which is set to be 4, r_{ij} is the separation between the candidate gas particle i and the preexisting sink particle j, and R_j is the sink radius of the preexisting sink particle j. Here, $X_{\rm sink} h_i$ is the sink radius if the gas particle i is replaced by the sink particle.
2. Minimum gravitational potential:
   The particle should reside at the local minimum of the gravitational potential. We calculate the gravitational potential around the candidate particles. We examine whether they are at the deepest in gravitational potential among other gas particles within h_i around the candidate. If not, we exclude the gas particle from the candidates.
3. Hill criterion:
   The candidate gas particle i should have sufficiently high density to contract under the disrupting tidal force from the preexisting sink particles j,
   $$\rho_i > \rho_{\rm Hill} \equiv \frac{3 X_{\rm Hill} a_{ij}}{4\pi G r_{ij}}, \tag{6.2}$$
   where G is the gravitational constant, ρ_i is the density of the candidate gas particle i, a_{ij} is the gravitational acceleration caused by the preexisting sink particle j, and $X_{\rm Hill}$ is an order of unity parameter that is set to be 4.

The sink radius of the newly formed sink particle i is set to be $X_{\rm sink} h_i$, which is ~ 20 AU in our simulation.

We assume a sink particle accretes all the gas particles in the interaction region instantaneously. This prescription sometimes overestimates the accretion rate (Bate *et al.*, 1995; Hubber *et al.*, 2013), since no gas particles exist around the sink particles. The negative pressure gradient accelerates the surrounding gas particles toward the sink particle. We allow the mergers of sink particles, once their separation becomes smaller than the sink radius or the stellar radius (R_*, see Section 6.2.5.1). This is necessary because the protostars have the radius comparable to the sink radius when they are accreting the matter at a rate of $\sim 0.1 - 1\ {\rm M}_\odot\ {\rm yr}^{-1}$, the typical rates in the DC model (e.g. Hosokawa *et al.*, 2013). We conserve the mass and momentum of the sink particles before and after the merger.

6.2.5 Stellar evolution model

We employ a simple analytic model to estimate the radius, luminosity, and effective temperature of such an accreting protostar. Our model reproduces essential behavior of the protostellar evolution with various accretion histories, which has been studied with more detailed calculations by numerically solving the stellar internal structure (e.g. Hosokawa *et al.*, 2013; Sakurai *et al.*, 2015). We only consider the following two evolutionary stages for simplicity: (1) the supergiant protostar phase, and (2) ZAMS phase.

6.2.5.1 Supergiant protostar phase

Hosokawa *et al.* (2012, 2013) show that, with high accretion rates exceeding $\dot{M}_{\rm crit} = 0.04\ M_\odot\ {\rm yr}^{-1}$, the evolution of the stellar radius is well described by the following relation

$$R_* = 38\ {\rm AU} \left(\frac{M_*}{1000\ M_\odot} \right)^{1/2}, \tag{6.3}$$

which means that the star has a very large radius and continuously inflates with increasing stellar mass, independent of different accretion rates. During this phase, the stellar effective temperature is almost regulated at $\simeq 5000$ K due to very strong temperature dependence of $\rm H^-$ opacity (e.g. Hayashi, 1961). The protostar only emits a small amount of ionizing photons with such a low effective temperature. The resulting UV feedback is thus too weak to prevent the accretion flow (e.g. Hosokawa *et al.*, 2016). Even if the accretion rate falls below $\dot{M}_{\rm crit}$, the protostar remains inflated for about ten times the KH time-scale (Sakurai *et al.*, 2015),

$$t_{\rm KH,\ surf} = 1000\ {\rm yr} \left(\frac{M_*}{500\ {\rm M_\odot}} \right)^{1/2}. \tag{6.4}$$

In our analytic model, we estimate the accretion rate onto the protostar by averaging instantaneous rates onto the sink particle over every 30 years. We just assume that the protostar is in the supergiant phase described by eq. (6.3) when the estimated accretion rate is higher than the critical value $\dot{M}_{\rm crit}$. We also consider that the protostar emits no ionizing photons during this phase. The protostar still remains in the supergiant stage unless the accretion rates are below $\dot{M}_{\rm crit}$ for a duration longer than $t_{\rm KH,surf}$.

6.2.5.2 ZAMS phase

When the above conditions are not met, the protostar begins to contract owing to the radiative energy loss (so-called KH contraction) leaving the supergiant phase (Sakurai *et al.*, 2015). The stellar effective temperature rapidly increases up to $\sim 10^5$ K during this stage. After the contraction over the KH time-scale, the accreting star begins to follow the mass-radius relation of the ZAMS stars.

For our analytic model, we simply assume that the protostar is in the ZAMS phase if not in the supergiant phase. We adopt our previous results of the stellar evolution calculations for the ZMAS stars, i.e., the radius, luminosity, and effective temperature, which is tabulated as functions of the stellar mass. We assume that the star immediately returns back to the supergiant phase once the accretion rate exceeds $\dot{M}_{\rm crit}$.

Since we neglect the finite KH time-scale for the supergiant star to contract toward the ZAMS star, our prescription overestimates the stellar emissivity of the ionizing radiation. As we will see in Section 6.4, however, the ionizing feedback hardly affects the accretion flow in our simulations even with the current stellar models.

6.2.6 Transfer of ionizing radiation

We solve the photo-ionization of neutral hydrogen and resulting heating using a ray tracing scheme proposed by Susa (2006). In this method, the optical depth of ionizing radiation, $\tau_{\rm UV}$, from a light source to the particle i is evaluated by the sum of the local optical depth, $\sum_j {\rm d}\tau_{{\rm UV},j}$. Here, ${\rm d}\tau_{{\rm UV},j}$ is the optical depth from the particle j to a particle located at the upstream of particle j. We then calculate the photon number which is locally consumed by the interaction with the neutral hydrogen. Because the optical depth of one SPH particle is relatively large, we use the so-called photon conserving method (Kessel-Deynet & Burkert, 2000; Abel *et al.*, 1999), where the reaction rate k and the photo-heating rate Γ are given by,

$$k = -\frac{1}{4\pi r^2}\frac{\rm d}{{\rm d}r}\int_{13.6~{\rm eV}/h}^{\infty}\frac{L_\nu e^{-\tau_\nu}}{h\nu}{\rm d}\nu, \tag{6.5}$$

$$\Gamma = -\frac{1}{4\pi r^2}\frac{\rm d}{{\rm d}r}\int_{13.6~{\rm eV}/h}^{\infty}\frac{L_\nu e^{-\tau_\nu}}{h\nu}(h\nu - 13.6~{\rm eV})\,{\rm d}\nu. \tag{6.6}$$

We discretize the differential in the above equations and take volume averages.

6.3 Results

6.3.1 Early collapse phase

In Chapter 4, we follow the cloud evolution until the central density reaches 10^8 cm^{-3}. We further follow the cloud collapse and the long-term evolution of the cloud for two clouds. First, the cloud collapse advances in a so-called "runaway" fashion as in Appendix A.1.3 until the protostellar core appears at the cloud center. During the collapse, the gas cools via atomic hydrogen emission as mentioned before. Panels with the smallest scale in Figure 6.1 show the snapshots at the moment when the central density reaches 10^{12} cm^{-3}. One cloud is elongated by the strong tidal field from the nearby galaxy and shows the filamentary structure (left top panel in Figure 6.1). The other cloud collapses keeping a almost spherical shape (right bottom panel in Figure 6.1). Hereafter, we call the former as "filamentary" cloud and the latter as "spherical" cloud.

Figure 6.2 shows the density-temperature phase diagram for gas particles within 10 pc from the cloud center. Both clouds collapse almost isothermally keeping the temperature between 8000 and 10000 K, due to strong atomic hydrogen cooling. At $n \gtrsim 10^8$ cm^{-3},

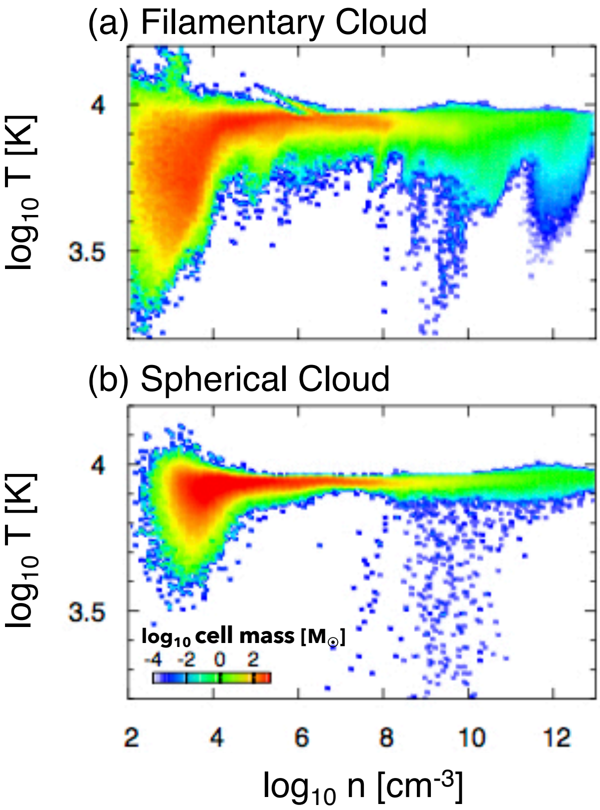

Figure 6.2. Mass distribution on the density-temperature phase diagram for (a) the filamentary and (b) the spherical clouds. The snapshots are taken when the maximum density reaches 10^{12} cm^{-3} in the early runaway stage. We divide the whole domain into 200 × 200 cells. The color scale shows the gas mass contained within each cell.

a small fraction of gas particles cool slightly below 8000 K owing to H_2 formation by three-body reaction. Inayoshi *et al.* (2014) point out that this cool gas is produced by the combination of cooling by the adiabatic expansion and cooling by H_2 formation.

Figure 6.3(a) shows radial density profiles for the filamentary (green) and the spherical (blue) clouds when the cloud density reaches 10^{13} cm^{-3}. Both clouds roughly follow the density profile with $n \propto R^{-2}$ (black), which is expected for the self-similar collapse of an isothermal cloud (Larson, 1969). However, in the filamentary cloud, the profile exhibits small bumps on the $n \propto R^{-2}$ profile at some point. The green arrows labeled by A, B, and C indicates these bumps in Figure 6.3(a). Figure 6.3(b) represents the radial profiles of the mass infall rate ($\dot{M}_{\rm infall}$) measured at the distance R,

$$\dot{M}_{\rm infall}(R) \equiv 4\pi R^2 \rho v_{\rm rad}, \tag{6.7}$$

where ρ is the density and $v_{\rm rad}$ is the radial velocity of gas. We find that the spherical and the filamentary cloud has $\dot{M}_{\rm infall} \gtrsim 1\ M_\odot$ yr^{-1} at $R < 10^6$ AU. In the filamentary cloud, however, $\dot{M}_{\rm infall}$ becomes much smaller than $1\ M_\odot$ yr^{-1} around scales A and C. As we will see later in Section 6.3.2.2, the filament starts to fragment at scales A and C

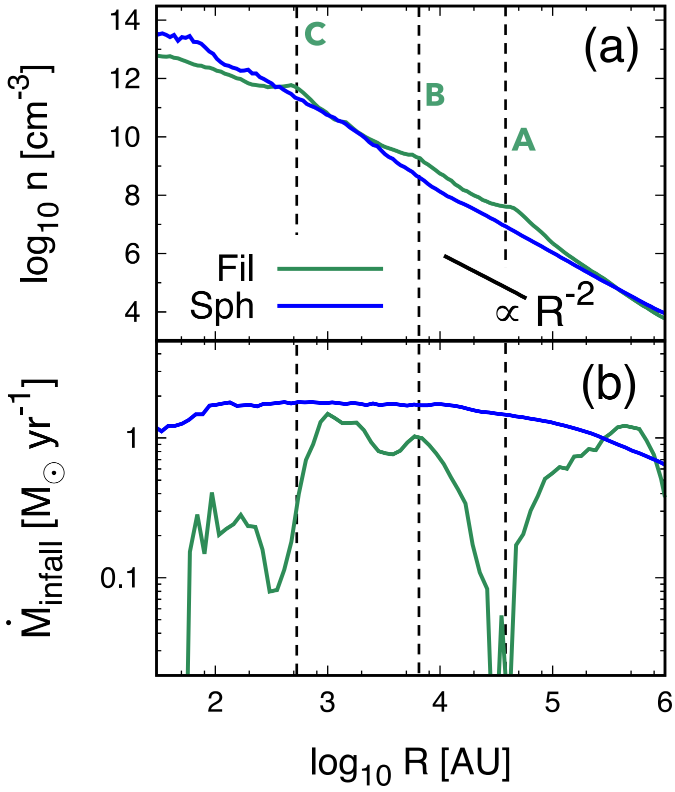

Figure 6.3. (a) Radial density profiles for the filamentary (green) and the spherical (blue) clouds. Three vertical lines A, B, and C indicate the characteristic length-scales, where the filamentary cloud shows the density bumps. The power-law profile with $n \propto R^{-2}$ is also depicted as the black solid line. (b) Radial profiles of the infall mass rate ($\dot{M}_{\rm infall}$, eq 6.7).

in the early stage of the accretion phase.

Figure 6.4 shows the projected density distributions around the protostar in the filamentary cloud. From the top to bottom panels, the density structure over the smaller length-scale are shown. The left and right panels show the projection maps from the different directions, labeled as “xy” (left) and “xz” (right). At the scale larger than A, the cloud appears to be sheet-like, that is, the cloud has the round shape projected onto “xy” plane while it is elongated and shows a filamentary structure projected onto “xz” plane. Below scale B, the cloud shows completely filamentary structure. We can see that around scale C, the filament is about to fragment. We will see the cloud also fragments at scale A at 6800 yr after the central protostar formation (Section 6.3.2.2).

In order to quantify the deviations from the spherical collapse in these clouds, we fit the iso-density structure around the cloud center by a set of ellipsoids. Figure 6.5 shows how the axial ratio $\mathcal{Q} \equiv a_3/a_1$ of the iso-density contour changes with different densities for the filamentary (blue) and the spherical (green) clouds. Here, a_1 and a_3 are the lengths of the axes which have the largest and smallest magnitudes, respectively. The filamentary cloud has smaller axial ratio than the spherical cloud. For example, at $n = 10^8$ cm^{-3}, the

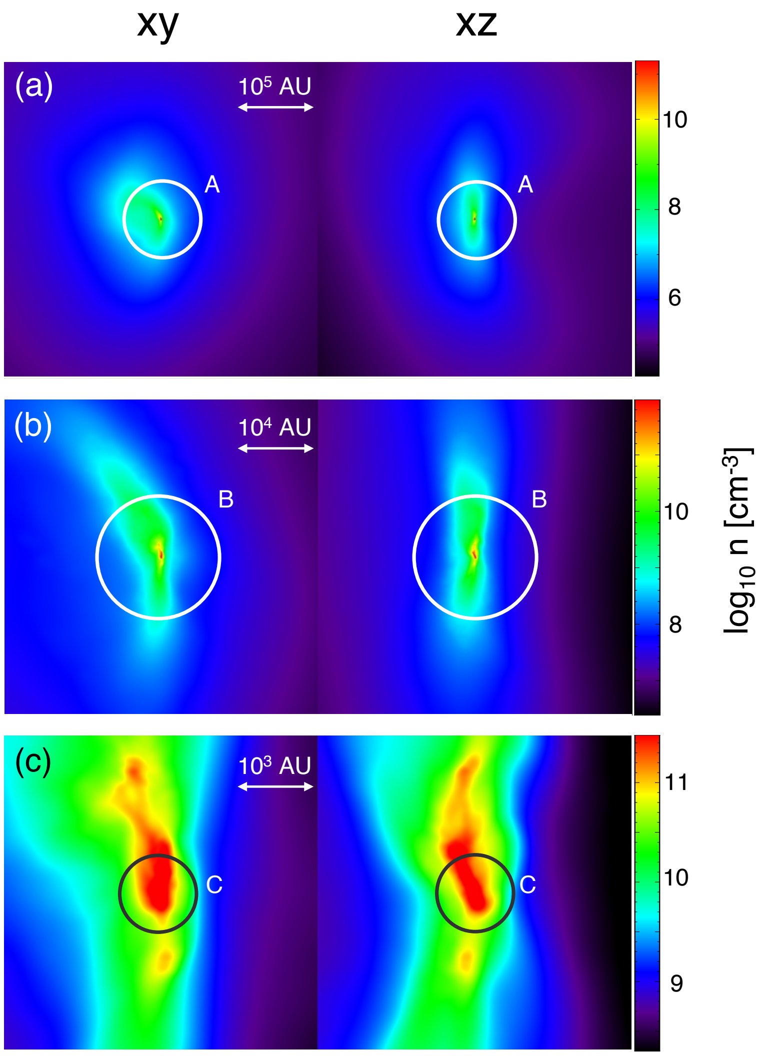

Figure 6.4. Projected density maps in the filamentary cloud when the maximum density reaches 10^{12} cm^{-3}. The physical scales become smaller from top to bottom. Left and right panels show the density maps projected onto the different planes, which are perpendicular to each other ("xy" and "xz"). Solid circles (A, B, and C) represent the scales shown in Figure 6.3.

filamentary and spherical clouds have the axial ratios of ~ 0.03 and ~ 0.3, respectively. In Figure 6.5, we also present the Jeans length ($R_{\rm J}$) as a function of the gas density (n) with the fixed temperature $T = 8000$ K,

$$R_{\rm J} = 0.22 \ {\rm pc} \left(\frac{n}{10^7 \ {\rm cm}^{-3}} \right)^{-1/2} . \tag{6.8}$$

For the collapsing cloud, $R_{\rm J}$ roughly gives the length-scale of the iso-density region with a given density n.

The axial ratios decrease at $n \gtrsim 10^{10}$ cm^{-3} in the spherical cloud since the disk-like structure appears around the density peak due to the angular momentum support. Meanwhile, the small axial ratio at $n \gtrsim 10^6$ cm^{-3} in the filamentary cloud is not caused by

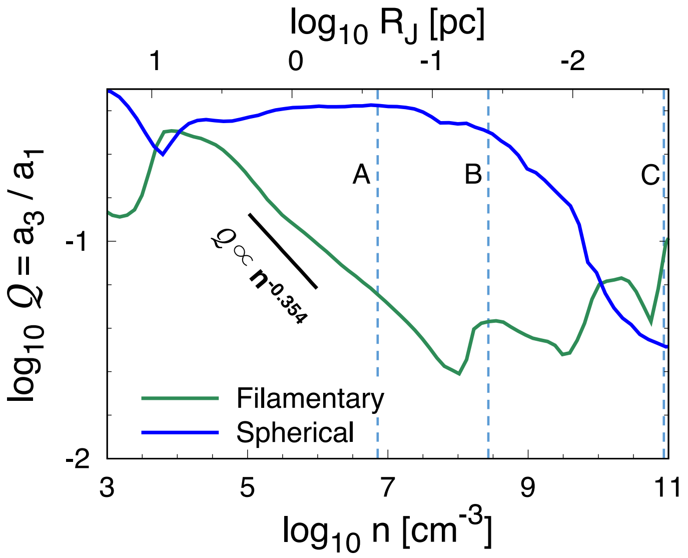

Figure 6.5. Evolution of the axial ratios $\mathcal{Q}$ during the cloud collapse for the filamentary (blue) and the spherical (green) clouds. To derive $\mathcal{Q}$, we first fit the iso-density region by sets of ellipsoids. The ratio, $\mathcal{Q}$ is then defined as the ratio of a_3 to a_1, where a_1 and a_3 are the length of longest and shortest axes of fitted ellipsoids. The upper horizontal axis denotes the Jeans length (eq. 6.8) the fixed temperature at 8000 K. The vertical dashed lines A, B, and C indicate the reference scales shown in Figure 6.3(a).

the disk formation. This is because the corresponding Jeans scale at this density is much larger than the scale where the angular momentum support is not efficient at this epoch. Rather, this small axial ratio is caused by a development of the bar mode in isothermal gas. Hanawa & Matsumoto (2000) show $\mathcal{Q} \propto n^{-0.354}$ at the linear regime due to the development of the bar mode perturbation. We can see the evolution of $\mathcal{Q}$ follows this relation in the filamentary cloud (black solid line). At $n \sim 10^8$ cm^{-3}, $\mathcal{Q}$ reaches 0.03 and enters the non-linear regime (Tsuribe & Omukai, 2006). Below this scale, the iso-density region is difficult to be fit by the ellipsoid.

Note again that the decrease of $\mathcal{Q}$ is not entirely driven by the tidal torque from the nearby massive galaxy. This is because the tidal radius is ~pc and has almost no effect at the scale smaller than $\lesssim$ pc and $n \gtrsim 10^5$ cm^{-3}. The initial perturbation is seeded by the tidal torque and it grows during the isothermal collapse in the filamentary cloud.

6.3.2 Later accretion phase

After the central protostar formation, gas accumulates around the protostar and the circumstellar disk appears due to the angular momentum barrier. In the self-gravitating gas disk, the angular momentum is transferred by the gravitational torque and the central protostar accretes the disk gas. Once the disk becomes massive enough to operate the gravitational instability, the disk fragments into multiple. In this section, we see the

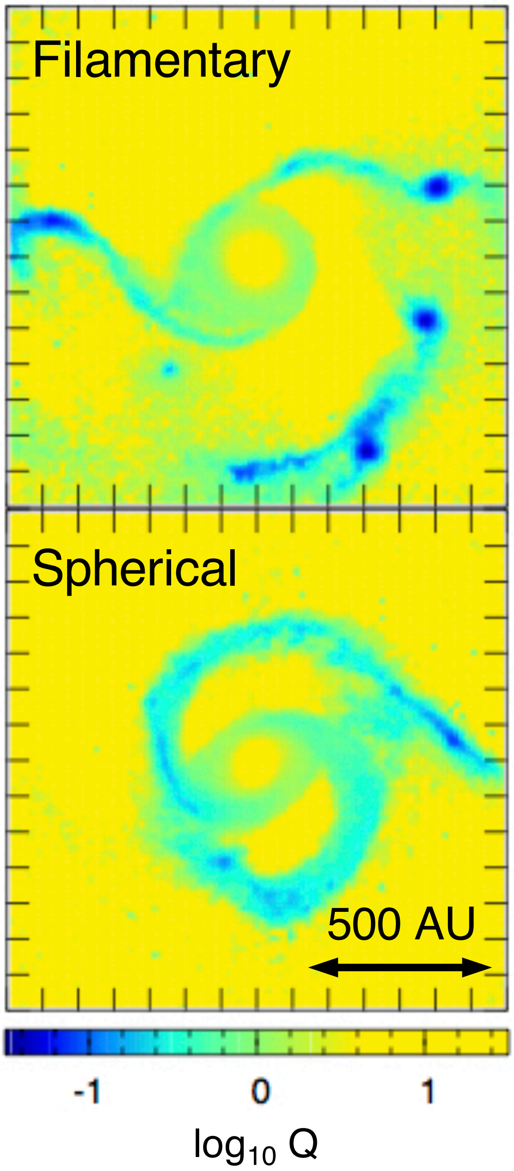

Figure 6.6. Distributions of Toomre-Q parameters (eq. 6.9) around the central protostar for the filamentary (top) and the spherical (bottom) clouds. The snapshot is $\sim$ 1500 yr after the central protostar is formed.

evolution of the protostars and the surrounding disk. Here, we will call the protostar first formed in the system as the "primary" protostar.

6.3.2.1 Disk and protostar evolution

After the disk is formed around the star, it experiences fragmentation due to the gravitational instability. To see this, we calculate the Toomre-Q parameter which is defined by,

$$Q = \frac{c_{\rm s}\Omega}{\pi G \Sigma}, \tag{6.9}$$

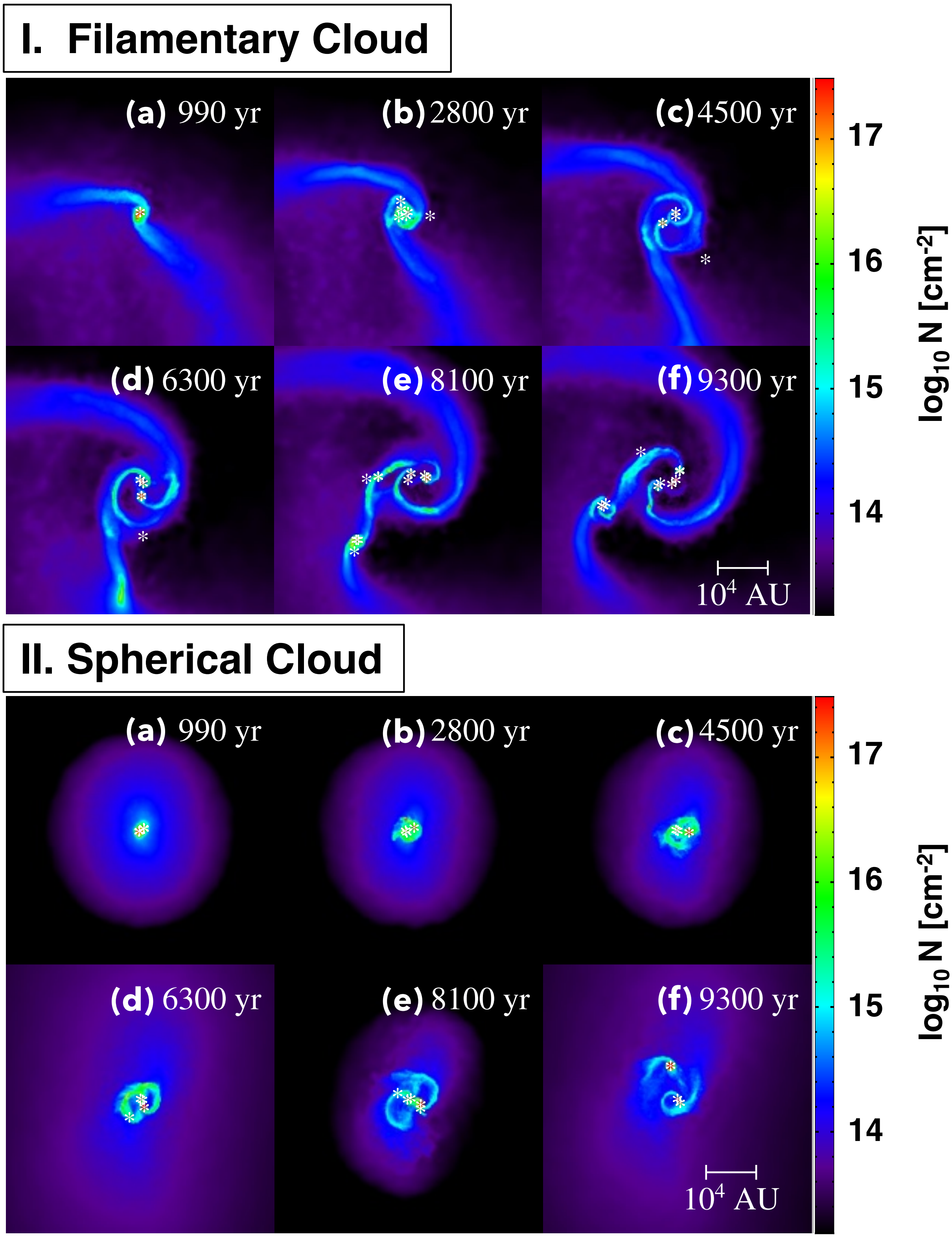

Figure 6.7. Face on view of the disk and stellar system in the filamentary (top) and the spherical (bottom) clouds. White asterisks represent the protostars. and the colors scale represents the column density of gas. Time origin is the moment at which the central protostar is formed. We note that no protostars are ejected outside the shown region.

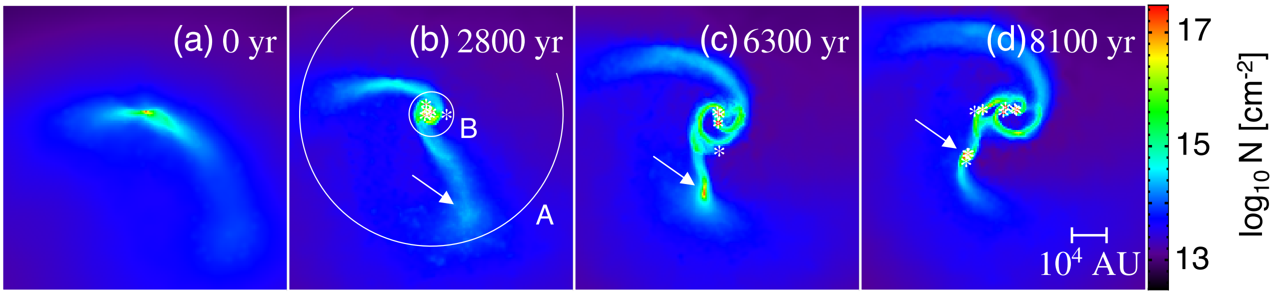

Figure 6.8. Filament fragmentation just occuring in the filamentary cloud. Arrows indicate where the new star and disk system forms through such an event. In panel (b), the white circles A and B indicate the reference scales shown in Figure 6.3.

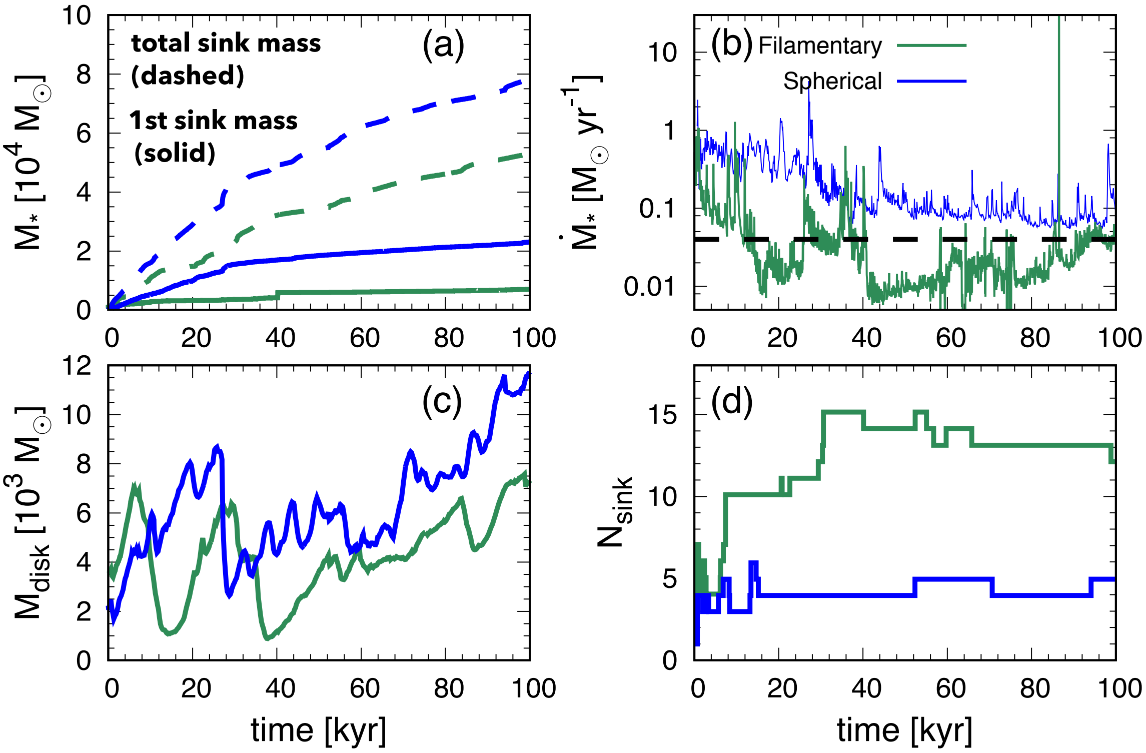

Figure 6.9. Evolutions of (a) the stellar mass, (b) the mass accretion rate, (c) the disk mass, and (d) the number of the protostars for the filamentary (green) and the spherical (blue) clouds. In panel (a), the solid and dashed lines represent the primary and total protostellar masses, respectively. Here, the primary protostar is the protostar which is first produced in the calculation. In panel (b), the dashed line indicates the critical mass accretion rate, below which the protostars contract into the ZAMS stage (Section 6.2.5). The accretion rate is averaged for every 30 years.

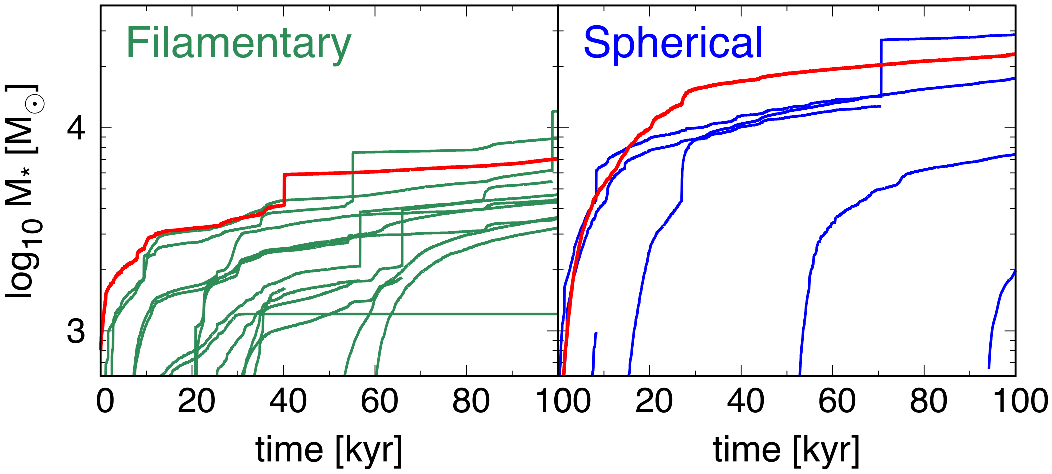

Figure 6.10. Mass evolution of all the protostars for the filamentary (left) and the spherical (right) clouds. The stellar mergers are marked as the vertical jumps shown in some lines. Note that the end point of each line represents the merger partner. The red lines show mass evolution of the primary protostars.

where c_s is the sound speed, Ω is the orbital frequency, and Σ is the surface density of the disk. Figure 6.6 shows the distribution of Q parameter on the disk surface around the central protostar at 1500 yr after the primary protostar formation. Toomre-Q becomes an order of unity inside the disk, while is smaller than unity along the spiral arms in the disk (Gammie, 2001; Takahashi *et al.*, 2016). These arms fragment into multiple clumps, where the Q is much smaller than unity ($Q \sim 0.1$). This shows that the disk fragmentation is caused by the gravitational instability.

The most unstable length- and mass-scales for the disk fragmentation are given by $\lambda \sim c_\mathrm{s}/\Omega$ and $M_\mathrm{frag} \sim \pi(\lambda/2)^2\Sigma$ assuming $Q = 1$. With the typical temperature and surface density in our DC cases, these scales are described as,

$$\lambda = \frac{\pi c_\mathrm{s}^2}{G\Sigma} = 17\ \mathrm{AU} \left(\frac{T}{8000\ \mathrm{K}}\right) \left(\frac{10^5\ \mathrm{g\ cm^{-2}}}{\Sigma}\right), \tag{6.10}$$

$$M_\mathrm{frag} = \frac{\pi^3 c_\mathrm{s}^4}{4G^2\Sigma} = 2.5\ M_\odot \left(\frac{T}{8000\ \mathrm{K}}\right)^2 \left(\frac{10^5\ \mathrm{g\ cm^{-2}}}{\Sigma}\right)^2. \tag{6.11}$$

The initial masses of the fragments are $\sim 5\ M_\odot$ and roughly coincides with the above estimation.

Figure 6.7 shows the evolution of the protostar-disk systems for the filamentary and spherical clouds, where the color scales show the column density (N) distribution projected onto the disk surface. The circumstellar disk is formed (Figure 6.7-Ia and IIa) and continuously acquires mass and grows in mass and size. The disk becomes gravitationally unstable and the spiral arms are excited in the disk. The arm fragments into the multiple clumps that finally contract into protostars (Figure 6.7-Ib and IIb). At the early stage of the disk evolution, some of the newly formed protostars rapidly fall onto the central

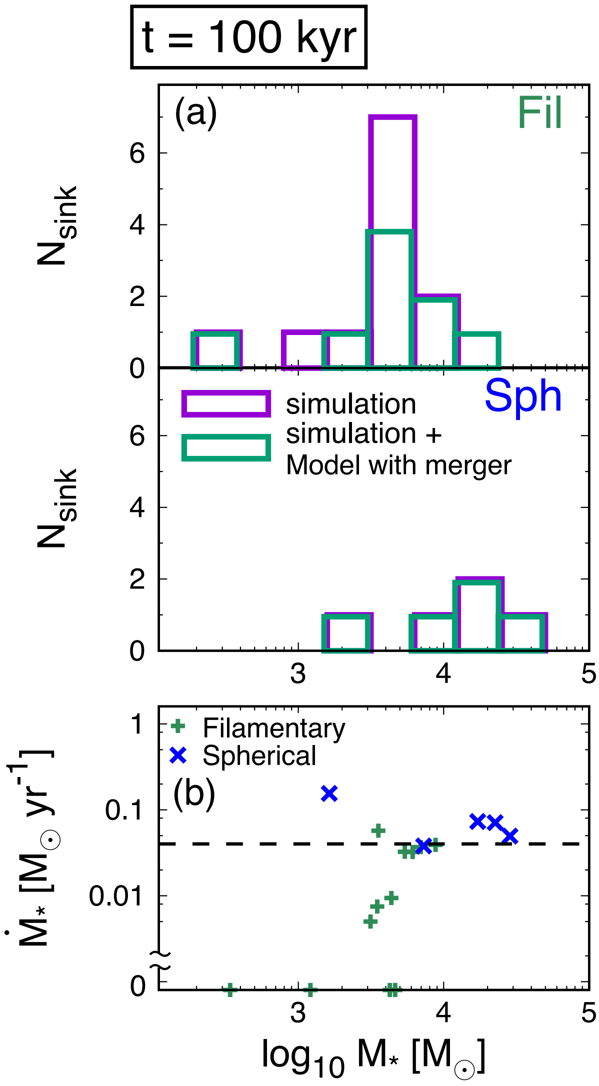

Figure 6.11. (a) Stellar mass distribution at $t = 100$ kyr for the filamentary (top) and the spherical (bottom) clouds. Purple histograms show the stellar mass in the simulation, while green histograms show the mass distribution with "Models with merge". In this model, we first pick up protostar pairs that experienced close encounters with < 200 AU and assume these protostar pair merges into a single protostar. The mass of combined protostar is the total mass of the original protostar pair. (b) Mass accretion rates ($\dot{M}$) versus stellar masses (M_*) at $t = 100$ kyr for the filamentary (green) and the spherical (blue) clouds. The dashed line indicates the critical mass accretion rate, below which the protostar contracts into the ZAMS stage.

protostar. Such an inward migration of the protostars is promoted by the interaction with the gas inside the disk (i.e. dynamical friction and Type-I migration). As a result, some of the infalling protostars are merged with the central star in the early phase.

The density around the disk center decreases with time since survived protostars accrete the surrounding gas (Figure 6.7-Ic and IId). This makes the interaction between the gas disk and the protostars less efficient and ceases the inward migration of protostars. More than three protostars are formed inside the disk and they are stable for several tens of the disk rotation periods. The picture is common in both the filamentary and the spherical clouds.

In the spherical cloud, only a single circumstellar disk is formed around the cloud center. The fragment appears inside the disk due to the gravitational instability. This multiple stellar system is stable and no star is ejected from the disk until the end of our calculation ($t \sim 0.1$ Myr). The separations among protostars are smaller than the disk scale, which is $\lesssim 10^4$ AU at 0.1 Myr.

In the filamentary cloud, another star-disk system appears far away from the cloud center (Figure 6.7-Ie). We emphasize the filament fragmentation in Figure 6.8 by arrows. In panel (b), white circles indicate the length-scales A and B. The filament starts to fragment just below scale A, at which the axial ratio of the iso-density contour becomes small enough and the bar mode perturbation grows in non-linear fashion (see Section 6.3.1). This fragment migrates toward the cloud center (panel d), which is caused by the growth of the density perturbation at larger scale than the disk scale. Since the angular momentum is not efficiently extracted during this migration due to the low density, the final separation between the star-disk systems is determined by the angular momentum barrier. This separation scale is much larger than that in the spherical cloud. For example, the separation of the protostars at the final snapshot is $\gtrsim 10^5$ AU. Thus, the filament fragmentation introduces the new separation scales among the protostars.

6.3.2.2 Stellar mass growth histories and disk fragmentation

Figure 6.9(a) shows the evolution of the total protostellar mass (dashed) and the mass of the primary protostars (solid line) for both the filamentary and spherical cases. Figure 6.9(b) shows the evolution of the mass accretion rate onto the primary protostar. Figure 6.10 shows the mass evolution of all the protostars produced in the simulation. In both figures, the green and blue lines show the quantities for the filamentary and spherical clouds, respectively.

The accretion rates rapidly oscillate with time, in both the filamentary and the spherical clouds. Such rapid fluctuations of the accretion rate have been often observed for the mass accretion through self-gravitating circumstellar disks, which is known as "episodic accretion" (e.g. Vorobyov *et al.*, 2013). For example, we can observe that the accretion rate suddenly increases up to ~ 1–$10\ M_\odot\ \mathrm{yr}^{-1}$ at $t \sim 27$ kyr in the filamentary cloud. At this epoch, the primary protostar experiences the three-body interaction with other protostars. Then, the primary protostar encounters with another protostar at the separation of $\lesssim$ 100 AU. This close encounter excites the strong density wake in the circumstellar disk and causes a large amount of the gas to fall onto the primary protostar.

In the spherical cloud, stars grow in mass at an almost constant rate with $0.1 - 1\ M_\odot\ \mathrm{yr}^{-1}$ until the end of our calculation. It is much higher than the critical accretion rate, $\dot{M}_{\mathrm{crit}} = 0.04\ M_\odot\ \mathrm{yr}^{-1}$, which keeps the stellar envelope expanded to the radius with several $\times 10$–100 AU. It makes the ionizing photon emissivity much smaller than the number of atomic hydrogen falling onto the protostars per unit time (Sakurai *et al.*, 2015), and the protostars cannot photo-ionize the surrounding gas.

However, in the filamentary cloud, $\dot{M}_*$ decreases occasionally below $\dot{M}_{\mathrm{crit}}$. Figure 6.9(c) represents the evolution of the disk mass, where the disk mass is as the total gas mass with $n > 10^9\ \mathrm{cm}^{-3}$. At $t \sim 10$ kyr, a new protostar forms and the disk mass and $\dot{M}_*$ suddenly decreases since the newly formed protostar accretes the disk mass. The primary protostar contracts into the ZAMS due to the slow accretion, which increases the stellar emissivity. Nevertheless, the ionizing radiation does not prevent the accretion flow, since the accreting mass is strongly bound by the central star. By $t \sim 25$ kyr, the gas is supplied from the envelope and accumulates around the protostar again. Then, the star returns back to the supergiant phase again. We will discuss the efficiency of the ionizing radiation later in Section 6.4

Figure 6.9(d) shows the number of the protostars in the simulation. The disks around the protostars become more stable with time. In fact, the total stellar mass grows at a faster rate than the disk mass, and that the Toomre-Q becomes larger with increasing time (see eq. 6.9). The number of protostars hardly changes after $t \sim 40$ and 20 kyr for the filamentary and the spherical clouds, respectively. In the filamentary cloud, fragmentation still occurs at later time than in the spherical cloud, because the fragmentation also occurs at the filament far from the disk (see Figures 6.7-Id, Ie, and 6.8). Note that the filament fragmentation itself is not stabilized by the growth of the protostars. For example, filament fragmentations take place at $t \sim 8$ and 30 kyr, which increase the number of protostars around these epochs.

6.3.2.3 Mass distribution of the protostars

Figure 6.11(a) presents the mass distributions of the protostars at $t = 100$ kyr for the filamentary (top) and the spherical (bottom) clouds. The purple histograms show the mass distribution in the simulations. Since the resolution of our simulation is limited, further migration within ~ 100 AU cannot be followed (Section 6.5.4). Since the stellar radius is an order of ~ 100 AU, the friction between the stellar envelopes can cause the stellar merger, and that the stellar mass of each star obtained in the simulation is probably underestimated. In the green histograms, we show the mass distributions assuming the protostar pairs merge once their separation gets smaller than 200 AU. We treat this pair as a single protostar, just summing up the masses of the merged protostar pair. We refer this model as “Model with merger”. In both models, the stellar mass distribution is concentrated around 3000–6000 $M_\odot$ in the filamentary cloud, while around 1–$2 \times 10^4\ M_\odot$ in the spherical cloud.

Figure 6.11(b) summarizes how rapid mass accretion still continues at the epoch of

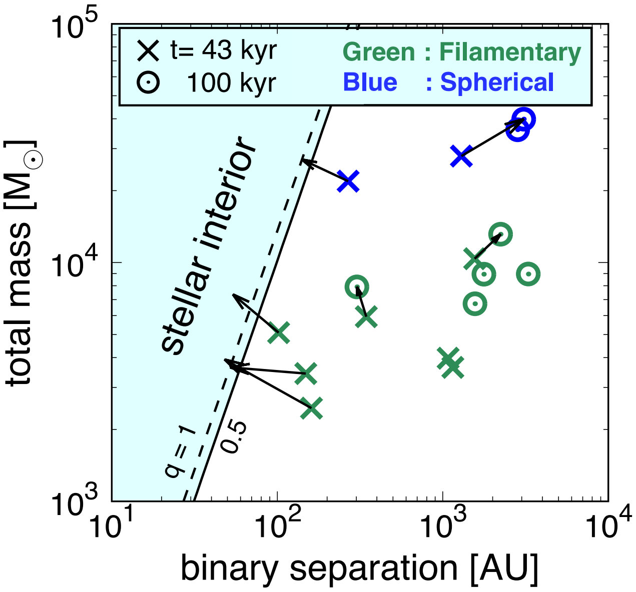

Figure 6.12. Separations and total masses of binaries found in the filamentary (green) and the spherical (blue) clouds. Different symbols represent the different epochs, $t = 43$ (cross) and 100 kyr (circle). The solid and dashed lines show the stellar radii, assuming member stars are in supergiant stage with the mass ration q to be 0.5 and 1, respectively. Once the binary enters the shaded region, it is assumed to coalesce in our simulation. Shaded region represents where the binary separation becomes smaller than the stellar radius. The arrows denote the evolution of the same binaries between two different epochs.

$t = 100$ kyr. The dashed line indicates the critical mass accretion rate below which the protostar contracts into ZAMS phase. For the spherical cloud, all the protostars grow in mass at a rate with $\gtrsim 0.1 \ M_\odot \ \mathrm{yr}^{-1}$. Consequently, the ionizing radiation feedback is inefficient for the entire period of our calculation. For the filamentary cloud, the accretion rate decreases with time and becomes smaller than this critical value for most of the protostars. The ionizing photon emissivity increases to cause the strong radiation feedback. Nevertheless, the ionizing radiation does not prevent mass accretion in our calculation, because the accreting gas is strongly bound by the central star (see in Section 6.4).

6.3.2.4 Merger and ejection of protostars

In our simulations, protostars interact gravitationally with other protostars. The close encounters of protostar pairs result in various events such as binary formation, merger, and ejection of the protostars. Mergers mainly take place within $\lesssim$ 1–2 kyr after the disk fragmentation, since the disk surface density decreases, which makes the disk-star interaction inefficient and the multiple stellar systems stable. Table 6.1 summarizes the number of protostars in the simulation. We also list the numbers of survived and ejected protostars and the number of protostars which belong to any binaries at $t = 100$ kyr. A

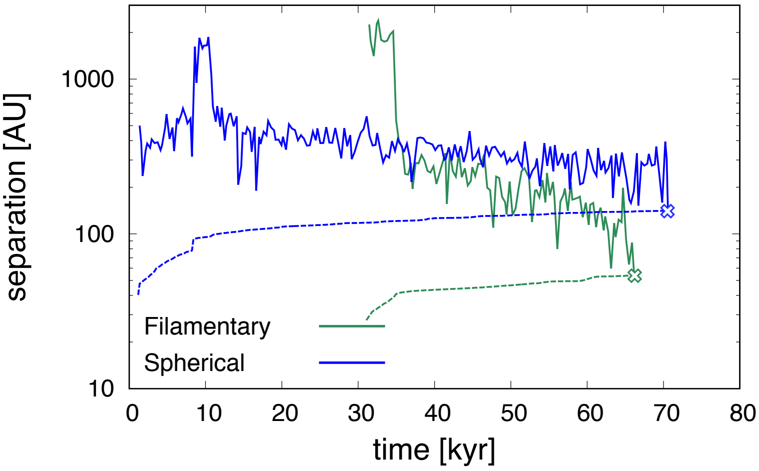

Figure 6.13. Examples of the time evolution of the binary separations. Shown are the merged binaries typical in the filamentary (green) and the spherical (blue) clouds. The solid and dashed lines show the separation and the radii of the binary stars, respectively. The start and end points of each line represent the epochs of formation and merger of the binary, respectively.

($t = 100$ kyr)	total	survived	ejected	binary
Filamentary	25	13	3	7
Spherical	13	5	0	4

Table 6.1. statistical properties of protostars at $t = 100$ kyr. Each column show the number of protostars in total, the number of survived and ejected protostars, and the number of protostars which belong to any binaries at $t = 100$ kyr from left to right.

protostar is assumed to be ejected if its velocity exceeds the escape velocity ($v_{\rm esc}$) of the cloud,

$$v_{\rm esc} = \sqrt{\frac{2GM_{\rm enc}(< R)}{R}}, \tag{6.12}$$

where R is the distance from the center of mass. Once a protostar pair becomes gravitationally bound, we classify this pair as a binary. We judge a pair is gravitationally bound if the total energy ($E_{\rm tot}$)

$$E_{\rm tot} = \frac{m_1 v_1^2}{2} + \frac{m_2 v_2^2}{2} - \frac{Gm_1 m_2}{r}, \tag{6.13}$$

becomes negative, where m_i is the mass of the protostar member, v_i is the relative velocity to the center of mass, and r is the separation of the members ($i = 1, 2$).

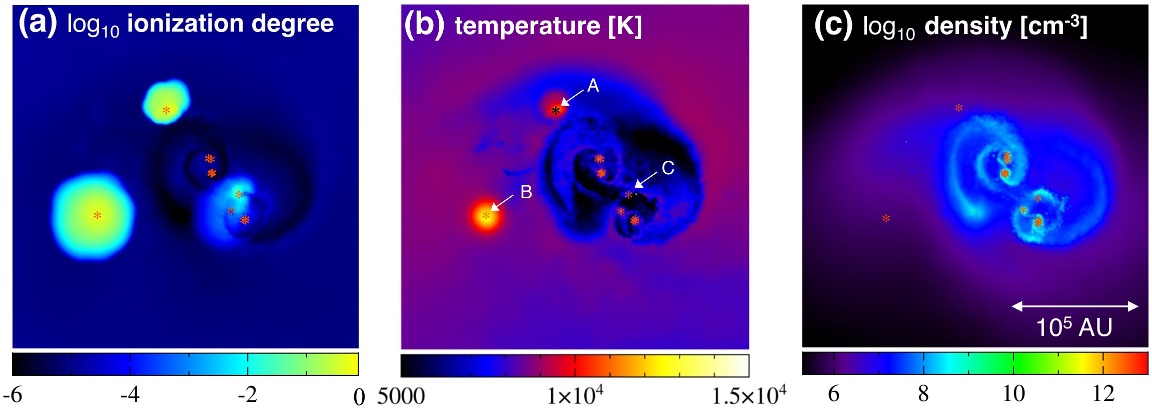

Figure 6.14. Distributions of (a) Ionization degree, (b) temperature, and (c) density distribution in the filamentary cloud at t = 38 kyr. The asterisks stress the position of the protostars. In panel (b), the white arrows indicate three protostars A, B, and C that emitting ionizing photons.

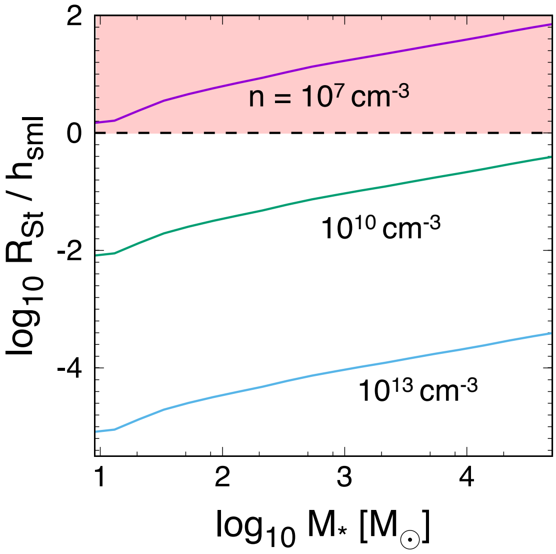

Figure 6.15. The ratios of the Stromgren radius ($R_{\rm St}$) to the smoothing length ($h_{\rm sml}$) of the SPH particles as functions of a stellar mass. The different lines show the ratio at the different densities with $n = 10^7$ (purple), 10^{10} (green), and 10^{13} cm^{-3} (cyan). The dashed line divides the regions where $R_{\rm St}$ becomes larger / smaller than $h_{\rm sml}$. Inside the shaded region, $R_{\rm St}$ becomes greater than $h_{\rm sml}$. When calculating $h_{\rm sml}$ following eq. (6.15), we use particle mass 1.6 $M_\odot$ ($n = 10^7$ cm^{-3}) and 9.6×10^{-3} $M_\odot$ ($n = 10^{10}$ and 10^{13} cm^{-3}) as in the simulation (Section 6.2.3).

Figure 6.12 represents the distributions of separations versus the total mass of binaries at different epochs of $t = 43$ (cross) and 100 kyr (open circle). We show the evolution of the mass and the separation of the binaries by arrows. The solid and dashed lines show the stellar radii with the mass ratio $q \equiv m_2/m_1$ to be 1 and 0.5, respectively ($m_1 > m_2$). Inside the shaded region, the binary separation is smaller than the stellar radius. We confirm the binary usually has $q \gtrsim 0.5$. We also assume both of the member stars are in a supergiant phase (eq. 6.3). At $t = 43$ kyr, some binaries have separations a little larger than the stellar radius. These stars grow in mass and the radius (eq. 6.3) and finally coalesce. At $t = 100$ kyr, the survived binaries have typical separations of a few times $\sim 10^3$ AU, an order of magnitude larger than the stellar radius. These binaries are likely to evolve into the BH binaries after the member stars end their lives. We will discuss the final fate of these binaries in Section 6.5.2.

Figure 6.13 represents the time evolution of the separation evolution of the merged binaries. Here, we show examples both from the filamentary (green) and the spherical (blue) clouds. The solid and dashed lines show the evolution of the binary separation and the stellar radius, respectively. We merge binary members when their separation becomes smaller than the stellar radius of more massive star. The separation decreases suddenly from ~ 1000 to ~ 100 AU because of the three-body interaction with another protostar (i.e. at 35 kyr in the filamentary cloud). The stellar radius gradually increases with time and the binaries finally merge with each other. Other binary mergers take place in a similar fashion.

The survival rate of the protostar in the filamentary cloud is larger than in the spherical cloud. This is due to the filament collapse, in which the separations between protostars are typically larger than those in the disk fragmentation. Furthermore, once the filament fragmentation takes place, the disk mass quickly decreases and the binary separation hardly decreases ($t \sim 10$ kyr in Figure 6.7c). Here, we compare our survival rate of protostars with other studies. The formation and evolution of multiple stellar system in the normal Pop III star formation has been studied by various authors (e.g. Stacy *et al.*, 2016; Greif *et al.*, 2012). They have found that about one third of forming protostars survive at the end of the calculation. In our calculation, the survival rate at $t = 100$ kyr is 52 and 38% in the filamentary and the spherical clouds, respectively. The survival rate in the spherical cloud is similar to their results, while in the filamentary cloud the survival rate is much larger than those found in the previous studies. We note that their calculated clouds and our spherical cloud do not show any filament fragmentation. This implies that the survival rate of the protostars is largely determined by the morphology of the collapsing cloud. Thus, the tidal field originating from the nearby massive galaxy is important to determine the final multiplicity of the stars, which has large impact on the cloud morphology.

Three ejection events are observed in the filamentary cloud. The ejection is caused by the three-body interaction. Meanwhile in the spherical cloud, no protostar ejections are observed. One reason is that the number of protostars are so small that the three-body encounter is unlikely to occur in the filamentary cloud. The other reason is that the gas

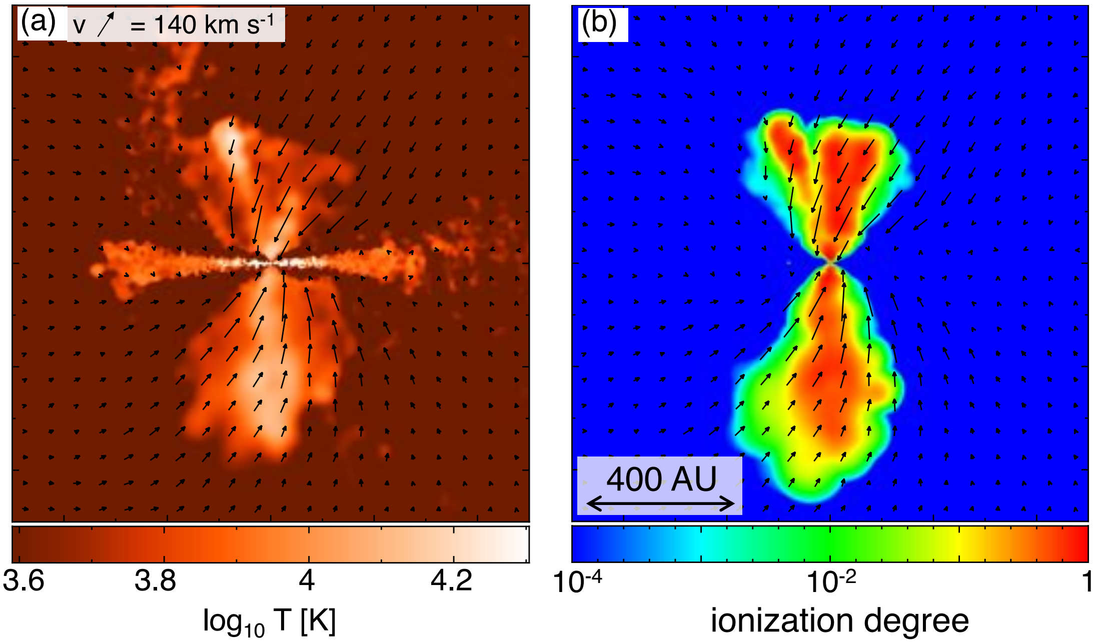

Figure 6.16. Projected temperature (left) and $X_{\rm ion}$ distribution around the protostar 100 yr after the splitting. The arrows show the velocity field of the infalling gas.

rich environment in the spherical cloud suppresses the protostar ejection (Figure 6.9b). When the three-body encounter occurs in the spherical cloud, a large amount of the disk gas is ejected instead of the protostars. Indeed, the total gravitational energy released by the binary formation is comparable in both clouds. The released energy is transferred to the kinetic energy of the surrounding gas in the spherical cloud.

6.4 Radiation Feedback

We calculate the radiative feedback from the accreting protostars using the simplified stellar evolution model (Section 6.2.5). Figure 6.14 shows (a) ionization degree, (b) temperature, and (c) density distributions in the filamentary cloud at $t = 38$ kyr. Ionization degree is defined as $y_{\rm HII}/(y_{\rm HI} + y_{\rm HII})$, where y_i describes the abundance of the chemical species i. Three protostars are emitting ionizing photons at this time, which are labeled as protostars A, B, and C. Protostars A and B are ejected from the central disk by the three-body interaction, creating compact HII regions around them whose size is ~ 0.1 pc. Meanwhile, protostar C remains around the disk center and ionization degree of the surroundings only increases up to 0.01–0.1. Even around protostars A and B, the temperature of the HII region only rises by a factor of $\lesssim 2$ than the surrounding neutral gas (Figure 6.14b). Thus the ionizing radiation has minor impact on the accretion flow.

In this section, we investigate the effect of the radiation feedback in more detail and discuss the importance of the radiation feedback.

6.4.1 Limitation of our radiative transfer model

One may suspect that the radiation feedback is not efficient because our calculation does not have enough numerical resolution: in order to follow properly the expansion of the ionization front, the calculation should resolve the initial Strömgren radius ($R_{\rm St}$), within which ionization and recombination balance. This is required since the expansion of the ionized region is mainly driven by the thermal pressure.

If the density ($\bar{n}$) is spatially uniform around the ionizing source, $R_{\rm St}$ can be written as,

$$\begin{aligned} R_{\rm St} &= \left(\frac{3L_{\rm UV}}{4\pi \bar{n}^2 \alpha_{\rm B} E_{\rm UV}} \right)^{1/3} \\ &= 300\ {\rm AU} \left(\frac{S_{\rm UV}}{10^{53}\ {\rm s}^{-1}} \right)^{1/3} \left(\frac{\bar{n}}{10^{9}\ {\rm cm}^{-3}} \right)^{-2/3}, \end{aligned} \tag{6.14}$$

where $\alpha_{\rm B}$ is the case-B recombination coefficient, $L_{\rm UV}$ is the ionizing luminosity, $E_{\rm UV}$ is the mean energy of the ionizing photons, and $S_{\rm UV}$ is the emissivity of the ionizing photons. To resolve the initial $R_{\rm St}$, the smoothing length of the gas particles ($h_{\rm sml}$) should be sufficiently smaller than $R_{\rm St}$. The smoothing length $h_{\rm sml}$ is determined in the simulation as,

$$N_{\rm neib} m_{\rm sph} = \frac{4\pi h_{\rm sml}^3}{3} \mu m_{\rm p} n, \tag{6.15}$$

where $N_{\rm neib} = 64$ is the number of the neighbor gas particles to determine $h_{\rm sml}$, $m_{\rm sph}$ is the particle mass, μ is the mean molecular weight, and n is the density of the gas particle. Equation (6.15) shows that $h_{\rm sml}$ decreases with decreasing $m_{\rm sph}$. However, since our goal is to follow the long-term evolution, we cannot reduce the particle mass further.

Figure 6.15 shows the ratio of $R_{\rm St}$ to $h_{\rm sml}$ for different stellar masses and ambient densities. We assume the star is contracted to ZAMS and gives the ZAMS luminosity to $S_{\rm UV}$. In the region with $n \gtrsim 10^9\ {\rm cm}^{-3}$, $R_{\rm St}$ is smaller than $h_{\rm sml}$ for $M_* \lesssim 10^4\ M_\odot$. As in Figure 6.14(c), the ejected protostars A and B lie at $n \sim 10^6$–$10^7\ {\rm cm}^{-3}$, while protostar C lies at $n \sim 10^9\ {\rm cm}^{-3}$. This explains why the ionized region expands only around the protostars A and B.

6.4.2 Radiation feedback with higher resolution

To further investigate the ionizing feedback effects, we accurately follow the expansion of the ionized region by adopting a higher spatial resolution. Here, we only focus on the radiation from the most massive protostar. We increase the mass resolution in the polar region, by splitting one gas particle into 10^3 particles. By this procedure, the polar region is filled with a sufficient number of the gas particles, which allows to follow the expansion of the ionization front. We only follow the expansion of the ionized region for a few hundred years after the splitting.

Figure 6.16 shows the temperature (left) and $X_{\rm ion}$ (right) distributions around the protostar. The arrows denote the velocity field of surrounding gas particles. The ionized region expands only in the polar direction. The gas in the polar region is heated up to 2×10^4 K, while the ionized gas continues to fall onto the disk and the ionized region does not expand beyond $R_{\rm St}$. This is because the temperature only increases by a factor of two due to the photo-heating and is still bound by the central star. We can evaluate the gravitational radius ($R_{\rm B}$), below which the gas is gravitationally bound by the central star as,

$$\begin{aligned} R_{\rm B} &= \frac{GM_*}{c_{\rm s,HII}^2} \\ &= 3.25 \times 10^3 \ {\rm AU} \left(\frac{M}{10^3 \ M_\odot} \right) \left(\frac{T}{2 \times 10^4 \ {\rm K}} \right)^{-1} \left(\frac{\mu}{0.6} \right) \end{aligned}$$

The protostar mass is 6000 $M_\odot$ at this epoch, and that $R_{\rm B}$ is much larger than the scale of the ionized region, ~ 400 AU . Thus essentially all the ionized gas is bound by the central star.

We follow the mass accretion with and without the ionizing radiation for a few hundred year. The infall velocity profiles and thus the accretion rates onto the protostar show almost no difference between these two cases, since the ionized gas is strongly bound and not photo-evaporated. This indicates that the photo-heating plays almost negligible role in this situation.

Our analytic estimate also supports the above conclusion. The details are listed at Appendix E. Specifically, we construct the density profiles along the polar direction and estimate whether the ionized region can expand. This model shows that the ionized gas remains gravitationally bound unless the central stellar mass is smaller or comparable to 10^5 $M_\odot$. This conclusion is consistent with the results of our radiation hydrodynamics calculations, where the ionizing radiation has negligible impact on the accretion flow.

6.5 Discussion

6.5.1 Final mass of the SMS and its fate

Although we have followed the evolution of the protostellar accretion for ~ 0.1 Myr, it is still way before the SMSs collapse into BHs. In order to determine how massive seed BHs are finally provided, we should further follow the further evolution for the stellar lifetime, ~ 2 Myr. It is, however, computationally too expensive to accomplish it. We estimate the final stellar and BH masses from the final outputs in our simulations.

Figure 6.17 represents the radial profiles of (a) the enclosed gas mass and (b) the infall velocity at the final epoch of our simulations for the filamentary (green) and the spherical (blue) clouds. Interestingly, the gas is outflowing at $R > 7$–8 pc in both clouds, which is caused by the tidal field due to the nearby massive galaxy. The infalling gas can reach the central star within the stellar lifetime. Panel (a) indicates the infalling gas mass is $\lesssim 3 \times 10^5$ $M_\odot$ for both clouds.

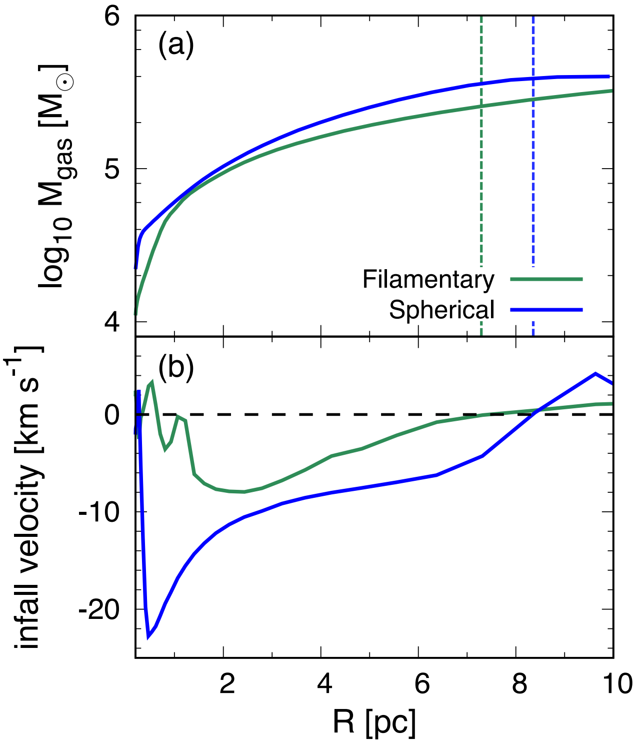

Figure 6.17. Radial profiles of (a) enclosed mass and (b) gas infall velocity at 0.1 Myr after the primary protostar formation for the filamentary (green) and the spherical (blue) clouds. The horizontal axis shows the distance (R) from the primary protostars In the panel (a), the dashed lines indicate the outer boundaries of the clouds, above which the gas is outflowing. In the panel (b), the dashed line shows the boundary between the inflow and outflow. Note that a positive velocity corresponds to the outflow in this plot.

Assuming that no further protostars appear via the disk fragmentation, and that the infalling gas equally accrete onto the existing protostars, we can evaluate the typical masses of final stars: $\sim 10^4\ M_\odot$ for the filamentary cloud and $\sim 10^5\ M_\odot$ for the spherical cloud. These stars are massive enough to collapse into BHs after exhaustion of nuclear fuel (e.g. Umeda *et al.*, 2016; Woods *et al.*, 2017). During the gravitational collapse, the most of the stellar mass is swallowed up by the BH (e.g. Shibata *et al.*, 2016; Uchida *et al.*, 2017). Therefore, we expect that the filamentary cloud yields around ten BHs with $\sim 10^4\ M_\odot$ and the spherical cloud yields several BHs with $\sim 10^5\ M_\odot$. Hereafter, we will call these BHs as "DCBHs".

6.5.2 Evolution of the DCBH binaries

We find that stellar binaries are formed in the cloud core. Some of them survive until at the end of the simulation, avoiding the merger with the companion. After the stellar lifetime, they evolve into the massive BH binaries with the mass of 10^3–$10^5\ M_\odot$ and with the separation of $10^2 - 10^3$ AU (see Figure 6.12). One main process for binaries to lose angular momentum and to merge is the GW emission. The coalescence time-scale is given by (Peters, 1964);

$$t_{\rm GW,merge} = 1.25 \times 10^{11}\ {\rm yr} \left(\frac{a}{100\ {\rm AU}}\right)^4 \left(\frac{M_{\rm BH}}{10^5\ M_\odot}\right)^{-3}, \tag{6.16}$$

which is about an order of magnitude larger than the Hubble time, even for the tightest binaries formed in our simulation. Thus, some additional processes are necessary to remove the angular momentum, i.e., the interaction with the surrounding gaseous and stellar components for a BH-BH merger.

If the gas or stars are accreted onto a binary, a fraction of the accreted material is scattered and carries away the angular momentum from the binary. Kashiyama & Inayoshi (2016) estimates the number of stars falling onto the central DCBH, assuming the possible stellar cluster formation. In our simulations, clusters with an order of between several to ten stars appear in the cloud. According to Kashiyama & Inayoshi (2016), the relaxation time of these cluster ($t_{\rm relax,cluster}$) is,

$$t_{\rm relax} \sim 1.6 \times 10^5\ {\rm yr} \frac{M_{\rm BH}}{10^5\ M_\odot} \frac{10^3\ M_\odot}{\langle M_* \rangle} \left(\frac{r}{\rm pc}\right)^{-3/2}, \tag{6.17}$$

where $M_{\rm BH}$ is the central BH mass, $\langle M_* \rangle$ is the mean mass of formed stars, ρ_* is the density of the stars, r is the size of the star cluster. Cluster member stars are scattered into the loss cone orbit with the time-scale of $t_{\rm relax}$ and fall onto the central DCBH. If the central object is a BH binary instead, part of the accreted stars will be ejected and carry away the angular momentum of the binary. If we assume that the accreted stars are ejected at the speed of the escape velocity $v_{\rm esc} = \sqrt{GM_{\rm BH}/a}$, then the time-scale of the angular momentum loss $t_{\rm star,merge}$ is,

$$\begin{aligned} t_{\rm star,merge} &\sim \frac{J}{\langle M_* \rangle v_{\rm esc} a / t_{\rm relax}} \sim \frac{M_{\rm BH}}{\langle M_* \rangle} t_{\rm relax} \\ &\sim 1.6 \times 10^7\ {\rm yr} \left(\frac{10^3\ M_\odot}{\langle M_* \rangle}\right)^2 \left(\frac{M_{\rm BH}}{10^5\ M_\odot}\right)^2 \left(\frac{100\ {\rm AU}}{a}\right). \end{aligned} \tag{6.18}$$

Thus, the binary can lose the angular momentum by the interaction with the star cluster formed in the same cloud.

After the formation of the DCBH, the host cloud will merge with the nearby massive galaxy, which has been a source of a huge number of LW photons. The stellar masses of the source galaxies are 10^6 (filamentary) and $10^7\ M_\odot$ (spherical cloud). The cold gas mass within the source galaxy is an order of magnitude larger than the stellar mass. These stellar and cold gas components interact with the DCBH binaries, which can carry away the angular momentum. If the binary separations become as small as ~ 10 AU, the binary will merge owing to the GW emission within the Hubble time (eq. 6.16).

The amplitudes of GW peaks at the frequency of 1–10 mHz at the rest frame. Thus the ground based GW detectors are difficult to detect GWs originating from the merging BH binaries. The space GW detectors such as Laser Interferometer Space Antenna (LISA) or

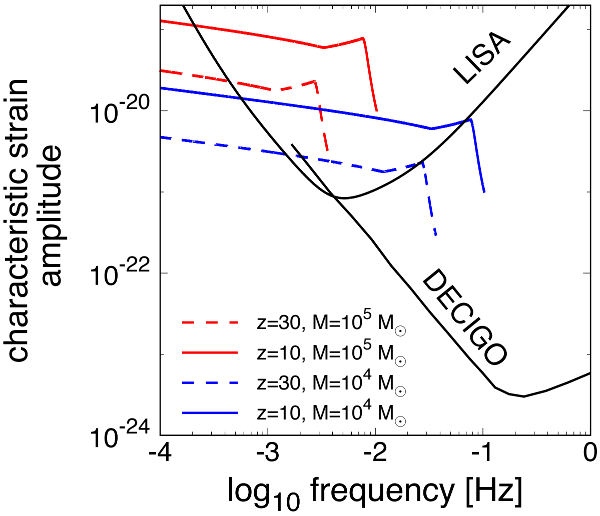

Figure 6.18. Characteristic strain amplitudes for merging BH binaries and a noise amplitude of the future space GW detectors. We consider equal mass binaries, with member masses of 10^4 (blue) and 10^5 $M_\odot$ (red). The solid and dashed lines show the binaries at $z = 10$ and 30, respectively. The black solid lines indicate the noise amplitudes of LISA (Danzmann et al., 2016 and fitting by Cornish & Robson, 2017) and DECIGO (Kawamura *et al.*, 2011).

Deci-hertz Interferometer Gravitational wave Observatory (DECIGO) can observe these GWs.

We construct wave forms of the GWs from the merging BH binaries based on Ajith *et al.* (2011). Wave forms in the Fourier domain at a given frequency f can be written as $h(f) \equiv A(f)e^{-i\Psi(f)}$, where $A(f)$ is the amplitude and $\Psi(f)$ is the phase of the GW. The amplitude $A(f)$ can be written as follows,

$$A(f) = \frac{(GM)^{5/6} f_1^{-7/6}}{d_{\rm L} c^{3/2} \pi^{2/3}} \sqrt{\frac{5\eta}{24}} \begin{cases} f'^{-7/6} P_1 & f < f_1, \\ w_{\rm m} f'^{-2/3} P_2 & f_1 < f < f_2, \\ \frac{w_{\rm r} \sigma^4 f^2}{[\sigma^2 + 4(f - f_2)]^2} & f_2 < f < f_3, \end{cases} \tag{6.19}$$

where $M \equiv M_1 + M_2$, $\eta \equiv M_1 M_2 / M^2$, d_L is the luminosity distance, f_i $(i = 1, 2, 3)$ and σ are the frequencies which characterize in-spiral, merger, and ring-down phases, $f' \equiv f/f_1$, P_i $(i = 1, 2)$ are the correction factor coming from the Post-Newtonian correction, and w_m and w_r are the normalization factors in order to make $A(f)$ continuous across the frequencies f_1 and f_2. The detectability of the GW is often estimated by the so-called "characteristic strain amplitude" $h_c(f)$, which is defined as,

$$h_c(f) = 2f|h(f)| = 2fA(f). \tag{6.20}$$

Figure 6.18 shows the characteristic strain amplitude $h_{\rm c}$ for merging binaries at $z = 10$ (solid) and 30 (dashed). We assume equal mass binaries, where the masses of each member are 10^4 (blue) and 10^5 $M_\odot$ (red). Black solid lines show the noise amplitudes of LISA (Cornish & Robson, 2017) and DECIGO (Kawamura *et al.*, 2011). Combining the both

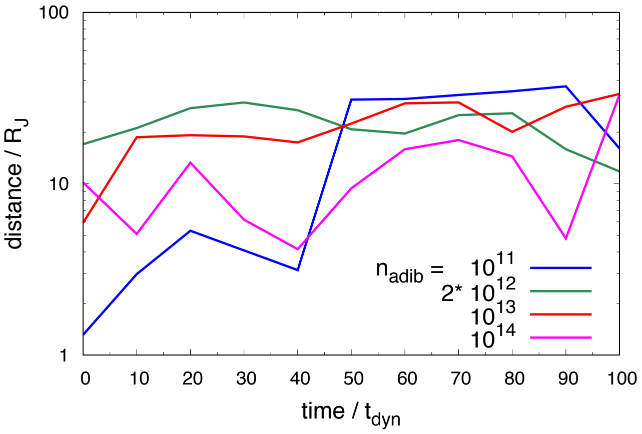

Figure 6.19. Time evolution of the separations between the most massive protostar and the closest protostar with different $n_{\rm adib}$, above which the gas particle evolves adiabatically. The separation and the time is normalized by the Jeans length with the fixed temperature $T_{\rm gas} = 8000$ K and free-fall time at $n_{\rm adib}$. The time origin is set to be the moment at which the first fragment appears in the disk.

detectors, binaries with 10^4–10^5 $M_\odot$ can be observed at $z \gtrsim 10$. If the seed BHs of the observed SMBHs are mainly provided by the DC model, we expect a large amount of BH binaries with 10^4–10^5 $M_\odot$ and GW signals of merging BH binaries. Still the exact number density of BHs provided by DC model is under debate, the detection of BH binaries in this mass range can place important constraints on the formation scenario of SMBHs.

6.5.3 The impact of FUV radiation inside the circumstellar disk

Since we do not consider the shielding against the external LW radiation, we may overestimate the photo-dissociation rate of H_2. To see whether the shielding effect modifies H_2 abundance in the disk, we perform following test simulations. We completely turn off LW radiation once the gas density exceeds $n_{\rm crit} = 10^6$ cm^{-3}, where the gas becomes optically-thick to the external LW radiation (Draine & Bertoldi, 1996). We have followed the evolution in the early accretion phase for 2000 years.

We find that almost no differences between the simulation with and without the shielding effect. In the simulation with shielding, H_2 is completely destroyed with the typical abundances of $\sim 10^{-8}$. The atomic hydrogen cooling dominates in this simulation. Thus we conclude that the external LW radiation is not important for the disk structure at the accretion stage and we can safely ignore the self-shielding of the LW radiation.

Actually, H_2 is mainly destroyed by the collisional dissociation, not by the LW radiation. (Inayoshi & Omukai, 2012) indicate that it occurs in the region with $n > 10^4$ cm^{-3} and $T > 5000$ K. In our calculation, most of the disk gas satisfies this condition and the collisional dissociation dominates the H_2 dissociation.

6.5.4 limitations in numerical method

In our study, the spatial resolution is limited by the adiabatic threshold density $n_{\rm adib}$, above which the gas evolves adiabatically with $\gamma = 5/3$. In reality, the threshold density is determined by the cooling process to 10^{16} cm^{-3} (Omukai, 2001). The reason why we adopt $n_{\rm adib} = 10^{13}$ cm^{-3} is to reduce the computational cost and to follow the long-term evolution. To see how different $n_{\rm adib}$ affects our results, we run test simulations with changing $n_{\rm adib}$ for the filamentary cloud.

We focus on the evolution of the separation ($R_{\rm sep}$) between the primary protostar and the closest protostar. Figure 6.19 shows the time evolution of $R_{\rm sep}$ for $n_{\rm adib} = 10^{11}$ (blue), 2×10^{12} (green), 10^{13} (red), and 10^{14} cm^{-3} (magenta). The time origin is set to be the moment at which the second protostar is formed. In the plot, we normalize the time by the dynamical time $t_{\rm dyn}$ and $R_{\rm sep}$ by the Jean's length $R_{\rm J}$ assuming a fixed temperature of 8000 K, as follows,

$$t_{\rm dyn} = 27\ {\rm yr} \left(\frac{n_{\rm adib}}{10^{13}\ {\rm cm^{-3}}} \right)^{-1/2}, \tag{6.21}$$

$$R_{\rm J} = 44\ {\rm AU} \left(\frac{n_{\rm adib}}{10^{13}\ {\rm cm^{-3}}} \right)^{-1/2} \left(\frac{T}{8000\ {\rm K}} \right)^{1/2}. \tag{6.22}$$

In all the test runs, the disk violently fragment into many pieces at the beginning ($t \lesssim 50 t_{\rm dyn}$). Some stars migrate toward the central star, whereas others survive and remain in the stable orbit for more than $50 t_{\rm dyn}$. Figure 6.19 shows that the separation converges to $\sim 10 R_{\rm J}$ from the central star for all the cases around $50 t_{\rm dyn}$. This implies that the tighter binary would be resolved if we use large $n_{\rm adib}$, by which the Jean's length becomes smaller (Machida & Doi, 2013b).

Recall that the radius of a rapidly mass accreting star with $10^3\ M_\odot$ is ~ 40 AU (see eq. 6.3) and tight binaries with the separation smaller than this stellar radius are assumed to be merged. The Jean's length with the adopted threshold density $n_{\rm adib} = 10^{13}$ cm^{-3} is ~ 40 AU and comparable to the radius of the bloating star. Tighter binaries will appear with the increasing threshold densities, while they are likely to be merged away if the member star is in a supergiant phase. Therefore, we conclude that our choice of the lower threshold density will have only limited effects on our results. It should be confirmed by future simulations with substantially higher spatial resolutions.

6.6 Chapter Summary

We have followed a long-term (~ 0.1 Myr) evolution in the later accretion stage of the SMS formation realized in the DC model by performing 3D radiation-hydrodynamic simulations. We here study the evolution of two clouds found in Chapter 4, where the gas density reaches 10^8 cm^{-3}. To follow further evolution, we include the ionizing radiation feedback from the protostars, where protostars are represented by sink particles. The protostar model is taken from Hosokawa *et al.* (2013).

What we find in this chapter is that the tidal force is also important at the later accretion phase, as in the galactic scale (Chapter 4). In our calculation, one cloud is distorted by the tidal force originating from the nearby massive galaxy. It collapses with a filamentary structure and the fragmentation of this filament yields ~ 10 protostars in the cloud. The massive star cluster with the mass of $10^4~M_{\odot}$ will be formed in this cloud at the end of the stellar lifetime. The other cloud collapses almost spherically until the primary protostar is formed at the cloud center. Only 4–5 protostars are formed due to the disk fragmentation. The final mass of protostars at 0.1 Myr are $\sim$ a few $\times~10^4~M_{\odot}$. Still, they accretes surrounding gas at a rate of $0.1~M_{\odot}~\mathrm{yr}^{-1}$. They are likely to evolve into the SMS with $10^5~M_{\odot}$ at the end of the stellar lifetime.

Throughout the simulation, the radiation feedback has only played a minor role. There are two reasons for this. One is that, the accretion rates onto the protostars are as high as $0.1~M_{\odot}~\mathrm{yr}^{-1}$ even the clouds fragment into multiple protostars and accretion rates onto each stars decrease. In such cases, the stars have no chance to shrink into the main-sequence and are at the supergiant phase, where the ionizing photon emissivity is too small to ionize the surrounding gas. In the filamentary cloud, some protostars contract into main-sequence phase when the number of protostars increase and the accretion rates onto some stars decrease. A large number of ionizing photons are emitted from these protostars. Even under such a case, the ionized region is gravitationally bound by the protostars and thus the ionizing photons do not prevent further mass accretion. Our analysis shows that the ionized region does not break out until the protostellar mass grows into $10^5~M_{\odot}$.

The SMS cluster is expected in the filamentary cloud and the member stars in this cluster finally collapse into BHs. Half the member belong to the binary with other BHs. These binaries will coalesce and emit a huge amount of GWs, which can be detected by the future space observatories, LISA and DECIGO. Our results suggest that a large number of BH binaries with 10^4–$10^5~M_{\odot}$ exist in the early universe. Therefore, detections of GWs emitted from BH binaries in the above mass range provide us a valuable opportunity to know the formation scenario of SMBHs.

Chapter 7

Conclusion

7.1 Summary

In this thesis, we have studied the feasibility of the DC model, especially the possibility of the SMS formation in the early universe, which can provide seed BHs with $10^5\ M_\odot$ for the observed SMBHs at $z \gtrsim 6$ (e.g. Mortlock *et al.*, 2011). To test the validity of this model, we carry out a set of cosmological simulations, which directly follow the formation and the evolution of the SMSs. The formation sites of SMSs are thought to be very rare, in a sense that the massive and luminous galaxies are located in the close vicinity. The collapsing clouds suffer the strong tidal force, which prevents the further cloud collapse in most of the cases. Our simulations have revealed that even in such an extreme environment, the SMSs with 10^4–$10^5\ M_\odot$ can actually form avoiding the disrupting effects of the tidal force. We stress that our studies are the first attempt to follow the SMS formation incorporating environmental effects such as tidal force of nearby luminous galaxies. Our conclusions are summarized as follows.

Importance of the Environmental Effects

Our cosmological simulations have revealed that the surrounding environment is important for the SMS formation, which is overlooked in previous studies. One of the most important effects is the tidal force from the nearby source galaxy. Indeed, the tidal force has great impact on the cloud evolutions at various scales, from the galaxy scales (1–10 kpc) to the cloud scales (~ 10–10^3 AU).

In the galaxy scale, the tidal force directly prevents the contraction of the cloud, and the cloud finally merges with the source galaxy without any star-formation in most of the cases (Chapter 4). Our analytical estimation also supports this result: the tidal force is strong enough to prevent the cloud collapse since the halo should be located close enough to the source galaxies to be irradiated by the strong dissociating radiation. Even under such a strong tidal force, we have found two “successful” cases. These cases are exceptional examples, in a sense that they experience the major mergers of the host halos just before the onset of the collapse. These mergers assemble a large amount of the gas around the cloud center, and that accelerate the cloud collapse.

In the cloud scale, the collapsing clouds still suffer the tidal force (Chapter 6). We further follow the hydrodynamical evolutions for two "collapsed" samples and find that the tidal force greatly affects the final masses of the forming stars in the cloud. If the cloud feels strong tidal force, the cloud is elongated filamentary during the collapse. In such a cloud, much larger number of the stars is formed due to the filament fragmentation in addition to the usual disk fragmentation. Consequently, the strong tidal force reduces the typical stellar mass by an order of magnitude. One might think that the tidal force cannot play significant roles at this scale, since the tidal radius is much larger than the cloud scale. Meanwhile, the tidal field only seeds the perturbation at the tidal scale. This perturbation grows during the isothermal collapse, as found in Hanawa & Matsumoto (2000).

Ionizing Radiation Feedback is Inefficient during the Accretion Phase

In order to follow the ionizing radiation both from the galaxies and from the protostars, we implement ray-tracing scheme developed by Susa (2006) into `Gadget-2` (Chapter 5). Our results show that the ionizing feedback effect on the protostar evolution is almost negligible for the following two reasons. One reason is that the ionizing photon emissivity is very small under the typical situation for DC model. For the atomic-cooling clouds, the mass accretion rate is typically so high as ~ 0.1–$1\ M_{\odot}\ \mathrm{yr}^{-1}$, which makes the stellar envelope inflated and reduces the emissivity. The other reason is that the protostars are massive enough to bind the ionized gas. Actually in our simulations, some protostars contract into ZAMS phase and the ionizing photon emissivity increases. Nonetheless, the ionizing radiation have no impact on the accretion flow, since the ionized gas is strongly bound by the central protostars. Our analytic model suggests that the ionizing radiation feedback is inefficient when the protostellar mass is smaller than $\sim 10^5\ M_{\odot}$.

Observational Signature of Supermassive Star Formation

Our results suggest that many binary BHs will appear if the DC model provides a dominant fraction of the seed BHs for the observed high-z SMBHs. If these binaries coalesce within the Hubble time-scale, we can observe the GW signals by the future GW detectors in the space, such as Laser Interferometer Space Antenna (LISA) and DECi-hertz Interferometer Gravitational wave Observatory (DECIGO).

7.2 Future Prospects

In order to understand the formation scenario of the observed high-z SMBHs, we should further follow the mass growth of the seed BHs. Here, we briefly discuss what we can learn the further evolutions of the seed intermediate-mass BHs ($\sim 10^4$–$10^5\ M_{\odot}$) from our

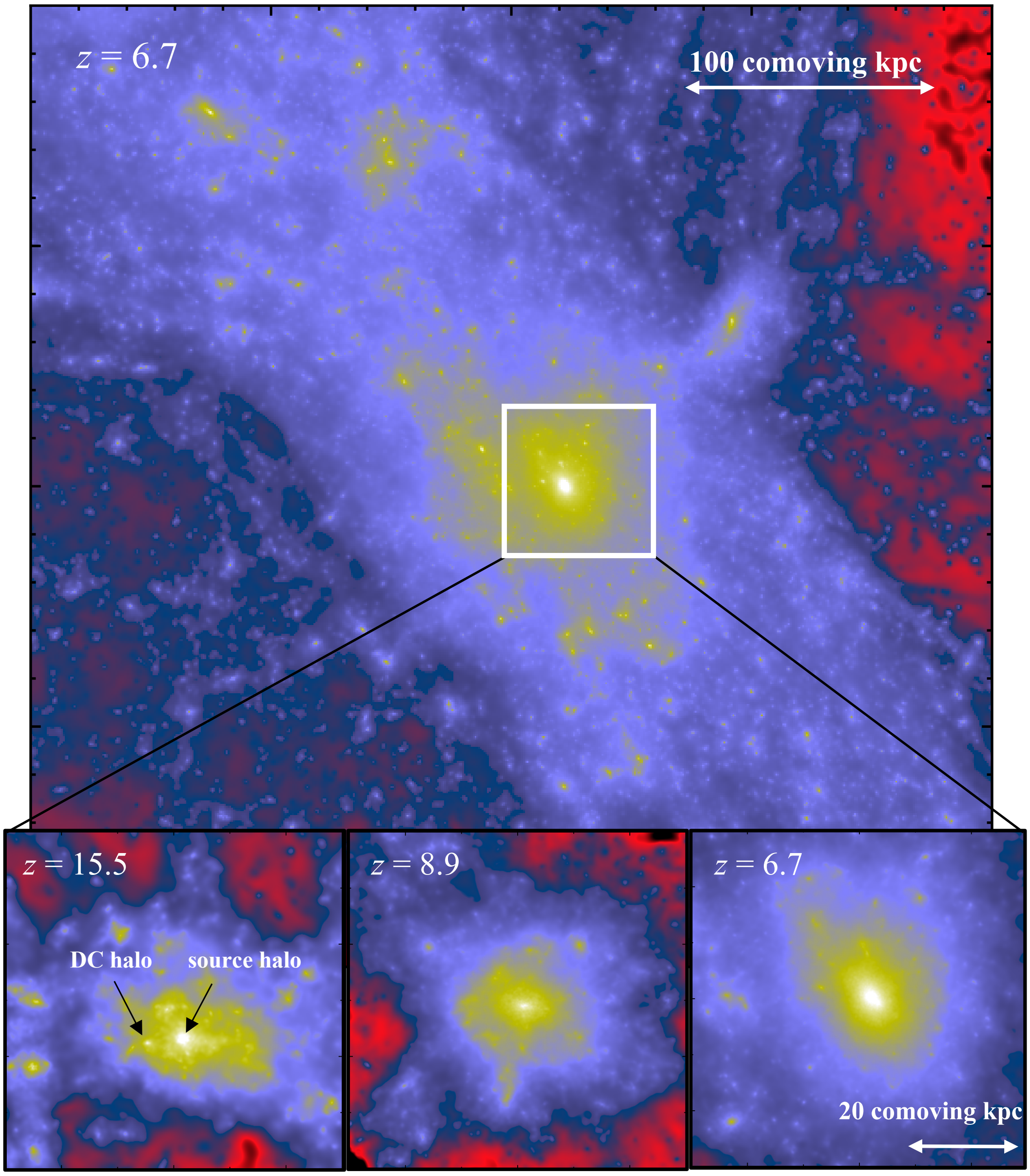

Figure 7.1. DM density distribution around the DC halo (the filamentary cloud in Chapter 6) after the formation of SMSs and the remnant DCBHs. The bottom three panels represent the time evolution of the density structure around the DC halo. The DC halo sinks toward the center of the massive galaxy at $z = 8.9$.

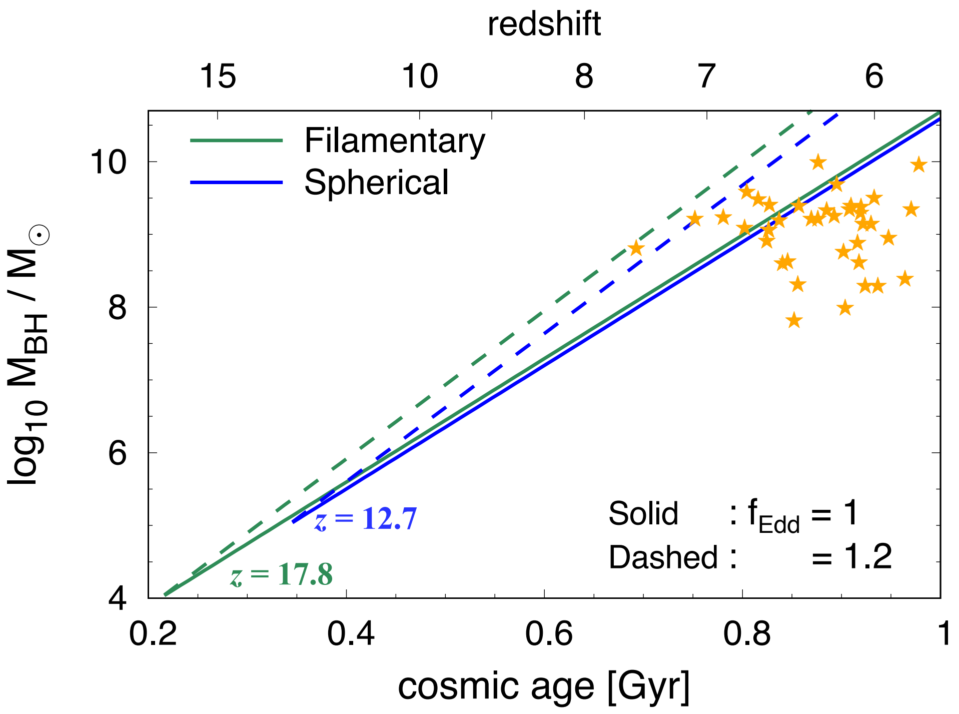

Figure 7.2. The mass evolutions of the BHs, starting from the remnant DCBHs of SMSs found in our simulations (Chapter 6). The blue and green lines show the mass evolutions for the seed BHs formed in the spherical and the filamentary clouds. The solid and dashed lines assume the accretion with $f_{\rm Edd} = 1$ and 1.2, respectively. Stellar symbols represent the mass and the redshift of the SMBHs at $z \gtrsim 5.5$. SMBH samples are taken from the results of NIR spectroscopies, listed at Table 2.1.

snapshots of the N-body simulation. The top panel in Figure 7.1 shows the DM density around the host halo (DC halo) of the seed BHs formed in the filamentary cloud at $z = 6.7$. The bottom three panels show the zoom-in view of the density around the DC halo at different three epochs ($z = 15.5$, 8.9, and 6.7 from right to left). We can see that the DC halo is located just close to the source galaxy center at $z = 15.5$ while it sinks toward the galaxy center and completely merges with the source galaxy at $z = 8.9$.

Since the host halo is massive, there should be a plenty of the gas that will accrete onto the BH. Figure 7.2 shows the mass evolutions of the DCBHs that accreting mass at Eddington (solid) and 1.2 times Eddington rates (dashed). If the mass accretion continues at the Eddington accretion rate, we can attain the BH mass of 10^8–10^{10} $M_\odot$ at $z \gtrsim 6$. There is another important process to uncover: the observational signature of the SMBHs. To directly link the mass distribution of SMBHs to the number density of the observed QSOs, we should know the observability of the evolving or evolved BHs. If the SMBHs are surrounded by the dense gas in the early universe, the observed number density will be greatly reduced. Indeed, our simulations yield much larger number density of seed BHs ($\sim 10^5$ Gpc^{-3}) than that of the observed SMBHs (~ 1 Gpc^{-3}), although our estimated number density is an order of magnitude smaller than the previous studies. It will be interesting to know that to what extent the BH activities and their observability can explain the above discrepancy of the number density.

Many future observations are believed to provide us valuable information about the high-z QSOs. In order to fully exploit these upcoming observations, we should arrange a theoretical background about the BH formation and evolution.

Acknowledgments

It is my great pleasure to express my gratitude to my supervisor Naoki Yoshida, who gives continuous encouragements and fruitful advices to me. He first invited me to the field of the numerical cosmology, and finally leads me to the exciting field of the galaxy and star formation in the early universe, both of which construct the basis of my work. I would like to thank Takashi Hosokawa, who is the specialist of the star formation and gives me a lot of comments and advices. He patiently support not only my work, but also my research life, which greatly stimulate all my works. Also, I want to give special thanks to Ayuki Kamada, Masato Shirasaki, Shingo Hirano, and Gen Chiaki, who used to be member of Yoshida group. They kindly told me how to use the basic tools for my research and spend precious time to the very basic and fundamental discussion.

I also express my gratitude to Prof. Yasushi Suto, who is main referee of this thesis. It was great experience to have the weekly seminars with him. His instructive comments and discussions during seminar gives a way to study the astrophysics. I also give great thanks to all the members of Theoretical Astrophysical Group (UTAP) and Research Center of Early Universe (RESCEU). The daily discussion with them covers broad range of the research fields and stimulate my research.

I also wish to express my collaborator Latif Muhammad, who kindly welcome me at Institut Astrophysique de Paris (IAP) and assist my short stay in Paris. I also thank all the participants in the conference, who gives me a lot of fruitful advices and comments, especially to Hajime Susa and Kazu Omukai. I would like to thank all the examiners, Satoshi Yamamoto, Masahiro Takada, Kazuhisa Mitsuda, and Hideyuki Tagoshi for their comments which improve the quality of my work.

Finally, I would like to thank all my family, who continuously support my research life and encourage me to accomplish this thesis.

Appendix A

Basics in Star Formation

Star formation process is largely divided into two stages. One is the "collapse phase" and the other one is the "accretion phase". In the collapse phase, the cloud contracts due to the self-gravity. As the cloud contracts, the gravitational energy is converted into the internal energy of the cloud. To proceed the cloud collapse, the internal energy should be subtracted by "cooling process". Otherwise, the gas pressure of the cloud counteracts the gravitational force and the collapse is finally stalled. Once the cloud density becomes so high and then the cloud itself becomes opaque to the radiation, the cloud evolves adiabatically and the cloud collapse ceases. This optically-thick cloud core is termed as the "protostellar core" or "protostar". The formation of protostellar core marks the end of the collapse phase.

In the accretion phase, the protostellar core acquires the mass from the infalling envelope. Since the accreting gas has a finite angular momentum, they form the gas disk around the protostar. This disk is called "circumstellar disk". The disk mass is comparable to the mass of the protostar. The self-gravity of the disk exerts the gravitational torque and removes the angular momentum of the gas. The mass accretion ceases when all the envelope gas falls onto the star or the disk gas is dissipated by the feedback from the central star.

A.1 Collapse Phase

Here, we review how the cloud collapses and the protostellar core is formed. The governing equations are as follows,

$$\frac{\partial \rho}{\partial t} + \rho \nabla \cdot \boldsymbol{v} = 0, \tag{A.1}$$

$$\rho \frac{\partial \boldsymbol{v}}{\partial t} + \nabla P + \rho \nabla \phi = 0, \tag{A.2}$$

$$\Delta \phi = 4\pi G \rho, \tag{A.3}$$

$$P = c_{\mathrm{s}}^2 \rho, \tag{A.4}$$

where t is the time, ρ is the cloud density, $\boldsymbol{v}$ is the velocity of the fluid element, P is the pressure, ϕ is the gravitational potential, and c_{s} is the sound speed. Equations (A.1), (A.2), (A.3), and (A.4) represent the continuity equation, equation of the motion of the fluid, Poisson equation, and the equation of state, respectively.

A.1.1 Linear analysis

First, we will derive the fundamental quantity in this system, so-called "Jeans scale". Suppose the isothermal gas cloud which has a uniform profiles and in hydrostatic equilibrium ($\boldsymbol{v} = 0$). We denote the physical quantities in the equilibrium by the subscript 0 (e.g. ρ_0). We perturb this system and denote the perturbed quantities by the subscript 1 (e.g. $\rho = \rho_0 + \rho_1$). Neglecting the second order of the perturbed quantities, we obtain

$$\frac{\partial \rho_1}{\partial t} + \rho_0 \nabla \cdot \boldsymbol{v}_1 = 0, \tag{A.5}$$

$$\frac{\partial \boldsymbol{v}_1}{\partial t} + \frac{c_\mathrm{s}^2}{\rho_0} \nabla \rho_1 + \nabla \phi_1 = 0, \tag{A.6}$$

$$\Delta \phi_1 = 4\pi G \rho_1, \tag{A.7}$$

Taking the divergence in eq. (A.6) yields the following equation,

$$\frac{\partial^2 \rho_1}{\partial t^2} = c_\mathrm{s}^2 \Delta \rho_1 + 4\pi G \rho_0 \rho_1. \tag{A.8}$$

Consider each physical quantity is expanded as the superposition of the plane waves, i.e. $\rho = \tilde{\rho} \exp(i\omega t - i\boldsymbol{k} \cdot \boldsymbol{x})$. Then we obtain the dispersion relation in this system,

$$\omega^2 = c_\mathrm{s}^2 \left(k^2 - \frac{4\pi G \rho_0}{c_\mathrm{s}^2} \right). \tag{A.9}$$

The above equation tells us that if the wave number k is smaller than $k_\mathrm{J} \equiv 4\pi G \rho_0 / c_\mathrm{s}^2$, the perturbation grows or dumps exponentially with time. The growing mode becomes dominant with increasing time, so that this system is unstable to the perturbation. In terms of a wave length λ, the unstable condition can be written as follows,

$$\lambda > \lambda_J \equiv \sqrt{\frac{\pi c_\mathrm{s}^2}{G \rho_0}}. \tag{A.10}$$

This length-scale is called Jeans length. The mass within the Jeans length is called Jeans mass M_J, where

$$\begin{aligned} M_\mathrm{J} &= \frac{4\pi\rho_0}{3} \left(\frac{\lambda_\mathrm{J}}{2} \right)^3 = \frac{\pi^{5/2} c_\mathrm{s}^3}{6 G^{3/2} \rho^{1/2}} \\ &= 3.3 \times 10^2 \ M_\odot \left(\frac{T}{100\ \mathrm{K}} \right)^{3/2} \left(\frac{n}{10^4\ \mathrm{cm}^{-3}} \right)^{-1/2}. \end{aligned} \tag{A.11}$$

These scales are the fundamental scales which appear in the self-gravitating fluid. The above instability is explained by an order of magnitude discussion as follows. Consider the equation of motion of the self-gravitating cloud. The pressure support term $\nabla P / \rho \sim c_\mathrm{s}^2 / R$ and the self-gravity term $GM(R)/R^2 \sim G\rho R$ determines how the cloud collapse, where $M(R) \sim \rho R^3$ is the enclosed gas mass within the radius R. The pressure term gets stronger at the smaller scale while the self-gravity term gets stronger at the larger scale. These two terms balance each other at the Jeans scale R_J.

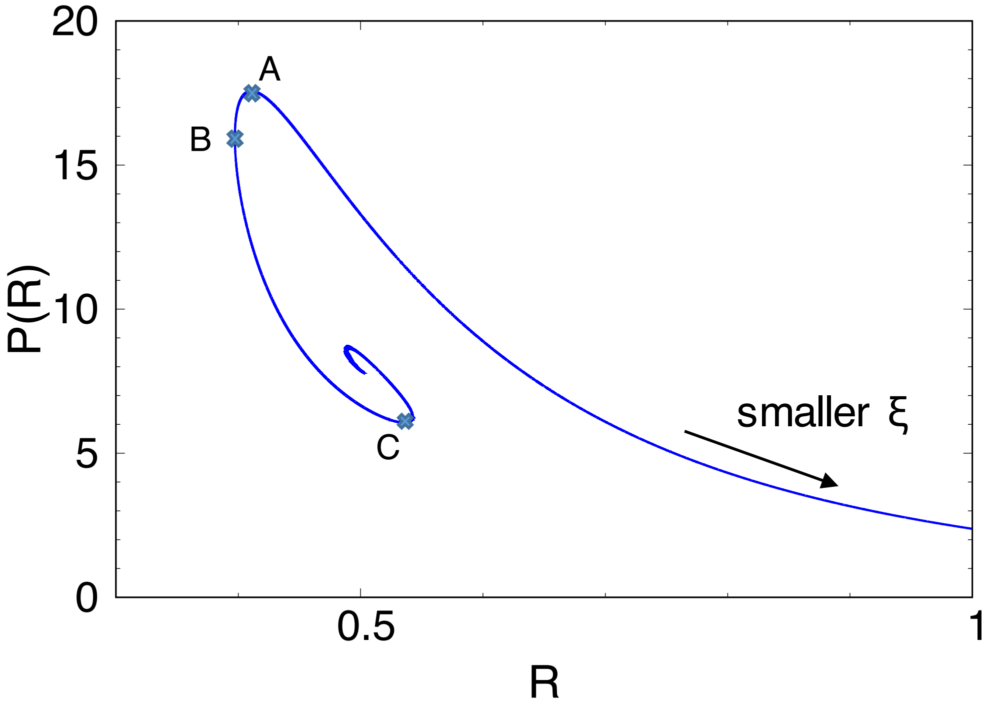

Figure A.1. The pressure P versus the cloud size R for the isothermal hydrostatic cloud.

A.1.2 Onset of the collapse in the isothermal cloud

The linear analysis above assumes the uniform density profile as an unperturbed state. However, it is known that such a system is cannot be in equilibrium (e.g. Jeans swindle, Binney & Tremaine, 2008). To show the above estimation works well, we consider the profiles in a hydrostatic equilibrium for an isothermal cloud. We will finally find the cloud becomes unstable once its mass exceeds M_{J}.

The basic equations are eqs. (A.1) – (A.4) and neglect the term with a time derivative. Eqs. (A.2) and (A.4) give

$$-\frac{\nabla P}{\rho} - \nabla\phi = -\nabla(c_{\mathrm{s}}^2 \ln\rho + \phi) = 0 \qquad \therefore \rho(r) = \rho_{\mathrm{c}} \exp(-\phi/c_{\mathrm{s}}^2), \tag{A.12}$$

where we have assumed the spherical symmetry and $\phi = 0$ and $\rho = \rho_{\mathrm{c}}$ at the center $r = 0$. Defining non-dimensional parameters $\psi \equiv \phi/c_{\mathrm{s}}^2$ and $\xi \equiv \alpha r$, we obtain the Lane-Emden equation for the isothermal sphere,

$$\frac{1}{\xi^2}\frac{\mathrm{d}}{\mathrm{d}\xi}\left[\xi^2 \frac{\mathrm{d}\psi}{\mathrm{d}\xi}\right] = \exp(-\psi), \tag{A.13}$$

where $\alpha = \sqrt{4\pi G\rho_{\mathrm{c}}/c_{\mathrm{s}}^2}$. This equation is second order differential equation and we need two boundary conditions. $\psi = \psi' = 0$ at the center $\xi = 0$, where the prime represents the differential by ξ. The former condition is $\phi = 0$, which we already gave. The latter guarantees the mass does not diverge at the center. Just around the center, enclosed mass $M(r)$ scales as r^3. This condition gives $\psi' \propto r \longrightarrow 0$. We can solve the equation, integrating it from the center.

$M(r)$ can be calculated as follows,

$$M(r) = \int_0^r 4\pi r^2 \rho \mathrm{d}r = \frac{c_\mathrm{s}^3}{(4\pi G^3 \rho_c)^{1/2}} \left[\xi^2 \frac{\mathrm{d}\psi}{\mathrm{d}\xi} \right]. \tag{A.14}$$

When we fix the cloud mass M, we can determine the cloud edge R where $M(R) = M$. Then, R and the pressure at the cloud edge $P(R)$ become,

$$R = \frac{\xi}{\alpha} = \frac{GM}{c_\mathrm{s}^2} \left(\xi \frac{\mathrm{d}\psi}{\mathrm{d}\xi} \right)^{-1}, \tag{A.15}$$

$$P(R) = c_\mathrm{s}^2 \rho = \frac{c_\mathrm{s}^8}{4\pi G^3 M^2} \xi^4 \left(\frac{\mathrm{d}\psi}{\mathrm{d}\xi} \right)^2 \exp(-\psi). \tag{A.16}$$

Figure A.1 shows $P(R)$ as a function of R, which are normalized by the prefactors in the above equations. The large radius corresponds to the small ξ. Starting from $R = \infty$, the cloud pressure increases as the cloud is compressed. At the point A, the pressure reaches the maximum and decreases afterwards. This point A corresponds to $\xi = \xi_\mathrm{c} \equiv 6.45$ and is called the critical state. This state is critical in a sense that when the small external overpressure compress the cloud, the cloud pressure decreases and the collapse is accelerated. That is, $\frac{\mathrm{d}P}{\mathrm{d}R} > 0$. Note that any clouds with $\xi > \xi_\mathrm{c}$ are unstable. Along BC in the P-R diagram, $\frac{\mathrm{d}P}{\mathrm{d}R} < 0$ and the cloud is seems to be stable. However, there is a radius r_c with $\xi = \xi_\mathrm{c}$ at the inner part of the cloud. Then, the part of the cloud inside r_c is unstable. Therefore, only the cloud between $R = \infty$ and point A is stable in the P-R diagram (Bonnor, 1956). The critical mass (M_BE) at point A ($\xi = \xi_\mathrm{c}$) is

$$M_\mathrm{BE} = 1.14 \times \frac{c_\mathrm{s}^4}{\sqrt{PG^3}} = 1.14 \times \frac{c_\mathrm{s}^3}{\rho^{1/2} G^{3/2}}. \tag{A.17}$$

This mass-scale is called "Bonnor Ebert mass" and has the same order as M_J (eq. A.11).

A.1.3 Runaway collapse

Once the cloud becomes gravitationally unstable, the cloud density increases. As the order of magnitude estimation shows, M_J represents the characteristic mass-scale under which the self-gravity and the thermal pressure balance. This is the case not only for the isothermal cloud but in general. Consider the gas with the barotropic equation of state $P \propto \rho^\gamma$, where γ is the adiabatic exponent. Then, the Jeans mass-scales with increasing density as,

$$M_\mathrm{J} \propto T^{3/2} \rho^{-1/2} \propto \rho^{3/2(\gamma - 4/3)}. \tag{A.18}$$

When $\gamma > \gamma_\mathrm{crit} \equiv 4/3$, the Jeans mass increases as the density increases while when $\gamma < \gamma_\mathrm{crit}$ vice versa. Only when $\gamma < \gamma_\mathrm{crit}$ is satisfied, the cloud is unstable to the self-gravity in the spherical system. That is, once the collapse begins, the collapse is never

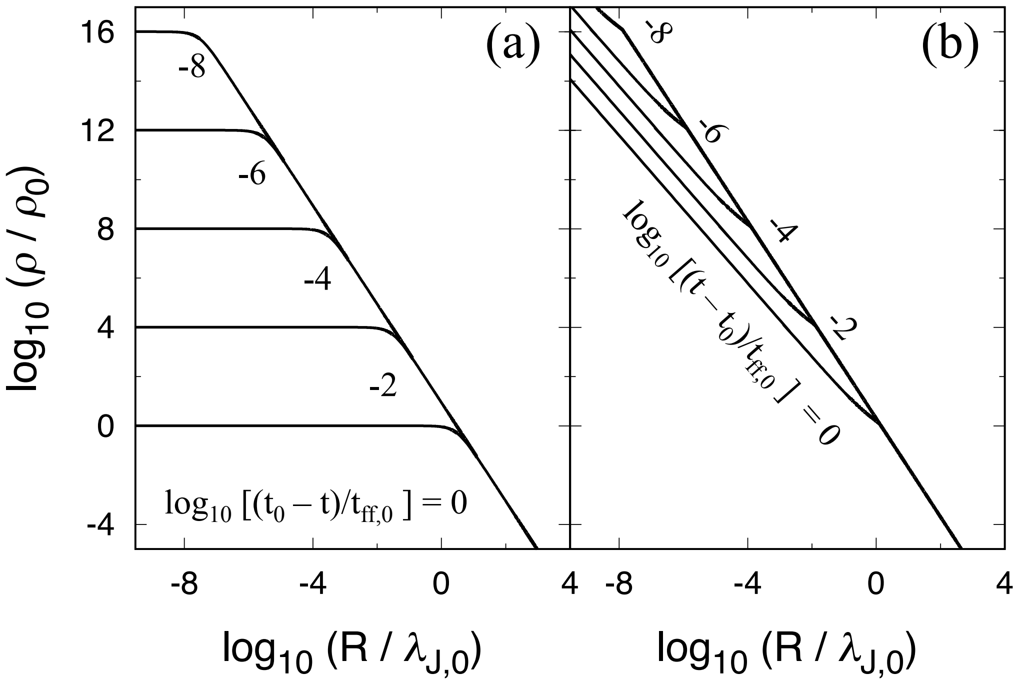

Figure A.2. The radial density profiles for the collapsing cloud. At the time t_0, the central density diverges and the protostar is though to be formed there. We set the density ρ_0 arbitrarily and set the corresponding free-fall time and Jeans length as $t_{\rm ff,0}$ and $\lambda_{\rm J,0}$, respectively. (a) the self-similar profiles obtained by Larson (1969) and Penston (1969) at $t < t_0$, just before the protostar formation. (b) the self-similar profiles obtained by Shu (1977) at $t > t_0$, just after the protostar formation.

hindered by the pressure support, because the self-gravity dominates over the pressure support all the way. The collapse continues until when the adiabatic exponent becomes larger than $\gamma_{\rm crit}$.

Assuming the cloud to be spherically symmetric, we can find the self-similar solution for the collapsing isothermal cloud. Again, we return to set of equations (A.1) – (A.4). When we introduce non-dimensional parameters, x, ξ, η, and m as follows,

$$r(t) = -c_{\rm s}(t - t_0)x \quad , \quad v(r,t) = -c_{\rm s}\xi(x), \tag{A.19}$$

$$\rho(r,t) = \frac{1}{4\pi G(t-t_0)^2}\eta(x) \quad , \quad M(r,t) = \frac{c_{\rm s}^3(t-t_0)}{G}m(x), \tag{A.20}$$

where t_0 denotes the epoch at which the cloud completely collapses and attains the infinite density. Then we can obtain the ordinary differential equations,

$$\frac{\mathrm{d}\xi}{\mathrm{d}x} = \frac{x-\xi}{x}\frac{\eta x(x-\xi)-2}{(x-\xi)^2-1}, \tag{A.21}$$

$$\frac{\mathrm{d}\ln\eta}{\mathrm{d}x} = \frac{x-\xi}{x}\frac{\eta x-2(x-\xi)}{(x-\xi)^2-1}. \tag{A.22}$$

The solutions are self-similar, in a sense that once we know the solution at time t', we can obtain the physical quantities at the arbitrary time t by scaling the quantities at t', e.g. $\rho(r,t) = \rho(r',t')(t'-t_0)^2/(t-t_0)^2$ where $r' = r(t-t_0)/(t'-t_0)$. Larson (1969) and Penston (1969) independently explored the smooth solution of the above set of equations with the boundary conditions which are (1) $\xi = 0$ at the center $x = 0$ and (2) $\eta x = 2$ at $x - \xi = 1$. The latter condition assures ξ and η to be continuous across $x - \xi = 1$.

Figure A.2(a) shows the evolution of the density profile $\rho(r,t)$. The profile is composed of two parts; inner core with a constant density and the envelope with $\rho \propto r^{-2}$. Initial core density is denoted by ρ_0 and the free-fall time and the Jeans length at the core are denoted by $t_{\mathrm{ff},0}$ and $\lambda_{\mathrm{J},0}$, respectively. Initially, the core radius is $\sim \lambda_{\mathrm{J},0}$ initially and supported by the thermal pressure of the gas. As the mass flows from the envelop, the outer part of the core becomes gravitationally unstable and starts to collapse. Therefore, the core density increases with time, while the density of the outer envelope remains constant with time (so-called "runaway collapse"). This is because the free-fall time of the outer envelope is much longer than that of the core. Numerical simulations confirm that the cloud collapses in the above fashion (Hunter, 1977; Foster & Chevalier, 1993; Vorobyov & Basu, 2005; Gong & Ostriker, 2009). The formation of the optically-thick core at the center marks the end of the collapse phase. Thereafter, the cloud enters the accretion phase.

A.2 Accretion Phase

Since the optically-thick core evolves adiabatically, the dynamical collapse is no more expected inside the core (see Section A.1.3). Rather, the core contracts in a quasi-static fashion, that energy loss at the core surface diminishes the internal energy and reduces the core size, which is termed as "Kelvin-Helmholtz (KH) contraction". The time-scale of the contraction is much larger than the dynamical time of the core in general. As a result, the accreting matter accumulates around the core and forms a gas disk, so-called "circumstellar disk".

Shu (1977) explored the evolution of the cloud profiles after the core formation. He solved self-similar equations (A.21) and (A.22), starting from the static isothermal sphere. Figure A.2(b) shows the evolution of the density profiles in the accretion phase. We can see that $\rho(r) \propto r^{-2}$ at the outer envelope, while $\rho(r) \propto r^{-1.5}$ just around the core. Around the core, the material is free-falling. The free-falling region expands outward at a speed of c_{s} ("expansion wave"). Numerical simulations show that the cloud evolution follows this solution in the accretion phase (e.g. Vorobyov & Basu, 2005). The infall mass rate onto the central core becomes $0.98c_{\mathrm{s}}^3/G$, which is independent of the density.

Since the infalling material has a finite angular momentum, the gas condenses around the central protostar. As a result, a gas disk which is supported by the angular momentum barrier is formed. At the early evolutional phase, the disk is massive and the self-gravity of the disk dominates over the gravitational force from the central star. Such a disk is gravitationally unstable and the spiral arms are formed. The Toomre-Q parameter represents the stability of the surrounding disk, which is defined as (Toomre, 1969),

$$Q = \frac{\kappa c_{\rm s}}{\pi G \Sigma}, \tag{A.23}$$

where κ is the epicyclic frequency and Σ is the surface density. If $Q \lesssim 1$, the disk is locally unstable to the self-gravity of the disk (e.g. Bertin *et al.*, 1989). Several studies show that the condition $Q \lesssim 1$ is sufficient for the disk to be globally unstable, and that the spiral arms are formed (e.g. Iye, 1978). These spiral arms transfer the angular momentum outwards and a part of the gas accretes onto the central star (Lynden-Bell & Kalnajs, 1972).

Appendix B

Implementation of Radiation Transfer

We solve the photo-ionization of neutral hydrogen and resulting heating using a ray tracing scheme developed by Susa (2006). In this method, the optical depth of ionizing radiation, $\tau_{\rm UV}$, from a light source to the particle i is evaluated by the sum of the local optical depth. Figure B.1 summarizes this method to evaluate the optical depth. The optical depth for the SPH particle i (τ_i) is evaluated as;

$$\tau_i = \tau_{i-1} + {\rm d}\tau_i = \sum_j {\rm d}\tau_{{\rm UV},j}, \tag{B.1}$$

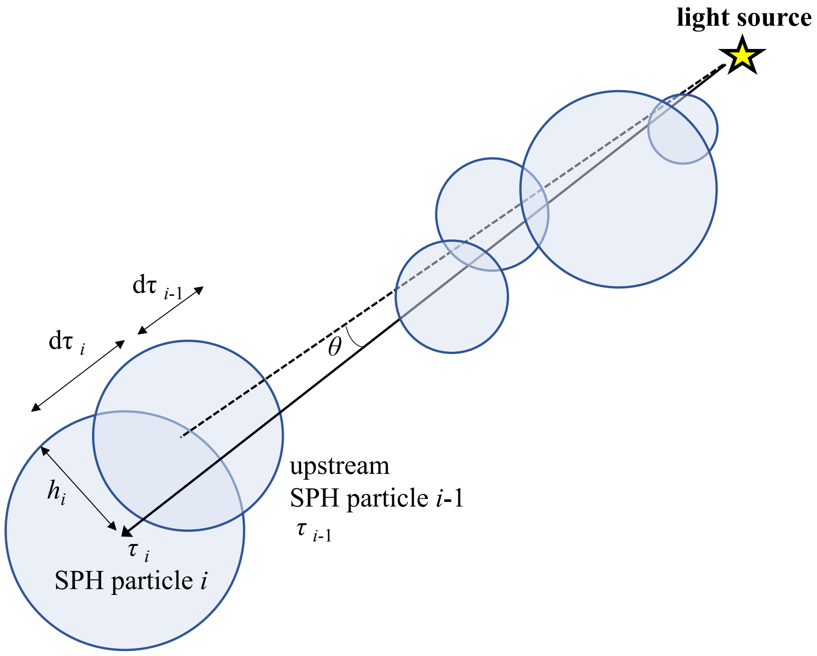
light source
dτ $_{i-1}$
dτ $_i$
θ
h_i
τ_i
SPH particle i
upstream
SPH particle i-1
τ_{i-1}

Figure B.1. Schematic picture for estimating the optical depth τ from the ionizing radiation source to the SPH particle i.

where $d\tau_{\mathrm{UV},i}$ is the optical depth from the particle i to a particle located at the upstream of particle i and j in the last equation runs the set of upstream particles of particle i.

The upstream particle j for the SPH particle i is chosen under following conditions:

1. A particle j is located within the smoothing length h_i of the particle i.
2. The distance from the light source to the particle j is smaller than that of the particle i.
3. The angle θ between two lines from the particle i and the particle j to the light source is smaller than $\Theta_{\mathrm{tol}} = 0.01$.
4. If there are more than one particle which satisfies above three conditions, we choose the particle which have the smallest θ. If there is no particle, we double the search radius and repeat above procedure.

We then calculate the photon number which is locally consumed by the interaction with the neutral hydrogen. Because the optical depth of one SPH particle is relatively large, we use the so-called photon conserving method (Kessel-Deynet & Burkert, 2000; Abel *et al.*, 1999), where the reaction rate k and the photo-heating rate Γ are given by,

$$k = -\frac{1}{4\pi r^2}\frac{\mathrm{d}}{\mathrm{d}r}\int_{\nu_{\mathrm{L}}}^{\infty}\frac{L_\nu e^{-\tau_\nu}}{h\nu}\mathrm{d}\nu, \tag{B.2}$$

$$\Gamma = -\frac{1}{4\pi r^2}\frac{\mathrm{d}}{\mathrm{d}r}\int_{\nu_{\mathrm{L}}}^{\infty}\frac{L_\nu e^{-\tau_\nu}}{h\nu}(h\nu - 13.6\ \mathrm{eV})\,\mathrm{d}\nu, \tag{B.3}$$

where ν_{L} is the frequency of the Lyman-limit, which satisfies $h\nu_{\mathrm{L}} = 13.6$ eV.

We discretize the differential in the above equations and take volume averages, which lead to:

$$k = \frac{1}{\Delta r}\frac{\Phi_1(r_i) - \Phi_1(r_i + \Delta r_i)}{r_i^2 + r_i\Delta r - \Delta r^2/3}, \tag{B.4}$$

$$\Gamma = \frac{1}{\Delta r}\frac{\Phi_2(r_i) - \Phi_2(r_i + \Delta r_i)}{r_i^2 + r_i\Delta r - \Delta r^2/3}, \tag{B.5}$$

where

$$\Phi_1(r) = \int_{\nu_{\mathrm{L}}}^{\infty}\frac{L_\nu e^{-\tau_\nu}}{4\pi}\mathrm{d}\nu, \tag{B.6}$$

$$\Phi_2(r) = \int_{\nu_{\mathrm{L}}}^{\infty}\frac{L_\nu e^{-\tau_\nu}}{4\pi}(h\nu - 13.6\ \mathrm{eV})\,\mathrm{d}\nu. \tag{B.7}$$

In our calculation, we only assume the black-body spectra for the radiation source. The extension to the other spectra is straightforward. We tabulate $\Phi_1(r)$ and $\Phi_2(r)$ as functions of the effective temperature T_{eff} and the optical depth τ.

Appendix C

Particle De-refinement Prescription

In order to speed up our hydrodynamical calculation, we develop a “de-refinement ” scheme that combines and subtracts SPH particles in the simulation. We combine particles by following procedure:

- we specify the region in which particles are combined,
- order the particles along the Peano-Hilbert curve, and
- group and combine the specified particles in the sorted order with every $N_{\rm comb}$ particles.

We combine every eight particles into one particle in the above procedure, and that the energy and momentum are conserved. As control parameters, we set two characteristic radii from the DC halo center R_1 and R_2, where $R_1 < R_2$. We perform the particle de-refinement once for particles in $R_1 < R < R_2$ and twice for particles in $R_2 < R$, where R is the separation between the particle and the DC halo center.

We carry out test runs for S1 halo, for which the de-refinement is performed for the snapshot at $z = 24.6$, which corresponds to the cosmic age of 0.13 Gyr. Figure C.1 represents the time evolution of the density in the S1 halo for the different de-refinement parameters R_1 and R_2. These parameters only yield less than a factor of two the difference of the central density at any snapshots. Nevertheless, the computation time with $(R_1, R_2) = (30\ {\rm ckpc}, 50\ {\rm ckpc})$ is about by an order of magnitude smaller than that with $(R_1, R_2) = (50\ {\rm ckpc}, 70\ {\rm ckpc})$.

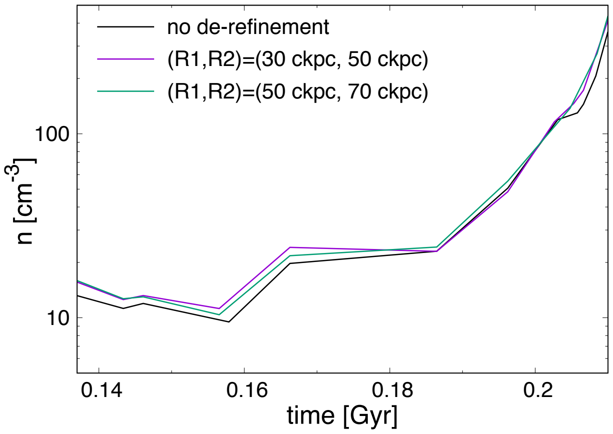

Figure C.1. Effects of varying the particle de-refinement criteria for the density evolution for the S1 halo. The lines show the evolution without (black) and with de-refinement with (R_1, R_2) = (30 comoving kpc, 50 comoving kpc) (purple), and (R_1, R_2) = (50 comoving kpc, 70 comoving kpc) (green).

Appendix D

The Infalling Velocities of DC Candidate Halos

We here show the analytic forms of the halo infalling velocity $v_{\rm inf}$ in the following steps: (1) we first assess the linear overdensity $\delta_{\rm in}$ and the mass $M_{\rm in}$ at a distance $d_{\rm LW}$, and (2) estimate the turnaround radius $R_{\rm turn}$ of the mass shell at $d_{\rm LW}$ by using the spherical collapse model. Here, the turnaround radius is defined by the radius at which the mass shell expansion turns to the contraction. The infalling velocity of the shell whose size is R is defined as $v_{\rm inf} = \sqrt{2{\rm G}M(1/R - 1/R_{\rm turn})}$, where $M = M(R)$ is the enclosed mass within R. The infalling time $t_{\rm inf}$, the time-scale over which the mass shell contracts from R_1 to R_2, is defined as

$$t_{\rm inf} = \int_{R_2}^{R_1} \frac{{\rm d}R}{v} = \int_{R_2}^{R_1} \frac{{\rm d}R}{\sqrt{2GM(1/R - 1/R_{\rm turn})}}. \tag{D.1}$$

Hereafter, we derive M and $R_{\rm turn}$ as functions of R, which allows us to perform the above integration. Since we focus on the high-z universe at $z > 8$, the matter dominant epoch, we assume the Einstein de-Sitter universe for simplicity.

D.1 Linear Over Density within R

The enclosed mass M and the linear over density δ within the shell radius R can be evaluated by the spherical collapse model. Here, $\delta \equiv \rho/\bar{\rho} - 1$, where ρ is the density and $\bar{\rho}$ is the mean density of the universe which is expressed as $\Omega_{\rm m}\rho_{\rm crit}(1+z)^3$. In the Einstein de-Sitter universe, the shell dynamics $R = R(t)$ is characterized by θ as follows:

$$\frac{R}{R_{\rm l}(t)} = \frac{3}{10\,\delta(t)}(1 - \cos\theta), \tag{D.2}$$

$$\delta(t) = \frac{3}{5}\left[\frac{3}{4}(\theta - \sin\theta)\right]^{2/3}, \tag{D.3}$$

where $R_{\rm l}(t) = [3M/(4\pi\bar{\rho}(t))]^{1/3}$. For the fixed t, two shells with δ_i and θ_i ($i = 1$ and 2) follow a relation as;

$$\frac{\delta_1}{\delta_2} = \left(\frac{\theta_1 - \sin\theta_1}{\theta_2 - \sin\theta_2}\right)^{2/3}. \tag{D.4}$$

The completely collapsed shell with $R = 0$ is expressed by the parameters with $\theta = 2\pi$ and $\delta = \delta_c \equiv 1.69$. Assuming that the source halo have just reached $\theta_2 = 2\pi$ and correspond to $\delta_2 = \delta_c$, then we obtain the following equation:

$$\delta_1 = \delta_c \left(\frac{\theta_1 - \sin\theta_1}{2\pi} \right)^{2/3}. \tag{D.5}$$

With eqs. (D.2) and (D.5), the shell radius is determined by the enclosed mass and the linear over density as $R = R(M, \delta)$.

D.2 Enclosed Mass and Turnaround Radius

We evaluate the enclosed mass M within the shell radius R following Barkana (2004), which is based on the extended Press-Schechter (EPS) theory in the Fourier space (Bond *et al.*, 1991) and the Press-Schechter (PS) theory in the real space. EPS theory can handle the contribution of the negative overdensity to the collapsed halo mass, while the negative overdensity never contributes in the PS theory and thus requires ad-hoc treatment. In the EPS theory, it is convenient to evaluate the density field in the Fourier space. Instead of the wave number k, the variance $S_k \equiv 1/(2\pi^2) \int_0^k \mathrm{d}k' k'^2 P(k')$ is used to represent the scale under consideration, where $P(k)$ is the power spectrum of the initial density fluctuation.

EPS theory provides the probability of the density lying between δ and $\delta + \mathrm{d}\delta$, $Q(\nu, \delta, S_k)\mathrm{d}\delta$, where ν is the critical overdensity for the collapsing halo. The cumulative mass function is obtained by integrating Q from ν to ∞, while its differentiation gives the differential mass function $f(\nu, S_k)\mathrm{d}S_k$. Q and f can be written as follows:

$$Q(\nu, \delta, S_k) = \frac{1}{\sqrt{2\pi S_k}} \left[\exp\left(-\frac{\delta^2}{2S_k} \right) - \exp\left(-\frac{(2\nu - \delta)^2}{2S_k} \right) \right], \tag{D.6}$$

$$f(\nu, S_k) = \frac{\partial}{\partial S_k} \left[1 - \int_{-\infty}^{\nu} \mathrm{d}\delta Q(\nu, \delta, S_k) \right] = \frac{\nu}{\sqrt{2\pi} S_k^{3/2}} \exp\left(-\frac{\nu^2}{2S_k} \right). \tag{D.7}$$

The probability distribution (δ, S_k) around $(\delta_\mathrm{c}, S_{k,M})$ is given by:

$$P(\delta|\delta_\mathrm{c}) = Q(\delta_\mathrm{c}, \delta, S_{k,M}) \frac{f(\delta_\mathrm{c} - \delta, S_{k,M} - S_k)}{f(\delta_\mathrm{c}, S_{k,M})}. \tag{D.8}$$

Therefore, the mean density profile $\langle \delta(r) \rangle$ around $(\delta_\mathrm{c}, S_{k,M})$ becomes

$$\frac{\langle \delta(r) \rangle}{\delta_\mathrm{c}} = 1 - \left(1 - \alpha + \frac{\alpha}{\beta} \right) \mathrm{erf}\left[\sqrt{\frac{\beta(1-\alpha)}{2\alpha}} \right] - \sqrt{\frac{2\alpha(1-\alpha)}{\pi\beta}} \exp\left[-\frac{\beta(1-\alpha)}{2\alpha} \right], \tag{D.9}$$

where $\alpha \equiv S_k/S_{k,M}$ and $\beta \equiv \delta_\mathrm{c}^2/S_{k,M}$.

It is pointed out by Barkana (2004) that in the rare halo limit where $\beta \sim 0$, the PS theory describes the density distribution more accurately than the EPS theory. In the PS theory, the mean density profile $\langle \delta(r) \rangle$ is given by

$$\frac{\langle \delta(r) \rangle}{\delta_\mathrm{c}} = \frac{\xi_r(r_M, r)}{\sigma^2(r_M)}, \tag{D.10}$$

where ξ_r is the two-point correlation function. To compromise the EPS and PS theories, he adopts

$$\alpha = \frac{\xi_r}{\sigma^2(r_M)}, \quad \beta = \frac{\nu^2 \alpha (1-\alpha)}{\sigma^2(r) - \alpha \xi_r(r_M, r)}, \tag{D.11}$$

instead of the values in the previous discussion.

Once the enclosed mass M is given, then we can derive the averaged density within the shell, $\delta = \delta(M)$ from eqs. (D.9) and (D.11). According to the discussion in Section D.1, the shell radius R and enclosed mass are related by $R = R(M, \delta(M))$. Therefore for a given radius R, M and δ within R is obtained by solving the equation $R = R(M, \delta(M))$.

With the obtained overdensity δ within the radius R, we can relate R and the turnaround radius $R_{\rm turn}$ corresponding to $\theta = \pi$ and $\delta = 1.06$ using eqs. (D.2) and (D.3) (Mo *et al.*, 2010),

$$R_{\rm turn} = \frac{2}{1 - \cos\theta_1} R, \tag{D.12}$$

where θ_1 is the parameter representing the considered shell given by eq. (D.3). Inserting $d_{\rm LW}$ and $d_{\rm tid}$ to R_1 and R_2 in eq. (D.1), the infalling time is calculated for the given redshift z and source halo mass $M_{\rm source}$.

Appendix E

Analytic Estimate of the Radiation Feedback Effects

We here analytically investigate whether the ionizing radiation from the protostar evacuates the surrounding gas. We consider a central star associated with a gas disk. As shown in our simulations, a photo-ionized region first expands toward polar regions where the density is relatively low (Figure 6.16). We first model the density profile along the polar axis by the following density profile,

$$n(r) = \begin{cases} \frac{c_{\mathrm{s,I}}^2}{G\mu_{\mathrm{I}} m_{\mathrm{p}}} r^{-2} & (r > R_{\mathrm{B,I}}), \\ \frac{c_{\mathrm{s,I}}^2}{G\mu_{\mathrm{I}} m_{\mathrm{p}}} R_{\mathrm{B,I}}^{-2} \left(\frac{r}{R_{\mathrm{B,I}}} \right)^{-\alpha} & (r < R_{\mathrm{B,I}}), \end{cases} \tag{E.1}$$

where $R_{\mathrm{B}} \equiv GM_*/c_{\mathrm{s}}^2$ is the gravitational radius, c_{s} the sound speed, and $1 < \alpha < 1.5$ a free-parameter to characterize the inner density profile. The physical quantities with subscripts I and II correspond to those in neutral and ionized regions. We have assumed that the density profile follows $n \propto r^{-2}$ in the outer region $r > R_{\mathrm{B,I}}$ and it becomes shallower within $R_{\mathrm{B,I}}$ because of the gravity of the central star (McKee & Tan, 2008b). The spherically collapsing cloud yields $\alpha = 1.5$, while α slightly decreases when the disk forms around the central star. In fact, our simulations suggest $1.1 \lesssim \alpha \lesssim 1.3$.

The Strömgren radius R_{St}, inside which the ionizing photon supply is fully consumed by the recombination, is calculated by solving

$$S_{\mathrm{UV}} = \int_{R_*}^{R_{\mathrm{St}}} 4\pi r^2 \alpha_{\mathrm{B}} n(r)^2 \mathrm{d}r, \tag{E.2}$$

where S_{UV} and R_* are the stellar UV emissivity and radius. With the density profiles given by eq. (E.1), we obtain

$$R_{\rm St} = \begin{cases} \left[\frac{(3-2\alpha)G^3\mu_{\rm I}^2 m_{\rm p}^2 M_*}{4\pi\alpha_{\rm B}c_{\rm s,I}^6} S_{\rm UV} + \left(\frac{R_*}{R_{\rm B,I}}\right)^{3-2\alpha}\right]^{1/(3-2\alpha)} R_{\rm B,I} & (\alpha < 1.5), \\ R_* \exp\left(\frac{G^3\mu_{\rm I}^2 m_{\rm p}^2 M_*}{4\pi\alpha_{\rm B}c_{\rm s,I}^6} S_{\rm UV}\right) & (\alpha = 1.5). \end{cases} \tag{E.3}$$

Note that the expression with $\alpha = 1.5$ coincides with that found in Omukai & Inutsuka (2002). We assume $S_{\rm UV}$ is equal to the Eddington luminosity, which is valid for very massive stars, and R_* as the ZAMS radius,

$$S_{\rm UV} = 10^{49}\ {\rm s}^{-1}\left(\frac{M*}{M_\odot}\right), \tag{E.4}$$

$$R_* = 4.24\ R_\odot \left(\frac{M_*}{100\ M_\odot}\right)^{0.59}. \tag{E.5}$$

To see whether the ionized gas is gravitationally bound, we compare the Strömgren radius to the gravitational radius of the ionized gas. For $\alpha < 1.5$, we get

$$\begin{aligned} \frac{R_{\rm St}}{R_{\rm B,II}} &= \left(\frac{c_{\rm s,II}}{c_{\rm s,I}}\right)^2 \left[\frac{(3-2\alpha)G^3\mu_{\rm I}^2 m_{\rm p}^2 S_{\rm UV} M_*}{4\pi\alpha_{\rm B}c_{\rm s,I}^6}\right]^{1/(3-2\alpha)} \\ &= 3\left[4.4\times 10^{-5}(3-2\alpha)\left(\frac{M_*}{10^3\ M_\odot}\right)^2\right]^{1/(3-2\alpha)}, \end{aligned} \tag{E.6}$$

where we have neglected the second term of eq. (E.3). In the last equation, we assume $\mu_{\rm I} = 1.2$, $\mu_{\rm II} = 0.6$, $T_{\rm I} = 8000$ K, and $T_{\rm II} = 1.5 \times 10^4$ K, which are motivated by our simulation results.

Figure E.1 shows $R_{\rm St}/R_{\rm B,II}$ as a function of M_* for different α. For $1 < \alpha < 1.5$, the Strömgren radius exceeds the gravitational radius only for $M_* \gtrsim 10^5\ M_\odot$. The ionized region is gravitationally bound and confined around the star until the stellar mass exceeds $\sim 10^5\ M_\odot$. Such a trapped ionized region never disturbs the mass accretion. We thus reinforce our argument in Section 6.4, i.e., the UV feedback plays almost no roles in the evolution followed in our simulations.

We have neglected the effect of the radiation pressure in the above estimate. Thomson scattering effectively counteracts the gravity, so that it helps the expansion of the ionized region. Such an effect is included in our modeling with reducing $R_{\rm B,II}$ by a factor of $\Gamma \equiv 1 - L/L_{\rm Edd}(M_{\rm tot})$, where L is the stellar luminosity, $L_{\rm Edd}$ the Eddington luminosity, and $M_{\rm tot}$ the total mass within the ionized region including the gas and star. Accordingly, the condition for the breakout of the ionized region is modified as $R_{\rm St}/R_{\rm B,II} = \Gamma$. The highest-mass stars that appear in our simulations have $\Gamma \sim 0.1$, but Figure E.1 still shows that the breakout occurs only for $M_* \gtrsim 10^4\ M_\odot$. Therefore, our conclusions are not affected by this effect.

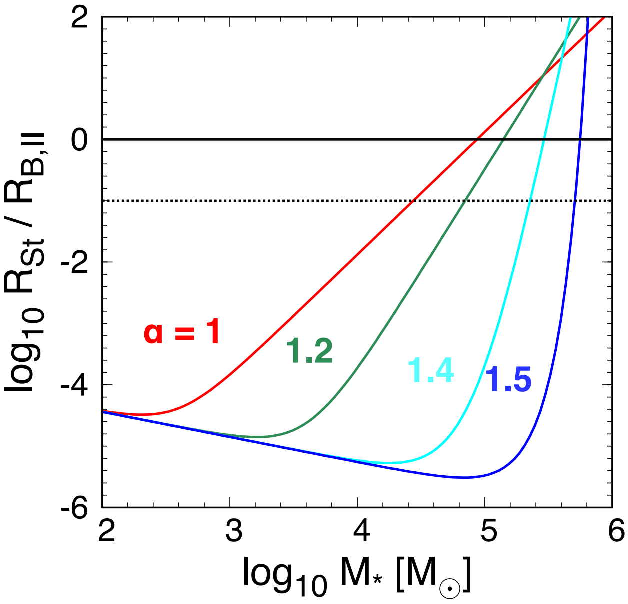

Figure E.1. Ratios of the Strömgren radius $R_{\rm St}$ (eq. E.3) to gravitational radius of the ionized gas $R_{\rm B,II}$ as a function of the mass of the central star. The red, green, cyan, and blue lines represent the different density profiles within the gravitational radius (eq. E.1) with $\alpha = 1$, 1.2, 1.4, and 1.5. The horizontal solid line is a critical line of $R_{\rm st} = R_{\rm B,II}$, above which a photo-ionized region extends beyond the gravitational radius. The horizontal dotted line is also another critical line for the breakout of the ionized region $R_{\rm st} = 0.1 R_{\rm B,II}$, considering the effect of the radiation pressure against the gravity (see text).

Bibliography

Abbott, B. P., Abbott, R., Abbott, T. D., Abernathy, M. R., Acernese, F., Ackley, K., Adams, C., Adams, T., Addesso, P., Adhikari, R. X. & et al. (2016a). *GW151226: Observation of Gravitational Waves from a 22-Solar-Mass Binary Black Hole Coalescence.* Physical Review Letters **116**(24), 241103.

Abbott, B. P., Abbott, R., Abbott, T. D., Abernathy, M. R., Acernese, F., Ackley, K., Adams, C., Adams, T., Addesso, P., Adhikari, R. X. & et al. (2016b). *Properties of the Binary Black Hole Merger GW150914.* Physical Review Letters **116**(24), 241102.

Abel, T., Norman, M. L. & Madau, P. (1999). *Photon-conserving Radiative Transfer around Point Sources in Multidimensional Numerical Cosmology.* ApJ**523**, 66–71.

Abel, T., Wise, J. H. & Bryan, G. L. (2007). *The H II Region of a Primordial Star.* ApJ**659**, L87–L90.

Agarwal, B., Dalla Vecchia, C., Johnson, J. L., Khochfar, S. & Paardekooper, J.-P. (2014). *The First Billion Years project: birthplaces of direct collapse black holes.* MNRAS**443**, 648–657.

Agarwal, B., Khochfar, S., Johnson, J. L., Neistein, E., Dalla Vecchia, C. & Livio, M. (2012). *Ubiquitous seeding of supermassive black holes by direct collapse.* MNRAS**425**, 2854–2871.

Ajith, P., Hannam, M., Husa, S., Chen, Y., Brügmann, B., Dorband, N., Müller, D., Ohme, F., Pollney, D., Reisswig, C., Santamaría, L. & Seiler, J. (2011). *Inspiral-Merger-Ringdown Waveforms for Black-Hole Binaries with Non-precessing Spins.* Physical Review Letters **106**(24), 241101.

Alvarez, M. A., Wise, J. H. & Abel, T. (2009). *Accretion onto the First Stellar-Mass Black Holes.* ApJ**701**, L133–L137.

Aykutalp, A., Wise, J. H., Spaans, M. & Meijerink, R. (2014). *Songlines from Direct Collapse Seed Black Holes: Effects of X-Rays on Black Hole Growth and Stellar Populations.* ApJ**797**, 139.

Bañados, E., Venemans, B. P., Mazzucchelli, C., Farina, E. P., Walter, F., Wang, F., Decarli, R., Stern, D., Fan, X., Davies, F., Hennawi, J. F., Simcoe, R., Turner, M. L., Rix, H., Yang, J., Kelson, D. D., Rudie, G. & Winters, J. M. (2017). *An 800 million solar mass black hole in a significantly neutral universe at redshift 7.5.* ArXiv e-prints .

Barkana, R. (2004). *A model for infall around virialized haloes.* MNRAS**347**, 59–66.

Barkana, R. & Loeb, A. (2001). *In the beginning: the first sources of light and the* *reionization of the universe.* Phys. Rep.**349**, 125–238.

Bate, M. R., Bonnell, I. A. & Price, N. M. (1995). *Modelling accretion in protobinary systems.* MNRAS**277**, 362–376.

Becerra, F., Greif, T. H., Springel, V. & Hernquist, L. E. (2015). *Formation of massive protostars in atomic cooling haloes.* MNRAS**446**, 2380–2393.

Belczynski, K., Bulik, T., Fryer, C. L., Ruiter, A., Valsecchi, F., Vink, J. S. & Hurley, J. R. (2010). *On the Maximum Mass of Stellar Black Holes.* ApJ**714**, 1217–1226.

Bellovary, J., Brooks, A., Volonteri, M., Governato, F., Quinn, T. & Wadsley, J. (2013). *The Relative Role of Galaxy Mergers and Cosmic Flows in Feeding Black Holes.* ApJ**779**, 136.

Bertin, G., Lin, C. C., Lowe, S. A. & Thurstans, R. P. (1989). *Modal Approach to the Morphology of Spiral Galaxies. II. Dynamical Mechanisms.* ApJ**338**, 104.

Binney, J. & Tremaine, S. (1987). *Galactic dynamics.* Princeton, NJ, Princeton Univ. Press.

Binney, J. & Tremaine, S. (2008). *Galactic Dynamics: Second Edition.* Princeton University Press.

Bond, J. R., Arnett, W. D. & Carr, B. J. (1984). *The evolution and fate of Very Massive Objects.* ApJ**280**, 825–847.

Bond, J. R., Cole, S., Efstathiou, G. & Kaiser, N. (1991). *Excursion set mass functions for hierarchical Gaussian fluctuations.* ApJ**379**, 440–460.

Bonnor, W. B. (1956). *Boyle's Law and gravitational instability.* MNRAS**116**, 351.

Bromm, V., Kudritzki, R. P. & Loeb, A. (2001). *Generic Spectrum and Ionization Efficiency of a Heavy Initial Mass Function for the First Stars.* ApJ**552**, 464–472.

Bromm, V. & Loeb, A. (2003). *Formation of the First Supermassive Black Holes.* ApJ**596**, 34–46.

Bullock, J. S., Dekel, A., Kolatt, T. S., Kravtsov, A. V., Klypin, A. A., Porciani, C. & Primack, J. R. (2001). *A Universal Angular Momentum Profile for Galactic Halos.* ApJ**555**, 240–257.

Casares, J. & Jonker, P. G. (2014). *Mass Measurements of Stellar and Intermediate-Mass Black Holes.* Space Sci. Rev.**183**, 223–252.

Cen, R. & Riquelme, M. A. (2008). *Lower Metal Enrichment of Virialized Gas in Minihalos.* ApJ**674**, 644–652.

Chiaki, G., Yoshida, N. & Hirano, S. (2016). *Gravitational collapse and the thermal evolution of low-metallicity gas clouds in the early Universe.* MNRAS**463**, 2781–2798.

Choi, J.-H., Shlosman, I. & Begelman, M. C. (2015). *Supermassive black hole formation at high redshifts via direct collapse in a cosmological context.* MNRAS**450**, 4411–4423.

Chon, S., Hirano, S., Hosokawa, T. & Yoshida, N. (2016). *Cosmological Simulations of Early Black Hole Formation: Halo Mergers, Tidal Disruption, and the Conditions for Direct Collapse.* ApJ**832**, 134.

Chon, S., Hosokawa, T. & Yoshida, N. (2017). *Radiation hydrodynamics simulations* *of the formation of direct-collapse supermassive stellar systems.* ArXiv e-prints .

Chon, S. & Latif, M. A. (2017). *The impact of ionizing radiation on the formation of a supermassive star in the early Universe.* MNRAS**467**, 4293–4303.

Clark, P. C., Glover, S. C. O., Smith, R. J., Greif, T. H., Klessen, R. S. & Bromm, V. (2011). *The Formation and Fragmentation of Disks Around Primordial Protostars.* Science **331**, 1040.

Cole, S., Aragon-Salamanca, A., Frenk, C. S., Navarro, J. F. & Zepf, S. E. (1994). *A Recipe for Galaxy Formation.* MNRAS**271**, 781.

Cornish, N. & Robson, T. (2017). Galactic binary science with the new LISA design. In: *Journal of Physics Conference Series*, vol. 840 of *Journal of Physics Conference Series*.

De Rosa, G., Decarli, R., Walter, F., Fan, X., Jiang, L., Kurk, J., Pasquali, A. & Rix, H. W. (2011). *Evidence for Non-evolving Fe II/Mg II Ratios in Rapidly Accreting z ~ 6 QSOs.* ApJ**739**, 56.

Dekel, A., Birnboim, Y., Engel, G., Freundlich, J., Goerdt, T., Mumcuoglu, M., Neistein, E., Pichon, C., Teyssier, R. & Zinger, E. (2009). *Cold streams in early massive hot haloes as the main mode of galaxy formation.* Nature**457**, 451–454.

Dekel, A. & Silk, J. (1986). *The origin of dwarf galaxies, cold dark matter, and biased galaxy formation.* ApJ**303**, 39–55.

Di Matteo, T., Khandai, N., DeGraf, C., Feng, Y., Croft, R. A. C., Lopez, J. & Springel, V. (2012). *Cold Flows and the First Quasars.* ApJ**745**, L29.

Dijkstra, M., Ferrara, A. & Mesinger, A. (2014). *Feedback-regulated supermassive black hole seed formation.* MNRAS**442**, 2036–2047.

Dijkstra, M., Haiman, Z., Mesinger, A. & Wyithe, J. S. B. (2008). *Fluctuations in the high-redshift Lyman-Werner background: close halo pairs as the origin of supermassive black holes.* MNRAS**391**, 1961–1972.

Draine, B. T. & Bertoldi, F. (1996). *Structure of Stationary Photodissociation Fronts.* ApJ**468**, 269.

Dubois, Y., Volonteri, M. & Silk, J. (2014). *Black hole evolution - III. Statistical properties of mass growth and spin evolution using large-scale hydrodynamical cosmological simulations.* MNRAS**440**, 1590–1606.

Fan, X., Strauss, M. A., Becker, R. H., White, R. L., Gunn, J. E., Knapp, G. R., Richards, G. T., Schneider, D. P., Brinkmann, J. & Fukugita, M. (2006). *Constraining the Evolution of the Ionizing Background and the Epoch of Reionization with z~6 Quasars. II. A Sample of 19 Quasars.* AJ**132**, 117–136.

Feng, Y., Di Matteo, T., Croft, R. & Khandai, N. (2014). *High-redshift supermassive black holes: accretion through cold flows.* MNRAS**440**, 1865–1879.

Forrey, R. C. (2016). *Quadrupole association and dissociation of hydrogen in the early Universe.* Journal of Physics B Atomic Molecular Physics **49**(19), 194002.

Foster, P. N. & Chevalier, R. A. (1993). *Gravitational Collapse of an Isothermal Sphere.* ApJ**416**, 303.

Fryer, C. L., Woosley, S. E. & Heger, A. (2001). *Pair-Instability Supernovae,* *Gravity Waves, and Gamma-Ray Transients.* ApJ**550**, 372–382.

Fuller, G. M., Woosley, S. E. & Weaver, T. A. (1986). *The evolution of radiation-dominated stars. I - Nonrotating supermassive stars.* ApJ**307**, 675–686.

Gammie, C. F. (2001). *Nonlinear Outcome of Gravitational Instability in Cooling, Gaseous Disks.* ApJ**553**, 174–183.

Gisler, G. R. (1976). *The fate of gas in elliptical galaxies and the density evolution of radio sources.* A&A**51**, 137–150.

Glover, S. C. O. & Brand, P. W. J. L. (2003). *Radiative feedback from an early X-ray background.* MNRAS**340**, 210–226.

Gong, H. & Ostriker, E. C. (2009). *Protostar Formation in Supersonic Flows: Growth and Collapse of Spherical Cores.* ApJ**699**, 230–244.

Greif, T. H., Bromm, V., Clark, P. C., Glover, S. C. O., Smith, R. J., Klessen, R. S., Yoshida, N. & Springel, V. (2012). *Formation and evolution of primordial protostellar systems.* MNRAS**424**, 399–415.

Grimm, H.-J., Gilfanov, M. & Sunyaev, R. (2003). *High-mass X-ray binaries as a star formation rate indicator in distant galaxies.* MNRAS**339**, 793–809.

Gunn, J. E. & Gott, J. R., III (1972). *On the Infall of Matter Into Clusters of Galaxies and Some Effects on Their Evolution.* ApJ**176**, 1.

Habouzit, M., Volonteri, M., Latif, M., Dubois, Y. & Peirani, S. (2016). *On the number density of 'direct collapse' black hole seeds.* MNRAS**463**, 529–540.

Hahn, O. & Abel, T. (2013). MUSIC: MUlti-Scale Initial Conditions. Astrophysics Source Code Library.

Hanawa, T. & Matsumoto, T. (2000). *Stability of a Dynamically Collapsing Gas Sphere.* PASJ**52**, 241.

Hayashi, C. (1961). *Stellar evolution in early phases of gravitational contraction.* PASJ**13**.

Heger, A., Fryer, C. L., Woosley, S. E., Langer, N. & Hartmann, D. H. (2003). *How Massive Single Stars End Their Life.* ApJ**591**, 288–300.

Heger, A. & Woosley, S. E. (2002). *The Nucleosynthetic Signature of Population III.* ApJ**567**, 532–543.

Hirano, S., Hosokawa, T., Yoshida, N., Omukai, K. & Yorke, H. W. (2015). *Primordial star formation under the influence of far ultraviolet radiation: 1540 cosmological haloes and the stellar mass distribution.* MNRAS**448**, 568–587.

Hirano, S., Hosokawa, T., Yoshida, N., Umeda, H., Omukai, K., Chiaki, G. & Yorke, H. W. (2014). *One Hundred First Stars: Protostellar Evolution and the Final Masses.* ApJ**781**, 60.

Hollenbach, D. & McKee, C. F. (1979). *Molecule formation and infrared emission in fast interstellar shocks. I Physical processes.* ApJS**41**, 555–592.

Hopkins, P. F., Hernquist, L., Cox, T. J., Di Matteo, T., Robertson, B. & Springel, V. (2006). *A Unified, Merger-driven Model of the Origin of Starbursts, Quasars, the Cosmic X-Ray Background, Supermassive Black Holes, and Galaxy Spheroids.* ApJS**163**, 1–49.

Hosokawa, T., Hirano, S., Kuiper, R., Yorke, H. W., Omukai, K. & Yoshida, N. (2016). *Formation of Massive Primordial Stars: Intermittent UV Feedback with Episodic Mass Accretion.* ApJ**824**, 119.

Hosokawa, T., Omukai, K. & Yorke, H. W. (2012). *Rapidly Accreting Supergiant Protostars: Embryos of Supermassive Black Holes?* ApJ**756**, 93.

Hosokawa, T., Omukai, K., Yoshida, N. & Yorke, H. W. (2011). *Protostellar Feedback Halts the Growth of the First Stars in the Universe.* Science **334**, 1250.

Hosokawa, T., Yorke, H. W., Inayoshi, K., Omukai, K. & Yoshida, N. (2013). *Formation of Primordial Supermassive Stars by Rapid Mass Accretion.* ApJ**778**, 178.

Hubber, D. A., Walch, S. & Whitworth, A. P. (2013). *An improved sink particle algorithm for SPH simulations.* MNRAS**430**, 3261–3275.

Hunter, C. (1977). *The collapse of unstable isothermal spheres.* ApJ**218**, 834–845.

Iben, I., Jr. (1963). *Massive Stars in Quasi-Static Equlibrium.* ApJ**138**, 1090.

Iliev, I. T., Mellema, G., Shapiro, P. R. & Pen, U.-L. (2007). *Self-regulated reionization.* MNRAS**376**, 534–548.

Iliev, I. T., Scannapieco, E. & Shapiro, P. R. (2005). *The Impact of Small-Scale Structure on Cosmological Ionization Fronts and Reionization.* ApJ**624**, 491–504.

Inayoshi, K. & Omukai, K. (2011). *Effect of cosmic ray/X-ray ionization on supermassive black hole formation.* MNRAS**416**, 2748–2759.

Inayoshi, K. & Omukai, K. (2012). *Supermassive black hole formation by cold accretion shocks in the first galaxies.* MNRAS**422**, 2539–2546.

Inayoshi, K., Omukai, K. & Tasker, E. (2014). *Formation of an embryonic supermassive star in the first galaxy.* MNRAS**445**, L109–L113.

Inayoshi, K. & Tanaka, T. L. (2015). *The suppression of direct collapse black hole formation by soft X-ray irradiation.* MNRAS**450**, 4350–4363.

Inayoshi, K., Visbal, E. & Kashiyama, K. (2015). *Direct collapse black hole formation via high-velocity collisions of protogalaxies.* MNRAS**453**, 1692–1700.

Inoue, A. K. (2011). *Rest-frame ultraviolet-to-optical spectral characteristics of extremely metal-poor and metal-free galaxies.* MNRAS**415**, 2920–2931.

Iye, M. (1978). *Global Gravitational Instability of Disk Galaxies.* PASJ**30**, 223–252.

Jiang, L., Fan, X., Annis, J., Becker, R. H., White, R. L., Chiu, K., Lin, H., Lupton, R. H., Richards, G. T., Strauss, M. A., Jester, S. & Schneider, D. P. (2008). *A Survey of z ˜ 6 Quasars in the Sloan Digital Sky Survey Deep Stripe. I. A Flux-Limited Sample at $z_{AB} < 21$.* AJ**135**, 1057–1066.

Jiang, L., Fan, X., Vestergaard, M., Kurk, J. D., Walter, F., Kelly, B. C. & Strauss, M. A. (2007). *Gemini Near-Infrared Spectroscopy of Luminous z ˜ 6 Quasars: Chemical Abundances, Black Hole Masses, and Mg II Absorption.* AJ**134**, 1150.

Jiang, L., McGreer, I. D., Fan, X., Strauss, M. A., Bañados, E., Becker, R. H., Bian, F., Farnsworth, K., Shen, Y., Wang, F., Wang, R., Wang, S., White, R. L., Wu, J., Wu, X.-B., Yang, J. & Yang, Q. (2016). *The Final SDSS High-redshift Quasar Sample of 52 Quasars at z5.7.* ApJ**833**, 222.

Johnson, J. L. & Bromm, V. (2007). *The aftermath of the first stars: massive black holes.* MNRAS**374**, 1557–1568.

Johnson, J. L., Dalla Vecchia, C. & Khochfar, S. (2013). *The First Billion Years project: the impact of stellar radiation on the co-evolution of Populations II and III.* MNRAS**428**, 1857–1872.

Johnson, J. L., Khochfar, S., Greif, T. H. & Durier, F. (2011). *Accretion on to black holes formed by direct collapse.* MNRAS**410**, 919–933.

Kashiyama, K. & Inayoshi, K. (2016). *Stellar Tidal Disruption Events by Direct-collapse Black Holes.* ApJ**826**, 80.

Kauffmann, G. & Haehnelt, M. (2000). *A unified model for the evolution of galaxies and quasars.* MNRAS**311**, 576–588.

Kauffmann, G., White, S. D. M. & Guiderdoni, B. (1993). *The Formation and Evolution of Galaxies Within Merging Dark Matter Haloes.* MNRAS**264**, 201.

Kawamura, S., Ando, M., Seto, N., Sato, S., Nakamura, T., Tsubono, K., Kanda, N., Tanaka, T., Yokoyama, J., Funaki, I., Numata, K., Ioka, K., Takashima, T., Agatsuma, K., Akutsu, T., suke Aoyanagi, K., Arai, K., Araya, A., Asada, H., Aso, Y., Chen, D., Chiba, T., Ebisuzaki, T., Ejiri, Y., Enoki, M., Eriguchi, Y., Fujimoto, M.-K., Fujita, R., Fukushima, M., Futamase, T., Harada, T., Hashimoto, T., Hayama, K., Hikida, W., Himemoto, Y., Hirabayashi, H., Hiramatsu, T., Hong, F.-L., Horisawa, H., Hosokawa, M., Ichiki, K., Ikegami, T., Inoue, K. T., Ishidoshiro, K., Ishihara, H., Ishikawa, T., Ishizaki, H., Ito, H., Itoh, Y., Izumi, K., Kawano, I., Kawashima, N., Kawazoe, F., Kishimoto, N., Kiuchi, K., Kobayashi, S., Kohri, K., Koizumi, H., Kojima, Y., Kokeyama, K., Kokuyama, W., Kotake, K., Kozai, Y., Kunimori, H., Kuninaka, H., Kuroda, K., Kuroyanagi, S., ichi Maeda, K., Matsuhara, H., Matsumoto, N., Michimura, Y., Miyakawa, O., Miyamoto, U., Miyoki, S., Morimoto, M. Y., Morisawa, T., Moriwaki, S., Mukohyama, S., Musha, M., Nagano, S., Naito, I., Nakamura, K., Nakano, H., Nakao, K., Nakasuka, S., Nakayama, Y., Nakazawa, K., Nishida, E., Nishiyama, K., Nishizawa, A., Niwa, Y., Noumi, T., Obuchi, Y., Ohashi, M., Ohishi, N., Ohkawa, M., Okada, K., Okada, N., Oohara, K., Sago, N., Saijo, M., Saito, R., Sakagami, M., ichiro Sakai, S., Sakata, S., Sasaki, M., Sato, T., Shibata, M., Shinkai, H., Shoda, A., Somiya, K., Sotani, H., Sugiyama, N., Suwa, Y., Suzuki, R., Tagoshi, H., Takahashi, F., Takahashi, K., Takahashi, K., Takahashi, R., Takahashi, R., Takahashi, T., Takahashi, H., Akiteru, T., Takano, T., Tanaka, N., Taniguchi, K., Taruya, A., Tashiro, H., Torii, Y., Toyoshima, M., Tsujikawa, S., Tsunesada, Y., Ueda, A., ichi Ueda, K., Utashima, M., Wakabayashi, Y., Yagi, K., Yamakawa, H., Yamamoto, K., Yamazaki, T., Yoo, C.-M., Yoshida, S., Yoshino, T. & Sun, K.-X. (2011). *The japanese space gravitational wave antenna: Decigo.* Classical and Quantum Gravity **28**(9), 094011. URL `http://stacks.iop.org/0264-9381/28/i=9/a=094011`.

Kessel-Deynet, O. & Burkert, A. (2000). *Ionizing radiation in smoothed particle* *hydrodynamics.* MNRAS**315**, 713–721.

Kitayama, T., Susa, H., Umemura, M. & Ikeuchi, S. (2001). *Criteria for the formation of Population III objects in the ultraviolet background radiation.* MNRAS**326**, 1353–1366.

Kitayama, T. & Yoshida, N. (2005). *Supernova Explosions in the Early Universe: Evolution of Radiative Remnants and the Halo Destruction Efficiency.* ApJ**630**, 675–688.

Kitsionas, S. & Whitworth, A. P. (2002). *Smoothed Particle Hydrodynamics with particle splitting, applied to self-gravitating collapse.* MNRAS**330**, 129–136.

Kołos, W. & Wolniewicz, L. (1965). *Potential-Energy Curves for the $X\,^1\Sigma_g{}^+$, $b^3\Sigma_u{}^+$, and $C\,^1\Pi_u$ States of the Hydrogen Molecule.* J. Chem. Phys.**43**, 2429–2441.

Kołos, W. & Wolniewicz, L. (1966). *Potential-Energy Curve for the $B\,^1\Sigma_u{}^+$ State of the Hydrogen Molecule.* J. Chem. Phys.**45**, 509–514.

Kolos, W. & Wolniewicz, L. (1968). *Vibrational and Rotational Energies for the $B^1\Sigma_u{}^+$ $C^1\Pi_u$, and $a^3\Sigma_g{}^+$ States of the Hydrogen Molecule.* J. Chem. Phys.**48**, 3672–3680.

Kormendy, J. & Ho, L. C. (2013). *Coevolution (Or Not) of Supermassive Black Holes and Host Galaxies.* ARA&A**51**, 511–653.

Krumholz, M. R. & Matzner, C. D. (2009). *The Dynamics of Radiation-pressure-dominated H II Regions.* ApJ**703**, 1352–1362.

Larson, R. B. (1969). *Numerical calculations of the dynamics of collapsing proto-star.* MNRAS**145**, 271.

Latif, M. A., Bovino, S., Grassi, T., Schleicher, D. R. G. & Spaans, M. (2015). *How realistic UV spectra and X-rays suppress the abundance of direct collapse black holes.* MNRAS**446**, 3163–3177.

Latif, M. A., Bovino, S., Van Borm, C., Grassi, T., Schleicher, D. R. G. & Spaans, M. (2014). *A UV flux constraint on the formation of direct collapse black holes.* MNRAS**443**, 1979–1987.

Latif, M. A., Schleicher, D. R. G., Schmidt, W. & Niemeyer, J. C. (2013). *The characteristic black hole mass resulting from direct collapse in the early Universe.* MNRAS**436**, 2989–2996.

Leitherer, C., Schaerer, D., Goldader, J. D., Delgado, R. M. G., Robert, C., Kune, D. F., de Mello, D. F., Devost, D. & Heckman, T. M. (1999). *Starburst99: Synthesis Models for Galaxies with Active Star Formation.* ApJS**123**, 3–40.

Li, Y., Hernquist, L., Robertson, B., Cox, T. J., Hopkins, P. F., Springel, V., Gao, L., Di Matteo, T., Zentner, A. R., Jenkins, A. & Yoshida, N. (2007). *Formation of z˜6 Quasars from Hierarchical Galaxy Mergers.* ApJ**665**, 187–208.

Loeb, A. & Furlanetto, S. R. (2013). *The First Galaxies in the Universe.* Princeton, NJ: Princeton Univ. Press.

Lynden-Bell, D. & Kalnajs, A. J. (1972). *On the generating mechanism of spiral structure.* MNRAS**157**, 1.

Machacek, M. E., Bryan, G. L. & Abel, T. (2001). *Simulations of Pregalactic Structure Formation with Radiative Feedback.* ApJ**548**, 509–521.

Machida, M. N. & Doi, K. (2013a). *The formation of Population III stars in gas accretion stage: effects of magnetic fields.* MNRAS**435**, 3283–3305.

Machida, M. N. & Doi, K. (2013b). *The formation of Population III stars in gas accretion stage: effects of magnetic fields.* MNRAS**435**, 3283–3305.

Magorrian, J., Tremaine, S., Richstone, D., Bender, R., Bower, G., Dressler, A., Faber, S. M., Gebhardt, K., Green, R., Grillmair, C., Kormendy, J. & Lauer, T. (1998). *The Demography of Massive Dark Objects in Galaxy Centers.* AJ**115**, 2285–2305.

Maoz, E. (1998). *Dynamical Constraints on Alternatives to Supermassive Black Holes in Galactic Nuclei.* ApJ**494**, L181–L184.

Matsuoka, Y., Onoue, M., Kashikawa, N., Iwasawa, K., Strauss, M. A., Nagao, T., Imanishi, M., Niida, M., Toba, Y., Akiyama, M., Asami, N., Bosch, J., Foucaud, S., Furusawa, H., Goto, T., Gunn, J. E., Harikane, Y., Ikeda, H., Kawaguchi, T., Kikuta, S., Komiyama, Y., Lupton, R. H., Minezaki, T., Miyazaki, S., Morokuma, T., Murayama, H., Nishizawa, A. J., Ono, Y., Ouchi, M., Price, P. A., Sameshima, H., Silverman, J. D., Sugiyama, N., Tait, P. J., Takada, M., Takata, T., Tanaka, M., Tang, J.-J. & Utsumi, Y. (2016). *Subaru High-z Exploration of Low-luminosity Quasars (SHELLQs). I. Discovery of 15 Quasars and Bright Galaxies at* $5.7 < z < 6.9$*.* ApJ**828**, 26.

Matzner, C. D. (2002). *On the Role of Massive Stars in the Support and Destruction of Giant Molecular Clouds.* ApJ**566**, 302–314.

Mayer, L., Kazantzidis, S., Escala, A. & Callegari, S. (2010). *Direct formation of supermassive black holes via multi-scale gas inflows in galaxy mergers.* Nature**466**, 1082–1084.

Mazzucchelli, C., Bañados, E., Venemans, B. P., Decarli, R., Farina, E. P., Walter, F., Eilers, A.-C., Rix, H.-W., Simcoe, R., Stern, D., Fan, X., Schlafly, E., De Rosa, G., Hennawi, J., Chambers, K. C., Greiner, J., Burgett, W., Draper, P. W., Kaiser, N., Kudritzki, R.-P., Magnier, E., Metcalfe, N., Waters, C. & Wainscoat, R. J. (2017). *Physical properties of 15 quasars at* $z \gtrsim 6.5$. ArXiv e-prints .

McCarthy, I. G., Frenk, C. S., Font, A. S., Lacey, C. G., Bower, R. G., Mitchell, N. L., Balogh, M. L. & Theuns, T. (2008). *Ram pressure stripping the hot gaseous haloes of galaxies in groups and clusters.* MNRAS**383**, 593–605.

McKee, C. F. & Tan, J. C. (2008a). *The Formation of the First Stars. II. Radiative Feedback Processes and Implications for the Initial Mass Function.* ApJ**681**, 771–797.

McKee, C. F. & Tan, J. C. (2008b). *The Formation of the First Stars. II. Radiative Feedback Processes and Implications for the Initial Mass Function.* ApJ**681**, 771–797.

Merritt, D., Ferrarese, L. & Joseph, C. L. (2001). *No Supermassive Black Hole in M33?* Science **293**, 1116–1119.

Milosavljević, M., Couch, S. M. & Bromm, V. (2009). *Accretion Onto Intermediate-*

Mass Black Holes in Dense Protogalactic Clouds. ApJ**696**, L146–L149.

Mo, H., van den Bosch, F. C. & White, S. (2010). *Galaxy Formation and Evolution.*

Mortlock, D. J., Patel, M., Warren, S. J., Venemans, B. P., McMahon, R. G., Hewett, P. C., Simpson, C., Sharp, R. G., Burningham, B., Dye, S., Ellis, S., Gonzales-Solares, E. A. & Huélamo, N. (2009). *Discovery of a redshift 6.13 quasar in the UKIRT infrared deep sky survey.* A&A**505**, 97–104.

Mortlock, D. J., Warren, S. J., Venemans, B. P., Patel, M., Hewett, P. C., McMahon, R. G., Simpson, C., Theuns, T., Gonzáles-Solares, E. A., Adamson, A., Dye, S., Hambly, N. C., Hirst, P., Irwin, M. J., Kuiper, E., Lawrence, A. & Röttgering, H. J. A. (2011). *A luminous quasar at a redshift of* $z = 7.085$*.* Nature**474**, 616–619.

Navarro, J. F., Frenk, C. S. & White, S. D. M. (1997). *A Universal Density Profile from Hierarchical Clustering.* ApJ**490**, 493–508.

Nelson, A. F. (2006). *Numerical requirements for simulations of self-gravitating and non-self-gravitating discs.* MNRAS**373**, 1039–1073.

Omukai, K. (2001). *Primordial Star Formation under Far-Ultraviolet Radiation.* ApJ**546**, 635–651.

Omukai, K. & Inutsuka, S.-i. (2002). *An upper limit on the mass of a primordial star due to the formation of an Hii region: the effect of ionizing radiation force.* MNRAS**332**, 59–64.

Omukai, K. & Nishi, R. (1998). *Formation of Primordial Protostars.* ApJ**508**, 141–150.

Omukai, K. & Palla, F. (2003). *Formation of the First Stars by Accretion.* ApJ**589**, 677–687.

O'Shea, B. W. & Norman, M. L. (2008a). *Population III Star Formation in a* Λ*CDM Universe. II. Effects of a Photodissociating Background.* ApJ**673**, 14–33.

O'Shea, B. W. & Norman, M. L. (2008b). *Population III Star Formation in a* Λ*CDM Universe. II. Effects of a Photodissociating Background.* ApJ**673**, 14–33.

Park, K. & Ricotti, M. (2012). *Accretion onto Black Holes from Large Scales Regulated by Radiative Feedback. II. Growth Rate and Duty Cycle.* ApJ**747**, 9.

Pelupessy, F. I., Di Matteo, T. & Ciardi, B. (2007). *How Rapidly Do Supermassive Black Hole "Seeds" Grow at Early Times?* ApJ**665**, 107–119.

Penston, M. V. (1969). *Dynamics of self-gravitating gaseous spheres-III. Analytical results in the free-fall of isothermal cases.* MNRAS**144**, 425.

Peters, P. C. (1964). *Gravitational Radiation and the Motion of Two Point Masses.* Phys. Rev. **136**, B1224–B1232.

Planck Collaboration, Ade, P. A. R., Aghanim, N., Armitage-Caplan, C., Arnaud, M., Ashdown, M., Atrio-Barandela, F., Aumont, J., Baccigalupi, C., Banday, A. J. & et al. (2014). *Planck 2013 results. XVI. Cosmological parameters.* A&A**571**, A16.

Raga, A. C. & Lora, V. (2015). *Approximate analytic solutions for the ionization structure of a dusty Strömgren sphere.* Revista Mexicana de Astronomia y Astrofisica, **51**, 189–197.

REES, M. J. (1978). *Quasars.* The Observatory **98**, 210–223.

REGAN, J. A. & DOWNES, T. P. (2017). *Fragmentation inside atomic cooling haloes exposed to Lyman-Werner radiation.* ArXiv e-prints .

REGAN, J. A. & HAEHNELT, M. G. (2009). *Pathways to massive black holes and compact star clusters in pre-galactic dark matter haloes with virial temperatures ˜10000K.* MNRAS**396**, 343–353.

REGAN, J. A., JOHANSSON, P. H. & WISE, J. H. (2016). *Forming supermassive black hole seeds under the influence of a nearby anisotropic multifrequency source.* MNRAS**459**, 3377–3394.

REGAN, J. A., VISBAL, E., WISE, J. H., HAIMAN, Z., JOHANSSON, P. H. & BRYAN, G. L. (2017). *Rapid formation of massive black holes in close proximity to embryonic protogalaxies.* Nature Astronomy **1**, 0075.

SAKURAI, Y., HOSOKAWA, T., YOSHIDA, N. & YORKE, H. W. (2015). *Formation of primordial supermassive stars by burst accretion.* MNRAS**452**, 755–764.

SAKURAI, Y., VOROBYOV, E. I., HOSOKAWA, T., YOSHIDA, N., OMUKAI, K. & YORKE, H. W. (2016). *Supermassive star formation via episodic accretion: protostellar disc instability and radiative feedback efficiency.* MNRAS**459**, 1137–1145.

SALES, L. V., MARINACCI, F., SPRINGEL, V. & PETKOVA, M. (2014). *Stellar feedback by radiation pressure and photoionization.* MNRAS**439**, 2990–3006.

SCHAERER, D. (2002). *On the properties of massive Population III stars and metal-free stellar populations.* A&A**382**, 28–42.

SCHLEICHER, D. R. G., PALLA, F., FERRARA, A., GALLI, D. & LATIF, M. (2013). *Massive black hole factories: Supermassive and quasi-star formation in primordial halos.* A&A**558**, A59.

SHANG, C., BRYAN, G. L. & HAIMAN, Z. (2010). *Supermassive black hole formation by direct collapse: keeping protogalactic gas H_2 free in dark matter haloes with virial temperatures T_{vir} rsim 10^4 K.* MNRAS**402**, 1249–1262.

SHIBATA, M., SEKIGUCHI, Y., UCHIDA, H. & UMEDA, H. (2016). *Gravitational waves from supermassive stars collapsing to a supermassive black hole.* Phys. Rev. D**94**(2), 021501.

SHLOSMAN, I., CHOI, J.-H., BEGELMAN, M. C. & NAGAMINE, K. (2016). *Supermassive black hole seed formation at high redshifts: long-term evolution of the direct collapse.* MNRAS**456**, 500–511.

SHU, F. H. (1977). *Self-similar collapse of isothermal spheres and star formation.* ApJ**214**, 488–497.

SIJACKI, D., SPRINGEL, V. & HAEHNELT, M. G. (2009). *Growing the first bright quasars in cosmological simulations of structure formation.* MNRAS**400**, 100–122.

SMITH, B. D., WISE, J. H., O'SHEA, B. W., NORMAN, M. L. & KHOCHFAR, S. (2015). *The first Population II stars formed in externally enriched mini-haloes.* MNRAS**452**, 2822–2836.

SPRINGEL, V. (2005). *The cosmological simulation code GADGET-2.* MNRAS**364**, 1105–1134.

Springel, V., White, S. D. M., Jenkins, A., Frenk, C. S., Yoshida, N., Gao, L., Navarro, J., Thacker, R., Croton, D., Helly, J., Peacock, J. A., Cole, S., Thomas, P., Couchman, H., Evrard, A., Colberg, J. & Pearce, F. (2005). *Simulations of the formation, evolution and clustering of galaxies and quasars.* Nature**435**, 629–636.

Stacy, A., Bromm, V. & Lee, A. T. (2016). *Building up the Population III initial mass function from cosmological initial conditions.* MNRAS**462**, 1307–1328.

Stahler, S. W., Palla, F. & Salpeter, E. E. (1986). *Primordial stellar evolution - The protostar phase.* ApJ**302**, 590–605.

Stecher, T. P. & Williams, D. A. (1967). *Photodestruction of Hydrogen Molecules in H I Regions.* ApJ**149**, L29.

Sugimura, K., Omukai, K. & Inoue, A. K. (2014). *The critical radiation intensity for direct collapse black hole formation: dependence on the radiation spectral shape.* MNRAS**445**, 544–553.

Susa, H. (2006). *Smoothed Particle Hydrodynamics Coupled with Radiation Transfer.* PASJ**58**, 445–460.

Susa, H., Hasegawa, K. & Tominaga, N. (2014). *The Mass Spectrum of the First Stars.* ApJ**792**, 32.

Takahashi, S. Z., Tsukamoto, Y. & Inutsuka, S. (2016). *A revised condition for self-gravitational fragmentation of protoplanetary discs.* MNRAS**458**, 3597–3612.

Tegmark, M., Silk, J., Rees, M. J., Blanchard, A., Abel, T. & Palla, F. (1997). *How Small Were the First Cosmological Objects?* ApJ**474**, 1.

Tonry, J. L. (1984). *Evidence for a central mass concentration in M32.* ApJ**283**, 27–30.

Toomre, A. (1969). *Group Velocity of Spiral Waves in Galactic Disks.* ApJ**158**, 899.

Toth, G. & Ostriker, J. P. (1992). *Galactic disks, infall, and the global value of Omega.* ApJ**389**, 5–26.

Truelove, J. K., Klein, R. I., McKee, C. F., Holliman, J. H., II, Howell, L. H. & Greenough, J. A. (1997). *The Jeans Condition: A New Constraint on Spatial Resolution in Simulations of Isothermal Self-gravitational Hydrodynamics.* ApJ**489**, L179.

Tsuribe, T. & Omukai, K. (2006). *Dust-cooling-induced Fragmentation of Low-Metallicity Clouds.* ApJ**642**, L61–L64.

Uchida, H., Shibata, M., Yoshida, T., Sekiguchi, Y. & Umeda, H. (2017). *Gravitational Collapse of Rotating Supermassive Stars including Nuclear Burning Effects.* ArXiv e-prints .

Umeda, H., Hosokawa, T., Omukai, K. & Yoshida, N. (2016). *The Final Fates of Accreting Supermassive Stars.* ApJ**830**, L34.

Venemans, B. P., Bañados, E., Decarli, R., Farina, E. P., Walter, F., Chambers, K. C., Fan, X., Rix, H.-W., Schlafly, E., McMahon, R. G., Simcoe, R., Stern, D., Burgett, W. S., Draper, P. W., Flewelling, H., Hodapp, K. W., Kaiser, N., Magnier, E. A., Metcalfe, N., Morgan, J. S., Price, P. A., Tonry, J. L., Waters, C., AlSayyad, Y., Banerji, M., Chen, S. S., González-

Solares, E. A., Greiner, J., Mazzucchelli, C., McGreer, I., Miller, D. R., Reed, S. & Sullivan, P. W. (2015). *The Identification of Z-dropouts in Pan-STARRS1: Three Quasars at 6.5< z< 6.7.* ApJ**801**, L11.

Venemans, B. P., Findlay, J. R., Sutherland, W. J., De Rosa, G., McMahon, R. G., Simcoe, R., González-Solares, E. A., Kuijken, K. & Lewis, J. R. (2013). *Discovery of Three z 6.5 Quasars in the VISTA Kilo-Degree Infrared Galaxy (VIKING) Survey.* ApJ**779**, 24.

Visbal, E., Haiman, Z. & Bryan, G. L. (2014a). *A no-go theorem for direct collapse black holes without a strong ultraviolet background.* MNRAS**442**, L100–L104.

Visbal, E., Haiman, Z. & Bryan, G. L. (2014b). *Direct collapse black hole formation from synchronized pairs of atomic cooling haloes.* MNRAS**445**, 1056–1063.

Voit, G. M. (1996). *Cosmological Blast Waves and the Intergalactic Medium.* ApJ**465**, 548.

Voit, G. M., Balogh, M. L., Bower, R. G., Lacey, C. G. & Bryan, G. L. (2003). *On the Origin of Intracluster Entropy.* ApJ**593**, 272–290.

Voit, G. M., Kay, S. T. & Bryan, G. L. (2005). *The baseline intracluster entropy profile from gravitational structure formation.* MNRAS**364**, 909–916.

Volonteri, M. (2010). *Formation of supermassive black holes.* A&A Rev.**18**, 279–315.

Vorobyov, E. I. & Basu, S. (2005). *The effect of a finite mass reservoir on the collapse of spherical isothermal clouds and the evolution of protostellar accretion.* MNRAS**360**, 675–684.

Vorobyov, E. I., DeSouza, A. L. & Basu, S. (2013). *The Burst Mode of Accretion in Primordial Protostars.* ApJ**768**, 131.

Wang, R., Wagg, J., Carilli, C. L., Walter, F., Lentati, L., Fan, X., Riechers, D. A., Bertoldi, F., Narayanan, D., Strauss, M. A., Cox, P., Omont, A., Menten, K. M., Knudsen, K. K., Neri, R. & Jiang, L. (2013). *Star Formation and Gas Kinematics of Quasar Host Galaxies at z ˜ 6: New Insights from ALMA.* ApJ**773**, 44.

Willott, C. J., Albert, L., Arzoumanian, D., Bergeron, J., Crampton, D., Delorme, P., Hutchings, J. B., Omont, A., Reylé, C. & Schade, D. (2010). *Eddington-limited Accretion and the Black Hole Mass Function at Redshift 6.* AJ**140**, 546–560.

Willott, C. J., McLure, R. J. & Jarvis, M. J. (2003). *A* 3×10^9 M_{solar} *Black Hole in the Quasar SDSS J1148+5251 at z=6.41.* ApJ**587**, L15–L18.

Wise, J. H., Turk, M. J., Norman, M. L. & Abel, T. (2012). *The Birth of a Galaxy: Primordial Metal Enrichment and Stellar Populations.* ApJ**745**, 50.

Wolcott-Green, J. & Haiman, Z. (2011). *Suppression of HD cooling in protogalactic gas clouds by Lyman-Werner radiation.* MNRAS**412**, 2603–2616.

Wolcott-Green, J., Haiman, Z. & Bryan, G. L. (2011). *Photodissociation of* H_2 *in protogalaxies: modelling self-shielding in three-dimensional simulations.* MNRAS**418**, 838–852.

Wolfire, M. G., Hollenbach, D., McKee, C. F., Tielens, A. G. G. M. & Bakes,

E. L. O. (1995). *The neutral atomic phases of the interstellar medium.* ApJ**443**, 152–168.

Woods, T. E., Heger, A., Whalen, D. J., Haemmerle, L. & Klessen, R. S. (2017). *On the Maximum Mass of Accreting Primordial Supermassive Stars.* ArXiv e-prints .

Woosley, S. E. & Weaver, T. A. (1995). *The Evolution and Explosion of Massive Stars. II. Explosive Hydrodynamics and Nucleosynthesis.* ApJS**101**, 181.

Wu, X.-B., Wang, F., Fan, X., Yi, W., Zuo, W., Bian, F., Jiang, L., McGreer, I. D., Wang, R., Yang, J., Yang, Q., Thompson, D. & Beletsky, Y. (2015). *An ultraluminous quasar with a twelve-billion-solar-mass black hole at redshift 6.30.* Nature**518**, 512–515.

Yajima, H., Choi, J.-H. & Nagamine, K. (2011). *Escape fraction of ionizing photons from high-redshift galaxies in cosmological SPH simulations.* MNRAS**412**, 411–422.

Yoshida, N. (2006). *From the first stars to the first galaxies.* New Astronomy Reviews, **50**, 19–23.

Yoshida, N., Abel, T., Hernquist, L. & Sugiyama, N. (2003). *Simulations of Early Structure Formation: Primordial Gas Clouds.* ApJ**592**, 645–663.

Yoshida, N., Oh, S. P., Kitayama, T. & Hernquist, L. (2007). *Early Cosmological H II/He III Regions and Their Impact on Second-Generation Star Formation.* ApJ**663**, 687–707.

Yoshida, N., Omukai, K. & Hernquist, L. (2008). *Protostar Formation in the Early Universe.* Science **321**, 669.

Yoshida, N., Omukai, K., Hernquist, L. & Abel, T. (2006). *Formation of Primordial Stars in a ΛCDM Universe.* ApJ**652**, 6–25.